Induced topological superconductivity in HgTe based nanostructures

Dissertation zur Erlangung des naturwissenschaftlichen Doktorgrades der Julius-Maximilians-Universität Würzburg

vorgelegt von

Jonas Wiedenmann

aus Würzburg

Würzburg, 2017

Eingereicht am: 26.10.2017
bei der Fakultät für Physik und Astronomie

1. Gutachter: Prof. H. Buhmann
2. Gutachter: Prof. B. Trauzettel
3. Gutachter: Prof. T. Klapwijk
der Dissertation

Vorsitzende(r): Prof. H. Hinrichsen
1. Prüfer: Prof. H. Buhmann
2. Prüfer: Prof. B. Trauzettel
3. Prüfer: Prof. M. Bode
im Promotionskolloquium

Tag des Promotionskolloquiums: 04.05.2018

Doktorurkunde ausgehändigt am: .....

CONTENTS

1

INTRODUCTION

With our kids I shared my enthusiasm (...) referring to balls changing color upon reflection of the walls and rising higher and higher until they would go over the roof.

T. M. Klapwijk, Proximity Effect From an Andreev Perspective[1]

A material which has zero electrical resistance and expels an external magnetic field completely from its interior is called a superconductor. This state of matter, which was discovered over a hundred years ago by Heike Kamerlingh Onnes [2] is to this day one of the most fascinating and active phenomena in condensed matter research [3]. Even though superconductivity is still an effect which occurs only at low temperatures, it has found numerous practical applications such as superconducting magnets used in medical nuclear magnetic resonance machines and superconducting tunnel devices used as sensitive magnetometers or particle detectors [4, 5]. Furthermore, quantum computers based on superconducting circuits are about to transition from academic research to industry [6–8].

After the discovery of superconductivity, it took almost 50 years until John Bardeeen, Leon Cooper and Robert Schrieffer developed a "Microscopic theory of superconductivity", nowadays known as the BCS-theory [9]. The breakthrough idea was that electrons form pairs (Cooper pairs) and overcome their Coulomb repulsion due to an arbitrarily small positive attraction originating from electron-lattice interactions [10]. Instead of describing the wave function of each electron individually with an individual phase, as is done in ordinary metals, the ground state of all Cooper pairs can be described by one coherent and macroscopic wave function with one phase ϕ.

In 1962, Brian Josephson predicted that Cooper pairs can tunnel through a thin insulating barrier separating two superconductors, described by phase ϕ_1 and ϕ_2 [11]. This prediction involves two physical processes which are formulated in the first and second Josephson equations respectively. The first one says that at zero voltage a supercurrent

can flow through the device, which depends on the phase difference of the two superconductors $\Delta\phi = \phi_1 - \phi_2$. The second equation predicts that a finite dc voltage drop across the junction generates an oscillating current. The Josephson effect has been verified in numerous experiments [12–15]. Even though the Josephson effect is a macroscopic quantum phenomenon it is influenced by microscopic properties of the superconductor and the barrier in between. The barrier between the two superconductors, sometimes also called "weak link", can be an insulator as in Josephson's pioneering work. It is also possible that the weak link consists of other materials such as a normal metal, a semiconductor, or a constriction. The transport through this barrier can then be described in the conceptual framework as introduced by Landau and Büttiker [16, 17] based on transmission matrices and the Andreev reflection process [18, 19]. The resulting microscopic description of the Josephson effect gives rise to states which are localized inside the barrier and are called Andreev bound states. The energy of these states and also the current depend on the phase difference $\Delta\phi$ of the two superconductors and the normal state transmission of each channel. Consequently, Josephson junctions can be used to probe the properties of the superconductors.

An example where this was successfully used was the proof of d-wave pairing symmetry in high temperature superconductors [20]. Most elemental supercondcutors have a superconducting gap which is isotropic. This is described by a wave function with zero angular momentum ($l_s = 0$) and is, in analogy to the atomic orbitals, called s-wave superconductivity. Electrons with opposite spin form a Cooper pair and the total spin is zero ($s_s = 0$). In contrast, a d-wave superconductor has higher order orbital contributions ($l_d = 2$), which resemble "pear-shaped lobes", but the total spin is still zero ($s_d = 0$). This combination of a symmetric wave function in momentum space and an antisymmetric wave function in spin space needs to be satisfied as fermions obey the Pauli exclusion principle (this statement is equivalent to demand that the total wave function of fermions has to be antisymmetric).

This implies that for a superconductor with odd momentum ($l_p = 1$) the total wave function is only antisymmetric if triplet Cooper pairs are formed ($s_p = 1$). It is exactly this triplet pairing, which makes p-wave superconductors fundamentally different from s- or d-wave superconductors. In general p-wave superconductors based on intrinsic superconductivity of the material are rare in nature. The compound Sr_2RuO_4 is potentially a p-wave superconductor, but so far it has not been successful to unambiguously prove the p-wave character [21]. This kind of superconductors are of great interest both from a fundamental and also practical perspective as a peculiar fermionic quasiparticle excitation at zero energy, a so called "Majorana zero mode", is predicted to emerge at vortices or edges of such a system. This new particle is its own anti-particle; the creation operator or annihilation operator of this state are the same. Furthermore, these states obey an exchange statistics different from "normal"fermions and belong to a class of quasiparticles called non-abelian anyons. These particles can be used as building blocks for topological quantum computation, which is predicted to be more stable than other quantum computing systems against certain types of decoherence [22].

An alternative approach to creating p-wave superconductivity is the combination of conventional superconductors with materials where the spin-degeneracy is inherently lifted [23, 24]. One possible method to realize this is to use topological insulators; this is a

material class with insulating bulk but metallic surface states where the electron spin and momentum are locked to each other [25, 26].

In this thesis, the theoretical proposals of Liang Fu and Charles Kane in Refs. [23, 24] are followed. Superconducting pair correlations are induced into the surface states of mercury telluride (HgTe), a well studied 2D and 3D dimensional topological insulator [27, 28]. In order to show that this system has topological properties, Josephson junctions where the weak link is a topological insulators are fabricated and the fractional Josephson effect, a signature of topological superconductivity is observed. In a topological Josephson junction, the phase of Andreev bound states varies 4π-periodic instead of the 2π-periodicity of conventional bound states.

The outline of the thesis is as follows:

- Chapter 2 introduces the theoretical concepts of topology in condensed matter systems and in particular in topological band insulators and topological superconductors from the perspective of an experimentalist. It is shown that HgTe with its inverted band structure is an ideal candidate for the realization of topological insulators. It is further shown that the combination of superconductivity and topological surface states leads to an effective p-wave superconductivity with Majorana bound states when the excitation gap locally closes. In order to study these states, Josephson junctions and the concept of Andreev bound states are described and the characteristic differences between a topological Josephson junction and a conventional Josephson junction are highlighted. At the end of the chapter a brief motivation for the interest in Majorana fermions in the context of quantum computation is given.

- Chapter 3 describes the ac behaviour of a Josephson junction based on thick tensile strained layers of HgTe. In such structures, a 4π-periodic Andreev bound state, a so-called gapless Andreev bound state, is predicted to exist. By illuminating the Josephson junction with microwaves, steps of constant voltage form in the $I-V$ characteristics. In a conventional Josephson junction, the distance in voltage between two consecutive steps is for a fixed frequency quantized. In contrast the steps are twice as high in a topological Josephson junction which contains gapless Andreev bound states. In a 3D TI based weak link one gapless mode but also many conventional modes are expected. The interplay between these two contributions is studied as a function of rf frequency and rf power.

- Chapter 4 deals with the numerical modelling of the $I-V$ characteristics of a topological Josephson junction under rf illumination, in order to understand the behaviour of the missing odd Shapiro steps. This is commonly done in a lumped element model where a Josephson junction is shunted by an ohmic resistor. This model is called the resistively shunted Josephson junction (RSJ) model. The linear combination of a 2π- and a 4π-periodic supercurrent (i.e. a $\sin\phi$ and $\sin\phi/2$ contribution) is leading to a non-linear differential equation.

- In chapter 5, the study of a Josephson junction based on a HgTe quantum well, a two dimensional topological insulator, is described. The material is characterized and the fabrication of the weak link is detailed. In such a weak link the one dimensional

helical edge channels in combination with conventional superconductivity give rise to 1D p-wave superconductivity. By studying the response to a magnetic field applied perpendicular to the sample plane, it is possible to determine the current distribution in the Josephson junction. This is done as a function of applied gate voltage. In addition, under microwave illumination, Shapiro steps emerge. A doubling of the voltage step size is expected due to the presence of gapless edge channels. This can evidence the presence of a 4π-periodic supercurrent contribution. The behaviour of a trivial HgTe quantum well, which is expected to behave like a conventional Josephson junction, is compared to the topological quantum well.

- Chapter 6 outlines a method for probing the periodicity of the Andreev bound states involving the measurement of the emitted Josephson radiation. This method is more direct than the Shapiro step measurements described in chapter 5. A dc voltage bias V across a conventional Josephson junction is converted into an ac radiation with frequency $f_J = 2eV/h$ according to the second Josephson equation. In contrast, the ac frequency of a topological Josephson junction with gapless Andreev bound states is half of the fundamental frequency, i.e. $f_J/2$. The emission spectrum of a weak link of a topological HgTe quantum well was measured as a function of applied bias voltage and gate voltage. The results are compared to the emission spectrum of a trivial quantum well.

- Chapter 7, the last part of the thesis describes the study of the proximity induced superconductivity in a 3D topological insulator using point-contact spectroscopy. This geometry allows the energy dependence of the proximity induced superconducting state to be accessed. The point-contact was defined lithographically and a superconductor was deposited to induce superconducting correlations. The differential conductance is studied as a function of temperature, magnetic field strength and gate voltage. In such a geometry effects like crossed Andreev reflections and specular Andreev reflection are expected due to the Dirac like band structure of the topological insulator. Furthermore, the induced state resembles that of a 2D $p_x + ip_y$ superconductor.

Finally a summary of the thesis is given. All chapters are written self-contained and it should be possible to read each chapter individually. Nevertheless, chapter 2 summarizes the theoretical background for all the following parts.

BIBLIOGRAPHY

[1] T. M. Klapwijk, *Proximity Effect From an Andreev Perspective,* Journal of Superconductivity **17**, 593 (2004).

[2] D. Van Delft and P. Kes, *The discovery of superconductivity,* Physics Today **63**, 38 (2010).

[3] H. Rogalla and P. H. Kes, *100 years of superconductivity* (Taylor & Francis, 2011).

[4] D. Twerenbold, *Cryogenic particle detectors,* Reports on Progress in Physics **59**, 349 (1996).

[5] J. Clarke and A. I. Braginski, *The SQUID Handbook: Applications of SQUIDs and SQUID Systems* (John Wiley & Sons, 2006).

[6] D. Castelvecchi, *Quantum computers ready to leap out of the lab in 2017,* Nature **541**, 9 (2017).

[7] M. H. Devoret, A. Wallraff, and J. M. Martinis, *Superconducting qubits: A short review,* arXiv preprint cond-mat/0411174 (2004).

[8] T. F. Rønnow, Z. Wang, J. Job, S. Boixo, S. V. Isakov, D. Wecker, J. M. Martinis, D. A. Lidar, and M. Troyer, *Defining and detecting quantum speedup,* Science **345**, 420 (2014).

[9] J. Bardeen, L. N. Cooper, and J. R. Schrieffer, *Microscopic Theory of Superconductivity,* Physical Review **106**, 1175 (1957).

[10] L. N. Cooper, *Bound Electron Pairs in a Degenerate Fermi Gas,* Physical Reviews **104**, 1189 (1956).

[11] B. Josephson, *Possible new effects in superconductive tunnelling,* Physics Letters **1**, 251 (1962).

[12] P. W. Anderson and J. M. Rowell, *Probable Observation of the Josephson Superconducting Tunneling Effect,* Physical Review Letters. **10**, 230 (1963).

[13] P. W. Anderson and A. H. Dayem, *Radio-Frequency Effects in Superconducting Thin Film Bridges,* Physical Review Letters **13**, 195 (1964).

[14] S. Shapiro, *Josephson Currents in Superconducting Tunneling: The Effect of Microwaves and Other Observations,* Physical Review Letters **11**, 80 (1963).

[15] R. C. Jaklevic, J. Lambe, A. H. Silver, and J. E. Mercereau, *Quantum Interference Effects in Josephson Tunneling,* Physical Review Letters. **12**, 159 (1964).

[16] M. Büttiker, *Absence of backscattering in the quantum Hall effect in multiprobe conductors,* Physical Review B **38**, 9375 (1988).

[17] S. Datta, *Electronic transport in mesoscopic systems* (Cambridge university press, 1997).

[18] M. Tinkham, *Introduction to superconductivity* (Courier Corporation, 1996).

[19] A. Andreev, *Thermal conductivity of the intermediate state of superconductors, II,* Journal of Experimental and Theoretical Physics (JETP) **20**, 1490 (1965).

[20] D. A. Wollman, D. J. Van Harlingen, W. C. Lee, D. M. Ginsberg, and A. J. Leggett, *Experimental determination of the superconducting pairing state in YBCO from the phase coherence of YBCO-Pb dc SQUIDs,* Physical Review Letters. **71**, 2134 (1993).

[21] A. P. Mackenzie, T. Scaffidi, C. W. Hicks, and Y. Maeno, *Even odder after twenty-three years: the superconducting order parameter puzzle of Sr_2RuO_4,* arXiv preprint arXiv:1706.01942 (2017).

[22] M. Freedman, A. Kitaev, M. Larsen, and Z. Wang, *Topological quantum computation,* Bulletin of the American Mathematical Society **40**, 31 (2003).

[23] L. Fu and C. Kane, *Superconducting Proximity Effect and Majorana Fermions at the Surface of a Topological Insulator,* Physical Review Letters **100**, 096407 (2008).

[24] L. Fu and C. Kane, *Josephson current and noise at a superconductor/quantum-spin-Hall-insulator/superconductor junction,* Physical Review B **79**, 161408 (2009).

[25] C. L. Kane and E. J. Mele, *Z_2 Topological Order and the Quantum Spin Hall Effect,* Physical Review Letters **95**, 146802 (2005).

[26] L. Fu and C. L. Kane, *Topological insulators with inversion symmetry,* Physical Review B **76**, 045302 (2007).

[27] C. Brüne, C. X. Liu, E. G. Novik, E. M. Hankiewicz, H. Buhmann, Y. L. Chen, X. L. Qi, Z. X. Shen, S. C. Zhang, and L. W. Molenkamp, *Quantum Hall Effect from the Topological Surface States of Strained Bulk HgTe,* Physical Review Letters **106**, 126803 (2011).

[28] M. König, S. Wiedmann, C. Brüne, A. Roth, H. Buhmann, L. W. Molenkamp, X.-L. Qi, and S.-C. Zhang, *Quantum Spin Hall Insulator State in HgTe Quantum Wells,* Science **318**, 766 (2007).

2

TOPOLOGY IN CONDENSED MATTER AND THE EMERGENCE OF MAJORANA FERMIONS

One of the most fascinating and ambitious goals in contemporary condensed matter physics is the experimental engineering, proof, and manipulation of Majorana bound states. In this thesis, theoretical ideas of such bound states when topological insulators are combined with conventional superconductors have been investigated. A comprehensive introduction is given in order to facilitate the understanding of the theoretical and experimental aspects of the topic. First, the concept of topology in condensed matter is explained. Second, using a Dirac Hamiltonian with linear band dispersion, the key properties of topological systems are discussed. Third, it is shown that the band structure of HgTe quantum wells can be cast into two time-reversal copies of a Dirac Hamiltonian forming a quantum spin Hall insulator, which is a two dimensional topological insulator. Fourth, this concept is extended to the case of a three dimensional topological insulator. Fifth, in order to expound the concept of topological superconductivity, a short primer on the theory of superconductivity and especially the Bogoliubov-de Gennes representation is introduced. Sixth, it is shown that an one dimensional spinless superconductor can under certain conditions host topological end states, so called Majorana fermions. Finally the concepts of conventional superconductivity and topological insulators are combined to form topological superconductivity. Topological superconductivity is the key idea of the present thesis. The experimental signatures of such a system, namely the fractional Josephson effect is derived. In fact, the main goal of this thesis is the experimental verification and proof of the fractional Josephson effect.

2.1. TOPOLOGY IN CONDENSED MATTER

The classification of objects which can be transformed into each other under continuous deformations is investigated in the mathematical field of topology. An often used example is that a sphere can be deformed into an ellipsoid by for example stretching it, but it is impossible to transform it into a doughnut without cutting a hole in it [1].Thus, by topological classification, the ellipsoid and the sphere belong to the same class, while the doughnut belongs to a different topological class.

This concept can now be applied to classify Hamiltonians by their topological properties and look for topological distinct phases. In fact, D. J. Thouless, F. D. M. Haldane and J. M.Kostelitz were awarded the Nobel prize in physics in 2016 "for theoretical discoveries of topological phase transitions and topological phases of matter ". Using this classification, two systems, described by the Hamiltonians H and H' are said to be topologically equivalent, if it is possible to find a smooth (adiabatic) transformation, which perseveres the symmetries from one Hamiltonian into the other, i.e.

$$H(\alpha) = \alpha H' + (1-\alpha)H, \tag{2.1}$$

where for $\alpha = 0$, the system is in its initial Hamiltonian H and for $\alpha = 1$ in the final Hamiltonian H'.

In this thesis we limit ourself to gapped systems, where the ground state and the excited state are separated by a finite energy gap, such as in the case in band insulators or, as we will see later, very similar in superconductors. Such systems are now said to be in the same topological class if the transformation described in Eq. 2.1 does not close the bulk band gap. As will be shown, the topological invariants of a given system heavily depend on the underlying symmetries and dimensions of the Hamiltonian [2]. The two major symmetries dealt with in this thesis are the time reversal symmetry (TRS), for topological band insulators and the particle-hole symmetry for topological superconductors.

In general this classification is done by finding integer numbers called topological invariants which can only change when the bulk gap closes. Historically the first condensed matter system which was found to be topological is the quantum Hall state (QH) [3, 4]. An electron in a two dimensional electron gas is forced on a circular motion by applying a perpendicular magnetic field. If the strength of the field is large enough, the motion of electrons form closed loops (Landau-levels), which are quantized . These closed loops turn a metallic bulk system insulating, while at the edges conducting channels, so called QH channels, form which lead to a quantized Hall conductivity of $\sigma_{xy} = Ne^2/h$. The number of filled Landau-levels N forms an integer which corresponds to these topologically protected edge states.

A simple Hamiltonian, which is linear in momentum and breaks TRS can be used to see how such edge states form, and what the topological invariant of the system is. Then, the amount of degrees of freedom are doubled which allows topological insulators without explicitly breaking TRS. We are able to show that the band structure of HgTe quantum wells resemble exactly such a state in the low energy limit.

2.2. TOPOLOGICAL BAND INSULATORS

The presence of topological invariants is directly linked to the symmetries of the underlying system. In the case of band insulators it is the TRS. A system is invariant under TRS if it does not change under the direction of time flow $t \mapsto -t$. In general this can be defined for an arbitrary Hamiltonian H as

$$THT^{-1} = H, \tag{2.2}$$

where T is the time reversal operator which can be defined for a fermionic spin 1/2 system as $T = i\sigma_y C$, with σ_i being the Pauli-matrices and C the complex conjugation operator [5]. Effectively, this operation takes the complex conjugate of the wave function and flips the spin. One important consequence of a TR-invariant system and also for topological matter is the Kramers' degeneracy theorem which states that each energy level is at least doubly degenerate[1]. Usually, this degeneracy is the spin of the system.

2.2.1. CHERN INSULATOR AND BULK BOUNDARY CORRESPONDENCE

Before discussing time-reversal invariant topological insulators (TIs), it is instructive to look at systems where TRS is explicitly broken. Due to its deep consequences and the fact that a lot of systems in chapters dealing with edge states of TIs and low energy Hamiltonian of the topological superconductivity, it is useful to introduce the two band Dirac Hamiltonian:

$$H_{\text{Dirac}}(k) = \hbar v_F k\vec{\sigma} + m\sigma_z = \begin{pmatrix} m & \hbar v_F(k_x - ik_y) \\ \hbar v_F(k_x + ik_y) & -m \end{pmatrix} \tag{2.3}$$

with v_F being the Fermi velocity, $\hbar$ the reduced Planck constant, $\vec{\sigma} = (\sigma_x, \sigma_y, \sigma_z)$ the Pauli matrices, and m the massive mass. The basis of the system is $\Psi = (\Psi_e, \Psi_h)$. This system can be used to for example describe a two dimensional electron gas with linear dispersion without spin degeneracy in presence of a perpendicular magnetic field $m\sigma_z$. The energy spectrum yields $E(k) = \pm\sqrt{|\hbar v_F k|^2 + m^2}$. For a finite mass, this is a gapped spectrum with a band gap at $k = 0$ and a separation of the bands by a value of $2m$. It is also possible to show that the mass term also explicitly breaks the TRS of the system. At this point it is a purely an academic question what happens if the sign of the mass changes. Looking at the energy dispersion, the change from $m \to -m$ does not affect the bulk properties of the system, but their topological invariants differ. The two cases refer to two distinct topological classes. The Chern number defined as the total Berry flux in the Brillouin zone characterizes the topological invariant of a Hamiltonian and is different for positive and negative mass [1]. The two Hamiltonians can only be transformed into each other by closing the bulk band gap.

[1] Proof: Consider two states $|\pm\rangle$ which are related by TRS $|+\rangle = T|-\rangle$. If the Hamiltonian is invariant under TRS the two states correspond to the same energy. Now using the property $T^2 = -1$, yields $\langle +|-\rangle = \langle -|T^\dagger T^{-1}|+\rangle = -\langle -|+\rangle^* = -\langle +|-\rangle$. This means that the product needs to be zero i.e. the two states are orthogonal.

BULK BOUNDARY CORRESPONDENCE

An important consequence of topological classification of matter occurs, if two insulating materials with different topology (i.e. here different mass signs) are brought into contact[2]. As the topology of the two systems cannot change adiabatically without closing the gap, the invariant has to change somewhere in between, crossing zero energy which results in the formation of gapless edge states.

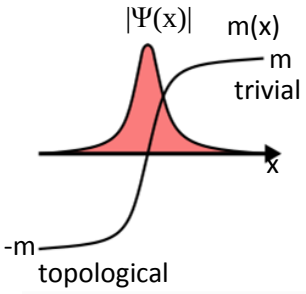

Figure 2.1: Sketch the mass m as a function of coordinate x as given in Eq. 2.4. The absolute value of the wave function Ψ is shown in red.

It is now worth following the idea by Jackiw and Rebbi [6] who looked at the one dimensional case of a mass sign change. In our case we can create such a system by assuming a semi-infinite plane with translational invariance along the y-axis and a mass change as a function of the coordinate x

$$m(x) \to \pm m \text{ for } x \to \pm\infty \text{ and } m(x=0) = 0. \tag{2.4}$$

The momentum k_y is still a good quantum number and it is therefore possible to separate both wave functions and use plane waves for the y-direction $\Psi(x,y) = e^{iky}\Phi(x)$. The system can be reduced to a one dimensional problem and we are now interested in states at zero energy, therefore we are looking for solutions for $H\Psi = 0$:

$$[-i\hbar v_F \sigma_x \partial_x + m(x)\sigma_z]\Psi(x) = 0 \tag{2.5}$$

where we used $k_x = -i\partial_x$. Solving this equation leads to

$$\Psi(x,y) \propto e^{iky} e^{\frac{1}{\hbar v_F}\int_0^x dx' m(x')} \begin{pmatrix} 1 \\ -1 \end{pmatrix} \tag{2.6}$$

with $E(k_x) = \hbar v_F k_x$. This solution describes a localized state at $(x = 0)$ which decays exponentially in the bulk as depicted in Fig. 2.1. It is a gapless or zero energy mode with a positive group velocity along the y-direction forming a chiral edge mode i.e. a quantum Hall insulator and is commonly referred to as a Chern Insulator where the

[2]Note that the vacuum is a trivial insulator. The energy gap of the vacuum is determined by $\Delta = 2m_e c^2 \approx 1 \times 10^6$ eV, which is the energy needed to create a electron-positron pair by ionising the vacuum.

topological invariant corresponds to the number of edge channels. This is an important consequence which must be emphasized ones again. At the boundary of two distinct topological phases, gapless surface states form. This result can be extended to other topological to trivial transitions as for example in superconductors. Using these concepts, the physical meaning of mass inversion, i.e. replacing m by $-m$ in the Hamiltonian, can now be established in the special case of the quantum spin Hall insulator and HgTe quantum wells. One has to keep in mind that edge states in a 2 dimensional system form 1 dimensional conduction channels while in 3 dimension, 2 dimensional surface states form.

2.2.2. QUANTUM SPIN HALL INSULATOR

In treating the Chern insulator model under section 2.2.1 the spin degree of freedom was neglected. The key idea of time reversal invariant topological matter is to double the degree of freedom of the spinless model by taking the electron spin into account. In this regard a strong spin-orbit interaction plays the role of a momentum depended effective magnetic field but with a different sign for each spin direction $(\uparrow,\downarrow)$. The simplest model,

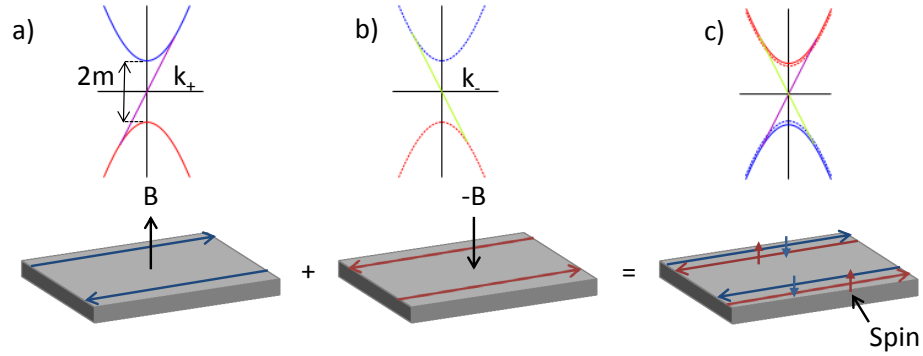

Figure 2.2: Construction of a quantum spin hall insulator from two counter propagating Chern insulators.

named after Bernevig, Hughes and Zhang the so called BHZ-model [7], is constructed from two Dirac Hamiltonians H_{Dirac}

$$H_{\text{BHZ}} = \begin{pmatrix} H_{\text{Dirac}} & 0 \\ 0 & T H_{\text{Dirac}} T^{-1} \end{pmatrix}. \tag{2.7}$$

This formalism enforces TRS of the system. The basis is now a four component spinor

$$\Psi(r) = [\Psi_{e\uparrow}(r), \Psi_{h\downarrow}(r), \Psi_{h\uparrow}(r), \Psi_{e\downarrow}(r)], \tag{2.8}$$

where the indices e or h stand for the electron or hole band and the arrows for the spin direction. Changing the sign of mass m in this system with spatial coordinates in analogy to the Chern insulator one gets two counter propagating edge channels, as shown in Fig. 2.2 since it is basically two copies of a quantum Hall state with different spin directions. It is worth mentioning that as we have now two counter propagating

edge channels, the Chern number of the total system is zero. But there exists another $\mathbb{Z}_2$ invariant which protects the edge channels.

The edge channels are helical, i.e. the wave function are related by $\Psi_{-k,\downarrow} = T\Psi_{+k,\downarrow}$. They are spin polarized with a quantized spin Hall conductance and thus this effect is called "Quantum Spin Hall Effect"(QSHE) in analogy to the QHE with quantized charge conductance. The two channels form Kramers pairs and are therefore forbidden from scattering into each other as long as TRS is preserved[3]. It is exactly this property of perfectly transmitting spin polarized edge channels which makes them so interesting. The energy dispersion can then be calculated using the fact that the two diagonal blocks are decoupled. The upper block yields

$$E^{(1,2)} = E^{(e\uparrow,h\downarrow)}(k) = \pm \mathrm{sgn}(m)\sqrt{(\hbar v k^2) + m^2} \tag{2.9}$$

and is related to the lower block by $E^{(e\uparrow,h\downarrow)}(k) = -E^{(h\uparrow,e\downarrow)}(k) = E^{(3,4)}$.

The band structure for the normal ($m > 0$) and negative case ($m < 0$) are shown in Fig. 2.3. At this point, we are finally able to identify the physical meaning involving the sign change of the mass. For a mass $m > 0$, the electrons form the conduction band and have a higher energy than the holes. Both are separated by a total energy gap of size $2m$. On the other hand for $m < 0$, the hole bands have a higher energy. This latter case is called an inverted band structure and is a necessary property of any topological band insulator.

One can now discuss an intuitive picture for the emergence of metallic edge states by considering the continuity of the bands when the mass changes sign. The bands need to reverse their order which leads to the formation of edge states as is shown in Fig. 2.3.

Finally we are able to summarize the requirements for a physical system to be a quantum spin Hall insulator (QSHI). It needs to contain electron and hole bands which are coupled by a linear term. Furthermore, the band structure needs to be inverted. Before it is shown that HgTe quantum wells of sufficient thickness host the quantum spin Hall phase a brief section on the determination and interpretation of the $\mathbb{Z}_2$ invariant is presented.

2.2.3. TOPOLOGICAL BAND THEORY

Using the translation symmetry of periodic crystals it is possible to describe the electronics states by the lattice momentum k spanning the Brillouin zone (BZ). The so called Bloch states $|u_n(k)\rangle$ are solutions for such a periodic system, where the index n accounts for possible spin or lattice degrees of freedom. For a TRS Bloch Hamiltonian for spin 1/2 particles, the two Kramers' partners are $|u_{\alpha\uparrow}(k)\rangle$ and $|u_{\alpha\downarrow}(-k)\rangle$. The periodicity of the Brillouin zone requires that momenta k which are separated by $n\frac{2\pi}{a}$, $n \in \mathbb{Z}$ and a being the lattice constant, should be equal. There exist special time reversal invariant momenta (TRIM) Λ where, due to TRS, the two Kramers' partners are mapped onto themselves and have to be degenerate at those points ($k = 0$ and π/a in the 1D BZ) [8, 9].

We define a matrix $w_{mn}(k) = \langle u_m(k)|T|u_n(-k)\rangle$ with the property $w_{mn}(-k) = -w_{nm}(k)$, which at the points Λ makes the matrix antisymmetric. The determinant of a antisym-

[3]The two states $|\pm\rangle$ are connected via TRS $|+\rangle = T|-\rangle$. The matrix element of a hermitian scattering potential $V = TVT^{-1}$ preserving TRS between the two edge channels $\langle +|V|-\rangle = -\langle +|V^\dagger|-\rangle = 0$ vanishes.

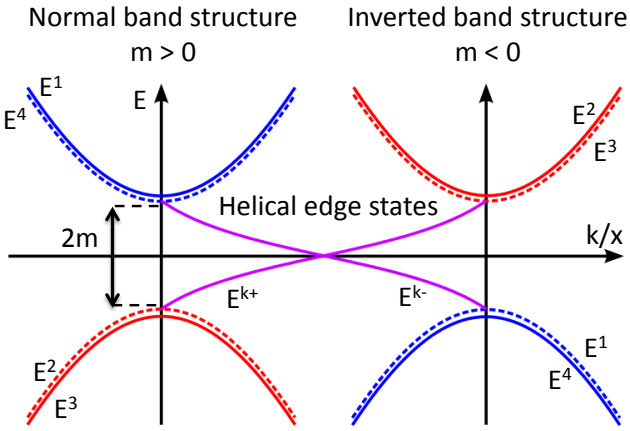

Figure 2.3: Band structure of a TRS Chern insulator for two different mass signs and the emergence of helical surface states at domain walls.

metric matrix is the square of its Pfaffian [9, 10]. It is now possible to calculate a number

$$\delta_a = \frac{\mathrm{Pf}[w(\Lambda)]}{\mathrm{Det}[w(\Lambda)]} = \pm 1, \tag{2.10}$$

where the $\mathbb{Z}_2$ invariant ν of the whole system can be calculated by $(-1)^\nu = \prod_{i=1}^{n} \delta_a$. Here n is the number of time invariant points Λ and can take the values 0 (trivial) or 1(topological). This number can in principle be calculated for any Hamiltonian H and is therefore a powerful tool to classify matter. This rather abstract formulation can be interpreted as how the Kramers' pairs of the bands are connected as shown in Fig. 2.4. The topological trivial case is shown in Fig. 2.4a) where the TRIM points are connected pairwise and it is possible to find a transformation such that there are no states cutting the Fermi energy E_F ($\nu = 0$). The situation is different if the TRIM are connected as shown in Fig. 2.4b, where independent of the position of E_F or the TRIM points there is always a level remaining ($\nu = 1$). Therefore, the number ν can be interpreted as either an even or odd number of band crossings and is usually described by a $\mathbb{Z}_2 = \nu \bmod 2$ invariant. This theory can be extended straight forwardly to higher dimensions, where now in addition to the strong invariant ν_0 calculated from Eq. 2.10, there exist three so called weak topological invariants (ν_1, ν_2, ν_3).

2.2.4. BAND STRUCTURE OF HGTE

HgTe is a II-VI compound, which grows in the zinc-blende lattice structure [7, 11]. The bonds are formed between the 6s electrons of the Hg and the 5p electrons of the Te atoms. The important bands lie at the Γ-point of the BZ. Due to the strong spin orbit interaction of the heavy Te atoms, the band structure is inverted with a negative energy gap of $E = -300\,\mathrm{meV}$ between the Γ_6 and the Γ_8 bands as depicted in Fig. 2.5. The s-type Γ_6-band lies below the p-type Γ_8-band ($J = 3/2$) which exhibits a light and heavy state dispersion. The Γ_7-band lies energetically well below the Γ_6-band and can, in a first order

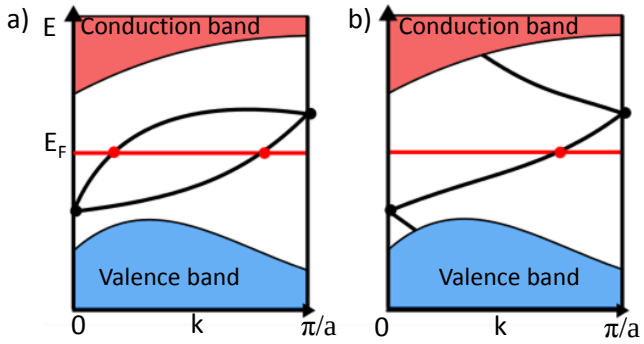

Figure 2.4: Figures a) and b) show the bandstructure of a bulk insulator and the different ways to connect the TRIM in the BZ of states in the gap.

approximation, be omitted in the discussion. The Fermi energy lies at the degenerate Γ_8-band making the bulk material a zero gap semiconductor. For comparison, also the band structure of $Cd_{0.7}Hg_{0.3}Te$, which is used as a barrier material in this thesis, is shown in Fig. 2.5. Here a normal band ordering leads to a gap of $E \approx +1\,\text{eV}$. Therefore we are already able to see that the (Hg,Cd) concentration allows the size of the band gap to be tuned and its sign to be reversed. Bulk HgTe exhibits no band gap, which is needed for a topological insulator as otherwise bulk modes would dominate the transport behaviour. However, in addition the possibility of adjusting the concentration, there are two other common methods which can be used to lift the degeneracy i.e. the opening of the energy gap at the Γ-point. The first one is to confine the material into lower dimensions and the second one by growing thin films of HgTe on CdTe which due to the different lattice constant leads to fully strained layers resulting in a finite gap of the bulk bands. Both methods have been used in this thesis. The Band structure of a HgTe quantum well (QW) is shown in the lower panel of Fig. 2.5. It is now possible to tune the band structure by adjusting the thickness of the HgTe layer between the $Cd_{0.7}Hg_{0.3}Te$. For very thin HgTe quantum well, the band structure is mostly dominated by the barrier material while the influence of the HgTe is increased by increasing the thickness of the QW. It is therefore possible, to tune the band structure from normal ordering (trivial) to an inverted (topological) regime. This transition occurs at a critical quantum well thickness of $d_c \approx 6.3\,\text{nm}$. Around the gap closing, all energy states apart from E_1 and H_1 are far away from the Fermi energy and it is therefore justified that a low energy Hamiltonian is reduced to these two bands as depicted in the lower part of Fig. 2.5. The eigenstates are now expressed in odd parity $E1$ and even parity $H1$ states which are both doubly degenerate due to TRS. Following the symmetry arguments of Winkler *et al.* [14], it is possible to construct the low energy Hamiltonian of HgTe quantum wells [7]. This basically yields the BHZ model of Eq. 2.7 with an additional quadratic term. This term actually plays no role in the topological properties of the system. Equation 2.11 omits two terms which are present in the original article [7]. The band offset C is chosen to be zero and we substitute $A = \hbar v_F$. Furthermore

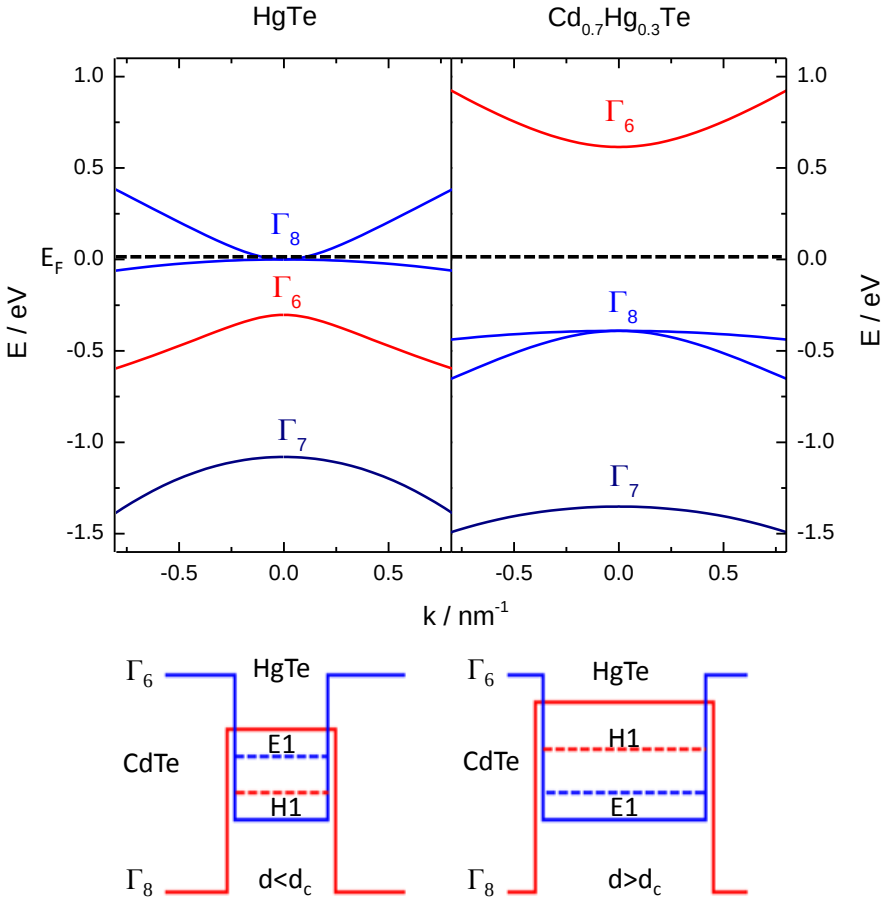

Figure 2.5: Upper panel: Bulk band structure of HgTe and $Cd_{0.7}Hg_{0.3}Te$ calculated by $k \cdot p$ method developed by [12, 13]. Lower panel: Schematic of a HgTe quantum well confined between two layers of CdTe. The band edges are shown and the confined energy levels of the electron and hole band are labelled E1 and H1 respectively. By adjusting the quantum well thickness d, it is possible to tune the band structure from a trivial regime for quantum wells below a critical thickness d_c (left) or into the topological for $d > d_c$ (right).

the basis is the same as in 2.7.

$$H_{\mathrm{HgTe}} = \begin{pmatrix} H_0(k) + H_{\mathrm{Dirac}}(k) & 0 \\ 0 & H_0^*(-k) + H_{\mathrm{Dirac}}^*(-k) \end{pmatrix} \tag{2.11}$$

where $H_0 = -D(k_x^2 + k_y^2)$.

Therefore, it is possible to state that the Hamiltonian of a HgTe quantum well of sufficient thickness can be reduced to the effective BHZ toy model which was shown to host the QSHI phase if brought into contact with a topological trivial material. Furthermore one can calculate the topological invariant of the system as discussed in section 2.2. This theoretical prediction was shortly thereafter experimentally verified by König *et al.* [15], by measuring the quantized longitudinal resistance in a transport experiment. Further experiments have proven the presence of edge channels by non-local transport and scanning SQUID[4] microscopy [16, 17] and the spin polarization of the edge states using the inverse spin Hall effect [18].

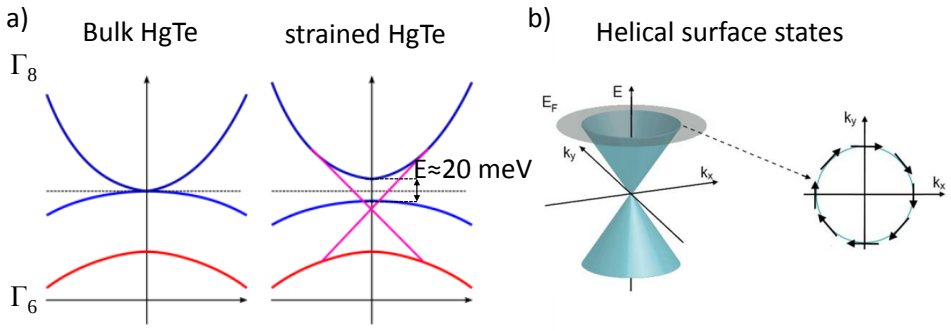

Figure 2.6: a) Band structure of bulk HgTe compared to tensile strained HgTe. b) Dispersion of the surface states with indicated spin momentum locking of the electrons.

2.2.5. STRAINED HGTE AS A THREE DIMENSIONAL TOPOLOGICAL INSULATOR

The concept of two the QSHI which resembles a 2-dimensional topological insulator (2D TI) was extended to 3 dimensions (3D TI) by considering eight TRIM points of the BZ and calculating the topological invariant for each side of a cube [9, 19, 20]. In total this yields three weak topological invariants ν_1, ν_2, and ν_3 and one strong topological invariant ν_0. In this thesis we limit ourselves only to the case of a strong topological insulator. There, 1D helical edge states of the QSH effect turn into 2D helical surface states of a bulk material as depicted in Fig. 2.6 b). Again the dispersion of a single surface can be described using the Dirac Hamiltonian with a helical pairing and zero mass[5]:

$$H_{\mathrm{surface}} = v_F(\sigma_x p_x + \sigma_y p_y) = v_F \begin{pmatrix} 0 & p_x - i p_y \\ p_x + i p_y & 0 \end{pmatrix} \tag{2.12}$$

[4] SQUID: Superconducting quantum interference device

[5] It is also possible to think of a QSHI as a thin 3D TI. If the thickness of the 3D TI is reduced in one dimension such that the wavefunctions of the surface states start to overlap e.g. the top and bottom surface they start interfering and cancelling each other out leaving only conducting edge channels.

with the basis $\Psi = (\Psi_\uparrow, \Psi_\downarrow)$. The energy dispersion is $E_{\text{surface}} = \pm v_F |p|$ which is sketched in Fig. 2.6b). It turns out that the requirements for a material to be a 3D TI are quite similar to the 2D case. A band inversion leads to the presence of surface states while a bulk band gap allows the surface states exclusively to be accessed. Again HgTe is a natural candidate with its inverted band structure however, the Fermi energy of HgTe bulk lies between the degenerate Γ_8-bands making HgTe a semimetal which would result in dominant bulk transport. By growing thin films of HgTe on a CdTe substrate, which has a different lattice constant, it is possible to open a band gap due to strain which lifts the degeneracy at the Γ-point opening a finite gap of about $\Delta E \approx 20\,\text{meV}$ [21]. The presence of Dirac like surface states with a linear dispersion was verified using ARPES[6] and transport measurements [21–23].

[6] ARPES: Angle resolved photoemission spectroscopy.

2.3. TOPOLOGICAL SUPERCONDUCTIVITY

Before being able to discuss topological superconductivity and the effects of introducing superconducting pairing into the edge states of topological insulators, an introduction to conventional superconductivity is presented. In this chapter the basic properties and a short introduction of the microscopic theory of superconductivity developed by Bardeen Cooper and Schrieffer (BCS) and the Bogoliubov-de Gennes representation are introduced. A comprehensive treatment of the topic is given, for example, in [24, 25].

2.3.1. PHENOMENOLOGY OF SUPERCONDUCTIVITY

For certain metals the electrical resistance vanishes and they become superconducting, when cooled down below a critical temperature T_c. For the metals used in this thesis, namely aluminium and niobium, the literature values given for T_c are 1.4 K and about 9.2 K, respectively [26]. The second defining property of superconductors is that they are ideal diamagnets, i.e., they exhibit a magnetic susceptibility $\xi = -1$ up to a critical field H_c. This effect is called the Meisssner effect and occurs due to screening current at the surface of the bulk superconductor. It implies that a magnetic field can not penetrate the bulk superconductor. It is important to note that there are some caveats to this. First in a narrow layer at the boundary of the superconductor a finite magnetic field can enter and decays exponentially to zero into the bulk superconductor on a characteristic length scale λ_L, known as the London penetration length [24]. Second superconductors can be divided into two classes called type I and type II. While a superconductor of type I expels a magnetic field up to its critical field H_c, at which the superconducting states breaks down, a type II superconductor has two critical fields. Up to H_{c1} a type II superconductor acts like the aforementioned ideal diamagnet, but superconductivity is not suppressed above this field. A finite magnetic field can enter the bulk in the form of so called Abrikosov vortices [27]. Each vortex carries exactly one flux quantum $\Phi_0 = h/2e$[7]. For the sake of completeness we mention also the third quantity which is able to break the superconductivity namely the critical current I_c.

2.3.2. MICROSCOPIC THEORY OF SUPERCONDUCTIVITY

A microscopic theory of superconductivity was developed by Bardeen, Cooper and Schrieffer, known as the BSC-theory [29, 30]. The key idea was to find an attractive interaction which exceeds the coulomb repulsion between two electrons forming a bosonic ground state. The authors found that a time retarded interaction mediated by the electron-phonon interaction can create an attractive interaction if the energy difference between the two electrons is smaller than $\hbar\omega_D$ where $\hbar$ is the reduced Planck constant and ω_D is the Debye frequency. A bound state with energy $E = -2\Delta$ can then form. Here Δ is the superconducting pair potential and determines the size of the superconducting gap $E_{\text{gap}} = 2\Delta$, which depends for a certain material on magnetic field, temperature, and current. Usually the attractive interaction is the largest if two electrons with opposite

[7] The critical fields for suppression of superconductors used in this thesis are $H_c \approx 10\,\text{mT}$ for bulk Al and about $H_c \approx 3$ T for Nb. It is important to mention that the differentiation made between type I and type II superconductors is more academic than lab reality. Most thin films superconductors act as type II. This property allows the use of thin films of Al (thickness $d \approx 7-10\,\text{nm}$) to withstand fields along the plane of the film up $2-3\,T$ [28].

momentum $\pm k$ pair. The BCS Hamiltonian in the second quantization formulation can be written as

$$H = \int d\mathbf{r} \sum_{\alpha,\beta=\uparrow,\downarrow} \left[\Psi^\dagger_\alpha(\mathbf{r}) H_{\alpha\beta}(\mathbf{r}) \Psi_\beta(\mathbf{r}) + \frac{g}{2} \Psi^\dagger_\alpha(\mathbf{r}) \Psi^\dagger_\beta(\mathbf{r}) \Psi_\beta(\mathbf{r}) \Psi_\alpha(\mathbf{r}) \right], \tag{2.13}$$

where $\Psi^\dagger_\alpha(\mathbf{r})$ and $\Psi_\alpha(\mathbf{r})$ creates and annihilates an electron at position $\mathbf{r}$ and spin $\alpha = \uparrow, \downarrow$ respectively. $H(\mathbf{r})_{\alpha\beta}$ is the single-particle Hamiltonian describing the system in the normal state and g an attractive interaction constant. It is usually solved within the mean-field approximation to decouple the second term in Eq. 2.13.

One important consequence is the presence of a superconducting pair potential, or order parameter, which is defined as $\Delta_{\alpha\beta}(\mathbf{r}) = -g\langle \Psi_\alpha(\mathbf{r}) \Psi_\beta(\mathbf{r}) \rangle$. The general form of the pair potential is a 2×2 matrix

$$\Delta(\mathbf{r}) = \begin{pmatrix} \Delta_{\uparrow\uparrow}(\mathbf{r}) & \Delta_{\uparrow\downarrow}(\mathbf{r}) \\ \Delta_{\downarrow\uparrow}(\mathbf{r}) & \Delta_{\downarrow\downarrow}(\mathbf{r}) \end{pmatrix} = \Delta i\sigma_y, \tag{2.14}$$

where the last equal represents the conventional homogeneous s-wave spin singlet case which is isotropic in real space. Everything which deviates from this form e.g. triplet pairing or a non-isotropic order parameter is generally called unconventional superconductivity. Furthermore, due to its implications on the topological properties discussed later, it is important to mention that the BCS-Hamiltonian does not conserve the number of electrons as electrons and Cooper pairs can be transformed into each other. The parity of the superconducting condensate however is a conserved quantity and can be even or odd. Adding a quasiparticle to the system changes the parity by one. Here we do not want to solve the BCS equation explicitly but exploit the so called Bogoliubov transformation to diagonalize the Hamiltonian (after approximating it by mean field theory).

2.3.3. BOGOLIUBOV-DE GENNES FORMALISM

The Bogoliubov-de Gennes (BdG) formalism is a very useful transformation to discuss excitations of spatial inhomogeneous superconductors and unconventional pairing potentials which is hard to treat in the BCS theory[8]. Excitations in condensed matter physics are usually treated in the quasiparticle picture. The elementary excitation of solid states systems are usually electrons and holes. This is represented in the formalism of second quantization by creation of an electron ($c^\dagger_{n\uparrow,\downarrow}$) and annihilation of an electron ($c_{n\uparrow,\downarrow}$) in state n with spin $\uparrow, \downarrow$. In a superconductor on the other, side excited states are a mixture of particle and hole excitations $u(r) = uc_{k,\uparrow} + v^* c^\dagger_{-k,\downarrow}$ as both are coupled through the pair potential. These quasi-particles are sometimes refereed to as Bogoliubons.

The general form of the BdG equation is given by:

$$\begin{pmatrix} H(r) & \Delta(r) \\ -\Delta^*(r) & -H^*(r) \end{pmatrix} \begin{pmatrix} u_n(r) \\ v_n(r) \end{pmatrix} = E_n \begin{pmatrix} u_n(r) \\ v_n(r) \end{pmatrix} \tag{2.15}$$

where $H(r)$ is the Hamiltonian describing the system in the normal state[9]. Usually, taking the spin degree of freedom into account this is a matrix with dimensions 4×4. The pairing

[8] The BdG transformation has the following form: $\Psi(r) = \sum_n [u_{\sigma n}(r)\gamma_n + v^*_{\sigma n}(r)\gamma^\dagger_n]$, $\Psi(r)^\dagger = \sum_n [v_{\sigma n}(r)\gamma_n + u^*_{\sigma n}(r)\gamma^\dagger_n]$. Here we just use the result after this transformation.

[9] For a conventional electron gas in the absence of a vector potential this is $H(r) = [\frac{\hbar^2}{2m^*}\nabla^2 + U(r) - \mu]\mathbb{1}_{2\times 2}$

potential in the homogeneous spin-singlet BCS case is given by $\Delta = i\sigma_y \Delta_0 e^{i\Phi}$ with the phase Φ being the order parameter of the superconductor. The factors $u_n(r)$ and $v_n(r)$ describe the fermionic quasiparticle excitations of energy E_n above the superconducting condensate. Solving this equation with the simple plane wave ansatz $\Psi(r) = e^{ikr}(u_0, v_0)$ for the conventional homogeneous spin singlet case yields

$$E = \pm\sqrt{|H(r)|^2 + |\Delta|^2} = \pm\sqrt{(k^2/2m - \mu)^2 + |\Delta|^2}, \tag{2.16}$$

where the second equation is the case for a conventional electron gas. This solution is a gapped spectrum with a gap size of 2Δ. The density of states of the system is then given by:

$$N_s(E) = N(0)\begin{cases} \frac{E}{\sqrt{E^2-\Delta^2}} & \text{for } (|E| > \Delta) \\ 0 & \text{for } (|E| < \Delta). \end{cases} \tag{2.17}$$

As depicted in Fig. 2.7. All excitations $|E| < \Delta$ are raised above Δ which results in the divergent density of states at the band edge.

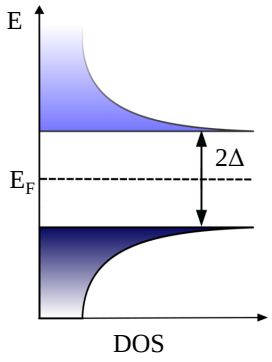

Figure 2.7: Density of states of a supercondcutor. Quasiparticles are pushed outside the gap as there are no allowed fermionic states.

It is worth at this point to introduce the so called Nambu-base (particle-hole representation) which is a spinor of the following form:

$$\begin{pmatrix} \Psi_\uparrow(\mathbf{r}) \\ \Psi_\downarrow(\mathbf{r}) \\ \Psi^\dagger_\uparrow(\mathbf{r}) \\ -\Psi^\dagger_\downarrow(\mathbf{r}) \end{pmatrix}. \tag{2.18}$$

This representation is obtained by a unitary transformation and the new Hamiltonian H' can then be rewritten in a 4×4 matrix[10].

$$H' = \begin{pmatrix} H(p,r) & \sigma_0\Delta(r) \\ \sigma_0\Delta^*(r) & -\Theta H(p,r)\Theta^{-1} \end{pmatrix} \tag{2.19}$$

[10] $H' = UHU^\dagger$ with $U = \begin{pmatrix} \sigma_0 & 0 \\ 0 & i\sigma_y \end{pmatrix}$

where the lower right block assures that the system obeys TRS. The Nambu basis is furthermore useful, as the upper left block describes the electronic part and the lower right block purely holes. Furthermore the Hamiltonian obeys particle-hole symmetry i.e. $PH_{\mathrm{BdG}}P^{-1} = -H_{\mathrm{BdG}}$. This has the consequence that for each positive solution of the BdG-equation there is a negative solution which means that the energy spectrum is symmetric around $E = 0$.

2.3.4. TOPOLOGICAL SUPERCONDUCTORS

Generally a superconductors is called unconventional when its pairing has a higher angular momentum than zero (so called s-wave superconductors). The energy spectrum of a BdG-Hamiltonian has a similar form than the band structure of an insulator. The gap of the superconductor 2Δ is similar to the band gap. Single electronic quasiparticles excitations do not exist inside both gaps. Hence, it is possible to define a topological invariant and classify superconductors by their topology. We will see, that the existence of so called Majorana zero modes is directly linked to topological superconductivity. In this context, a heuristic motivation of Majorana fermions in superconductors is given.

PHENOMENOLOGY OF MAJORANA FERMIONS

A Majorana fermion is a particle which is its own antiparticle and was predicted by Ettore Majorana [31]. It is possible to construct such a particle from solid state excitations. Then the condition can be reformulated to satisfy that the creation of a particle is the same as the annihilation i.e. $\gamma = \gamma^\dagger$. Quasiparticles like electrons and holes can be seen as particles and antiparticles. A Majorana mode should then be built from equal parts of electrons and holes. This can be done by a linear combination $\gamma = c + c^\dagger$. This kind of excitation is already very similar to the ones of the quasiparticle excitations in a superconductor, presented in the previous section: $\gamma = uc_\uparrow + vc_\downarrow^\dagger$. In order to fulfil the Majorana conditions, u and v need to be equally weighted with the consequence that $E = 0$. The last issue is that the operators have a spin and therefore $\gamma_\uparrow \neq \gamma_\uparrow^\dagger$. One can avoid this problem by removing the spin degree of freedom by using a spin polarized triplet superconductor. As the total wave function needs to be antisymmetric for fermions, the simplest possible way is to use p-wave pairing.

To summarize, we are searching for Majoranas as zero energy excitations in spinless p-wave superconductors. We recall from section 2.2.1, that such zero energy excitations are directly connected to a change in the topology of the system.

KITAEV CHAIN

Using the ideas from the previous section, we can now construct the simplest possible system, a one dimensional chain of spinless electrons with superconducting pairing, which can generate topological excitations. The model stems from Kitaev, who was the first to discuss the problem within the context of Majorana end states [32]. Written in second quantisation, the Hamiltonian is given by:

$$H = -\mu \sum_j c_j^\dagger c_j + \sum_{j=0}^{N-1} \left[-t(c_{j+1}^\dagger c_j + c_j^\dagger c_{j+1}) - |\Delta|(c_j c_{j+1} + c_{j+1}^\dagger c_j^\dagger) \right]. \tag{2.20}$$

This Hamiltonian contains the onsite energy μ, a hopping parameter t between two neighbouring sites and Δ is the superconducting pairing. This is an ansatz to create a

superconductor without spin where we hope to find Majorana modes. As the creation and annihilation operators are generally complex, it is possible to split them into two real operators

$$c^\dagger = \frac{1}{2}(\gamma_1 + i\gamma_2), \qquad c = \frac{1}{2}(\gamma_1 - i\gamma_2). \tag{2.21}$$

which are called the Majorana operators. Importantly they obey the Majorana condition $\gamma_1 = \gamma_1^\dagger$ and the fermionic anticommutation relation, namely $\gamma_1\gamma_2 + \gamma_2\gamma_1 = 0$. These Majoranas can be seen as half a real fermion and therefore always come in pairs. The goal now is to create an isolated Majorana mode by splitting electrons in a smart way. The previous single electron Hamiltonian can be rewritten in the language of Majorana operators as:

$$H = \frac{i}{2}[-\mu \sum_j \gamma_{2j-1}\gamma_{2j} + (t + |\Delta|)\gamma_{2j}\gamma_{2j+1} + (-t + |\Delta|)\gamma_{2j-1}\gamma_{2j+2}]. \tag{2.22}$$

As depicted in Fig. 2.8 there exist two ways to pair these Majorana operators. The trivial

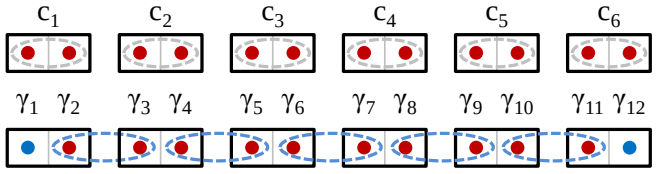

Figure 2.8: Two different ways a one dimensional superconductor can pair neighbouring sites. The upper row shows the trivial pairing while the lower row shows the topological pairing with two isolated Majoranas at each end. The operators c_i indicate electron sites and γ_i a Majorana site with $c_i = \frac{1}{2}(\gamma_{2n-1} - i\gamma_{2n})$ with $n \in \mathbb{N}$.

case is for $|\Delta| = t = 0$ and $\mu < 0$ where Majoranas from the same site are paired. The Hamiltonian reduces in this case to

$$H = \frac{i}{2}\mu \sum_{j=1}^{N} \gamma_{2j-1}\gamma_{2j}. \tag{2.23}$$

On the contrary, when $|\Delta| = t > 0$ and $\mu = 0$, the Hamiltonian reduces to

$$H = it \sum_{j=1}^{N-1} \gamma_{2j}\gamma_{2j+1} \tag{2.24}$$

and Majoranas from neighbouring sites are paired, which leaves one unpaired Majorana at each end of the wire giving rise to edge states (lower panel of Fig. 2.8). It is possible to show, that the bulk properties for both systems are similar. The existence of edge states in the second case describes the topological case. The two Majoranas γ_1 and γ_{10} form one fermion, which can be either occupied or unoccupied (both cases yield the same energy). This fact leads to a ground state degeneracy in the topological case which is determined by the total parity of the system. In contrast in the trivial case, fermions of neighbouring sites form Cooper pairs and the total number of unpaired fermions is zero.

This system only has one non-degenerate ground state with an even number of fermions. Adding a single fermion to the system leads to an unbound electron which is energetically unfavourable.

By making the wire a circle and therefore imposing translational invariance on the system, it is possible to go to momentum space using the Bloch transformation[11]

$$H(k) = (-2t\cos k - \mu)\tau_z + 2\Delta \sin k \tau_y. \tag{2.25}$$

In the low energy limit at $k = 0$ it is possible to linearise the Hamiltonian to

$$H = (-\mu - 2t)\tau_z + 2\Delta k \tau_y = m\tau_z + 2\Delta k \tau_y. \tag{2.26}$$

Thus, we end again with a Dirac like dispersion and again as in the preceding section 2.2.1 a change in the sign of the mass can be associated to a topological phase transition. The energy spectrum is given by $E = \pm\sqrt{m^2 + 4\Delta^2 k^2}$.

The model in this section was introduced with the purpose of creating Majorana fermions without thinking of a realistic system in which such spinnless superconductivity might be realised. In the next section, we show that it is possible to engineer such a system by combining conventional superconductivity and topological insulators.

2.3.5. INDUCED SUPERCONDUCTIVITY IN TOPOLOGICAL INSULATORS

There exist predictions of spinless p-wave superconductors in nature like for example Sr_2RuO_4 [33]. However, it has not yet been possible to unambiguously prove the unconventional pairing of the electrons due to the low crystal quality. In the last years, various research groups came up with new ideas on how to engineer p-wave superconductivity by using conventional s-wave superconductors which can be combined with strong spin-orbit coupled materials. This can be done for example by putting a conventional s-wave superconductor in proximity to a topological insulator surface or to the helical edge states [34, 35]. Under these conditions the Cooper pairs have a finite probability to leak into the topological insulators thereby inducing superconducting correlations into the surface states[12].

Still using the Nambu basis as introduced in section 2.3.3, it is possible to express the helical edge channels as $H_{\text{Dirac}} = \hbar v_F k \tau_z \sigma_z - \mu\tau_z$ and the superconducting correlations $H_\Delta = \Delta(\Psi_\uparrow^\dagger \Psi_\downarrow^\dagger + \text{H.c})$ with $\Delta = \Delta_0 e^{i\phi}$. The total Hamiltonian is given by:

$$H = -i\hbar v_F \tau_z \sigma_x \partial_x - \mu\tau_z + \Delta_0(\cos\phi\tau_x + \sin\phi\tau_y) = -i v_F \tau_z \sigma_x \partial_x + \Delta_0 \tau_x, \tag{2.27}$$

where for simplicity we set in the phase and the chemical potential in the last part equal to zero. The Pauli matrices σ_j are acting on the right and left moving edge channels, while the matrices τ_j mix the electron and hole blocks. The energy spectrum is then given by $E = \pm\sqrt{(\hbar v_F k)^2 + \Delta^2}$. At first sight it still seems as if Eq. 2.27 still contains only s-wave pairing but the spin degeneracy is lifted by the helical edge channels. This leads to effective p-wave correlations. The Hamiltonian is reminiscent of the low energy Kitaev chain

[11] $|k\rangle = \sqrt{N}\sum_{n=1}^{N} e^{-ikn}|n\rangle$

[12] At this point we omit the discussion of how to properly treat the proximity effect for a superconductor-topological insulator interface and just assume a finite probability of Cooper pairs in the TI.

model. The main difference lies in the geometrical form, namely that the edge channels in the QSHE do not have an end, i.e., they are moving around the structure without backscattering and no localized zero energy states can form. By introducing a Zeeman field $H_Z = M\sigma_x$, it is possible to break TRS and thereby opening a gap which allows the formation of zero energy states. This Zeeman field could be a local ferromagnetic insulator or an inplane magnetic field which opens a gap in the helical edge states and allows the formation of isolated Majorana fermions at the domain wall.

It was further shown by Fu and Kane [34] that also the higher dimensional analogue of the QSHE, a 3D TI proximitized with a superconductor, mimics the behaviour of a 2D $p_x + ip_y$ superconductor which does not violate TRS due to similar reasons as presented above. Locally breaking TRS by inserting a magnetic impurity, a localized state, a so called Abrikosov vortex, as depicted in Fig. 2.9 forms. This state locally closes the superconducting excitation gap and subgap states depending on the size of the bound state form as indicated by the blue and red lines. The energy levels are symmetric around zero ($E_n = -E_{-n}$) due to the particle-hole symmetry of the superconductor. While in the trivial case no state at zero energy exists, the topological one hosts a localized Majorana fermion at zero energy caused by shift in energy due to the π Berry's phase of the Dirac like band structure. Again this zero mode obeys $\gamma = \gamma^\dagger$.

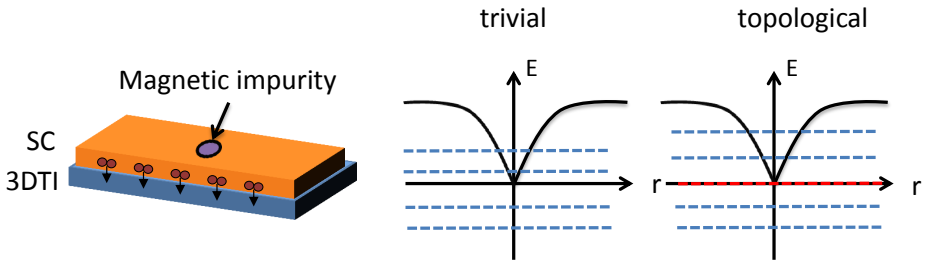

Figure 2.9: a) Schematic of induced superconductivity in a 3D topological insulator with a vortex placed on the superconductor. b) and c) show the energy spectrum of a vortex core for a s-wave superconductor in b) an a p-wave superconductor in c).

The next question is how this prediction can be tested experimentally. One way is by realizing a topological Josephson junction (JJ) with two localized Majoranas which leads to the doubling of the periodicity of the Andreev bound states. This is discussed in the next section.

2.4. JOSEPHSON EFFECT AND ANDREEV BOUND STATES

This section presents a basic introduction to the physics of the Josephson effect. The special case of a radio frequency (rf) driven Josephson junction is discussed. An important aspect of this is how to apply the method of rf driven junctions to resolve signatures of topological superconductivity. This prepares the ground for the experimental investigations involving Josephson junctions presented in chapter 3 to 6.

Brian Josephson made the ground breaking prediction, that a dissipationless supercurrent can flow between two superconducting electrodes separated by a tunnel barrier[13] [36]. Here we just state the results relevant to our case. The first Josephson equation says that a current I_s can flow through the junction even at zero applied dc bias and it depends on the phase difference $\Delta\phi = \phi_1 - \phi_2$ between the two leads:

$$I_s = I_c \sin\Delta\phi. \tag{2.28}$$

The critical current I_c is the maximum amount of current which can flow without dissipation. The phases ϕ_1 and ϕ_2 are the two macroscopic phases of the superconducting condensate which makes the classic Josephson effect a macroscopic quantum phenomena. The second Josephson equation relates the phase velocity $d\Delta\phi/dt$ to a finite voltage drop across the junction:

$$\frac{d\Delta\phi}{dt} = \frac{2eV}{\hbar}. \tag{2.29}$$

Consequently, for a finite voltage drop across the junction, an alternating ac-current is created by an applied dc-voltage with a frequency $f_J = 2eV/h$, which is called the Josephson frequency[14]. This can be understood as the energy change of a single Cooper pair transferred across the junction as depicted in Fig. 2.10.

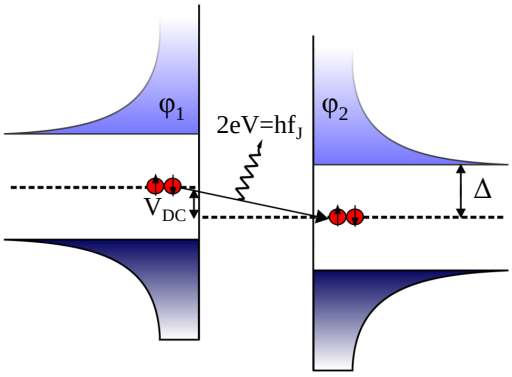

Figure 2.10: Two superconducting leads separated by a barrier. A Cooper pair, indicated by two red dots may tunnel from the left to the right lead and emits a photon.The frequency of the photon is called the Josephson frequency f_J and is direct proportional to the applied voltage V. The superconductors are described by their macroscopic phases ϕ_1 and ϕ_2 and the energygap 2Δ.

[13] In his case the barrier was a thin tunnel barrier. As we will see in next sections this concept can be extended to a barrier being a normal metal or other exotic materials like topological insulators.

[14] For $V(t)$ =const the phase evolves as $\phi = 2eVt/\hbar$. Plugging this into the first Josephson equation yields $I_s = I_c \sin 2eVt/\hbar = I_c \sin 2\pi f_J$.

2.4.1. DYNAMICS OF JOSEPHSON JUNCTIONS

The treatment of Josephson junctions for the voltage carrying state is usually done in the framework of the resistively shunted junction model (RSJ)[15] as shown in Fig. 2.11a). This model consists of a Josephson element in parallel with an ohmic resistor, which describes the normal state resistance $R_n = V/I$ of the system as shown in Fig. 2.11a). By using Kirchhoffs laws with the first Josephson equation Eq. 2.28, it is possible to calculate the total current in the circuit:

$$I = I_c \sin\phi + V/R \tag{2.30}$$

by applying the second Josephson equation Eq. 2.29 one gets:

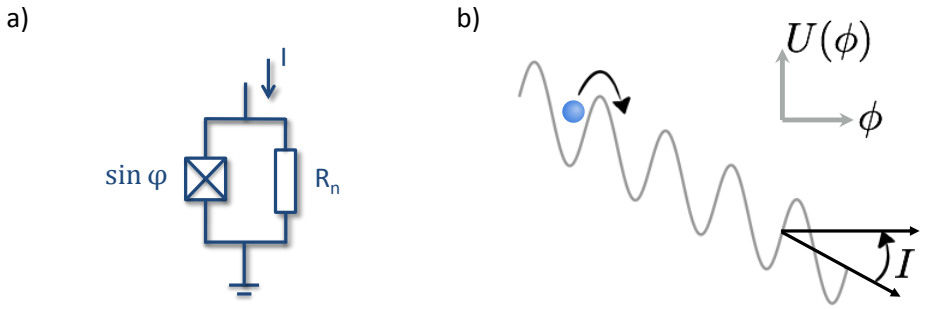

Figure 2.11: a) Equivalent circuit of the RSJ model. A Josephson junction is shunted by a resistor R_n. b) Potential energy of a phase particle in a tilted washboard potential.

$$I - I_c \sin\phi = \frac{\hbar}{2eR}\frac{d\phi}{dt}. \tag{2.31}$$

Equation 2.31 can be seen as the motion of a fictitious phase particle with coordinate ϕ in a potential $U(\phi)$ given by

$$U(\phi) = \frac{\hbar}{2e}(-I_c \cos\phi - I\phi). \tag{2.32}$$

Equation 2.32 is commonly referred to as the tilted washboard potential and is useful in describing the dynamics of the JJ. The value $E_J = \hbar I_c/2e$ is called the Josephson energy and sets a characteristic energy scale of the Josephson junction. The potential has a linear term representing the applied bias I and a periodic modulation given by the phase[16]. In analogy to a pendulum it is possible to interpret the resistance of the device R_n as a friction term, while a potential capacitance would play the role of a mass.

The washboard potential for different applied bias values is shown in Fig. 2.12a). For zero applied bias, the phase particle is trapped in a minimum and the average phase velocity $<\phi>$ is zero, and there is no voltage drop across the junction ($V = 0$). At $I = I_c$, the slope is steep enough so that the phase particle starts to "fall"down the washboard

[15] For simplicity we restrict ourselves to the case where other elements like capacitors (RS**C**J), inductors or noise fluctuations can be neglected.

[16] The potential energy $U(\phi)$ can be calculated by $-dU(\phi)/dt = IV$

potential and a finite voltage drop occurs. The phase particle gets faster as the voltage across the junction increases. For a large bias $I > I_c$, the voltage drop is then mostly determined by the normal state resistance R_n. The current voltage characteristic of a Josephson junction is shown in Fig. 2.12b). This $I-V$ characteristic follows the simple form $V = R_n\sqrt{I^2 - I_c^2}$. The coloured dots mark the corresponding situation in the washboard potential.

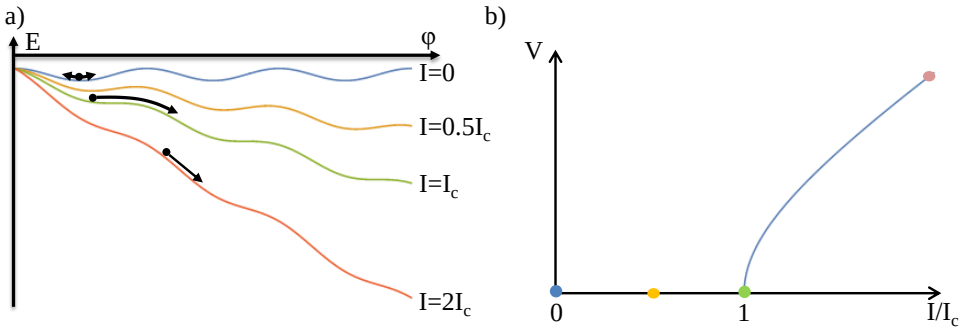

Figure 2.12: a) Washboard potential for different applied bias I. b) Current voltage characteristic of a Josephson junction. The coloured dots represent the applied current of figure a).

2.4.2. RF-DRIVEN JUNCTIONS

If a Josephson junction is driven by an ac-current, steps of constant voltage (Shapiro steps) form in the dc $I-V$ trace [37]. The step height is quantized and given by $V_n = n\hbar\omega/2e$ with $n \in \mathbb{Z}$. The influence of an ac drive can be taken into account by adding an alternating current to the bias in accordance with the relation:

$$I = I_0 + I_1 \cos\omega t. \tag{2.33}$$

Following Ref. [38], it is practical to rewrite the Josephson equation in normalized units

$$\alpha_0 + \alpha_1 \sin\xi\tau = \frac{d\phi}{d\tau} + \sin\phi. \tag{2.34}$$

Here, $\alpha_i = I_i/I_{\max}$ are the normalized currents, $\tau = \omega t = 2eI_{\max}R_n/\hbar t$ the normalized time, the normalized microwave frequency is $\xi = \hbar\omega/2eI_{\max}R_n$. This differential equation is non-linear due to the sine terms and has no simple analytic solution but it can be solved numerically. The time averaged voltage for a given bias can be calculated by considering $\phi(t)$ and determining the time for one period T for ϕ to advance 2π. Then the voltage V is given by $2eV/\hbar = 2\pi/T$[17]. Two examples with and without applied rf bias are shown in Fig. 2.13b). Steps of constant voltage appear in the I-V trace at values $V = hf/2e$. These are the so called Shapiro steps. An intuitive way to understand this behaviour is to consider the washboard potential. The ac-bias leads to a time dependent periodic

[17] Or precisely $\langle V\rangle = \frac{1}{T}\int_0^T \frac{\hbar}{2e}\frac{d\phi}{dt}dt = \frac{1}{T}\frac{\hbar}{2e}[\phi(T) - \phi(0)]$

perturbation as indicated in Fig. 2.13. This perturbation may lead to a locked motion of the phase particle, i.e., for a given dc-slope, the particle drops an integer number of periods until it is stopped by $I - I_{rf}$. These integer number of periods is then related to a constant voltage drop which leads to the formation of steps. It is worth noting that there exists an analytic solution for an rf driven junction when treated in the voltage biased case. The resulting current can be expressed as Bessel functions:

$$I_s = I_c \sum (-1)^n J_n(2eV_1/\hbar\omega_1)\sin(\phi_0 + 2eV_{\mathrm{dc}}/\hbar - n\omega_1 t). \tag{2.35}$$

If the driving frequency $\omega_0 = 2eV_{\mathrm{dc}}$ matches integer multiples of the applied frequency $V_n = n\hbar\omega_1/2e$, then the sine term equals zero and steps of constant voltage form. The current bias regime on the other hand does not have an analytic solution. Here a quasi-Bessel like oscillatory behavior was found by for example Russer *et al.* [38]. While Brian

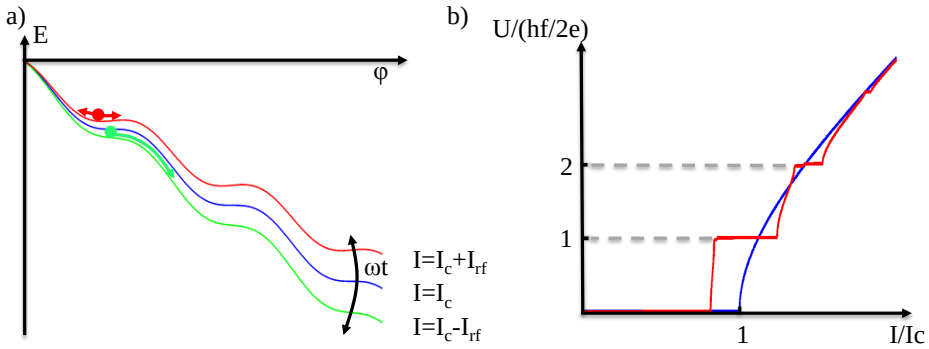

Figure 2.13: a) Washboard potential representation for an applied ac-current. b) I-V trace of a Josephson junction with (red) and without (blue) applied ac-bias.

Josephson and Sidney Shapiro worked in the tunnel limit (i.e. transmission $\tau \rightarrowtail 0$), the concepts can be extended to a barrier constituted by a normal metal or also to topological insulators as is the case in this thesis (section 2.5).

2.5. EXPERIMENTAL SIGNATURES OF TOPOLOGICAL JOSEPHSON JUNCTIONS

Amongst a number of proposals on how to detect Majorana fermion (MF) [39, 40], there are two which are currently of major interest for the electrical detection. The first focuses on the tunnelling of electrons through a Majorana zero mode [41]. This effect is predicted to occur at an interface between a normal metal and a superconductor separated by a barrier. If a MF is placed in this barrier the conductance is quantized to $2e^2/h$ irrespective of the height of the barrier. This kind of signature is the main focus in experiments on nanowire based realizations of Majorana fermions [42–45].

The second proposal is called the fractional Josephson effect due to the tunnelling of electrons through two hybridized Majorana modes. This thesis focuses on the second approach. In this thesis, we are especially interested in the difference in barriers formed by normal metals or topological materials as depicted in Fig. 2.14a) and 2.14b). Due

to the gapped spectrum of the superconducting density of states, a Cooper pair with $|E| < \Delta$ can only enter the normal part N by splitting into an electron and hole with opposite momenta. This conversion process is called Andreev reflection (AR) and a more extensively discussion is given in chapter 7. The AR is a phase coherent process over time. If the distance between the two superconducting leads is short enough, another AR may occur at the second interface with a backwards travelling electron. When the total phase acquired by the electron during these two reflections is a multiple of 2π, a bound state, so called Andreev bound state forms. The energy of this state depends on the applied phase difference $\phi = \phi_1 - \phi_2$ and the transmission of the normal states. These states can be calculated by solving the BdG equation $H_{\mathrm{BdG}}\Psi = E\Psi$ for a spatial inhomogeneous superconductor in one dimension. The superconducting gap can be expressed as $\Delta(x) = \Delta_0[\Theta(-x-L/2) + e^{i\phi}\Theta(x-L/2)]$. Following Kwon *et al.* [46] and using the ansatz of travelling waves bound to the normal part, the subgap solutions $|E| < \Delta_0$ have the form

$$\Psi_{\sigma\beta} = e^{\beta\kappa x}\left[A_\beta \begin{pmatrix} c\Psi_{\beta\sigma+} \\ \Psi^\dagger_{\beta\sigma+} \end{pmatrix} e^{ik_F x} + B_\beta \begin{pmatrix} c\Psi_{\beta\sigma-} \\ \Psi^\dagger_{\beta\sigma-} \end{pmatrix} e^{-ik_F x}\right], \tag{2.36}$$

where the $\pm$ labels the right and left moving electrons respectively, $\beta = \pm$ accounts for the right and left leads respectively. This equation describes states which are bound to the normal area and decay on a length scale $1/\kappa$ into the superconductors. It is possible to solve these equations using the appropriate boundary conditions for $\Psi(x)$ at $x = \pm L/2$[18]. For simplicity we assume to be in the short junction limit, i.e. that $L \lesssim v_F/\Delta$. This means that only a single ABS resides inside the JJ. Furthermore, for $L \ll v_F/\Delta$ the barrier can be reduced to a delta function $\delta(x)$. By solving the equation for the conventional [47] and the QSH case [46, 48] the energy spectrum yields

$$E(\phi) = \pm\Delta_0\sqrt{1 - D_c\sin^2(\phi/2)} \quad \text{for a conventional Josephson junction (s-wave)} \tag{2.37}$$

$$E(\phi) = \pm\Delta_0\sqrt{D_t}\cos(\phi/2) \quad \text{for a topological Josephson junction (p-wave)} \tag{2.38}$$

where D_c and D_t account for the transmission of the ABS in the conventional and the topological case respectively. The two spectra for various transmission values are shown in Fig. 2.14c) and d). In the case of perfect transmission ($D_c = D_t = 1$) the two spectra are almost indistinguishable. The difference between both solutions is that the trivial case has a ground state (red) and a excited state (blue) and the periodicity of the two states is 2π periodic. The topological bound states on the other hand have a 4π-periodicity and in general no ground and excited state exists. Both states differ by their parity and the crossing at $\phi = \pi$ is protected by exactly this parity.

If we now introduce impurities in the conventional N part, the transmission may become finite $D_c < 1$. Then, the ground and excited state are separated by a gap which depends on the transmission $E_g = 2\Delta\sqrt{1-D_c}$ as depicted in Fig. 2.14c). In the case of the topological junction such impurities would not induce a finite transmission, as the edge channels are protected against backscattering from TRS preserving impurities and therefore $D_t = 1$. Time reversal symmetry can be broken explicitly by applying a

[18] Matching conditions for $L \to 0$ are $\Psi_{\alpha\beta}(-0) = \Psi_{\alpha\beta}(+0)$ and $\Psi'(+0) - \Psi'(-0) = \frac{2mV}{\hbar^2}\Psi(0)$

finite Zeeman field $H_Z = M/2\Psi^\dagger\sigma_x\Psi$ perpendicular to the current direction of the edge channels. The transmission coefficient then becomes finite an reads:

$$D_t = \frac{1}{1+(M\sinh(\kappa L)/\kappa)^2}. \tag{2.39}$$

Even in this case, no gap around $\phi = \pi$ opens as still parity is conserved as visible in Fig. 2.14d). However, breaking TRS lifts the Kramers degeneracy at $\phi = 2n\pi$ with n an integer. This leads to a decoupling of the ABS from the continuum (i.e. states $E > |\Delta|$.

The current carried by ABS is connected to the energy by [49]

$$I_{\text{ABS}} \propto \frac{2e}{\hbar}\frac{\partial E}{\partial \phi} \tag{2.40}$$

which is plotted in the last row of Fig. 2.14 for the conventional and topological case respectively. This gives a clear illustration of the experimental signature of a topological Josephson junction which we are looking to detect in this thesis namely the periodicity of the ABS. The total current, taking a finite temperature into account, is then given by the sum over the individual ABS states

$$I_{\text{total}} = \frac{2e}{\hbar}\sum_{n=0}^{m}\frac{\partial E_n}{\partial \phi}\tanh\left(\frac{E_n}{2k_BT}\right). \tag{2.41}$$

The conventional bound states [Fig. 2.14c) and e)] have a 2π periodicity while the topological states have double the periodicity i.e. 4π [Fig. 2.14d) and f)]. As will be shown in the experiments it is possible to measure the periodicity using the ac Josephson effect. It is also worth mentioning that in the limit of low transmission, the sinusoidal current phase relation of a tunnel junctions is recovered, as introduced by Brian Josephson. In the bound state picture this means that the energy levels are pushed to the continuum edge.

This chapter treats the origin of topological superconductivity in an extremely simplified toy model framework. It is important to keep in mind that things like the proximity effect, finite temperature, finite size effects and bias may alter the system significantly. Moreover, we neglect stochastic effects such as quasiparticle poisoning which might destroy the coherence of the ABS and thereby may turn a topological 4π-periodicity into a effective 2π-periodic behaviour. Furthermore, in reality we may be confronted by the fact that conventional bulk modes contribute to the current in parallel to the topological ABS, thus making the current phase relationship a mixture of both types.

2.6. BRAIDING OF MAJORANA FERMIONS

The motivation for the arduous pursuit of the detection of Majorana fermions is the theoretical prediction that these particles behave like "*non-abelian anyons, which can be used for fault tolerant topological quantum computation*". The aim of this chapter is to try to give the reader a glimpse of the meaning of this phrase which in this or a similar formulation is frequently used in this field. First we try to define the words one after another and then develop the idea of topological quantum computation. Herby, we omit all problems which are still open related to the creation, manipulation and read out of Majorana bound states. It is assumed that all these operations can be done adiabatically i.e without perturbing the ground state. This part closely follows [39, 50, 51].

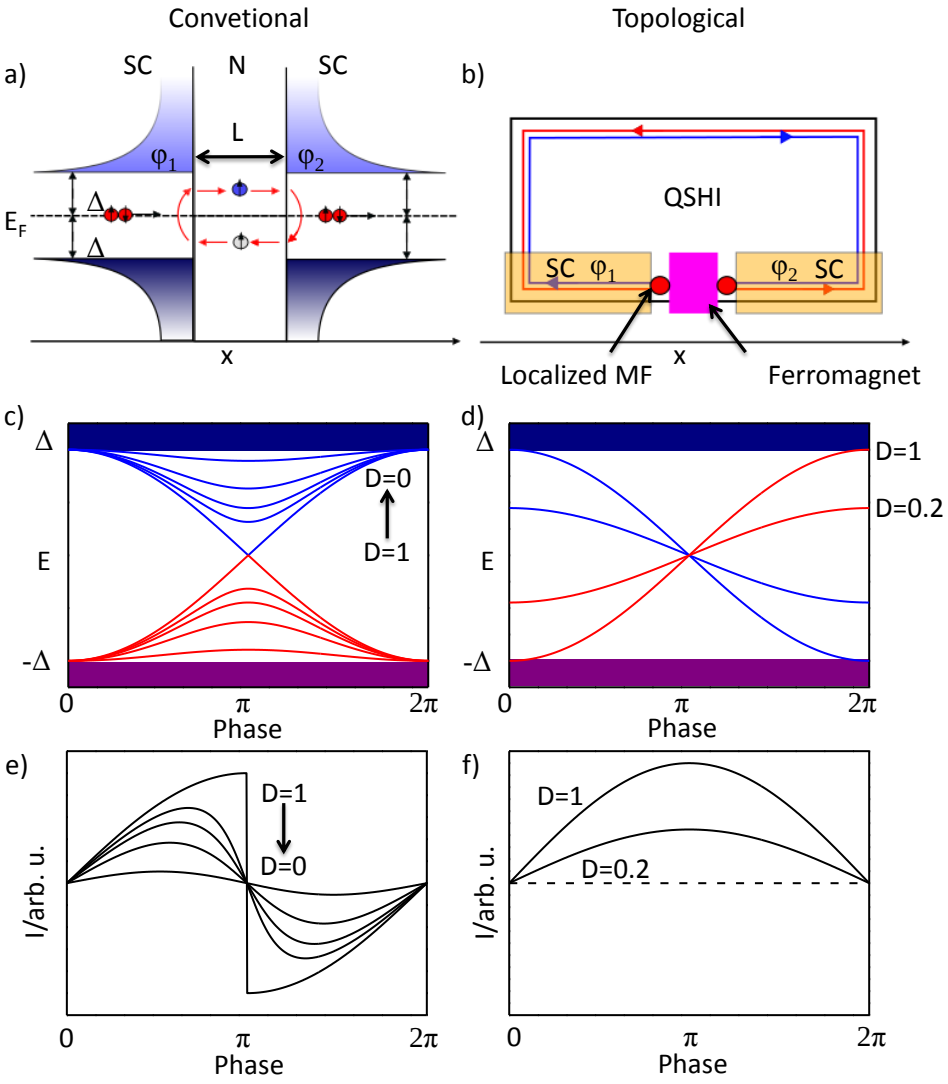

Figure 2.14: Sketch of the density of state situation of a Josephson junction with a) a conventional s-wave superconductor and b) a Josephson junction hosting Majorana end states. Figures c) and d) show the energy dispersion of the ABS for a conventional and topological Josephson junctions for different transmission values. The last row shows the current phase relationship for conventional and topological ABS with the same transmission values as above.

Consider a wave function describing a system of many identical particles

$$|\Psi\rangle = |n_1, n_2, n_3 ...\rangle \tag{2.42}$$

in three spatial dimensions and one time dimension. The exchange of two particles changes the sign of the wave function in the case of fermions while it stays the same in the case of bosons. Generally speaking, the exchange of a particle may introduce a phase shift $|\Psi\rangle \rightarrow e^{i\phi}|\Psi\rangle$ where for a boson (fermion) $\phi = 0\,(\pi)$. For any values of ϕ, the particle is called an *anyon* and the exchange of two such particles is called *braiding*. Interestingly, such kind of particles are allowed to exist in only two dimensions.

The expression, *"non-abelian"* is stating that the braiding operation is non-commutative, which means that the order in which particles are exchanged is important. Assume a unitary operation U_{ij} which exchanges two particles i and j, then the exchange operations do not commute: $U_{12}U_{23} \neq U_{23}U_{12}$.

Next, we show that Majorana fermions belong to this class of particles. Therefore, we assume four Majoranas γ_i as depicted in Fig. 2.15. We recall that it is possible to write

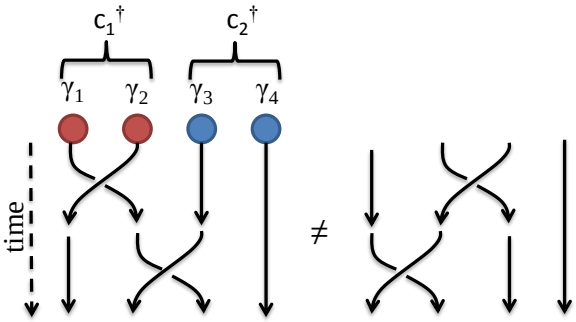

Figure 2.15: Two pairs of Majoranas can be described as two fermions. The braiding operation $U_{12}U_{23}$ is non abelian.

pairs of Majorana fermions as fermionic operators namely: $c_n^\dagger = (\gamma_{2n-1} + i\gamma_2 n)/2)$, each state being either occupied or empty i.e. $|1\rangle$ or $|0\rangle$. The occupation of one state is then given by $n_i = c_i^\dagger c_i = [1 + i\gamma_{2i-1}\gamma_{2i})]$. This way, we are able to construct the ground state of the system as

$$|\Psi\rangle = a|00\rangle + b|11\rangle + c|01\rangle + d|10\rangle\,. \tag{2.43}$$

An exchange of particles is described by the unitary operator $U_{nm} = e^{\pm\frac{\pi}{4}\gamma_n\gamma_m} = (1 \pm \gamma_n\gamma_m)/\sqrt{2}$. Here the $\pm$ sign stands for the direction which can be either clockwise or counter-clockwise. We neglect the latter case for now. The operator U_{nm} is a matrix with dimensions $N \times N$ i.e. here 4×4. While the consequence of exchanging two Majoranas from one fermion yields just a phase factor[19]

$$U_{12}|00\rangle = e^{i\frac{\pi}{4}(1)}|00\rangle\,, \tag{2.44}$$

[19] The general relations yield $U_{12}|n_1, n_2\rangle = e^{i\frac{\pi}{4}(1-2n_1)}|n_1, n_2\rangle$ and $U_{23}|n_1, n_2\rangle = \frac{1}{\sqrt{2}}\left(|n_1, n_2\rangle + i(-1)^{n_1}|1-n_1, 1-n_2\rangle\right)$.

exchanging two Majoranas from neighbouring sites however exchanges half a fermion yielding a superposition of states:

$$U_{23}\,|0,0\rangle = \frac{1}{\sqrt{2}}\left(|00\rangle + i\,|11\rangle\right). \tag{2.45}$$

Both processes are depicted in the braiding diagram in the of Fig. 2.15. In the figure on the right side, first two Majoranas from the same lattice site are exchanged (U_{12}) and then two of neighbouring sites U_{23}. It is now a straightforward exercise to show that the final state depends on the order in which the process is carried out i.e. they obey non-abelian statistics as predicted.

It is now possible to use the states $|n_i\rangle$ as a basis of a qubit with two states either full or empty. Usually, qubits are sensitive to several kinds of pertubations which limit the life time of the quantum state and therefore the time it can be used to conduct a computation. In the case of topological quantum computing the information of one state can be stored in two well separated Majorana fermions which makes it, theoretically, immune against certain types of local decoherence effects. A computation involving Majorana fermions would be conducted by braiding operations which as we have seen "remember" the history of the state as the outcome depends on the order of the braiding operations. This kind of computation is therefore called *fault tolerant topological quantum computation*.

As the physical exchange of the position of Majorana fermions is a rather challenging task, several other ideas emerged in the last few years for braiding without actually exchanging the position of the Majorana fermions. Relevant references are listed here for the sake of completeness [52–55].

BIBLIOGRAPHY

[1] M. Z. Hasan and C. L. Kane, *Colloquium: Topological insulators,* Reviews of Modern Physics **82**, 3045 (2010).

[2] S. Ryu, A. P. Schnyder, A. Furusaki, and A. W. W. Ludwig, *Topological insulators and superconductors: Tenfold way and dimensional hierarchy,* New Journal of Physics **12** (2010).

[3] D. J. Thouless, M. Kohmoto, M. P. Nightingale, and M. den Nijs, *Quantized Hall Conductance in a Two-Dimensional Periodic Potential,* Physical Review Letters **49**, 405 (1982).

[4] M. Kohmoto, *Topological invariant and the quantization of the Hall conductance,* Annals of Physics **160**, 343 (1985).

[5] G. Tkachov, *Topological Insulators: The Physics of Spin Helicity in Quantum Transport* (Pan Stanford Publishing Pte Ltd, 2015).

[6] R. Jackiw and C. Rebbi, *Solitons with fermion number,* Physical Review D **13**, 3398 (1976).

[7] B. A. Bernevig, T. L. Hughes, and S.-C. Zhang, *Quantum Spin Hall Effect and Topological Phase Transition in HgTe Quantum Wells,* Science **314**, 1757 (2006).

[8] C. L. Kane and E. J. Mele, *Z_2 Topological Order and the Quantum Spin Hall Effect,* Physical Review Letters **95**, 146802 (2005).

[9] L. Fu, C. L. Kane, and E. J. Mele, *Topological Insulators in Three Dimensions,* Physical Review Letters. **98**, 106803 (2007).

[10] Y. Ando, *Topological insulator materials,* Journal of the Physical Society of Japan **82**, 1 (2013).

[11] M. König, H. Buhmann, W. Molenkamp, Laurens, T. L. Hughes, C.-X. Liu, X.-L. Qi, and S.-C. Zhang, *The Quantum Spin Hall Effect: Theory and Experiment,* Journal of the Physical Society of Japan **77**, 031007 (2008).

[12] A. Pfeuffer-Jeschke, F. Goschenhofer, S. Cheng, V. Latussek, J. Gerschütz, C. Becker, R. Gerhardts, and G. Landwehr, *Cyclotron masses of asymmetrically doped HgTe quantum wells,* Physica B: Condensed Matter **256–258**, 486 (1998).

[13] X. C. Zhang, K. Ortner, A. Pfeuffer-Jeschke, C. R. Becker, and G. Landwehr, *Effective g factor of n-type HgTe/$Hg_{1-x}Cd_xTe$ single quantum wells,* Physical Review B **69**, 115340 (2004).

[14] R. Winkler, *Spin-orbit Coupling Effects in Two-Dimensional Electron and Hole Systems*, 1st ed. (Springer, 2003).

[15] M. König, S. Wiedmann, C. Brüne, A. Roth, H. Buhmann, L. W. Molenkamp, X.-L. Qi, and S.-C. Zhang, *Quantum Spin Hall Insulator State in HgTe Quantum Wells,* Science **318**, 766 (2007).

[16] A. Roth, C. Brüne, H. Buhmann, L. W. Molenkamp, J. Maciejko, X.-L. Qi, and S.-C. Zhang, *Nonlocal Transport in the Quantum Spin Hall State,* Science **325**, 294 (2009).

[17] K. C. Nowack, E. M. Spanton, M. Baenninger, M. König, J. R. Kirtley, B. Kalisky, C. Ames, P. Leubner, C. Brüne, H. Buhmann, L. W. Molenkamp, D. Goldhaber-Gordon, and K. A. Moler, *Imaging currents in HgTe quantum wells in the quantum spin Hall regime,* Nature Materials **12**, 787 (2013).

[18] C. Brüne, A. Roth, H. Buhmann, E. M. Hankiewicz, L. W. Molenkamp, J. Maciejko, X.-L. Qi, and S.-C. Zhang, *Spin polarization of the quantum spin Hall edge states,* Nature Physics **8**, 486 (2012).

[19] J. E. Moore and L. Balents, *Topological invariants of time-reversal-invariant band structures,* Physical Review B **75**, 121306 (2007).

[20] L. Fu and C. L. Kane, *Topological insulators with inversion symmetry,* Physical Review B **76**, 045302 (2007).

[21] C. Brüne, C. X. Liu, E. G. Novik, E. M. Hankiewicz, H. Buhmann, Y. L. Chen, X. L. Qi, Z. X. Shen, S. C. Zhang, and L. W. Molenkamp, *Quantum Hall Effect from the Topological Surface States of Strained Bulk HgTe,* Physical Review Letters **106**, 126803 (2011).

[22] C. Brüne, C. Thienel, M. Stuiber, J. Böttcher, H. Buhmann, E. G. Novik, C.-X. Liu, E. M. Hankiewicz, and L. W. Molenkamp, *Dirac-Screening Stabilized Surface-State Transport in a Topological Insulator,* Physical Review X **4**, 41045 (2014).

[23] D. A. Kozlov, Z. D. Kvon, E. B. Olshanetsky, N. N. Mikhailov, S. A. Dvoretsky, and D. Weiss, *Transport Properties of a 3D Topological Insulator based on a Strained High-Mobility HgTe Film,* Physical Review Letters **112**, 196801 (2014).

[24] M. Tinkham, *Introduction to superconductivity* (Courier Corporation, 1996).

[25] K. K. Likharev, *Superconducting weak links,* Reviews of Modern Physics **51**, 101 (1979).

[26] J. Eisenstein, *Superconducting elements,* Reviews of Modern Physics **26**, 277 (1954).

[27] A. Abrikosov, *The magnetic properties of superconducting alloys,* Journal of Physics and Chemistry of Solids **2**, 199 (1957).

[28] R. Meservey and P. M. Tedrow, *Spin-polarized electron tunneling,* Physics Reports **238**, 173 (1994).

[29] J. Bardeen, L. N. Cooper, and J. R. Schrieffer, *Microscopic Theory of Superconductivity,* Physical Review **106**, 1175 (1957).

[30] J. Bardeen, L. N. Cooper, and J. R. Schrieffer, *Theory of superconductivity,* Physical Review **108**, 1175 (1957).

[31] E. Majorana and L. Maiani, *A symmetric theory of electrons and positrons, Ettore Majorana Scientific Papers*, , 201 (2006).

[32] A. Y. Kitaev, *Fault-tolerant quantum computation by anyons,* Annals of Physics **303**, 2 (2003).

[33] A. P. Mackenzie and Y. Maeno, *P-Wave Superconductivity,* Physica B: Condensed Matter **280**, 148 (2000).

[34] L. Fu and C. L. Kane, *Superconducting Proximity Effect and Majorana Fermions at the Surface of a Topological Insulator,* Physical Review Letters **100**, 096407 (2008).

[35] L. Fu and C. Kane, *Josephson current and noise at a superconductor/quantum-spin-Hall-insulator/superconductor junction,* Physical Review B **79**, 161408 (2009).

[36] B. Josephson, *Possible new effects in superconductive tunnelling,* Physics Letters **1**, 251 (1962).

[37] S. Shapiro, *Josephson Currents in Superconducting Tunneling: The Effect of Microwaves and Other Observations,* Physical Review Letters **11**, 80 (1963).

[38] P. Russer, *Influence of Microwave Radiation on Current-Voltage Characteristic of Superconducting Weak Links,* Journal of Applied Physics **43**, 2008 (1972).

[39] J. Alicea, *New directions in the pursuit of Majorana fermions in solid state systems,* Reports on Progress in Physics **75**, 076501 (2012).

[40] C. W. J. Beenakker, *Search for Majorana fermions in superconductors,* Annual Review of Condensed Matter Physics **4**, 15 (2013).

[41] K. T. Law, P. A. Lee, and T. K. Ng, *Majorana Fermion Induced Resonant Andreev Reflection,* Physical Review Letters **103**, 237001 (2009).

[42] V. Mourik, K. Zuo, S. M. Frolov, S. R. Plissard, E. P. a. M. Bakkers, and L. P. Kouwenhoven, *Signatures of Majorana Fermions in Hybrid Superconductor-Semiconductor Nanowire Devices,* Science **336**, 1003 (2012).

[43] A. Das, Y. Ronen, Y. Most, Y. Oreg, M. Heiblum, and H. Shtrikman, *Zero-bias peaks and splitting in an al-inas nanowire topological superconductor as a signature of majorana fermions,* Nat Phys **8**, 887 (2012).

[44] S. M. Albrecht, A. P. Higginbotham, M. Madsen, F. Kuemmeth, T. S. Jespersen, J. Nygård, P. Krogstrup, and C. M. Marcus, *Exponential protection of zero modes in majorana islands,* Nature **531**, 206 (2016).

[45] H. Zhang, Ö. Gül, S. Conesa-Boj, M. P. Nowak, M. Wimmer, K. Zuo, V. Mourik, F. K. de Vries, J. van Veen, M. W. de Moor, *et al.*, *Ballistic superconductivity in semiconductor nanowires,* Nature Communications **8** (2017).

[46] H.-J. Kwon, K. Sengupta, and V. M. Yakovenko, *Fractional ac Josephson effect in unconventional superconductors,* Low Temperature Physics **30**, 613 (2004).

[47] C. W. J. Beenakker and H. van Houten, *Josephson current through a superconducting quantum point contact shorter than the coherence length,* Physical Review Letters **66**, 3056 (1991).

[48] L. Fu and C. L. Kane, *Josephson current and noise at a superconductor/quantum-spin-Hall-insulator/superconductor junction,* Physical Review B **79**, 161408 (2009).

[49] V. Ambegaokar and A. Baratoff, *Tunneling Between Superconductors,* Physical Review Letters **10**, 486 (1963).

[50] A. Akhmerov, J. Sau, B. van Heck, S. Rubbert, and R. Skolasiński, *Course on topology in condensed matter,* https://topocondmat.org/, accessed: 2017-06-17.

[51] C. Nayak, S. H. Simon, A. Stern, M. Freedman, and S. Das Sarma, *Non-Abelian anyons and topological quantum computation,* Reviews of Modern Physics **80**, 1083 (2008).

[52] B. Van Heck, A. R. Akhmerov, F. Hassler, M. Burrello, and C. W. J. Beenakker, *Coulomb-assisted braiding of Majorana fermions in a Josephson junction array,* New Journal of Physics **14** (2012), 10.1088/1367-2630/14/3/035019, 1111.6001 .

[53] S. Vijay and L. Fu, *Braiding without Braiding: Teleportation-Based Quantum Information Processing with Majorana Zero Modes,* arXiv preprint arXiv:1609.00950 (2016).

[54] T. Hyart, B. Van Heck, I. C. Fulga, M. Burrello, A. R. Akhmerov, and C. W. J. Beenakker, *Flux-controlled quantum computation with Majorana fermions,* Physical Review B **88**, 1 (2013).

[55] D. Aasen, M. Hell, R. V. Mishmash, A. Higginbotham, J. Danon, M. Leijnse, T. S. Jespersen, J. A. Folk, C. M. Marcus, K. Flensberg, and J. Alicea, *Milestones toward Majorana-based quantum computing,* Physical Review X **6**, 1 (2016).

3

4π-PERIODIC JOSEPHSON SUPERCURRENT IN A HGTE-BASED TOPOLOGICAL JOSEPHSON JUNCTION

This chapter is based on the publication: 4π-PERIODIC JOSEPHSON SUPERCURRENT IN HGTE-BASED TOPOLOGICAL JOSEPHSON JUNCTIONS.
J. Wiedenmann, E. Bocquillon, R.S. Deacon, S. Hartinger, O. Herrmann, T.M. Klapwijk, L. Maier, C. Ames, C. Brüne, C. Gould, A. Oiwa, K. Ishibashi, S. Tarucha, H. Buhmann, and L.W. Molenkamp, *Nature Communications, 10303* (2016).

In this chapter, a weak link based on the three dimensional topological insulator strained HgTe is studied under microwave irradiation. The current state of literature of strained HgTe without and with superconducting contacts is reviewed and a short overview over the theoretical treatment of induced superconductivity into the surface states with a focus on Josephson junctions is introduced. A perfectly transmitting Andreev bound state perpendicular to the leads ($k_y = 0$) is predicted due to its topological protection. A signature of this perfectly transmitting Andreev mode, is that the phase exhibits a 4π-periodicity rather than the 2π-periodicity of conventional states. This can be evidenced, by the observation of the fractional Josephson effect. Before the discussion of the ac driven Josephson junction, a comprehensive analysis of the dc-transport of a HgTe based Josephson junction is given. By applying microwave irradiation to the Josephson junction, a missing first Shapiro step is observed, which can be attributed to a 4π-periodic contribution to the supercurrent. This observation is then studied as a function of rf power rf frequency, and device length. Other effects which can be responsible for a disappearance of the first Shapiro step can be excluded and trivial Andreev bound states as a likely explanation for our observation are ruled out. Thus, the 4π-periodicity is attributed to the presence of gapless Andreev bound state.

3.1. INTRODUCTION TO THE THREE DIMENSIONAL TOPOLOGICAL INSULATOR HGTE

This chapter begins with an introduction to the physics of strained HgTe as a 3D topological insulator (3D TI). An overview of the current state of research is given with a focus on magnetotransport experiments in the normal state. Theoretical models detailing weak links based on 3D TIs are discussed. This is followed by a review of work on HgTe based Josephson junctions (JJ) carried out in our group. Then, the fabrication process of the JJs is outlined and dc characterization of the Josephson junction is discussed. Finally, the investigation of the Josephson junction in presence of an rf drive is presented as a function of rf power, rf frequency, magnetic field, and device length L.

3.1.1. MATERIAL AND CHARACTERIZATION WITH MAGNETOTRANSPORT

Strained HgTe was predicted to be a 3D TI by Fu and Kane already in 2007 in Ref. [1]. The two necessary material properties for a 3D TI are recalled from chapter 2, namely (i) an inverted band structure and (ii) a band gap separating the conduction and valence bands. Due to strong spin orbit coupling, bulk HgTe has already inherently an inverted band structure where the s-like Γ_6-band lies below the p-like Γ_8-band. However, the Fermi energy E_F lies between the degenerate Γ_8-band's $J = 3/2$ and $J = 1/2$ states, which makes HgTe a zero gap semiconductor. As we would like to access the surface state transport exclusively, we need to induce a finite gap as else the transport would be dominated by a large parallel bulk contribution. It is possible to lift the degeneracy of the Γ_8-bands by applying uniaxial strain. This can be done by growing HgTe on a CdTe substrates [2]. The lattice constant difference of about 0.3% between the two materials enables a fully strained growth of HgTe films with thickness up to $d \approx 150\,\text{nm}$[1] [3]. This strain opens a band gap of about $\Delta E \approx 22\,\text{meV}$ [4], which is large enough to achieve transport through the surface states at low enough temperatures of the order of $T < 4.2\,\text{K}$.

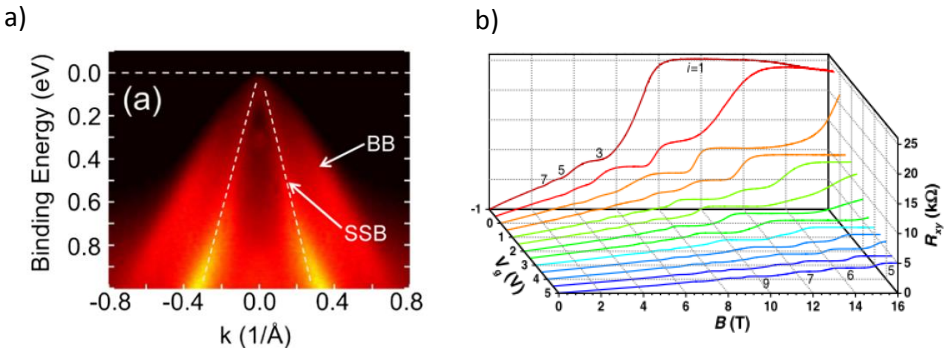

Figure 3.1: a) Shows the ARPES spectrum of bulk HgTe. The bulk bands and surface state bands are labelled BB and SSB respectively (figure taken from [4]). b) Quantum Hall measurements of a strained HgTe based Hall-bar for different gate voltages V_g. The dark red curve ($V_g = -1\,\text{V}$) shows the signature of two Dirac like surface states (figure taken from [2]).

[1] Lattice constant of HgTe: $a_{\text{HgTe}} = 0.646\,\text{nm}$. Lattice constant of CdTe: $a_{\text{CdTe}} = 0.6482\,\text{nm}$.

A first evidence for the presence of topological surface states was obtained by measuring angle-resolved photo emission spectra (ARPES) of HgTe [4]. Figure 3.1a) shows a spectrum of a rather thick, relaxed HgTe structure. As ARPES is a very surface sensitive technique, it is still possible to observe the presence of a linear dispersion originating from the surface states bands (SSB) indicated by the dashed lines. In addition, the hole like bulk bands (BB) are also visible. Crauste *et al.* [5] were also able to show the spin polarization by circular dichroism measurements.

This observation was corroborated by magnetotransport experiments using fully strained HgTe [4]. In this regard, the quantum Hall effect (QHE), an effect which only exists in two dimensional systems, was observed. This was taken as a evidence of the presence of two dimensional states in bulk HgTe. The Landau level sequence was modelled using two Dirac like states with different chemical potentials on each surface. The main advantages of HgTe compared to other 3D TI candidates (like bismuth based compounds), are the low intrinsic doping (electron density of the order of $10^{11}\,\mathrm{cm}^2$) and the rather high mobility of the MBE[2] grown films of the order of $\mu \approx 30\,000\,\mathrm{cm}^2/\mathrm{Vs}$. This allows on the one hand the access of the surface states close to the Dirac point and on the other hand the observation of the quantum Hall effect. An example of a measurement of the transversal resistance of a Hall bar structure (Hall resistance) is shown in Fig. 3.1b) for different applied gate voltages [2]. Beyond the presence of the quantum Hall effect itself, it is possible to get further insight into the physics of the topological surface states. The first is that at a gate voltage $V_g = -1\,\mathrm{V}$, a sequence of only odd quantum Hall plateaus $\nu = 1, 3,$ and 5 can be seen. This sequence is a signature of two degenerate Dirac like surface states with equal charge carrier densities, each contributing $(n+1/2)e^2/h$ to the total conductance. This is comparable to graphene (more precisely half of graphene). This sequence, i.e. $(2n+1)e^2/h$, is a footprint of a system with linear dispersion, i.e., a Dirac system. In contrast, a conventional spin-degenerate quantum well, would exhibit a sequence of even numbered Landau levels. Furthermore, the QHE was observed in the whole accessible electron density range starting from very low densitiy of the order of $1 \times 10^{11}\mathrm{cm}^{-2}$ up to $n = 2 \times 10^{12}\mathrm{cm}^{-2}$ which implies that the transport in high magnetic fields is surface state dominated. The results of simple $k \cdot p$ simulations show that at such high densities bulk transport is expected to coexist. This result was explained by an extended $k \cdot p$ theory, where the surface states are electrostatically decoupled from the bulk bands by assuming a different dielectric constant for the surface and bulk states [2]. From Fig. 3.1b) it can also be deduced that by changing the gate voltage, even quantum Hall plateaus appear. This is interpreted by considering the different gate influence for the top and bottom surface. The bottom surface state is further away from the top gate electrode and thus expected to have a reduced gate efficiency. This leads to different chemical potentials on both surfaces and different densities.

In summary, these results show that the transport is dominated by Dirac like states originating from two individual surfaces over a wide range of densities. The low intrinsic doping and the high mobility make HgTe an ideal candidate for combination with superconductors in experiment to test predictions about unconventional superconductivity in such systems.

[2] MBE: Molecular beam epitaxy

3.1.2. THEORETICAL TREATMENT OF JOSEPHSON JUNCTIONS BASED ON 3D TIS

Next, after it was proven that strained HgTe is a topological insulator, we investigate the interplay of superconductivity and topological insulators. The emphasize here is on a simple geometry, a Josephson junction, where the barrier constitutes the helical surface states. It is intended to show that such a structure gives rise to signatures of exotic superconductivity.

In a 3D topological insulator based Josephson junction, in which superconductivity is induced into the surface states via the proximity effect of a nearby s-wave superconductor, Andreev bound states appear in the induced gap Δ_i (see Fig. 3.2). This was already discussed by Fu and Kane [6], who predict the formation of Majorana zero modes when superconducting correlations and the helical surface states are combined. Beside the discussion of a Majorana bound state due to a vortex placed on the surface it also discusses a gapless Andreev mode which occurs in a one dimensional TI nanoribbon. This work was extended to finite dimensions [7], including a ferromagnetic barrier [8] or a generic scattering barrier in the junction [9]. One common feature of all these theories is a gapless mode for perpendicular propagation, *i.e.* $k_y = 0$, and gapped states for finite transverse momenta. Here, we follow the work of Tkachov *et al.* [9], where superconducting correlations are induced into the surface state of a TI at a finite tunnelling rate. This closely follows the approach introduced by McMillan *et al.* [10] for standard metal superconductor proximity structures. The strength of the proximity effect is described by a tunnelling parameter. This yields an effective induced gap $\Delta_i \leq \Delta_{SC}$. The approach is rather simple. In reality the interaction of a topological insulators and superconductors might be much more sophisticated. Nevertheless, it is a good starting point and the Hamiltonian for the system is given by:

$$\left[E\mathbb{1} - \begin{pmatrix} -i\hbar v_F \vec{\sigma} \nabla + U(x) - \mu & i\sigma_y \Delta_{\text{ind}} e^{i\phi_{L,R}} \\ -i\sigma_y \Delta_{\text{ind}} e^{-i\phi_{L,R}} & -i\hbar v_F \vec{\sigma^*} \nabla - U(x) + \mu \end{pmatrix}\right] \begin{bmatrix} u(r) \\ v(r) \end{bmatrix} = 0, \tag{3.1}$$

where we introduce a finite scattering potential $U(x) = U\delta(x)$ in the barrier. Compared to chapter 2.5 the problem is extended to two dimensions. The energy spectrum for the Andreev amplitudes yields in this case

$$E_\Theta^\pm = \pm\Delta_{\text{ind}} \sqrt{1 - T_\Theta \sin^2 \frac{\phi}{2}}. \tag{3.2}$$

The subscript $\pm$ stand for the positive and negative solution, the angle is defined as $\cos\theta = \sqrt{1-(k_y/k_F)^2}$. The momentum k_y has the direction as indicated in Fig. 3.2a) and $k_F = \sqrt{2mE_F}$ is the Fermi momentum. The transmission is now a function of angel Θ and given by

$$T_\Theta = \frac{\cos^2\Theta}{1 - \sin^2\Theta/(1+Z^2)} \tag{3.3}$$

with $Z = U/(\hbar v_F)$, a dimensionless parameter which depends on the size of a scattering potential U. A polar plot of the transmission is shown in Fig. 3.2a). It is possible to see that perfect transmission $T_\Theta = 1$ exist only for zero transverse momentum and a non

perfect transmission for oblique incidence depending on the angle and the scattering potential. The energy spectrum of the ABS for different angles Θ is shown in Fig. 3.2b). The spectrum is only gapless in the case of of perpendicular momentum, i.e., $k_y = 0$ (depicted in blue) and has a finite gap for finite transversal momentum (shown in red). The peculiarity of this perpendicular mode, sometimes also called a chiral Majorana mode, is its 4π-periodicity as the crossing at $\phi = \pi$ is protected. Its contribution to the

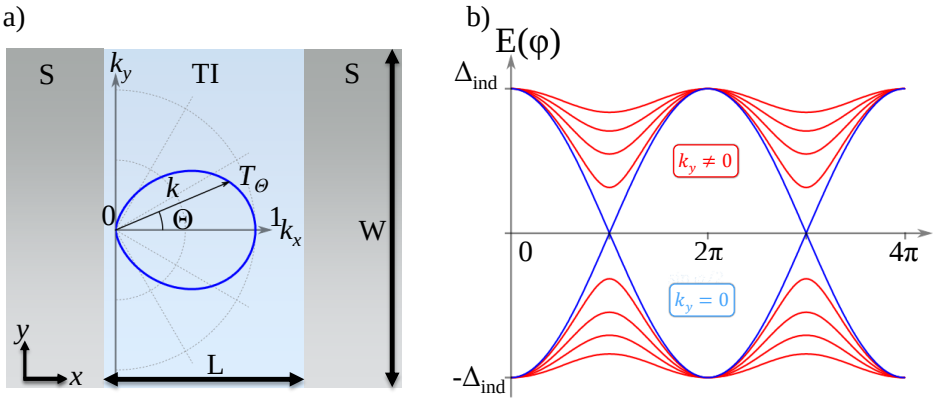

Figure 3.2: a) Schematic of a JJ with size annotations and a polar plot of the transmission probability as a function of angle Θ. b) Andreev bound state spectrum from a 3D TI JJ where the gapless $k_y = 0$ mode is depicted in blue and and in red for oblique incidence.

supercurrent is then given by[3] $I_{4\pi} = \sin\phi/2$.

This 4π-contribution to the supercurrent is a single channel phenomena and in a finite size Josephson junction overshadowed by a large number of conventional 2π-periodic modes. Furthermore, the gapless ABS may restore a 2π-periodicity due to its finite lifetime. In equilibrium, the electron is likely to follow the lower branch as quasiparticle poisoning from the superconducting leads allows a change of parity. Therefore a principle aim of the present thesis is to probe the non-equilibrium case of a JJ by using the ac Josephson effect. However, before discussing the ac response of the topological JJ, we give a short overview of dc response done by Oostinga *et al.* [11].

REVIEW OF HGTE BASED JOSEPHSON JUNCTIONS

First attempts on inducing superconductivity in HgTe have been described in references [11, 12]. As the devices used for studies described in this chapter are very similar to the ones discussed in these papers, a summary of the main results is given.

Lateral Josephson junctions, as depicted in Fig. 3.3a) were fabricated using fully strained films of HgTe with a thickness of $d_{\mathrm{HgTe}} \approx 70\,\mathrm{nm}$. The superconducting leads are made from sputtered niobium, covered with a protective layer of aluminium and ruthenium against oxidation. The distance between the leads is about 200 nm and the width of the HgTe mesa is 2 µm. A dissipationless supercurrent is observed with a critical

[3] Calculated for zero temperature by $I_\Theta = \partial E^+_\Theta/\partial\phi$. The total supercurrent is given by integrating over all angles and is again 2π-periodic due to the large contribution of gapped modes.

current value of about $I_c = 3.8\,\mu A$ and a normal state resistance of $R_n = 50\,\Omega$ as shown in Fig. 3.3b). Hysteresis in the $I-V$ characteristics is commonly observed. This means that the critical current has a different value depending on the sweep direction of the applied bias. Such a behaviour is commonly observed in so called underdamped Josephson junctions which have a large capacitance and normal state resistance. It is possible to quantify this by calculating the Stuart-McCumber parameter $Q = \sqrt{2eI_c/\hbar C R_n C}$ which gives in the present case $0.002 \ll 1$. Here the geometrical capacitance C of the superconducting contacts is estimated to be $C = 52\,aF$ by considering the dimensions of the junction. A small Stuart-McCumber parameter indicates an overdamped junction $Q \ll 1$ rather than an underdamped junction $Q \gg 1$. The other frequently mentioned source of hysteresis is self-induced heating. In this case, electrons in the voltage carrying state are scattered elastically which creates Joule heating. This can locally influence the induced gap and thus reduce the critical current. In contrast, in the zero voltage state Cooper pairs do not exchange heat such that the effective temperature is lower and a larger critical current is measured. The $I_c R_n = 0.2 < \Delta_{Nb} = 1\,mV$ can be used to classify the junction to be in the long junction limit. The position of the nodes in the Fraunhofer pattern can in principle

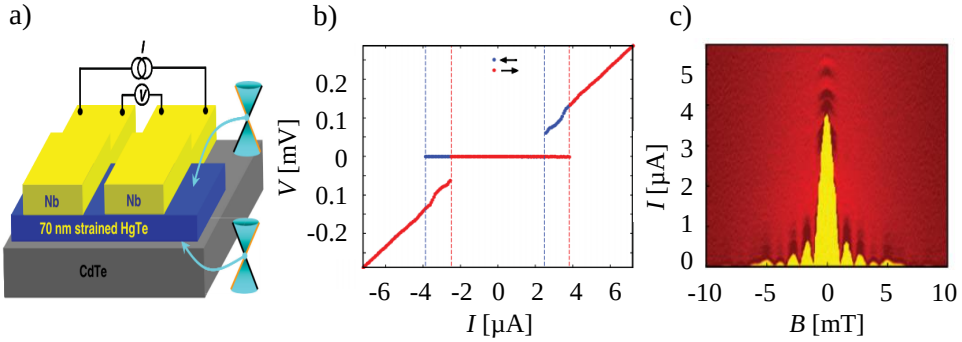

Figure 3.3: a) Schematic of a HgTe based Josephson junction. b) $I-V$ measurement of a HgTe based Josephson junction. The arrows indicated the sweep direction. c) Response of the Josephson junction to a magnetic field applied perpendicular to the plane of the substrate and shows a Fraunhofer diffration pattern. Figures are taken and from [11] and have been modified.

reveal the periodicity of the current phase relationship, as the distance between two neighbouring minima is given by $\Delta B = \phi / A$ for a $\sin\phi$ periodicity and is twice as much for a $\sin\phi/2$ supercurrent. The diffraction pattern is shown in the Fig. 3.3c). It shows a conventional 2π-periodicity when taking the penetration depth of the superconducting leads $\lambda_{Nb} = 350\,nm$ into account. This behaviour is somewhat expected as quasiparticle poisoning might restore the conventional periodicity in dc-transport and only a small fraction of the supercurrent is carried by the gapless modes. The current phase relationship was also directly measured using a scanning SQUID by Sochnikov *et al.* [13]. They report an almost length independent skewness of the ABS which might already be related to the helical nature of the surface states.

To conclude, it was possible to fabricate a Josephson junction based on HgTe and observe a Josephson effect. So far mostly conventional behaviour has been observed. The skewed current phase relation shows the high transparency of the ABS.

3.2. FABRICATION & CHARACTERIZATION OF THE HGTE JOSEPHSON JUNCTIONS

The devices are fabricated from coherently strained undoped HgTe layers of 65 – 90 nm thickness, epitaxially grown on a commercial CdTe substrate. The mobility and charge density relevant for the experiment are evaluated from Hall-bar measurements produced from the same wafer as the presented junctions and typically yield values around $\mu = 2-4\times10^4\,\mathrm{cm^2V^{-1}s^{-1}}$, and $n_e = 3-7\times10^{11}\,\mathrm{cm^{-2}}$. To calculate this density the linear part of the Hall-slope is evaluated. The Fermi wavevector is then given by $k_F = 2\sqrt{\pi n} \approx 0.2\,\mathrm{nm^{-1}}$, where a factor of two was used to account for the two different surface states assuming equal charge carrier densities. From these values it is possible to calculate the mean free path $l_{\mathrm{mfp}} = \mu\hbar k_F/e \approx 200\,\mathrm{nm}$.

The JJs are fabricated by defining a HgTe mesa using argon sputtering. Before deposition of the superconducting niobium contacts by magnetron sputtering, a short argon sputtering cleaning step is used to achieve a transparent interface. A detailed recipe and description of the lithographic process can be found in the Phd thesis of Luis Maier [14] and the appendix A. Two SEM[4] pictures with corresponding length scales of the devices are shown in Fig. 3.4c) and d). Each superconducting contact has a width of $1-4\,\mu\mathrm{m}$[5]. The HgTe weak link has a width of $W = 2\,\mu\mathrm{m}$ (corresponding to the width of the mesa stripe) and a variable length L ranging from 150 nm to 600 nm. This means that the device is close to the ballistic regime for the shortest length scale ($l_{\mathrm{mfp}} \lesssim L$) and more in the diffusive regime for all other junctions ($l_{\mathrm{mfp}} > L$). Another classification of the junction can be done by comparing the length of the junction with the superconducting coherence length ξ_{SC}. If the superconducting coherence length ξ_{SC} is much larger than L, only a single ABS per channel is existing between the leads. On the other hand if $\xi_{\mathrm{SC}} \gg L$, then the device is in the long junction limit. The superconducting coherence length of niobium is given by $\hbar v_F/\pi\Delta(T=0) \approx 40\,\mathrm{nm}$ and therefore much shorter than L. The junction is thus expected to be in the long junction limit [15]. This is only true when considering the gap of the superconducting leads and ABS form inside the niobium gap. On the other hand there exists the possibility that the proximity effect turns the topological insulator superconducting and then subsequently the ABS can form between the induced states. The induced superconducting gap is expected to be much smaller than the niobium gap. As the coherence length scales inversely with the gap size ($\xi_{\mathrm{SC}} \propto 1/\Delta$), it is possible that the induced superconducting coherence length is up to several microns long and the classification of long and short Josephson junction needs to be taken with care. Independent of this characterization, a topological junction will always host a protected crossing at $\phi = \pi$. The last number which we can already estimate in advance is the number of transport channels by considering the density and width of the mesa $N = W k_F/\pi \simeq 100$.

The sample is cooled down in a dry dilution refrigerator with a base temperature of $T \approx 20\,\mathrm{mK}$ fitted with low pass RC and copper powder filters for each line. A typical $I-V$ curve obtained at 30 mK is presented in Fig. 3.5. The critical current in this device is $I_c \approx 5\,\mu\mathrm{A}$ and exhibits hysteresis, as previously discussed. We find that the critical

[4] SEM: scanning electron microscope

[5] The change in width was an attempt to reduce the heating and therefore the hysteretic behaviour of the junction. In general no change in the hysteresis or the behaviour of the junction was observed for varying contact width.

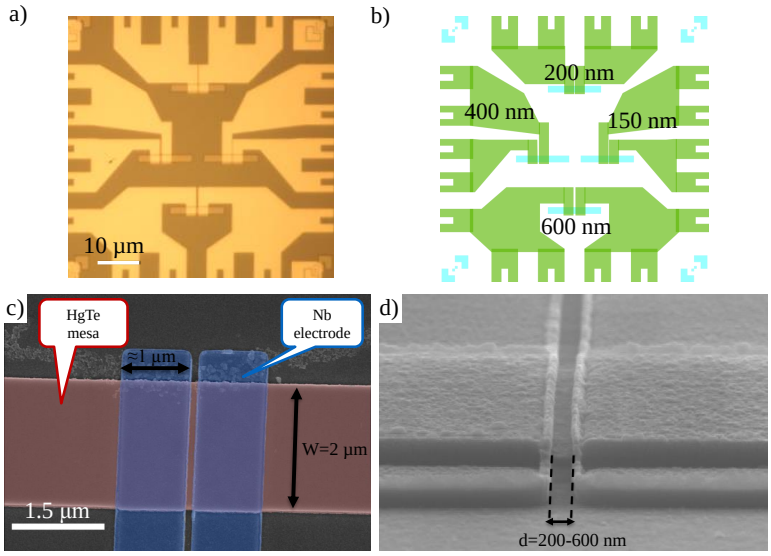

Figure 3.4: a) Microscope and b) design drawing of the HgTe based JJs. The blue area is the HgTe mesa and the green the superconducting leads. The numbers indicate distance between the superconducting leads. c) and d) SEM pictures of a HgTe based JJ with length scales.

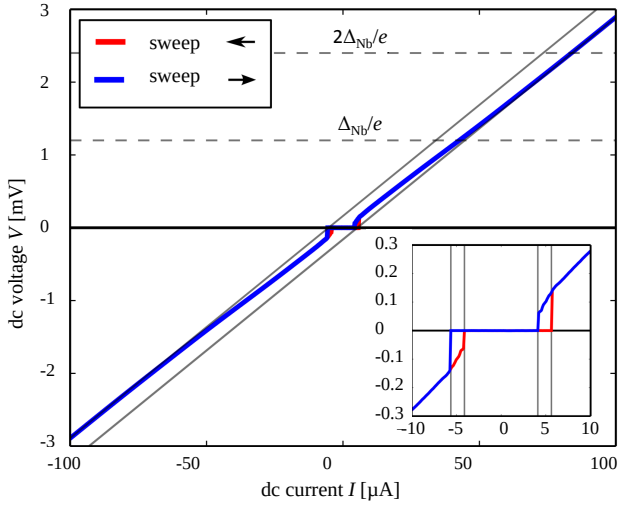

Figure 3.5: $I-V$ measurement of a device with $L = 150\,\text{nm}$ at base temperature of $T \approx 30\,\text{mK}$. The red and blue lines indicate different sweep directions of the bias voltage. The grey lines indicate the asymptotes of the slope taken $V > 2\Delta_{Nb}$.

current of devices with the same dimensions varies by about 30%, which underlines the reproducibility and quality of the fabrication process. A recurring feature in all devices is the presence of an excess current in the I-V curve (see Fig. 3.5). For high biases $V > 2\Delta_{Nb}$, the $I-V$ curves become linear with an asymptote which does not go through the origin but is shifted towards higher currents. This excess current I_{exc} stems from the fact that each Andreev reflection transfers the charge $2e$, twice the amount than a normal electron [16, 17]. It thus illustrates the presence of Andreev reflections at both S-TI interfaces and emphasizes the high interface quality and reproducibility of our devices. The excess current can reach twice the normal state current for two perfect transmitting NS contacts. A finite barrier due to elastic scattering reduces the Andreev probability and therefore also the excess current. Furthermore, the average transparency over all transport channels can be estimated from the size of the excess current [18] and yields $Z \approx 0.6$. This means that the average transparency is moderate compared to other semiconductor superconductor hybrid systems. The temperature dependence of the critical current I_c is shown in Fig. 3.6.

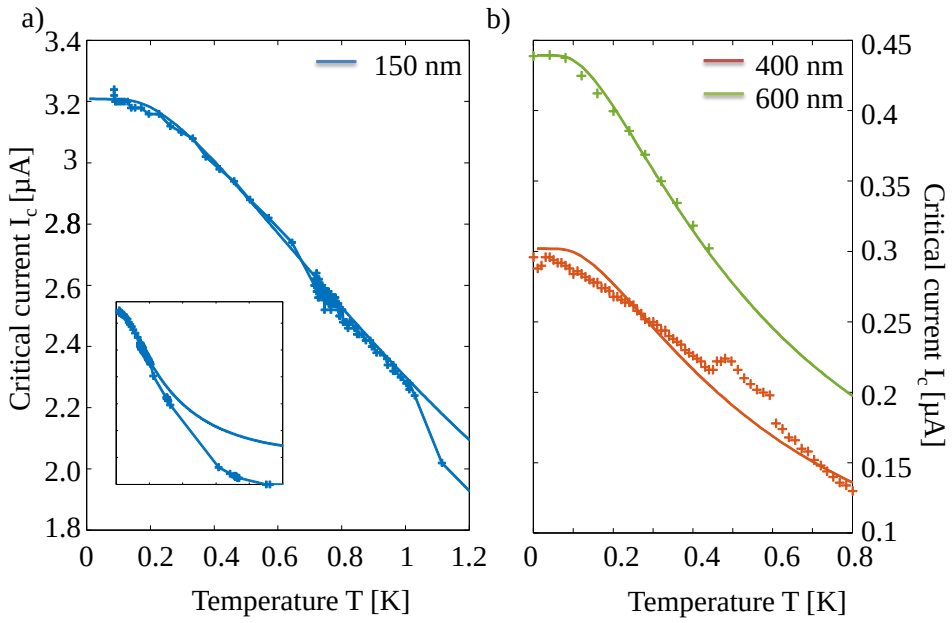

Figure 3.6: a) and b) Fit of the critical current vs. temperature for the junction length 150 nm in a) and 400 600 nm in b). The data is represented as symbols and the solid lines are fits using the equation 3.4.

By using the appropriate theory[6] from Tkachov *et al.* mentioned in Eq.3.2, it is possible to estimate the induced superconducting gap Δ_{ind}. Here, each mode is described by an angle dependent transmission. The critical current as a function of temperature is given

[6] Apart from the theory, which is used to fit the data, a rather broad range of models exists which describe the behaviour of the critical current. Fits using the Eilenberger theory [19] for ballistic junctions did not yield a reasonable agreement with the experimental data. The diffusive regime is described by the Usadel equations [20] but the theory should not be apply in our case as the we are closer to the ballistic limit.

	L/nm	I_c/μA	R_n/Ω	Δ_{ind}/meV	N	Z
A	150	3.3	33	0.35	117	0.1
B	400	0.29	158	0.1	33	1
C	600	0.44	165	0.1	48	1

Table 3.1: Summary of measured and estimated parameters for the three different JJs A,B and C in this chapter. The length L is set by the design parameters and varies between 150 – 600 nm. The values for the critical current I_c and the normal state resistance R_n are directly measured from the $I-V$ characteristics. The values of the induced superconducting gap Δ_{ind} is estimated using the temperature dependence of Eq. 3.6. The number of normal modes and the height of the barrier were fitting parameters for the temperature behaviour of the critical current.

by

$$I_c(T) = \frac{e\Gamma}{4\hbar}\sum_{k_y}\sin\phi cos\Theta\frac{T_\Theta(1-\gamma+\frac{5}{2}\gamma^2-\frac{3}{2}\gamma^2 T_\Theta\sin^2\frac{\phi}{2})}{1-T_\Theta\sin^2\frac{\phi}{2}}$$
$$\tanh\Gamma\frac{(1-\gamma+\gamma^2)(1-T_\Theta\sin^2\frac{\phi}{2})^{1/2}+\frac{1}{2}\gamma^2(1-T_\Theta\sin^2\frac{\phi}{2})^{3/2}}{2k_BT} \tag{3.4}$$

with $\gamma = \Gamma/\Delta_{\text{Nb}}$ and the induced gap is given by $\Delta_{\text{ind}} = \Gamma(1-\gamma+\frac{3}{2}\gamma^2)$. As seen in Fig. 3.6 the agreement for low temperatures is very good. This approach breaks down for higher temperatures where the induced gap becomes comparable to Δ_{Nb}. The quality of the fit is also not as good for the longer junction which might be due to the fact that the model is using the short junction limit i.e. $L \ll \xi_{\text{SC}}$ which might not be fulfilled for the longer lead separation. All relevant parameters are summarized in table 3.1. The values for the number of conducting channels and the induced gap is comparable to the values estimated in [13]. The estimated values have to be taken with a lot of caution due to the limitations of the model and the uncertainties on the microscopic details of each individual JJ.

3.3. AC CHARACTERIZATION OF THE JOSEPHSON JUNCTION

By illuminating the devices with microwaves, Shapiro steps form as described in chapter 1. In the experiment this is achieved by using a coaxial line with an open end which effectively works as an antenna. The antenna is placed around 1 mm close to the chip carrier to allow a good coupling to the sample. The frequency range in this geometry is 1 – 12 GHz. As just an open coaxial cable is used, the coupling to the chip carrier is not calibrated and might even change from device to device on the same substrate. Here, we present three devices produced from the same wafer. The width is set to $W = 2\,\mu$m, the respective length are $L = 150$ nm, 400 nm and, 600 nm. The experiment presented here has been repeated on more than 10 devices made out of three different wafers, all grown on CdTe substrates, with a HgTe thickness ranging between 50 – 77 nm [7] in three different measurement setups. All yield similar results. The measurements were

[7] Substrates Q2602,Q2644 Q2781 and Q2711. The presented sample here is "The Rock"from substrate Q2711.

conducted at $T = 800\,\text{mK}$ in order to avoid unstable jumps stemming from the hysteresis of the junction.

Under rf irradiation, we observe the appearance of Shapiro steps in the $I-V$ characteristic at quantized voltages $V_n = nhf/2e$, where $n \epsilon \mathbb{Z}$ is the step index [21]. In contrast to the standard JJ response, with steps at each n, we find at lower frequencies that the $n = 1$ step is missing. To illustrate this anomalous Shapiro response of our junctions, we present three I–V curves corresponding to three different excitation frequencies in 3.7a) (for the junction with $L = 150\,\text{nm}$). The applied rf power is chosen such that all curves display similar critical currents. For a high-frequency $f = 11.2\,\text{GHz}$, one typical I–V curve is plotted as a blue line. The voltage is normalized to $hf/2e$ such that the step height is constant for all frequencies. Several steps are clearly visible with step height $hf/2e$. At lower frequencies $f = 5.3\,\text{GHz}$ (green line), higher order steps are visible but a clear reduction of the amplitude of the $n = 1$ step occurs. For a frequency of $f = 2.7\,\text{GHz}$ (red line), this first odd step is fully suppressed, showing an anomalous first step at hf/e. The presence or absence of the $n = 1$ step can be conveniently detected by binning the measurement data according to the voltage (with a $0.25hf/(2e)$ bin size). The resulting histograms of the voltage V are presented as bar plots in Fig. 3.7b). For $V_n = nhf/2e$ with n being an integer, Shapiro steps appear as peaks in the bin counts, the amplitude of which then reflects the length of the current step (in nA). For $f = 11.2\,\text{GHz}$, all steps emerge clearly from the background. For $f = 2.7\,\text{GHz}$, the peak at $V = hf/2e$ is absent, reflecting the suppression of the $n = 1$ Shapiro step. This anomalous behaviour of the Shapiro steps constitutes the main finding in this chapter. Below, we carefully analyse its origin and conclude that it indicates the existence of a 4π-periodic contribution to the supercurrent.

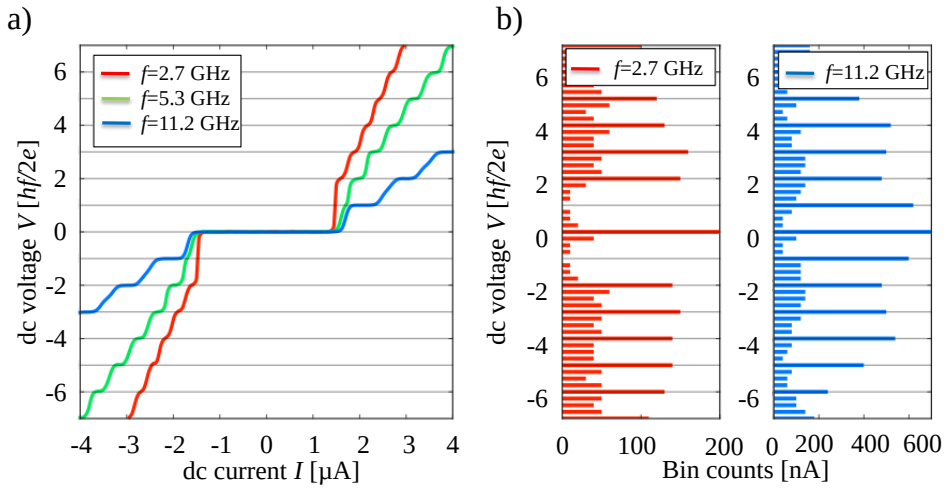

Figure 3.7: a) Shapiro steps for a junction with $L = 150\,\text{nm}$. Three different frequencies measured at $T \approx 800\,\text{mK}$. The plotted voltage scale is in normalized units $hf/2e$. b) Bar plots obtained by binning the measurement data according to voltage, for $f = 2.7\,\text{GHz}$ and $11.2\,\text{GHz}$. The Shapiro steps appear as peaks in the bin counts for $V_n = nhf/(2e)$, $n \epsilon \mathbb{Z}$. While all steps are visible for $f = 11.2\,\text{GHz}$, the first Shapiro step ($n = 1$) is absent at $f = 2.7\,\text{GHz}$.

3.3.1. POWER DEPENDENCE OF THE SHAPIRO STEP EVOLUTION

We now examine the crossover from high to low frequency, for which the first odd Shapiro step $n = 1$ progressively disappears. To this end, we scan the presence of Shapiro steps for a range of rf powers at fixed frequencies and generate two-dimensional colour plots of the bin counts at the voltage V (which indicates the current height of the Shapiro step when present) as a function of the voltage V and rf current I_{rf}. As shown in Fig. 3.8 (for the junction with $L = 150\,\mathrm{nm}$), such plots reveal the presence of Shapiro steps as maxima at constant quantized voltages (horizontal lines). A high bin count signals the presence of a plateau, which can be identified with the expected voltage value $V = hf/2e$. Let us first examine measurements taken at $f = 11.2\,\mathrm{GHz}$. (Fig. 3.8c). At $I_{\mathrm{rf}} = 0$, a single maximum at $V = 0$ reflects the presence of a supercurrent. As I_{rf} increases, Shapiro steps progressively appear, starting from low values of n, while the amplitude of the supercurrent ($n = 0$) decreases and eventually vanishes (here around $I_{\mathrm{rf}} \approx 0.3$). From now on, everything below the first crossing will be called the *low power regime* and everything above the *high power regime*. The position where the supercurrent vanishes for the first time is labeled the first crossing. In the high power regime, the steps show an oscillatory pattern, reminiscent of Bessel functions occurring in the voltage bias case [15, 22]. Horizontal linecuts at constant voltages give access to the amplitude of the first steps ($n = 0, 1, 2, 3$ and 4), presented in the lower panels of Fig. 3.8 as a function of rf current I_{rf}. For high frequencies such as $f = 11.2\,\mathrm{GHz}$, our device exhibits the conventional behaviour that is seen in various other systems (carbon nanotubes [23], graphene [24] or Bi_2Se_3 [25] weak links), that always (regardless of frequency) show a clear presence of the $n = 1$ step. The case of atomic contacts (with a few ballistic highly transparent modes) is particularly well understood, and also exhibits a strong $n = 1$ Shapiro resonance in excellent agreement with theoretical models [26, 27]. In contrast to the conventional Shapiro features commonly reported, our HgTe-based junctions exhibit a very clear vanishing of the first step $n = 1$ when the excitation frequency f is decreased. Measurements at $f = 5.3\,\mathrm{GHz}$ show that the first step is suppressed below a certain value of I_{rf} (indicated by the red arrow), and that it is completely absent at $f = 2.7\,\mathrm{GHz}$. In the oscillatory regime at higher rf currents, a suppressed first oscillation (dark fringe indicated by the dark grey arrow) becomes clearly visible at the low frequency, demonstrating the range of influence of the vanishing first step on the rest of the pattern. In the lower panels, a complete suppression of the first step or disturbances in the oscillations at higher rf currents can similarly be observed. This crossover has been observed on all working devices, up to 800 mK. In some cases, hysteretic behaviour at low temperatures hinders the observation of low-index steps. Shapiro steps in a Josephson junction with a hysteresis due to electron heating in Nb-Au-Nb junctions were studied by Cecco *et al.* [28]. There, the authors found that hysteresis introduces unstable switching of the critical current which may lead to the vanishing of several Shapiro steps. The asymmetry of the switching currents (I_s and I_r) also leads to a clear asymmetry in the Shapiro response for the "positive"and "negative "current branch. At low temperature and low rf-powers where we observe hysteresis we sometimes find such a behaviour In this case we increased the temperature such that no hysteresis is measured any more. Furthermore, measurements on junctions with a shunt resistor such that hysteresis is fully suppressed have been conducted which also showing a missing first step [29].

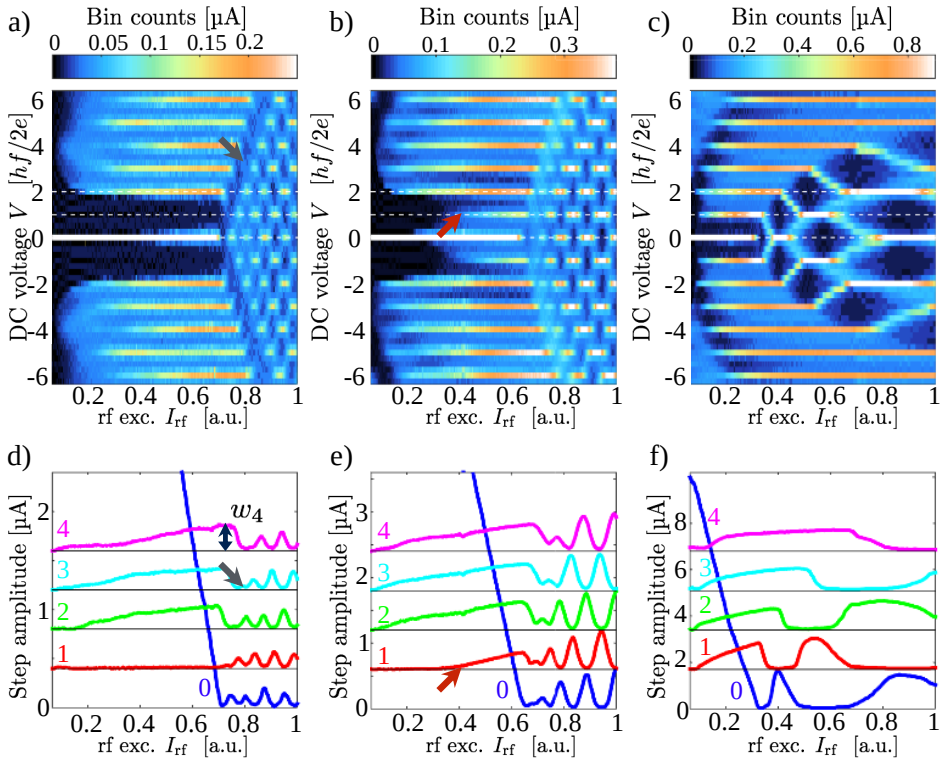

Figure 3.8: 2D map of the bin counts for frequencies $f = 2.7, 5.3$ and $11.2\,\text{GHz}$, respectively. Shapiro steps are identified as maxima for constant voltages V_n (white dashed lines emphasize $n = 0, 1$ and 2). For $f = 11.2\,\text{GHz}$, all steps are visible. When the frequency is lowered ($f = 5.3\,\text{GHz}$), the first odd step ($n = 1$) is absent up to a rf excitation indicated by the red arrow. Finally, at $f = 2.7\,\text{GHz}$, the first step is completely invisible up to the crossing point that marks the beginning of the oscillatory regime at higher rf currents. A dark fringe (indicated by a dark grey arrow) is observed at finite voltages in the oscillating pattern concomitant with the missing $n = 1$ step. (d–f) Horizontal linecuts through the previous colormaps (frequencies $f = 2.7, 5.3$ and $11.2\,\text{GHz}$) that give access to the amplitudes of steps 0–4. While all Shapiro steps are clearly visible at high frequencies, the step $n = 1$ progressively disappears as f decreases. From these plots, we access the maximum widths w_n of each step (see the example of w_4 at $f = 2.7\,\text{GHz}$). For clarity, the different curves are offset by 0.4, 0.6 and 1.7 μA for d–f, respectively.

In contrast to a missing $n = 1$ step, additional subharmonic steps (for $n = p/q$ fractional value) are often observed [26, 30] as a consequence of non-linearities, capacitance effects or higher harmonics in the current phase relation. Such higher harmonics have been predicted [9] and detected [13] in our junctions. At higher frequencies, we indeed observe half-integer steps ($n = 1/2, 3/2$ and so on) as slightly visible Fig. 3.8. Such higher harmonics appear at much higher frequencies in a different regime from where we observe the missing $n = 1$ step.

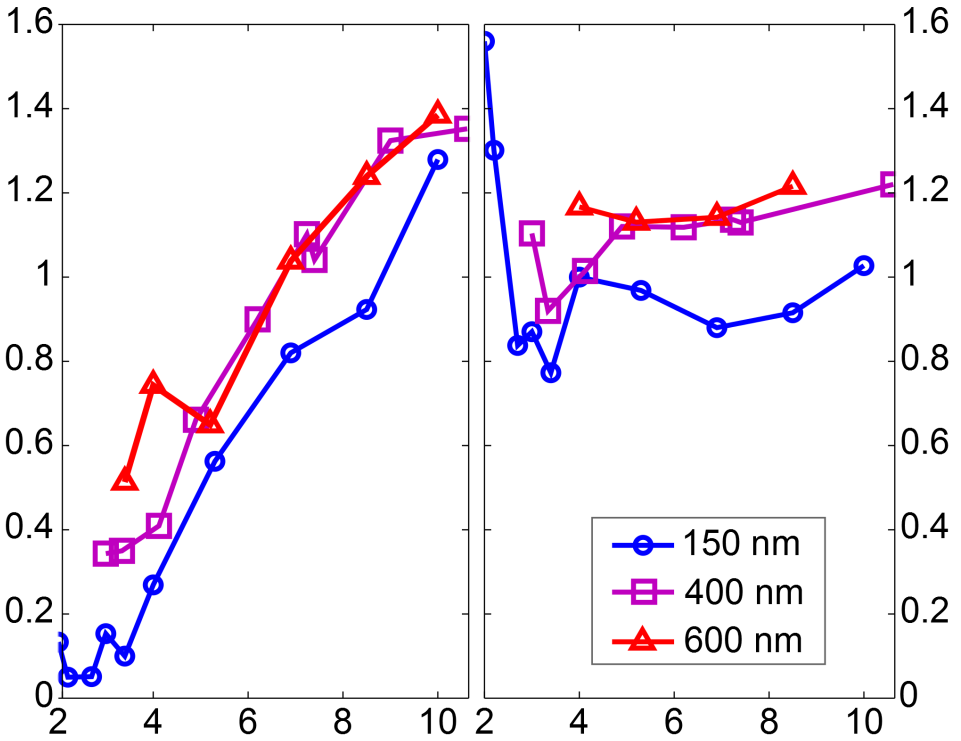

Figure 3.9: For each length L of the JJ, we calculate the ratios of step amplitudes $Q_{12} = w_1/w_2$ (a) and $Q_{34} = w_3/w_4$ (b) and plot them as a function of the rf frequency. Q_{12} shows a clear decrease as frequency f is lowered. A minimum around 0.05 is obtained for the 150 nm junction, but we observe that this minimum tends to increase with the length L of the junction. In contrast, even if the measurements show some scattering, the ratio of higher order steps Q_{34} does not show significant variation. For comparisons, we evaluated Q_{12} and Q_{34} from a conventional RSJ model, and show the results as a grey area.

3.3.2. ANALYSIS OF THE AMPLITUDE OF THE 4π-CURRENT

The presence of a 4π-periodic contribution in the supercurrent $I_{4\pi} \sin\phi/2$ is the only known mechanism to result in the observed doubling of the Shapiro step size. As already mentioned, microscopic models based on Bogoliubov-de Gennes equations have predicted such a 4π-periodic contribution in the current phase relation (CPR) [7, 9, 31, 32], which originates from the presence of a gapless topological Andreev doublet. This anoma-

lous CPR can then be supplemented with the Josephson equation on the time-evolution of the phase difference to simulate the dynamics of such a system. This dynamics is captured in the extended resistively shunted junction (RSJ) model of Dominguez *et al.* [33]. It takes into account the presence of a $\sin\phi/2$ contribution in the supercurrent and explains the crossover between the two frequency regimes by the highly non-linear dynamics of the junction. When a small 4π-periodic contribution $I_{4\pi}\sin\phi/2$ is superimposed on a large 2π-periodic supercurrent $I_{2\pi}\sin\phi$ in the CPR, the latter dominates the high-frequency Shapiro response, but the weak 4π-periodic contribution is revealed at low frequencies by doubled Shapiro steps. Doubled Shapiro steps are observed only when the driving frequency f_{rf} becomes smaller than the characteristic frequency $f_{4\pi} = 2eR_nI_{4\pi}/h$ (with R_n the normal state resistance of the device). This frequency scale based on the amplitude of the 4π-periodic supercurrent is expected to be much smaller than the typical Josephson frequency scale $f_J = 2eR_nI_c/h \simeq 53\,\mathrm{GHz}$ for the 150 nm long junction, as $I_{4\pi} \ll I_{2\pi} \simeq I_c$. To estimate $I_{4\pi}$, we introduce two indicators Q_{12} and Q_{34} as follows. From the maximum amplitude of the first lobe of each step, denoted by w_n, $n\epsilon\mathbb{Z}$, (see Fig. 3.8a where the measurement is indicated for the $n = 4$ step), we define and compute the ratios $Q_{12} = w_1/w_2$, $Q_{34} = w_3/w_4$, and plot them as a function of the rf excitation frequency (Fig. 3.9). Despite some scattering, we observe a clear decrease of Q_{12} towards 0 with decreasing frequency, while Q_{34} remains constant around 1, for all lengths. For the shortest junction (150 nm), Q_{12} reaches a value of 0.05 around 2 GHz, and the first step $n = 1$ is invisible. For comparison, we have also plotted the boundaries (grey dashed lines) between which the ratios Q_{12} and Q_{34} vary in the standard RSJ model [34, 35] (with only a $\sin\phi$ component in the supercurrent). While the ratio Q_{34} remains close to the grey region, the behaviour of Q_{12} is not properly described. Assuming the validity of the above criterion for $f_{4\pi}$, one can evaluate the number of 4π-periodic channels. We estimate the crossover frequency where the ratio is 50% which gives $f_{4\pi} = 4.5$–$5\,\mathrm{GHz}$ and $I_{4\pi} = 250$–$300\,\mathrm{nA}$ for the 150 nm junction, and $f_{4\pi} = 4\,\mathrm{GHz}$ and $I_{4\pi} = 50$–$70\,\mathrm{nA}$ for the longer junctions (400 and 600 nm). One can compare these values with the maximum supercurrent carried by one channel [36], given by $e\Delta_i/\hbar$ per channel, where Δ_i is taken from table 3.1. With $\Delta_i = 0.35\,\mathrm{meV}$ (150 nm) and $\Delta_i = 0.1$–$0.15\,\mathrm{meV}$ (400 and 600 nm), we estimate that the 4π-periodic contribution amounts to that of 1–3 channels that is compatible with the presence of one topological mode in our system, despite uncertainties on the exact value of $f_{4\pi}$ and Δ_i.

MAGNETIC FIELD DEPENDENCE OF THE MISSING FIRST STEP

Further investigations of the anomalous Shapiro response have been carried out in the presence of a magnetic field perpendicular to the plane of the device. First, when the $I-V$ curve is measured without rf irradiation, a Fraunhofer-like diffraction pattern of the critical current is observed as visible in Fig. 3.10. The distance between two neighboring minima yields $\Delta B = 0.8\,\mathrm{mT}$ which is in agreement with earlier reports on similar devices with comparable aspect ratios [11] and corresponds to a conventional 2π-periodicity, when considering the finite penetration depth of the niobium contacts. It is interesting that the observability of the missing first Shapiro step, quantified by the ratio Q_{12} follows this behaviour. It is possible to explain this behavior by assuming a constant value of the fraction $I_{4\pi}/I_c$. The frequency $f_{4\pi}$ at which a missing step can be observed rapidly reduces when I_c decreases. The magnetic field breaks TRS and should therefore have an effect on the splitting of the ABS from the continuum states. Bulk HgTe has a large Landé-factor of

$g \simeq 20$ [37]. The Zeeman splitting per mT yields $E_Z/B = g\mu_B \approx 1\mu eV/mT$ and is therefore for the accessible fields $B < 3\,mT$ negligible compared to the induced gap $\Delta_i \approx 100\,\mu eV$. It will be interesting to use a more suitable configuration of the superconducting contacts to study the influence of larger fields especially along the plane of the HgTe mesa as there higher fields are allowed before the supercurrent vanishes. Depending on the magnetic field direction to the current direction different effects are expected. First of all, by applying an in-plane magnetic field the pairing of Cooper-pairs is expected to change due to the spin momentum coupling [38]. Furthermore, the Andreev bound states can be manipulated by the Zeeman effect and it should be possible to induce some kind of backscattering for a perpendicular to current alignment while a parallel to current alignment only shifts the Fermi momenta.

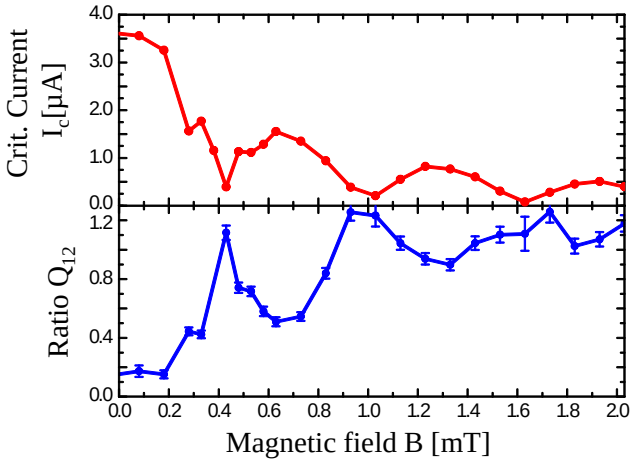

Figure 3.10: Upper panel: critical current I_c as a function of perpendicular magnetic field. Lower panel: The ratio Q_{12} as a function of the perpendicular magnetic field B.

DISCUSSION OF TRIVIAL ORIGIN OF A 4π-CONTRIBUTION TO THE SUPERCURRENT

A possible trivial origin of a $\sin\phi/2$ contribution are Landau-Zener transitions (LZTs) as depicted in Fig. 3.11. Such non-adiabatic transitions are possible to occur at the anticrossings at $\phi = (2n+1)\pi$, with $n \in \mathbb{Z}$, and causing highly transparent modes which have a small gap δ to behave effectively as 4π-periodic. The probability of a transition can be estimated using the exponential function $P_{LZT} = \exp(-8\pi\delta^2/E_J\hbar\dot{\phi})$. This means that a small gap δ or equivalently a high transmission is enhancing the LZT probability. Furthermore, as the derivative of the phase is proportional to the voltage this effect gets stronger for a larger applied bias V as $\dot{\phi} \propto V$. We do not observe the missing Shapiro steps at high applied microwave frequencies or powers. In fact, we observe the opposite the first step is stronger suppressed at low voltage bias and low rf frequency. This reasoning make LZT an unlikely candidate for the origin of the missing first Shapiro step.

It is worth noting that here only the first step $n = 1$ is missing while all higher odd steps are visible. In the following chapter 4 we will see that this behaviour can be understood within the resistively shunted Josephson junction framework of two contributions to the

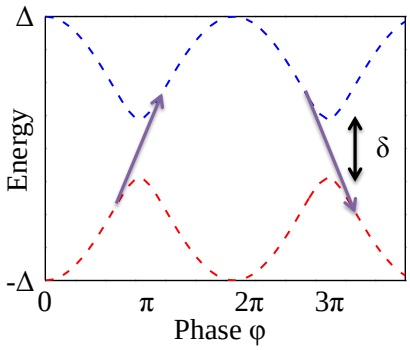

Figure 3.11: a) Sketch of Landau-Zener crossings which can turn a conventional 2π-periodic bound state 4π-periodic. If the driving bias is strong enough a electron can be excited into the upper energy level close to the anticrossings. The size of the gap between the two branches is δ.

supercurrent and that it is also possible to observe higher order missing odd steps when the number of modes is reduced. The next chapter is devoted to the numerical modelling of a Josephson junction with a $\sin\phi$ and $\sin\phi/2$ contribution to understand the observed behaviour.

3.3.3. CONCLUSION

To conclude, we have presented robust evidence for a 4π-periodic contribution to the supercurrent flowing in JJs based on the 3D TI HgTe. The consistency of the measurements in Hall-bars and JJs indicates that our devices are well-controlled, with well-defined proximity-induced superconducting HgTe contacts connected via a ballistic HgTe surface. Under rf irradiation, a suppression of the first Shapiro step is observed at low frequencies and, for a wide range of temperatures from 20 mK up to 800 mK. We attribute this to the existence of a 4π-periodic component in the supercurrent. The study of its order of magnitude and of Landau–Zener transitions reveal that these experimental observations are compatible with the presence of a few 4π-periodic gapless Andreev bound states. The topologically non-trivial behaviour of HgTe has been established in the previous works. There is evidence, that such states would likely stem from the topologically protected gapless Andreev doublet.

BIBLIOGRAPHY

[1] L. Fu and C. L. Kane, *Topological insulators with inversion symmetry,* Physical Review B **76**, 045302 (2007).

[2] C. Brüne, C. Thienel, M. Stuiber, J. Böttcher, H. Buhmann, E. G. Novik, C.-X. Liu, E. M. Hankiewicz, and L. W. Molenkamp, *Dirac-Screening Stabilized Surface-State Transport in a Topological Insulator,* Physical Review X **4**, 41045 (2014).

[3] C. Ames, *Molecular Beam Epitaxy of 2D and 3D HgTe, a Topological Insulator*, Ph.D. thesis, Universität Würzburg, Fakultät für Physik und Astronomie (2015).

[4] C. Brüne, C. X. Liu, E. G. Novik, E. M. Hankiewicz, H. Buhmann, Y. L. Chen, X. L. Qi, Z. X. Shen, S. C. Zhang, and L. W. Molenkamp, *Quantum Hall Effect from the Topological Surface States of Strained Bulk HgTe,* Physical Review Letters **106**, 126803 (2011).

[5] O. Crauste, Y. Ohtsubo, P. Ballet, P. A. L. Delplace, D. Carpentier, C. Bouvier, T. Meunier, A. Taleb-Ibrahimi, and L. Lévy, *Topological surface states of strained Mercury-Telluride probed by ARPES,* arXiv preprint arXiv:1307.2008 (2013).

[6] L. Fu and C. Kane, *Superconducting Proximity Effect and Majorana Fermions at the Surface of a Topological Insulator,* Physical Review Letters **100**, 096407 (2008).

[7] C. T. Olund and E. Zhao, *Current-phase relation for Josephson effect through helical metal,* Physical Review B **86**, 1 (2012).

[8] M. Snelder, M. Veldhorst, A. A. Golubov, and A. Brinkman, *Andreev bound states and current-phase relations in three-dimensional topological insulators,* Physical Review B **87**, 1 (2013).

[9] G. Tkachov and E. M. Hankiewicz, *Helical Andreev bound states and superconducting Klein tunneling in topological insulator Josephson junctions,* Physical Review B **88** (2013).

[10] W. L. McMillan, *Tunneling Model of the Superconducting Proximity Effect,* Physical Review **175**, 537 (1968).

[11] J. B. Oostinga, L. Maier, P. Schüffelgen, D. Knott, C. Ames, C. Brüne, G. Tkachov, H. Buhmann, and L. W. Molenkamp, *Josephson Supercurrent through the Topological Surface States of Strained Bulk HgTe,* Physical Review X **3**, 021007 (2013).

[12] L. Maier, J. B. Oostinga, D. Knott, C. Bruene, P. Virtanen, G. Tkachov, E. M. Hankiewicz, C. Gould, H. Buhmann, L. W. Molenkamp, and C. Brüne, *Induced superconductivity in the three-dimensional topological insulator HgTe,* Physical Review Letters **109**, 186806 (2012).

[13] I. Sochnikov, L. Maier, C. A. Watson, J. R. Kirtley, C. Gould, G. Tkachov, E. M. Hankiewicz, C. Brüne, H. Buhmann, L. W. Molenkamp, and K. A. Moler, *Nonsinusoidal current-phase relationship in josephson junctions from the 3D topological insulator HgTe,* Physical Review Letters **114**, 1 (2015).

[14] L. Maier, *Induced superconductivity in the topological insulator mercury telluride*, Ph.D. thesis, Universität Würzburg, Fakultät für Physik und Astronomie (2015).

[15] M. Tinkham, *Introduction to superconductivity* (Courier Corporation, 1996).

[16] G. E. Blonder, M. Tinkham, and T. M. Klapwijk, *Transition from metallic to tunneling regimes in superconducting microconstrictions: Excess current, charge imbalance, and supercurrent conversion,* Physical Review B **25**, 4515 (1982).

[17] T. M. Klapwijk, G. Blonder, and M. Tinkham, *Explanation of subharmonic energy gap structure in superconducting contacts,* Physica B+C **109-110**, 1657 (1982).

[18] K. Flensberg, J. B. Hansen, and M. Octavio, *Subharmonic energy-gap structure in superconducting weak links,* Physical Review B **38**, 8707 (1988).

[19] A. Brinkman and A. A. Golubov, *Coherence effects in double-barrier josephson junctions,* Physical Review B **61**, 11297 (2000).

[20] K. D. Usadel, *Generalized diffusion equation for superconducting alloys,* Physical Review Letters **25**, 507 (1970).

[21] S. Shapiro, *Josephson Currents in Superconducting Tunneling: The Effect of Microwaves and Other Observations,* Physical Review Letters **11**, 80 (1963).

[22] P. Russer, *Influence of Microwave Radiation on Current-Superconducting proximity effect and majorana fermions at the surface of a topological insulatorVoltage Characteristic of Superconducting Weak Links,* Journal of Applied Physics **43**, 2008 (1972).

[23] J.-P. Cleuziou, W. Wernsdorfer, S. Andergassen, S. Florens, V. Bouchiat, T. Ondarçuhu, and M. Monthioux, *Gate-tuned high frequency response of carbon nanotube Josephson junctions,* Physical Review Letters **99**, 117001 (2007).

[24] H. B. Heersche, P. Jarillo-Herrero, J. B. Oostinga, L. M. Vandersypen, and A. F. Morpurgo, *Bipolar supercurrent in graphene,* Nature **446**, 56 (2007).

[25] L. Galletti, S. Charpentier, M. Iavarone, P. Lucignano, D. Massarotti, R. Arpaia, Y. Suzuki, K. Kadowaki, T. Bauch, A. Tagliacozzo, F. Tafuri, and F. Lombardi, *Influence of Topological Edge States on the Properties of $AlBi_2Se_3Al$ Hybrid Josephson Devices,* Physical Review B **89** (2014).

[26] M. Chauvin, P. Vom Stein, H. Pothier, P. Joyez, M. E. Huber, D. Esteve, and C. Urbina, *Superconducting atomic contacts under microwave irradiation,* Physical Review Letters **97**, 1 (2006).

[27] J. C. Cuevas, J. Heurich, a. Martín-Rodero, a. Levy Yeyati, and G. Schön, *Subharmonic shapiro steps and assisted tunneling in superconducting point contacts.* Physical Review Letters **88**, 157001 (2002).

[28] A. De Cecco, K. Le Calvez, B. Sacépé, C. Winkelmann, and H. Courtois, *Interplay between electron overheating and ac josephson effect,* Physical Review B **93**, 180505 (2016).

[29] J. Wiedenmann, E. Bocquillon, R. S. Deacon, S. Hartinger, O. Herrmann, T. M. Klapwijk, L. Maier, C. Ames, C. Brüne, C. Gould, A. Oiwa, K. Ishibashi, S. Tarucha, H. Buhmann, and L. W. Molenkamp, *4π-periodic Josephson supercurrent in HgTe-based topological Josephson junctions,* Nature Communications **7**, 10303 (2016).

[30] P. Dubos, H. Courtois, O. Buisson, and B. Pannetier, *Coherent low-energy charge transport in a diffusive S-N-S junction.* Physical Review Letters **87**, 206801 (2001).

[31] L. Fu and C. L. Kane, *Superconducting Proximity Effect and Majorana Fermions at the Surface of a Topological Insulator,* Physical Review Letters **100**, 096407 (2008).

[32] C. W. J. Beenakker, *Search for Majorana fermions in superconductors,* Annual Review of Condensed Matter Physics **4**, 15 (2013).

[33] F. Domínguez, F. Hassler, and G. Platero, *Dynamical detection of Majorana fermions in current-biased nanowires,* Physical Review B **86**, 140503 (2012).

[34] P. Russer, *Influence of Microwave Radiation on Current-Voltage Characteristic of Superconducting Weak Links,* Journal of Applied Physics **43**, 2008 (1972).

[35] D. E. McCumber, *Effect of ac Impedance on dc Voltage-Current Characteristics of Superconductor Weak-Link Junctions,* Journal of Applied Physics **39**, 3113 (1968).

[36] C. Beenakker and van Houten H, *Josephson current through a superconducting quantum point contact shorter than the coherence length.* Physical Review Letters **66**, 3056 (1991).

[37] X. Zhang, K. Ortner, A. Pfeuffer-Jeschke, C. Becker, and G. Landwehr, *Effective g factor of n-type HgT e/$Hg_{1-x}Cd_xTe$ single quantum wells,* Physical Review B **69**, 115340 (2004).

[38] S. Hart, H. Ren, M. Kosowsky, G. Ben-Shach, P. Leubner, C. Brune, H. Buhmann, L. W. Molenkamp, B. I. Halperin, and A. Yacoby, *Controlled finite momentum pairing and spatially varying order parameter in proximitized HgTe quantum wells,* Nature Physics **13**, 87 (2017).

4

MODELLING OF A RESISTIVLEY SHUNTED JOSEPHSON JUNCTION WITH TWO SUPERCONDUCTING CONTRIBUTIONS

The dynamics of a Josephson junction are commonly described by the resistively shunted Josephson junction model. This chapter starts by reviewing the case of only a $\sin\phi$ *periodicity under rf-irradiation. In order to explain the missing of odd Shapiro steps, the model is extended by a linear combination of a* 2π*- and a* 4π*-periodic supercurrent in phase. The observation of a missing first step in chapter 3 is explained first qualitatively using the washboard potential. It is possible to show that at low frequencies or low voltage the system behaves effectively* 4π*-periodic even though the contribution to the total supercurrent is small (*$I_{4\pi} \ll I_{2\pi}$*). Numerical modelling of a topological Josephson junction is then used to verify the picture. Further extensions to the model for a non-sinusoidal current phase relation, a finite capacitance and non-adiabatic transitions are discussed.*

4.1. THE TWO SUPERCURRENT RSJ MODEL

This chapter discusses the resistively shunted junction model (RSJ model) in presence of a 2π- and a 4π-periodic supercurrent. In chapter 2 section 2.4.1 it was shown that the RSJ model and the washboard potential can be used to describe the dynamics of a Josephson junction and the formation of Shapiro steps under microwave irradiation. In this chapter an extended RSJ model is used to explain the missing of odd Shapiro steps due to the contribution of a 4π-periodic supercurrent. Theory has predicted that Majorana zero modes in a Josephson junction contribute a 4π-periodicity in weak links based on topological insulators [1, 2]. In order to extend the RSJ model to the special case and include effects from Majorana zero modes, first the applicability is justified. Then, it is shown how the model operates in the presence of two superconducting contributions given by $\sin\phi$ and a $\sin\phi/2$ first using the qualitative washboard potential and second by numerical simulations. Finally, the influence of additional effects such as the Landau-Zener tunnelling, highly transmitting Andreev bound states, or the effect of a capacitance are discussed. It is possible to derive the current phase relationship using microscopic models, i.e. the explicit calculation of the energy spectrum of the Andreev bound states (ABS) using the Bogoliubov-de Gennes-equation and also the energy spectrum of gapless Andreev bound states due to Majorana zero modes. So far there exists no accessible microscopic way to describe the time evolution of the phase and therefore a calculation of the current voltage characteristics across the junction. The most common way to describe the dynamics of the junction is to use an equivalent circuit of lumped elements, the so called RSJ model, as introduced by [3–5]. In this part, a simplification is used as the system is restricted to the overdamped limit, i.e. zero capacitance $C = 0$. This assumption is for now justified in our devices, as the geometrical capacitance of the junction is rather small with $C \approx \epsilon_0 t_{SC} W_{SC}/L \approx 34\,\text{aF}$. Here, ϵ_0 is the vacuum permittivity, t_{SC} the thickness of the superconducting leads and W_{SC} the width of the superconducting electrodes [6]. This approximation for C is rather crude as it considers only the contribution from the Josephson junction and ignores the leads and the capacitance to the ground. Nevertheless, it is the dominant term since the geometrical capacitance scales inversely with the distance L and the two superconducting leads are the closest parts of the system. The Stuart McCumber parameter for the device is small ($\beta_c = 2\pi R_n^2 C/\phi_0 \ll 1$) and thus the effect of the small capacitance can be neglected for now. This shows that the present junction is in the overdamped limit and justifies the neglection of the geometrical capacitance for now[1]. Following Russer *et al.* [7], the current biased RSJ model in normalized units[2] is given by

$$\alpha + \alpha_{rf}\sin\xi\tau = \frac{d\phi}{d\tau} + I_{CPR}(\phi)/I_c. \tag{4.1}$$

By writing the equivalent circuit this way, several assumptions where used. The normal state resistance R_n and the supercurrent $I_{CPR}(\phi)$ are constant and independent on the applied bias $I_{ext}(t)$. This is a simplification as, for example, subgap states which are expected to reside inside the Josephson junction and their occupation, might change with bias or temperature. So far, it is not possible to quantify the microscopical effects in the

[1] Later another intrinsic contribution to the capacitance is discussed in 4.4.

[2] Normalized currents: $\alpha = I_{dc}/I_c$ and $\alpha_{rf} = I_{rf}/I_c$, the renormalized time $\tau = \frac{2eI_cR_n}{\hbar}t$ and frequency $\xi = \frac{\hbar\omega_{rf}}{R_N 2eI_c}$. The voltage normalized by current and resistance is given by: $d\phi/d\tau = V/I_cR_n$.

HgTe based devices and more controlled devices or knowledge of the environment are needed.

The next assumption is that the current phase relationship can be written as a linear combination of two supercurrents, namely

$$I_{\mathrm{CPR}} = I_{2\pi}\sin\phi + I_{4\pi}\sin\phi/2. \tag{4.2}$$

This implies that the two superconducting contributions are originating from two completely independent parts, or can at least be effectively summarized as two independent contributions of the time averaged system. Furthermore, the use of a sinusoidal 2π-periodic current phase relation is only valid in the limit of low transmission for the conventional Andreev bound states (ABS). The effect of a high transmission using the formula for ABS with a finite transmission is discussed in section 4.4.

We also do not consider stochastic processes like quasiparticle poisoning or other relaxation mechanisms. Such effects might turn a 4π-periodicity into 2π. Also effects like Landau-Zener transition are not considered which could in principle do the opposite, i.e. turning a 2π-periodicity into 4π. So far, we do not account for such effects directly, but treat the two contributions as the time averaged occupation per period. To make this more explicit, we consider the example of a single gapless Andreev bound state in a Josephson junction ($I_{4\pi} = I_c$ and $I_{2\pi} = 0$). The lifetime of this state is finite due to e.g. quasiparticle poisoning and therefore at some point, a 2π-periodicity is restored even though initially no conventional ABS are present. This effect is then considered implicitly by a finite contribution $I_{2\pi}$. A more comprehensive discussion of these stochastic effects is presented in section 4.4. Finally, we also ignore finite size effects, or even the use of dimensionality in general (role of 1D edge channels in a 2D quantum well or 3D bulk modes).

Despite the limitations of the model, we will show, that it is sufficient to capture the key aspects of the dynamics in the Josephson junctions in our case and describes our observation of missing odd Shapiro steps for low frequencies. The measurable observable in this system is the voltage given by the second Josephson equation $V(t) = \hbar d\phi/(2ed\tau)$. The critical current of the device is defined as $I_c = \max\{I(\phi)\}$. The differential equation 4.1 is highly non-linear leading to non-intuitive dynamics. In the next section, we explain the dominant 4π-periodic behaviour using the washboard potential. In fact, even in the case of $I_{4\pi} \ll I_{2\pi}$, it is possible to observe a predominately 4π-periodic behaviour.

4.2. QUANTITATIVE DISCUSSION USING THE WASHBOARD POTENTIAL

It is possible to explain the missing of odd Shapiro steps in presence of a 2π- and 4π-periodic contribution to the supercurrent using the washboard potential. We recall the formation of Shapiro steps as a time dependent perturbation of the washboard potential. This perturbation locks the motion of the phase particle to the external rf-drive. The washboard potential is shown at finite bias without applied ac excitation in the case of two superconducting contributions as dashed lines in the upper panel of Fig. 4.1. The phase particle is able to continuously develop in time, if the applied dc bias is larger than the critical current $I_0 > I_c$. The second Josephson equation relates a finite phase velocity to a

voltage drop across the junction. This is visible more explicitly in the derivative $dE_{\mathrm{pot}}/d\phi$ (lower panel of Fig. 4.1). A positive value in the derivative corresponds to a positive slope in the washboard potential and, therefore, a potential trap for the phase particle. Thus no voltage drop is observed. For a negative value in the derivative, the particle can move down the washboard potential with a certain phase velocity and develop a voltage drop.

Adding an ac bias I_{rf}, leads to a time dependent perturbation. The maximal values are given by $+I_{\mathrm{ac}}$ and $-I_{\mathrm{ac}}$ as indicated by the blue and red lines respectively. Steps of constant voltage appear due to the fact that the motion of the phase particle is locked to the ac frequency over a certain bias range. During one ac period, the particle falls down an integer number of steps. The number of steps is determined by the speed of the particle (the applied bias) and the time of one period given by the external frequency. Then steps of constant voltage form with a step size of $V_n = nhf/2e$ with n any integer. If the total supercurrent is now a combination of a 2π and a 4π-periodicity as described

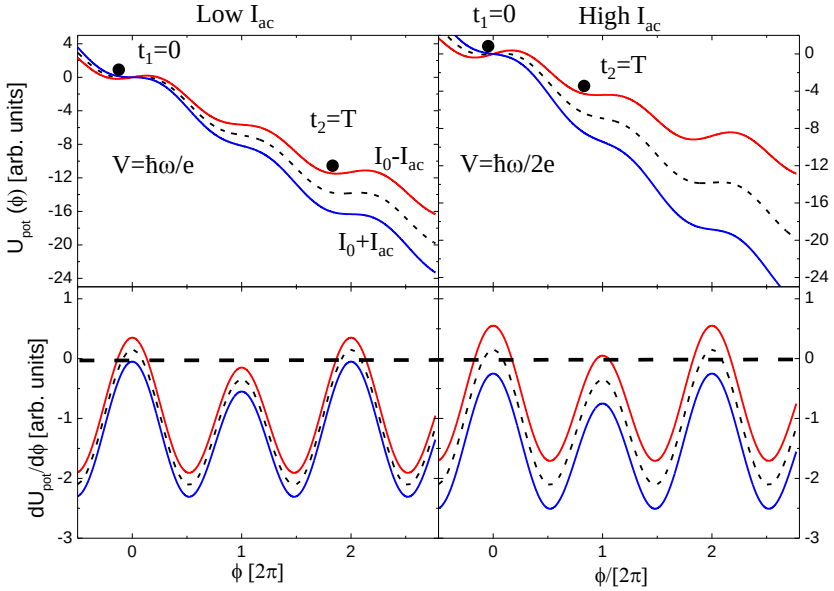

Figure 4.1: Washboard potential for two superconducting contributions $I_{2\pi}\sin\phi$ and $I_{4\pi}\sin\phi/2$ with $I_{2\pi} = 2I_{4\pi}$ with an applied dc-bias of $I_0 = 1.1I_{2\pi}$ in (black dashed lines). The effect of a rf-excitation can be represented as a time dependent change in the slope as shown by the red and blue lines. The left side shows a low rf bias $I_{\mathrm{ac}} = 0.2I_0$, while the right shows a larger bias $I_{\mathrm{ac}} = 0.4I_0$. The lower panel shows the respective colour encoded $dE_{\mathrm{pot}}/d\phi$.

by Eq. 4.2, the total periodicity is 4π with a steeper down slope in every "odd"minimum and a reduced slope every "even"minimum. In the derivative $dE_{\mathrm{pot}}(\phi)/d\phi$ (lower panel of Fig. 4.1 this is directly visible by positive or negative values. For a negative value in the derivative the phase particle can move down the washboard potential while it stops at a positive value. It is now possible that for a low ac amplitude, a minimum in the washboard potential is only achieved every 4π (red curve). This leads to the missing of odd Shapiro steps and a dominant 4π-periodic behaviour. Contrary to the case of a large ac bias,

the phase particle stops at every 2π period and all Shapiro steps are present. This is the expected conventional behaviour of a Josephson junction with only a $\sin\phi$ term. This already indicates that even though the distribution of 2π and 4π is fixed, the behaviour of the periodicity of the Shapiro steps may differ by changing the amplitude of the ac bias. Close to I_c, the system is very sensitive. It can then be understood that even a small $I_{4\pi}$-contribution ($I_{4\pi} \ll I_{2\pi}$) can still give a dominant 4π-periodic response if the applied bias is just small enough. This allows for the identification of a single gapless mode in a large background of conventional modes in the experiment. In the experiment, it was estimated that the $I_{4\pi}$-contribution can be as low as $0.05 I_0$. It is noted, that a similar reasoning applies for the dominant 4π-periodic behaviour by lowering the ac frequency ξ.

As the system is a highly non-linear differential equation a general analytic solution does not exists. Dominguez *et al.* [8] discussed several limits of the intensity I_{ac} pertubativley. We solve the differential equation numerically in the next section.

4.3. MODELLING OF THE SUPERCURRENT OF A JOSEPHSON JUNCTION

We present the procedure for obtaining the current voltage characteristics of a Josephson junction as a function of applied rf-power. First, equation 4.1 is solved using a Runge-Kutta method (RK4) for a fixed bias $I = I_0 + I_{\mathrm{rf}}$. The time evolution of the phase $\phi(t)$ is calculated. The dc voltage is then given by the derivative $V = \Delta\phi/\Delta t = [\phi(t = T) - \phi(t = 0)]/T$. By repeating this calculation as a function of bias I_0, it is possible to construct the full $I - V$ characteristics. In the following, we normalize the voltage to the expected step height of $hf/2e$. First, we discuss the $I - V$ curves for increasing $I_{4\pi}$-contribution as shown in Fig. 4.2a). For $I_{4\pi} = 0$ (black curve) the conventional behaviour is observed and all steps are visible. By gradually increasing the contribution of $I_{4\pi} = \alpha I_{2\pi}$, the odd steps become narrower until they completely disappear. This shows that a 4π-periodic supercurrent contribution causes odd steps to vanish.

Next we set in Fig. 4.2b) a constant $I_{4\pi} = 0.5 I_{2\pi}$ and vary the applied amplitude I_{rf}. For zero power $I_{ac} = 0$ (black curve), the $I - V$ trace shows the characteristic non-linear behaviour and no steps are visible. With increasing ac amplitude, first only odd steps are observed (red curve). For a higher ac bias, all integer steps start to appear. This is in agreement with the explanation using the washboard potential and also as observed in the measurements described in chapter 3.

A convenient way to present the data is by calculating a histogram for each value of I_{rf} of the simulated $I - V$ and plot it in a two dimensional map of applied dc bias as a function of rf power. Then, Shapiro steps appear as maxima in the voltage histogram as depicted in Fig. 4.3. It is possible to extract horizontal cuts of the histograms along the lines for the voltages $V_n = nhf/2e$, with $n \in \mathbb{Z}$. This represents the width of a step for a given power and is shown in the lower panels of Fig. 4.3a)-f). For the simulations without an additional 4π-periodic component (Fig. 4.3a)-c)) the first step (blue) always appears first and the other steps follow one after each other. All steps are clearly visible and for a higher frequency ξ, steps appear for lower powers. The line cuts resemble the results obtained by Russer *et al.* [7].

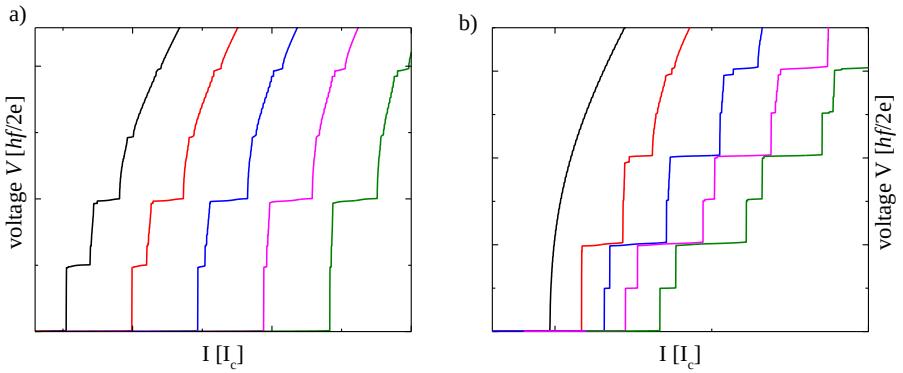

Figure 4.2: a) I-V curves for different values of $I_{4\pi} = \alpha_{4\pi} I_{2\pi}$-contribution with $\alpha_{4\pi} = 0$, (black) 0.2, (red) 0.3, (blue) 0.4 (magenta) and 0.5 (green). The other values are $I_{2\pi} = 1$, $\xi = 0.3$, and $I_{\mathrm{ac}} = 0.3$ b) I-V curves for different values of I_{ac}. The parameters for the RSJ simulations are $\alpha = 0.5$, $I_{2\pi} = 1$, $\xi = 0.2$. The values for the ac drive from left to right are $I_{\mathrm{ac}} = 0$, 0.3, 0.6, 0.9 and 1.1. All curves are offset consecutively in the x-direction, by $0.4 I_c$ for clarity.

The behaviour changes, when a small $I_{4\pi}$-contribution $I_{4\pi} = 0.15 I_c$ is added as shown for the Fig. 4.3d), e) and f). In order to compare the influence of the rf drive frequency to the Josephson current, we use the Josephson frequency in the following discussion. This is possible as the current is proportional to the Josephson frequency $f = 2eRI_c/\hbar$. This means that $I_{4\pi} = 0.15 I_c$ is equivalent to $f_{4\pi} = 0.15 f_J$ for the remainder of the discussion. At high frequencies, i.e. $f > f_{4\pi}$, as shown in Fig. 4.3d), all steps are visible, and the result is comparable to the one obtained without a 4π-periodic contribution. As the frequency is decreased, the amplitude of the odd steps is reduced as shown in Fig. 4.3e) for a frequency $f = f_{4\pi}$ and Fig. 4.3f) at a frequency $f < f_{4\pi}$. At low power, the odd steps are completely suppressed and the behaviour for the $n = 1$ step is similar to the experimentally observations presented in chapter 3. The crossover frequency from only odd to all Shapiro steps was calculated by Dominguez *et al.* [9] and occurs roughly at $f_{\mathrm{ac}} \approx f_{4\pi} = 2eR_n I_{4\pi}/\hbar$. This result holds only in the current biased case as in the experiment of chapter 3. In the voltage biased case, the differential equation can be solved analytically solution exists and the two superconducting contributions would be weighted with the size of the critical current. This would make an identification of a 4π-periodic contribution much harder in the limit of $I_{4\pi} \ll I_c$. The oscillatory pattern of the step amplitude is also modulated, leading to an even odd pattern in the high power regime. This is in fact also observed in the experiment as dark fringes (c.f. chapter 3 section 3.3.1) and visible in the step height of the odd steps.

4.3.1. INFLUENCE OF CONVENTIONAL MODES WITH A HIGH TRANSMISSION

So far we have assumed that the conventional contribution is sinusoidal, i.e. $I_{2\pi}(\phi) = I_{2\pi} \sin\phi$. This approximation is only valid in the limit of low transmission. In a structure where the weak link is for example a metal or a high mobility semiconductor, the

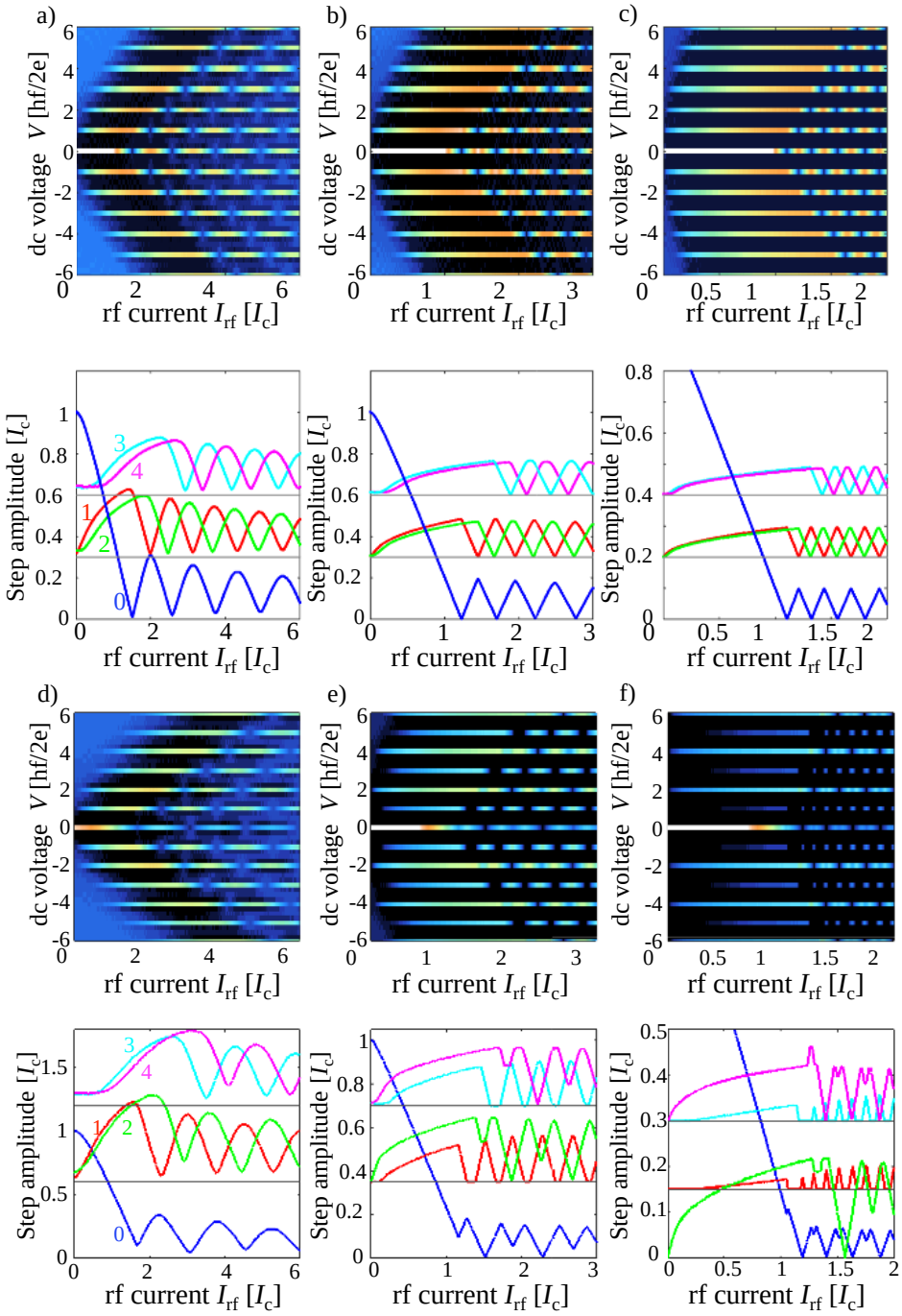

Figure 4.3: Figures a), b) and c) show the simulated Shapiro response for a conventional Josephson junction. The colour maps are obtained by bin counting the voltage of the single $I-V$ traces as a function of rf-drive I_{rf}. For three different frequencies $f = 0.4 f_J$ in a), $f = 0.2 f_J$ in b) and $f = 0.1 f_J$ in c). The line-cuts show the step amplitude along the different Shapiro plateaus. The graphs d), e) and f) show the simulated Shapiro response including a 4π-periodic term obtained the same way. The parameter values are $f_{4\pi} = 0.15 f_J$, $f = 0.5 f_J$ for d), $f = f_{4\pi}$ for e) and $f = 0.05 f_J$ for f). With decreasing frequency, odd steps are more and more suppressed at low powers.

supercurrent is carried by Andreev bound states. The current of these states is given by

$$I_s(\phi,\tau) = \frac{e\Delta}{\hbar}\frac{\tau\sin\phi}{\sqrt{1-\tau\sin^2\phi/2}}. \tag{4.3}$$

This current depends on the transmission coefficient τ and the size of the superconducting gap. The total current is then the sum over all individual channels $1/N\sum_{n=1}^{N} I_s(\phi,\tau_n)$. In our case it is not yet possible to access the states individually as the number of modes contributing to the signal is quite large $N \gg 10$. One would therefore need to know the transmission coefficient of each channel and fit a curve with at least a number of variables equal to the number of channels in the junction (assuming the same superconducting gap). The simulations are thus done with an averaged transmission over all channels. The

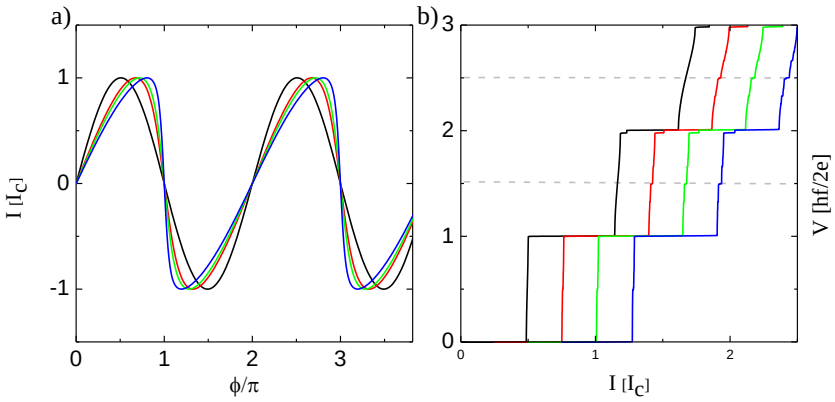

Figure 4.4: a) The current phase relationship for various values of transmission coefficient τ. The black line represents a low transmission of $\tau = 0.1$ while red, green and blue have a high transmission of $\tau = 0.9$, 0.95, and 0.99. b) simulated $I-V$ curves for the four different transmission values with an applied microwave amplitude $I_{\mathrm{rf}} = I_c$ and a frequency $\xi = 0.5$. For higher transmissions fractional steps at half the expected plateau value start to appear. No additional $I_{4\pi}$ contribution was added. The curves are vertically offset for clarity.

current phase relationship for various values of transmission is plotted in Fig. 4.4 together with their respective $I-V$ curves under applied rf radiation. No 4π-periodic behaviour is found even for the highest transmission of $\tau = 0.99$. A higher transmission leads to a non-sinusoidal behaviour and is reminiscent of a saw tooth like behaviour. This can be approximated by higher harmonics of the fundamental frequency $\sin n\phi$, with $n \in \mathbb{Z}$. Such higher harmonics are visible in the $I-V$ traces under applied microwave bias. At higher power values, fractional steps start to develop indicated by the grey dashed lines in Fig. 4.4b). In fact a similar explanation as in the case of the $\sin\phi$ and $\sin\phi/2$ behaviour is valid here (doubling effectively both frequencies $\phi \to 2\phi$). The higher harmonics start to become dominant at higher I_{rf} values.

To conclude, a linear combination of a 4π-periodic supercurrent and a 2π supercurrent allows the observation of either only odd Shapiro steps or all integer Shapiro steps depending on the parameter regime. Especially at low frequencies f_{ac} and low power I_{rf}, the phase dynamics are predominantly 4π-periodic. A small $I_{4\pi}$-contribution is thus able

to observe odd steps even in the presence of a majority of conventional modes as expected in the experiment. In addition, no generic 2π-periodic current phase relation is able to make odd steps vanish. The observed behaviour is in agreement with the experimental results in chapter 3 apart from the fact that only the first step vanishes.

4.3.2. INFLUENCE OF CAPACITANCE

The influence of a finite capacitance in the RSJ model in the presence of two superconducting contributions was discussed by Picó-Cortés *et al.* [10]. The authors showed that by taking a finite capacitance into account, the first step is more likely suppressed than higher order steps in presence of a small 4π-contribution. So far, the geometrical capacitance was shown to be negligible and thus we need to justify why it can still be a relevant contribution.

In this regard, it is important to take into account the so called intrinsic capacitance. In general, the total capacitance C_{tot} of a JJ is given by the sum of the geometrical C_{geo} and intrinsic capacitances C_{int} i.e. $C_{\text{tot}} = C_{\text{geo}} + C_{\text{int}}$. The intrinsic capacitance originates from ground state fluctuations of quasiparticles [11, 12] while the geometrical capacitance due to charging effects. For a bias close but slightly smaller than the critical current I_c, the phase particle is in a metastable state. Even if the bias is smaller than I_c, quantum or thermal fluctuations may spontaneously switch the junction into the resistive branch also the bias is smaller than the critical current. This switching behaviour can be understood using the washboard potential. There, a capacitance can be interpreted as giving the phase particle a mass m. Once the mass starts to "roll down"the potential, it now has a finite inertia and may be able to overcome the positive slope. In tunnel junctions with a rather large geometrical capacitance, the effect of the intrinsic capacitance can be usually neglected due to its small contribution to C_{tot}. Antonenko *et al.* [13] and Galaktionov *et al.* [14] showed that in the case of weak link consisting of a normal metal with a small normal state resistance and highly transmitting ABS the intrinsic capacitance is the dominating contribution and can even drive the device into a hysteretic regime. The general expression for the intrinsic capacitance is then given by $C_{\text{int}}(\phi) = \alpha(\phi)G/E_g$ where $\alpha(\phi)$ is a model dependent parameter of the order 1, G the normal state conductance and E_g the value of the induced gap. The conductance can in this context be related to the transmission of the normal state transport. A high conductance signals the presence of highly transmitting modes and thus a non-sinusoidal current phase relation. Once the phase particle tunnels through the potential, the steep slope accelerates the particle and it can get over the minimum. Considering the contribution C_{int}, the Stuart-McCumber parameter is approximated by $\beta_C = 2e\alpha(\phi)I_cR/E_g \approx 1-2$. The values used for the calculation are taken from the 3DTI Josephson junctions discussed in the previous chapter 2 and are: $R_n \approx 50\,\Omega$, $I_c \approx 2\,\mu$A, $E_g = 100-200\,\mu$eV. Therefore, the device could behave hysteretic due to the intrinsic capacitance. Although, the intrinsic capacitance and its full contribution have not been explicitly fully explored, it has become a useful parameter to the explain the observed hysteresis and the missing of predominantly the first Shapiro step.

In summary, we can argue using theoretical model of Picó-Cortés *et al.* [10] that the missing of only the first step can be caused by the capacitance of the Josephson junctions. As the Josephson junction is very likely to host some ballistic modes with a

high transmission, the intrinsic capacitance can be large enough to justify a reasonable total capacitance.

4.4. PROCESSES AFFECTING THE JOSEPHSON JUNCTION DYNAMICS

In the last part of this section the numerical treatment of Landau-Zener transitions and also other stochastic processes, which affect the Josephson dynamics are discussed. Various stochastic effects which can change the periodicity of the Andreev bound states from 4π to 2π or, vice versa are illustrated in Fig. 4.5a). Gapped Andreev bound states with a 2π periodicity may turn 4π by Landau-Zener processes which have the highest probability at the anti-crossings at $\phi = (2n+1)\pi$, $n \in \mathbb{Z}$. This process is highlighted in Fig. 4.5a) by the black arrows and occurs with a estimated probability of

$$P_{\mathrm{LZ}} = \exp(-2\pi\delta^2/\Delta_i \hbar\dot{\phi}). \tag{4.4}$$

According to this classical approximation, the probability decays exponentially with the size of the gap δ. This gap is directly related to the transmission of the ABS by $2\delta = 2\Delta_i\sqrt{1-\tau}$. A high transmission is therefore favouring this process. The probability increases with increasing phase velocity $\dot{\phi} \propto V$, which is proportional to the applied bias V according to the second Josephson equation. This is contrary to our experimental observations as we observe missing odd Shapiro steps only at a low bias. The second process is related to the dephasing rate Γ_d which is caused by voltage fluctuations e.g. from the external source which destroy the coherence of the Andreev bound state over time. The time t_d is expected to be much shorter than the time to change the phase by 2π. Interference effects between two consecutive Landau-Zener transitions can thus be neglected [9].

Two more decay processes can influence the periodicity of the Andreev bound states. The first process is the relaxation of the excited Andreev bound state into the ground state and related to the relaxation rate Γ_r. The second process is quasiparticle poisoning by adding or removing a quasiparticle from the quasi-continuum into the Andreev bound state and related with a rate Γ_{qp}. Both time scales (rates) are unknown in our device. They can be quite long in conventional Josephson devices (up to minutes but is usually µs) [15]. The rather long quasiparticle poisoning time scale compared to the ac bias frequency ($1\,\mathrm{GHz} \approx 10^{-3}$µs) is exactly the reason Shapiro steps and the measurement of the Josephson emission are suitable for the measurement of the periodicity of the current phase relation of a topological Josephson junctions. A comprehensive numerical study of Landau-Zener transitions was reported in Ref.[8]. We summarize the main here. By assuming a single mode model [9], it is possible to estimate numerically the influence of Landau-Zener transitions in the following way. A typical plot of $\phi(t)$ and $V(t)$ is shown in Fig. 4.6b), with $\phi(t)$ as a red line and $V(t) \propto \dot{\phi}(t)$ as a blue line for the following parameters: $I = 0.5I_c$, $I_{\mathrm{rf}} = 0.8I_c$, $f = 0.2f_J$. The phase ϕ (blue) follows an anharmonic motion synchronized with the excitation drive at a frequency f: during one period of duration $1/f$, the phase ϕ increases by 2π, yielding an averaged voltage $V = hf/2e$ as expected for the first Shapiro step. Equivalently, one can calculate the average of $V(t)$ and obtain $V =< V(t) >= hf/2e$. Then, we access the time t for which ϕ reaches the anticrossing for example for $\phi(t) = 3\pi$

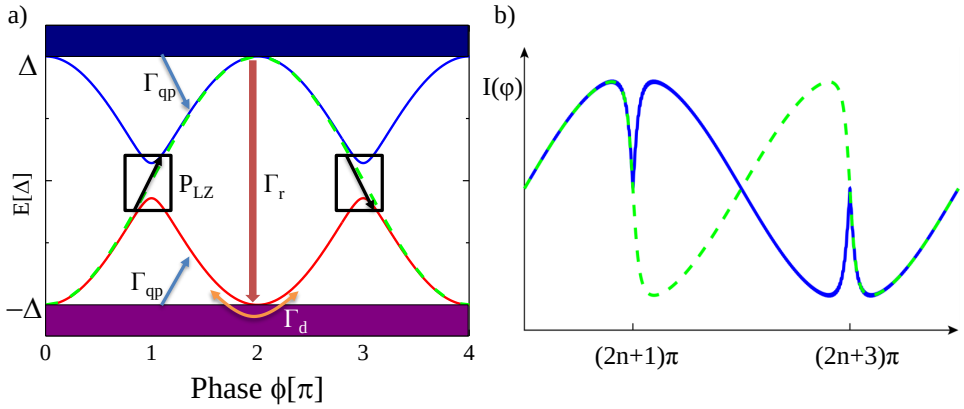

Figure 4.5: a) Andreev bound state spectrum with possible relaxation processes. The ground and excited Andreev bound state are shown in red and blue respectively. It is possible that a Landau-Zener transition occurring at the anti-crossing turns the spectrum 4π-periodic as indicated by the green dashed line. A quasiparticle from the continuum can change the occupation of the ABS on a time scale related to Γ_q. The exited state might itself relax on a time scale related to the decay rate Γ_r. The coherence of the Andreev bound state is lost by dephasing rate Γ_d (orange arrow). b) The current phase relationship with two consecutive Landau-Zener transitions (blue) and no Landau-Zener transitions (dashed green). Figure b) is taken from [9] with small modifications.

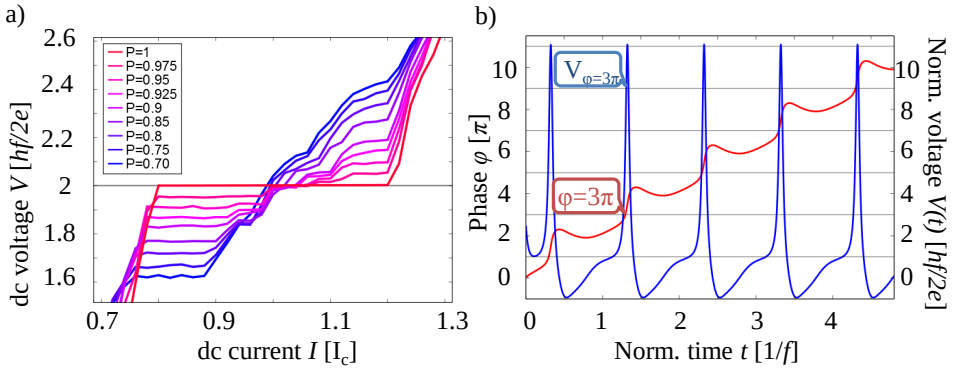

Figure 4.6: a) The effect of Landau-Zener transitions in the RSJ model on the Shapiro step $n = 2$. The numbers P in the legend are the probability of a Landau-Zener transition. For finite values $P < 1$ the Shapiro step deteriorates from the expected quantized value. b) Time evolution of phase $\phi(t)$ (red) and voltage $V(t)$ (blue) is calculated via RSJ equations and plotted as a function of time t in units per rf period $1/f$.

and calculate the derivative of the phase $\dot{\phi}_{3\pi}$ at this point or equivalently the voltage $V_{3\pi}$. For a given ABS with gap δ, it is then possible to calculate P_{LZ} using Eq. 4.4 and compare it to a random number to check if a Landau-Zener transition occurs. If a transition occurs the current phase relationship is multiplied by -1 to account for the population of the excited state as shown in Fig. 4.5b) (blue). If the Landau-Zener probability is one i.e. at each anti crossing, the state is excited by the external drive and the junction behaves undistinguishable to a 4π-periodicity. In Fig. 4.6a), the effect of finite Landau-Zener probabilities $P < 1$ on the $n = 2$ step is shown. The quantization of the Shapiro steps is lost and splits in two branches departing from the plateau. This can be understood since the Landau-Zener transition is a stochastic process and the result is an average value between the 2π and 4π processes depending on the probability of each process. It is still possible to estimate a lower bound of the gap δ and therefore the minimum transmission of an Andreev bound state which could cause such an effect. As we do not observe a deviation from the Shapiro step, we can still estimate a lower bound of the probability of a Landau-Zener transition which is needed within our measurement accuracy. With the lowest accessible frequency ($2\,\mathrm{GHz} \approx 8\,\mu\mathrm{eV}$) in the experiment, it is possible to estimate the gap $\delta \lesssim 9\,\mu\mathrm{eV}$. The transmission can then be calculated by $2\delta = 2\Delta_{\mathrm{ind}}\sqrt{1-\tau^2}$ which leads to a transmission $\tau \geq 0.994$. To our knowledge such a high transmission was never reported in superconducting hybrid devices and is even rare in atomic break junctions.

In summary, we showed that the observed phenomena presented in chapter 3 can be described using a two Josephson supercurrent model in the RSJ framework. The influence of several parameters were discussed and it was concluded that a 4π-periodic supercurrent needs to be present to observe the vanishing of odd steps. It was shown, that for low frequencies or powers, the junction behaves predominately 4π-periodic even though the total contribution of the $I_{4\pi}$ is rather small. Stochastic processes were discussed. Especially Landau-Zener transitions can turn a conventional Andreev bound state to effectively behave 4π-periodic. The probability of this process is enhanced at high powers, high frequencies or a large applied dc bias and therefore likely to occur in the completely opposite regime where we observe missing odd steps.

BIBLIOGRAPHY

[1] L. Fu and C. L. Kane, *Superconducting Proximity Effect and Majorana Fermions at the Surface of a Topological Insulator,* Physical Review Letters **100**, 096407 (2008).

[2] L. Fu and C. L. Kane, *Josephson current and noise at a superconductor/quantum-spin-Hall-insulator/superconductor junction,* Physical Review B **79**, 161408 (2009).

[3] D. E. McCumber, *Effect of ac Impedance on dc Voltage-Current Characteristics of Superconductor Weak-Link Junctions,* Journal of Applied Physics **39**, 3113 (1968).

[4] L. Aslamazov and A. I. Larkin, *Josephson Effect in Superconducting Point Contacts,* (1969).

[5] E. D. Thompson, *Perturbation theory for a resistivity shunted Josephson element,* Journal of Applied Physics **44**, 5587 (1973).

[6] J. B. Oostinga, L. Maier, P. Schüffelgen, D. Knott, C. Ames, C. Brüne, G. Tkachov, H. Buhmann, and L. W. Molenkamp, *Josephson Supercurrent through the Topological Surface States of Strained Bulk HgTe,* Physical Review X **3**, 021007 (2013).

[7] P. Russer, *Influence of Microwave Radiation on Current-Superconducting proximity effect and majorana fermions at the surface of a topological insulatorVoltage Characteristic of Superconducting Weak Links,* Journal of Applied Physics **43**, 2008 (1972).

[8] F. Domínguez, O. Kashuba, E. Bocquillon, J. Wiedenmann, R. Deacon, T. Klapwijk, G. Platero, L. Molenkamp, B. Trauzettel, and E. Hankiewicz, *Josephson junction dynamics in the presence of 2 π-and 4 π-periodic supercurrents,* Physical Review B **95**, 195430 (2017).

[9] F. Domínguez, F. Hassler, and G. Platero, *Dynamical detection of Majorana fermions in current-biased nanowires,* Physical Review B **86**, 140503 (2012).

[10] J. Picó-Cortés, F. Domínguez, and G. Platero, *Signatures of a 4π-periodic supercurrent in the voltage response of capacitively shunted topological Josephson junctions,* arXiv preprint arXiv:1703.09100 (2017).

[11] U. Eckern, G. Schön, and V. Ambegaokar, *Quantum dynamics of a superconducting tunnel junction,* Physical Review B **30**, 6419 (1984).

[12] Y. Song, *Origin of "capacitance" in superconducting microbridges,* Journal of Applied Physics **47**, 2651 (1976).

[13] D. S. Antonenko and M. A. Skvortsov, *Quantum decay of the supercurrent and intrinsic capacitance of Josephson junctions beyond the tunnel limit,* Physical Review B **92** (2015).

[14] A. V. Galaktionov and A. D. Zaikin, *Fluctuations of the Josephson current and electron-electron interactions in superconducting weak links,* Physical Review B **82**, 1 (2010).

[15] D. J. van Woerkom, A. Geresdi, and L. P. Kouwenhoven, *One minute parity lifetime of a NbTiN Cooper-pair transistor,* Nature Physics **11**, 547 (2015).

5

GAPLESS ANDREEV BOUND STATES IN THE QUANTUM SPIN HALL INSULATOR HGTE

This chapter is based on the publication: GAPLESS ANDREEV BOUND STATES IN THE QUANTUM SPIN HALL INSULATOR HGTE.
E. Bocquillon, R.S. Deacon, J. Wiedenmann , P. Leubner., T.M. Klapwijk, C. Brüne, K. Ishibashi, H. Buhmann and L.W. Molenkamp,
Nature Nanotechnology 12, 137–143 (2017).

This chapter reports on the fabrication and analysis of superconductivity induced in a HgTe quantum well, a two dimensional topological insulator that exhibits the quantum spin Hall effect. By irradiating a Josephson junction with microwaves, Shapiro steps emerge and demonstrate that the supercurrent has a 4π-periodicity in the superconducting phase difference, as indicated by a doubling of the voltage step for multiple Shapiro steps. In addition, the response to a perpendicular magnetic fields is investigated and an interference pattern reminiscent of a superconducting quantum interference device is observed. This indicates that the 4π-periodic supercurrent originates from states located on the edges of the junction and shows signatures expected to occur in strong spin orbit coupled systems. Both features, namely the missing of odd Shapiro steps and the SQUID like diffraction pattern appear strongest towards the quantum spin Hall regime, and thus provide evidence for induced topological superconductivity in the helical edge states. The chapter is organized as follows. First, a short review of the theoretical predictions and previous experimental work on induced superconductivity into quantum spin Hall insulators prior to starting this work is presented. Then, the fabrication is detailed followed by a zero magnetic field characterization of the device without applied ac-bias. The behaviour in a perpendicular magnetic field is discussed followed by Shapiro measurements on a topological and trivial quantum well.

5.1. SIGNATURES OF INDUCED TOPOLOGICAL SUPERCONDUCTIVITY

In 2000 Alexei Kitaev investigated a simple model, a one dimensional superconducting chain without spin degeneracy [1]. He predicted, that in such a system, unpaired Majorana bound states at the end of the wire may occur. His main interest was to use these localized bound states as qubits which are predicted to be less sensitive to decoherence as other qubit systems. They form the basic building blocks for so called topological quantum computation [2]. One experimental implementation of this phase can be obtained by combining recently discovered topological states with conventional s-wave superconductivity [3–5]. Possible realization so far have been the combination of strong spin-orbit coupled nanowires with a superconductor and an applied Zeeman field [6, 7]. In this regard, most of the experimental focus to date has been on 1D InAs or InSb nanowire systems, which may undergo a topological phase transition under an appropriate applied magnetic field. Although first results have been obtained [8, 9], the topological origin of the observed phenomena remains unclear partly because the helical transport in the normal state has not been demonstrated[1] and partly because several trivial artefacts can give rise to similar responses. For example Ref. [11] gives a detailed discussion. Furthermore, in order to braid Majorana fermions, several nanowires need to be connected in complex networks. This is a tough challenge as nanowires must either be randomly put on the substrate or positioned one by one. A newer development is to use two dimensional quantum wells and pattern one dimensional channels which can then be combined to scalable networks [12].

An interesting alternative platform is provided by quantum spin Hall (QSH) insulators, in which electrons flow in two counterpropagating 1D edge states with opposite spins [13, 14] as depicted in Fig. 5.1a). Unlike nanowires, this topological state is present in the absence of a magnetic field, and thus renders the requirements for high critical field superconductors unnecessary [15]. However, the localization in nanowires is more natural due to the finite length, a time-reversal symmetry breaking mechanism such as a (local) magnetic field is needed to localize Majoranas in the QSH case. The main difference to the discussion of a 3D topological insulator based weak link presented in chapter 2 is the dimension of the effective topological superconductor. In the 3D topological insulator a two dimensional surface state is in proximity with a superconductor and a 2D $p_x + ip_y$ superconducting state is created. In the QSH case, superconducting correlations are induced in one dimensional edge channels effectively forming a 1D $p_x + ip_y$ superconductor similar to the proposed model of Kitaev.

Ideally, a Josephson junction formed from a QSH insulator and conventional s-wave superconducting contacts is expected to emulate spinless 1D p-wave superconductivity at its edge. At each edge, the junction contains one Andreev doublet with a topologically protected crossing for a superconducting phase difference $\phi = \pi$ [Fig. 5.1b)]. The two states of this gapless topological Andreev doublet (usually called Majorana bound states) have a 4π periodicity in the superconducting phase difference ϕ and can thus carry a 4π-periodic supercurrent, $I_{4\pi} \sin\phi/2$, along the edges of the sample [16, 17]. This contrasts

[1] Recently an article appeared which claims the observation of a helical gap in a nanowire without applied magnetic field [10].

with conventional 2π-periodic Andreev bound states (ABSs) that carry a current $I_{2\pi}\sin\phi$ (+ higher harmonics). This theoretical expectation for an unconventional Josephson effect motivates the experiment in this chapter.

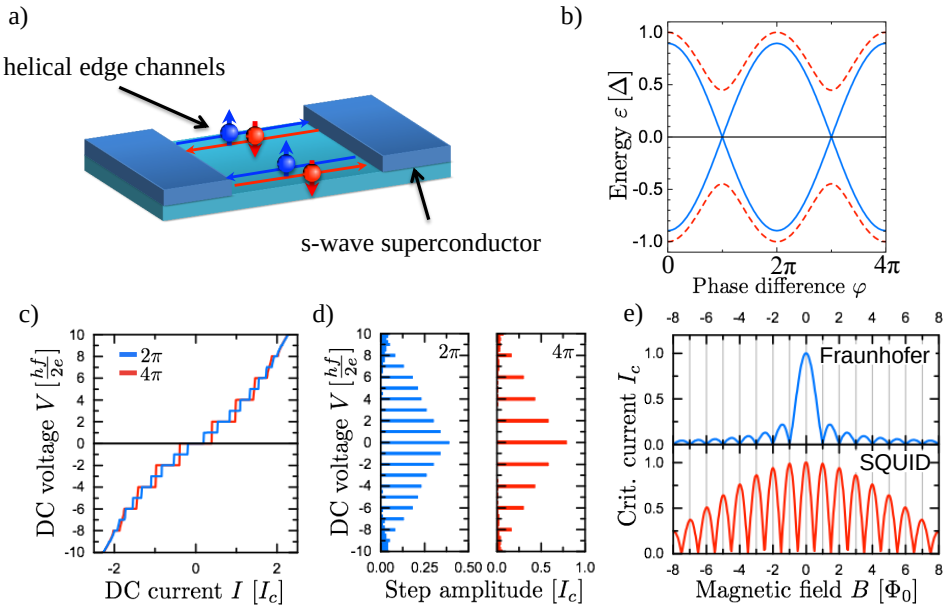

Figure 5.1: a) Schematic of a topological Josephson junction with induced superconductivity. A superconducting weak link in the QSH regime contacted by two superconducting s-wave electrodes hosts induced p-wave superconductivity. b) Andreev spectrum of a topological p-wave Josephson junction (in the short junction limit). The Andreev bound states, located on the edges of the samples, have a protected crossing at zero energy ε and a 4π periodicity in the superconducting phase difference ϕ (blue lines), in contrast with the conventional 2π-periodic Andreev bound states (red dashed lines). c) Simulated dc current–dc voltage (I–V) curves in the presence of rf excitation for 2π- and 4π-periodic supercurrents, obtained with the RSJ model [18] extended to account for 4π-periodic supercurrents [19, 20]. d) Histograms of the voltage distribution (in bins of $0.25\,hf/2e$). e) Simulated normalized critical current I_c as a function of the magnetic field B (in units of the number of flux quanta through the junction area), following formulas in Barone and Paterno [21]. For an uniform planar current, a Fraunhofer pattern (blue line) is depicted. For current flowing on the edges, a dc SQUID pattern (red line) is expected.

Here, the realization of a device, that follows the proposal of Fu and Kane [3] using HgTe quantum wells [14] is reported. Owing to their inverted-band structure [13], HgTe quantum wells of suitable thickness are QSH insulators in which superconductivity can be induced by means of, for example, Al electrodes [22]. The anticipated presence of gapless Andreev bound states on the edges of such a device should be evidenced by two remarkable signatures, which are presented as simulations in Fig. 5.1c) and e). A 4π-periodic supercurrent is expected in the ac Josephson effect [Fig. 5.1c)]. When phase locking occurs between the junction dynamics and an external radio frequency (rf) excitation, Shapiro steps appear at discrete voltages given by $V = nhf/2e$, where n is the step index [23]. Usually all integer n steps are expected to be visible [Fig. 5.1d) blue line]. On the contrary, in the presence of a 4π-periodic supercurrent, an unconventional sequence

of even steps with missing odd steps is expected [Fig. 5.1d) red line], which reflects the doubled periodicity of the Andreev bound states [24–26]. The exact sequence of visible steps can be highlighted by plotting a histogram of the voltage distribution as presented (Fig. 5.1d, right panel).

In this chapter, the experimental observation of an even sequence of Shapiro step, with missing odd steps up to $n = 9$ is reported. The estimated amplitude of the 4π-periodic supercurrent is compatible with the presence of two gapless Andreev doublets. By changing the electron density, the missing of odd steps occurs predominant near the expected QSH regime. In contrast, a non-topological HgTe quantum well is found with a conventional Shapiro response.

A second signature of topological edge transport can be obtained by a magnetic field applied perpendicular to the plane of the quantum well. This provides information on the spatial dependence of the current density [Fig. 5.1e)]. When the current distribution is homogeneous, the uniform flow through the plane of the quantum well results in a standard Fraunhofer pattern [21] (illustrated by a blue line in Fig. 5.1e). When current flows only on the edges, a dc superconducting quantum interference device (SQUID) response is expected [21, 22] [Fig. 5.1e), red line]. Our measurements show a mixture of these two cases; this shows that at least a dominant part of the supercurrent flows along the edges. Additionally, in the SQUID regime, strong modulations of the odd lobes are observed, yielding an apparent doubling of the periodicity in the magnetic flux from Φ_0 to $2\Phi_0$.

5.2. EXPERIMENTAL REALIZATION OF A TOPOLOGICAL JOSEPHSON JUNCTION

The experimental realization of a topological JJ using HgTe QWs as described in this chapter of the thesis is based on the proposal of Fu and Kane [27]. In this regard, the fabrication process outlined in chapter 3 for uncapped 3D topological insulators has to be modified in order to suit the goals of the thesis involving buried quantum wells. First, the MBE grown material is characterized by magnetotransport measurements to ascertain the high quality of the epitaxial layers. Then, the fabrication process of the Josephson junction is outlined and the device is characterized at millikelvin temperatures. The section ends with the classification of the junction into the corresponding transport regimes.

5.2.1. CHARACTERIZATION OF THE HGTE QUANTUM WELL

The Josephson junction is based on the substrate QC0280. The substrate is an 8 nm thick, nominally undoped HgTe quantum well sandwiched between two $Hg_{0.3}Cd_{0.7}Te$ layers as depicted in Fig. 5.2a). The bottom barrier is grown on a commercially available CdZnTe substrate and has a thickness of 136 nm and the capping layer has a thickness of 23.5 nm. All these nominal values were verified using x-ray spectroscopy techniques. The Zn content in the substrate changes the lattice constant of the substrate such that it allows a lattice matched growth of the HgTe quantum well and leads to a higher crystalline quality in general. The upper capping layer is chosen to be thin (< 30 nm) to allow ion beam etching (IBE) of the capping layer followed by in-situ deposition of the superconducting

leads. The thickness d of the quantum well is chosen to exhibit an inverted band structure ($d > d_c = 6.3\,\text{nm}$) as discussed in Ref. [13]. The band structure of the quantum well was calculated using a k·p algorithm, developed by Pfeuffer-Jeschke [28]; the result is shown in Fig. 7.5b). At this thickness, an inverted band structure with an indirect band gap is calculated. The direct gap at $k = 0$ is about 33 meV at $k = 0$. The mobility and

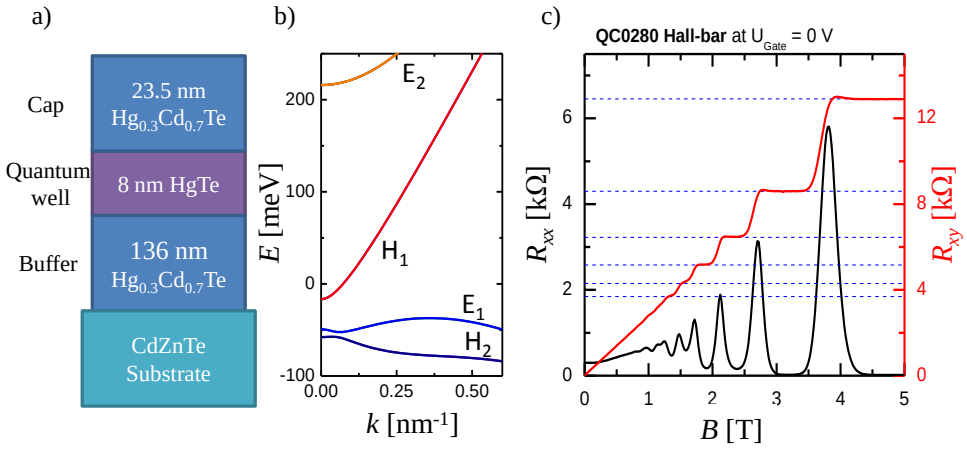

Figure 5.2: a) Sketch of the thickness of the layers of the epitaxial grown heterostructure QC0280, which is used for the experiments in this chapter. A 8 nm thick HgTe quantum well is grown on a commercially available CdZnTe substrate and protected by two $Hg_{0.3}Cd_{0.7}Te$. b) Band dispersion of a 8 nm HgTe quantum well on a CdZnTe substrate obtained by k·p calculation. c) Characterization measurements from an optical produced Hall-bar from the substrate QC0280 with dimensions 200 µm×600 µm. The longitudinal (black) and transversal (red) resistance are measured as a function of magnetic field at 4.2 K.

charge carrier density of the substrate used to fabricate the Josephson junctions were evaluated by measuring the longitudinal and transversal resistance of a Hall-bar with length × width dimensions of 600 µm×200 µm. The results of the magneto-transport measurements are shown in Fig. 5.2c). From this, an electron like charge carrier density of $n_e = 2.3 \times 10^{11}\,\text{cm}^{-2}$ and a mobility of $\mu = 300\,000\,\text{cm}^2\text{V}^{-1}\text{s}^{-1}$ can be deduced. From these values, the elastic mean free path was estimated to be $l_{\text{mfp}} \simeq 2.4\,\mu\text{m}$.

5.2.2. FABRICATION OF THE JOSEPHSON JUNCTIONS

The HgTe quantum wells used for fabricating the QSH based JJ have a $Hg_{0.7}Cd_0.3Te$ capping layer with a thickness of 23.5 nm. In order to achieve a good transparent interface between the HgTe and the superconductor, it is necessary that the interface is (i) clean and (ii) in direct proximtiy to each other. Therefore, the capping layer needs to be etched away in the area where the supercondcuting leads are deposited. Without this layer the mobility is drastically reduced. The HgTe would partially oxidise under air such that the exact thickness would not be known. In addition, it is beneficial to apply the superconductor right after the etching to avoid oxidation of the HgTe. Furthermore, a working process to deposit a gate insulator was developed which allows the charge carrier density in the material to be controlled. The whole process is outlined below.

DESIGN OF THE JOSEPHSON JUNCTIONS

The design of the structure is depicted in Fig. 5.3a). The mesa (blue) are three rectangles with dimensions width × length of 4 × 10 µm^2. The width is designed to avoid overlap of the wave functions of the edge channels, as this would lift the helical protection and allow backscattering from the edge channels. The localization of the wave function of the edge channels is estimated to be around 200 to 400 nm [22, 29, 30]. Hence there should be no backscattering due to a finite overlap. The superconducting leads are shown in green. The distance L between the leads is $L = 500$ nm for the bottom junction, 600 nm for the middle junction and 800 nm for the topmost junction as indicated in the picture. The width of the leads is chosen to be 1 µm. As a superconducting material, 5 nm Ti followed by 150 nm of Al was chosen. This makes it possible to use directional electron-gun (egun) evaporation which allows an easier and sidewall free process compared to isotropic magnetron sputtering of Nb. The Ti layer is necessary because samples made purely with Al contacts did not show a supercurrent. The reason is likely to be that the Al reacts with the Te atoms forming an interfacial telluride; However, the samples with only Al showed high contact resistances $R_{\text{contact}} >$ kΩ. The introduction of a thin Ti layer apparently solves this issue and allows good induced superconductivity. In addition, Ti is superconducting by itself ($T_c(Ti) \approx 400$ mK); it is therefore expected, that the Ti adapts the superconducting gap size of the Al due to the proximity effect and the thin height of the Ti layer. A gate is structured (red) between the superconducting leads in order to be able to control the occupation of states. The whole process is sketched in Fig. 5.4 and the detailed process steps can be found in the appendix B. Figure 5.4a) shows the material as grown by the MBE. This is cleaved into a roughly 3 mm ×3 mm large piece using a scalpel. The first step is the definition of the mesa by IBE [2]. Therefore, a so called sacrificial layer of 10 nm SiO_2 is deposited by a low temperature plasma-enhanced chemical vapour deposition (PECVD) at 80 °C. This step is shown in Fig. 5.4b). A poly(methyl methacrylate)(PMMA) in ethylacetat resist is applied and the desired mesa is defined by using electron-beam lithography (Ebeam) with 2.5 kV acceleration voltage. After development in isopropanole, a 20 nm Ti etch shield is applied by egun evaporation and the metal is lift-off in acetone [Fig. 5.4c)]. The SiO_2 exposed sacrificial layer is removed by reactive ion etching (RIE). The mesa is etched using argon sputtering to etch through the cap and bulk layer [Fig. 5.4d)]. The residual titanium etch mask is removed using buffered oxide etch. A optical microscope picture of the finished mesa is shown in Fig. 5.3b) and a sketch in Fig. 5.4e).

The next step is the definition and evaporation of the superconducting leads. For this reason a double layer of PMMA is spin coated using PMMA 600K 6% in ethylacetat and a 950K 4% in ethylacetat resist. The rather thick resist allows for up to 50 nm insitu IBE etching. The chosen PMMA layers form an undercut as the two resists have different sensitivity and avoids the formation of side-walls which makes the deposition of a gate in a later step simpler and less susceptible to gate leakage. The thickness of the PMMA on the other hand limits the resolution which affects especially the distance between the two superconducting leads L. Using this resist, it was possible to achieve a separation of about

[2] An alternative dry etch process for the definition of the mesa was later developed using BaF as an etch mask which simplifies the overall process. Information about this process can be found in e.g. [31]. Recently wet etching of the mesa was also established in our group using a KI:I:HBr solution. The reason this kind of etchant was introduced due to the fact that the quality of especially small heterostructure is lowered by IBE.

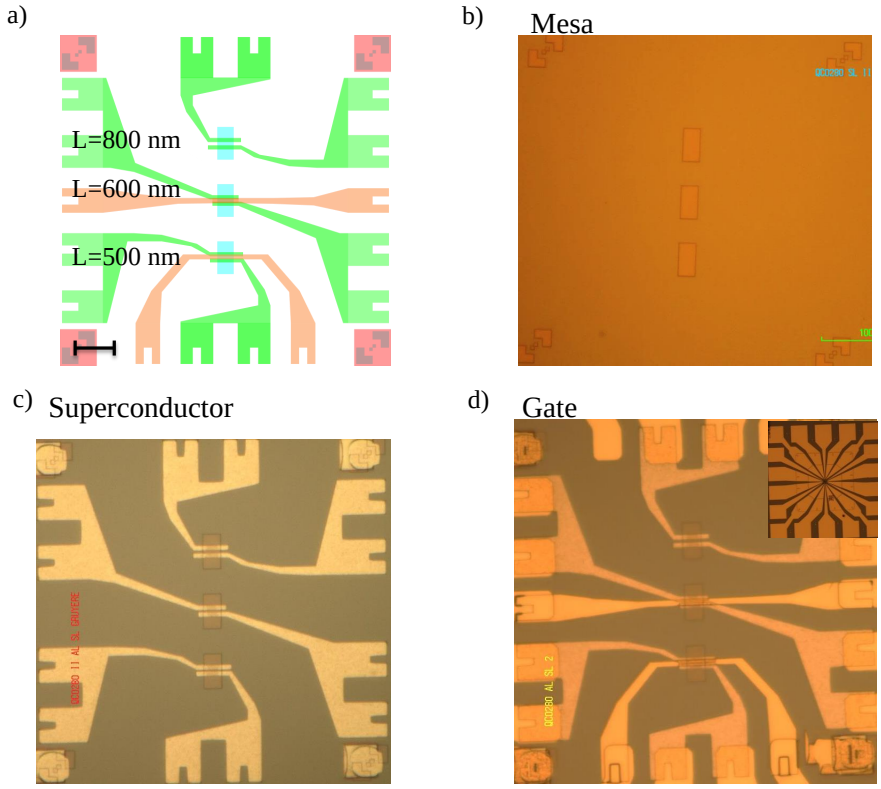

Figure 5.3: a) Design of the Josephson junctions. The mesa (blue) is contacted by superconducting leads (green). A gate (orange) is applied between the superconducting leads. The black bar indicates a distances of 10µm. b)and c) Show the structure after the finished mesa and superconductor step respectively. d) Shows the finished structure with applied gate and optical contacts. The small inset shows an overview of the final structure including the optically defined bonding pads.

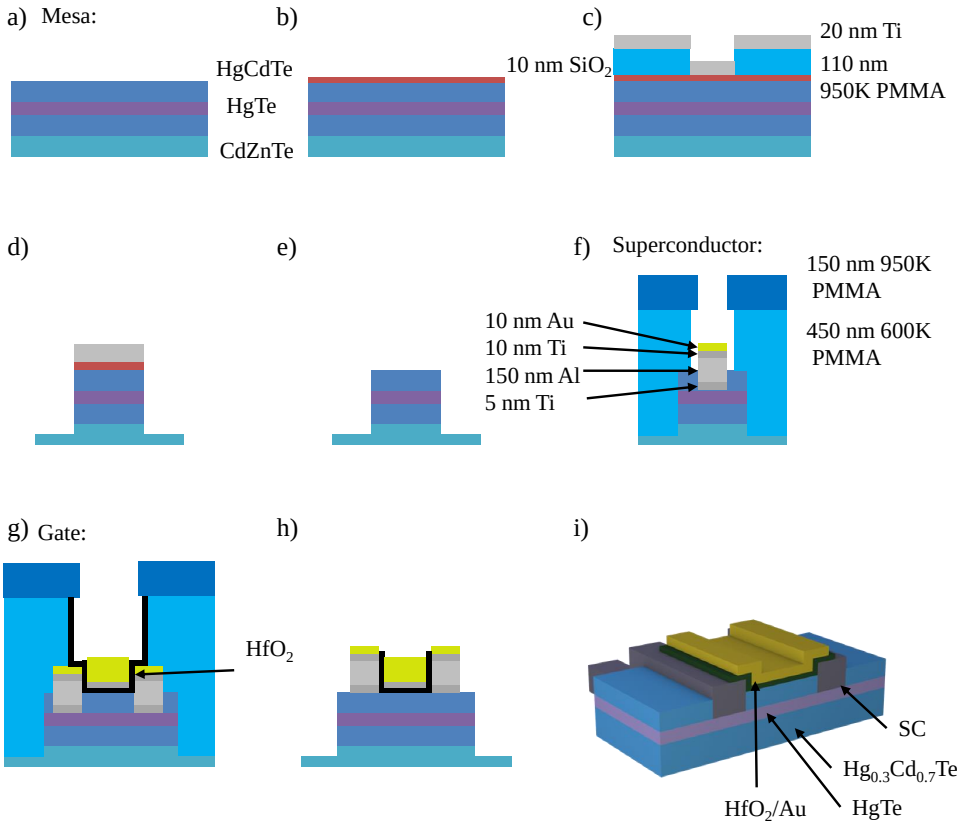

Figure 5.4: Fabrication process of a topological Josephson junction: a) The process starts with a MBE grown HgTe quantum well material grown on a CdZnTe substrate. b) Ten nanometer of SiO_2 is grown using plasma-enhanced chemical vapor deposition. The sample is spin coated with 950 K 3%, exposed to an a ebeam writer to produce the mesa pattern 20 nm Ti are deposited. d) The Ti layer is lift off in acetone and the exposed SiO_2 is removed via reactive ion etching. The uncovered HgTe parts are then ion milled. e) The Ti and SiO_2 are removed using a buffered hydrofluoric acid (HF) solution. f) A double layer resist is applied and the superconducting leads are written using ebeam lithography. Argon milling is used to etch down to the quantum well and a superconducting layer stack as indicated in the picture is deposited. g) A double layer resist is applied and the gate structure is written using ebeam lithography. A HfO_2 dielectric is grown with a thickness of $d \approx 15$ nm by atomic layer deposition at 35° C and a gate electron (5 nm Ti and ≈ 100 nm Au) is evaporated. h) The layer is lift of in acetone. i) Artist's view of the finished device.

$L \gtrsim 400$ nm. The structure is written by Ebeam exposure using 30 kV acceleration voltage. The resist is developed using a 1:1 Ar:IPA solution for 60 s followed by 30 s isopropanole and deionized water. The higher acceleration voltage compared to the 2.5 kV previously used is needed due to the thick double layer resist (total thickness approx. 650 nm). The capping layer is etched away using IBE etching. The best results were achieved when trying to etch as close as possible to the HgTe quantum well (about 1-2 nm away). Etching completely through the quantum well did not result in any observable supercurrent[3]. The sample is transferred to the egun evaporation chamber without breaking vacuum and the following layer stack is deposited: 5 nm Ti, 150 nm Al, 10 nm Ti and $\gtrsim$ 10 Au. The last layer is used to protect the Al against oxidation, while the Ti spacer layer is used to avoid a high resistance gold-aluminium intermetallic called purple plague layer. In Fig. 5.3c) the device after deposition of the superconductor is shown. In this picture, the surface of the superconducting leads is rough. THis is presumably due to the thin Au layer which sometimes leads to clustering. Then, using the same process as in the superconducting lead step, the gate structure is defined by Ebeam exposure and developed. This process allow the growth of an ALD gate oxide followed by metallization of the gate electrode. To avoid sticking problems of the insulator on the substrate a 3 – 5 s oxygen plasma cleaning step in the RIE was introduced before approximately 20 nm of HfO_2 are grown by ALD at 35° C. This low temperature grown HfO_2 has been proven to be a good choice for a reliable insulator, which allows to access a wide range of carrier density. One has to keep in mind, that the metallic gate structure is close to the active HgTe structure and the superconducting leads. This proximity might influence the electrostatic environment Due to the chosen undercut of the resist and the isotropic growth by ALD, it is possible now to apply the metallic gate using egun evaporation (5 nm Ti and 100 nm Au).

In a last step, the wire bond pads are defined using an optical process and 50 nm AuGe, 5 nm Ti and 50 nm Au are evaporated. The final device is shown in Fig. 5.3d). A sketch of a final device is shown in Fig. 5.4i). The measured distance between the superconducting leads using a scanning electron microscope (Fig. 5.5) yields a slightly shorter distance (400 nm) then the nominal distance of 500 nm.

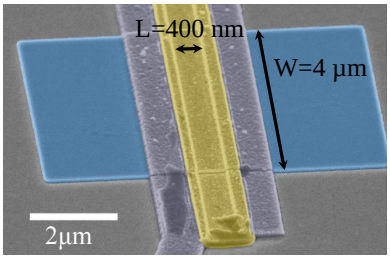

Figure 5.5: Colorized scanning electron microscope picture of a Josephson junction. The HgTe mesa is blue, the Ti/Al superconducting contacts are in grey and the gate is in yellow and lies between the superconducting contacts.

[3] Recently the combination of wet etch of the mesa and applying superconducting contacts on the edges of the mesa without the need to etch away the capping layer was successful.

As the mean free path estimated from the magneto-transport measurements $l_{\mathrm{mfp}} > 2\,\mu\mathrm{m}$ is larger than the distance between the two superconducting leads, the junction is in the ballistic limit. The mobility value was evaluated using a larger macroscopic Hall-bar. The mobility can be reduced in the micro-structure and therefore the estimate of the mean free path is an upper limit. The device is quite close to the short junction limit, i.e., the coherence length of the Al $\xi \approx 0.7 - 2\,\mu\mathrm{m}$ is comparable to the distance L between the superconducting leads. Therefore, only one or few ABS in the junction per channel are expected.

5.2.3. DC CHARACTERIZATION OF THE JOSEPHSON JUNCTION

The current-voltage characteristic measured at 30 mK and zero applied gate voltage and magnetic field is shown in Fig. 5.6a). The junction exhibits a supercurrent with a critical current value $I_c = 1.1\,\mu\mathrm{A}$ and then jumps into a resistive branch. Hysteresis is observed between forward and reverse sweeps (red and blue), with a retrapping current $I_r < I_c$. There is a strong indication that the difference between I_c and I_r depends on the size of the critical current. For voltages larger than the energy gap of the aluminium ($\Delta_{\mathrm{Al}} \simeq 170\,\mu\mathrm{V}$), the I–V curve reaches an asymptote that does not go through the origin (grey line). The slope indicates the normal state resistance of the device R_n, while the intercept is the excess current I_{exc}. The excess current [32] stems from the enhanced probability of Andreev reflections in an energy window near the superconducting gap. It thus signals the presence of Andreev reflections at the single superconductor/TI interfaces and shows therefore good transparent contacts. By comparing the amplitude of the excess current $I_{\mathrm{exc}} = 1.4 I_c$ with numerical simulations using Ref. [33], the barrier transparency t was estimated to be about $t = 0.6$ to 0.8.

To identify the QSH regime, it is instructive to plot the normal state resistance R_n and the critical current I_c as a function of the gate voltage V_g [Fig. 5.6b)]. From this plot it is possible to describe three regimes. For gate voltages between $V_g = -1.1$ and 0 V, R_n is low (below 300 Ω) and I_c is large (above 200 nA), which thus characterizes a high-mobility n-type conduction as also observed in the reference Hall-bar. For gate voltages below $V_g \approx -1.6\,\mathrm{V}$, the normal state resistance again decreases. We take this as a sign for increasing density again, which indicates the p-conducting regime. Owing to a lower mobility in this region, likely due to the dispersion of the heavy hole bands, the critical current I_c lies below 50 nA and is always finite up to the most negative gate voltages. Between $V_g = -1.7$ to $-1.1\,\mathrm{V}$, R_n exhibits a peak with a maximum around 1.5 kΩ (for $V_g = -1.45\,\mathrm{V}$), for which I_c is almost suppressed but still has a finite value $I_c \approx 10\,\mathrm{nA}$. This indicates the region in which the QSH edge states should be most visible. However, the peak value of R_n is lower than the expected quantized value of $h/2e^2 \approx 12.9\,\mathrm{k\Omega}$.The observed resistance suggests the presence of residual bulk modes in the junction [22], possibly because of diffusion of the contact material (Ti and Al) [34] into the HgTe material. Additionally, local n-doping caused by Al may result in p–n barriers at the interface between the Al-capped and gated areas. This would contribute to the two-point normal state resistance R_n and could obscure a correct identification of the QSH transition.

In Fig. 5.7a), the $I_c R_N$ product is shown as a function of gate voltage V_g. It saturates for the n-regime around 110 μV and decays when the gate voltage is reduced below −1 V and saturates again around 20 μV. The $I_c R_N$ product yields a lower bound for the

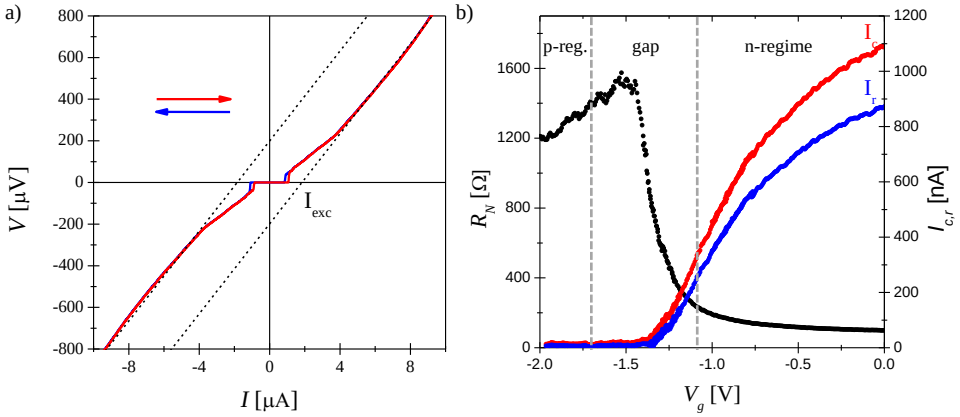

Figure 5.6: a) $I-V$ curve measured at a gate voltage $V_g = 0\,\mathrm{V}$. This exhibits a critical current $I_c \approx 1.1\,\mu\mathrm{A}$, with a weak hysteresis visible between the forward and reverse sweep (blue and red lines). For high biases, the asymptotes (grey dotted lines) yield the normal state resistance R_n and signals the presence of an excess current I_{exc}. b) Normal state resistance R_n (black), critical current I_c (red) and retrapping current I_r (blue) as a function of gate voltage V_g.

induced gap $\Delta_{\mathrm{ind}}/e \geq I_c R_n$ which is compatible with the Al superconducting gap of the leads ($\Delta_{\mathrm{ind}} < \Delta_{\mathrm{Al}} \approx 120\,\mu\mathrm{eV}$). It also shows that there is a clear transition between the high mobility n-regimes and low mobility p-regime and a much better induced superconductivity in the n-regime in general likely due to the formation of a $p-n$ barrier. Such a $p-n$ barrier still allows the observation of a supercurrent in the p-regime of graphene based Josephson junctions [35]. In addition, the gapless edge states are not affected by such a barrier due to Klein-tunneling. Therefore the p-n barrier needs to be stronger due to the finite band gap of the bulk quantum well or alternatively the low mobility in the p-regime is causing this suppression of supercurrent. In Fig. 5.7b)

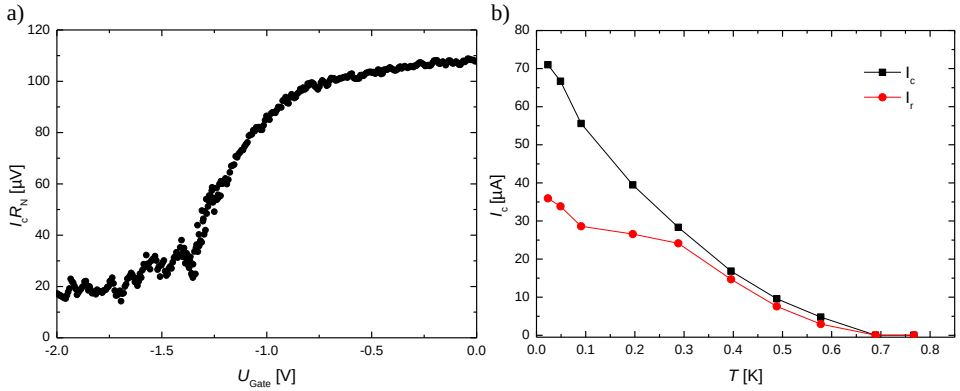

Figure 5.7: a $I_c R_N$ product as a function of gate voltage measured at 30 mK b) critical current I_c (black) and retrapping current I_r (red) at $V_g = -1.35\,\mathrm{V}$ as a function of temperature T.

the critical current I_c and retrapping current I_r are shown as a function of temperature. The decay is observed down to 600 mK, which would correspond to an effective gap of $\Delta_{\text{ind}} \simeq 90\,\mu\text{eV}$ in agreement with the values given by the $I_c R_N$ product. However, attempts to model the exact dependence with Kulik-Omelyanchuk formula (for a single ballistic channel) or with Eilenberger equations (for a multi mode junction), following Veldhorst *et al.* [36] have not been successful. Possible reasons for this are that our system is a two component system consisting of bulk and edge states both can react different to temperature or the proximity-induced gap might be different from a BCS-like behaviour used in the assumption of the models.

Given the vanishing of the critical current at 600 mK, the estimate of the induced gap yields $\Delta_{\text{ind}} < \Delta_{\text{Al}}$. Thus, one can evaluate the natural coherence length $\xi \geq \hbar v_F/(\pi\Delta_{\text{Al}}) \approx 1\,\mu\text{m}$ with an estimated Fermi velocity of the edge channels of $v_F \approx 5 \cdot 10^5 ms^{-1}$ [14]. The junction is thus possibly close to the short junction limit ($L \lesssim \xi$).

5.3. RESPONSE TO A MAGNETIC FIELD

5

Before investigating the rf response,the behaviour of the junction in a magnetic field applied perpendicular to the plane of the junction is detailed. Considering a junction as it is depicted in Fig. 5.8a). The magnetic field is applied along the y-direction and the junction itself is in the $x-z$-plane. The two leads A and B are separated by a distance L and the width of the electrodes is W. The gauge-invariant phase across the Josephson junction is given by

$$\phi = \phi_B - \phi_A - \frac{2\pi}{\Phi_0}\int_1^2 \mathbf{A}d\mathbf{l}, \tag{5.1}$$

where the limits of the integral go from electrode A to B [37]. The phase difference between

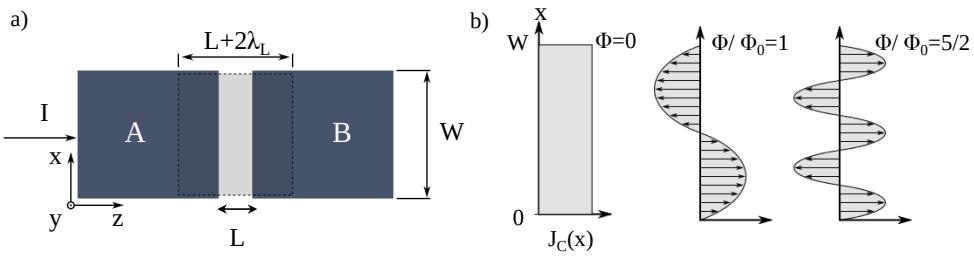

Figure 5.8: a) Schematic diagram of an extended Josephson junction. The distance between the two superconducting leads is L. The current flows along the z-direction and the magnetic field is applied along the y-axis. b) Current distribution for certain magnetic flux values Φ through a Josephson junction.

the two leads is obtained by considering the enclosed flux Φ which is approximately equal to the applied magnetic field strength B_y times the area A. The effective area is obtained by the length x and the London screening length λ_L of each superconductor times the width W. This gives a position dependent phase difference:

$$\phi(x) = \frac{2\pi}{\Phi_0} B_y (d + 2\lambda_L) x + \phi_0. \tag{5.2}$$

This expression can be inserted into the Josephson current phase relation CPR(ϕ) where the tunnel limit is used, i.e. $I(\phi) = I_c \mathrm{CPR}(\phi) = I_c \sin\phi$ and yields the total supercurrent density for a given magnetic field by integrating over the spatial dimensions of the junction one obtains:

$$I_c(B) = \int\int J_c(x,z)\,dx\,dz = \int_0^W J_c(x) \sin[\frac{2\pi}{\Phi_0} B_y(d+2\lambda_L)x + \phi_0]\,dx. \tag{5.3}$$

The last equation is valid for our 2 dimensional system. By assuming a homogeneous current distribution $J_c(x,z) = J_c$ as depicted in Fig. 5.8b), the critical current is given by $I_c = AJ_c$; with this the well known Fraunhofer diffraction pattern in analogy to the single slit diffraction pattern is obtained:

$$I_c(\Phi) = I_c(0) \frac{\sin\frac{\pi\Phi}{\Phi_0}}{\frac{\pi\Phi}{\Phi_0}}, \tag{5.4}$$

where $\Phi = B_y A = B_y W(2\lambda_L + L)$. This diffraction pattern is shown in Fig. 5.9b) (grey) and stems from the fact that in the presence of a magnetic field, the phase and therefore also the current distribution is position dependent as illustrated in Fig. 5.8b) for various flux ratios. At integer multiples of Φ_0 the distribution of forward and backward directed current yields a destructive interference and the total supercurrent is zero. The nth maximum occurs for $\Phi = (n+1/2)\Phi_0$.

It is worth noting that Eq. 5.3 represents a Fourier-transformation of the supercurrent distribution $I_c(x)$. This fact was used in previous studies on HgTe and InSb/GaAs quantum wells [22, 38], where the authors observed in the case a deviation of a homogeneous current distribution, a change from a Fraunhofer like diffraction pattern, to an edge dominated transport. This edge dominated transport can be interpreted as two Josephson junctions in parallel separated by an insulating bulk. Such a structure is reminiscent of a superconducting quantum interference device (SQUID) and the diffraction pattern satisfies the relation $I_c \propto \cos(\pi\Phi/\Phi_0)$ [c.f. Fig. 5.1e)]. This was taken as a proof of edge transport in the quantum spin Hall regime. Here, it is shown that the device is compatible with these previous observations in a similar gate regime. In Fig. 5.9, the differential resistance dV/dI is presented as a function of dc current I and magnetic field B for $V_g = 0$ V. The junction exhibits to a large extend a conventional Fraunhofer pattern of the critical current as a function of magnetic field, which rapidly decays as the magnetic field increases. In this regime, the electron density is high and the current flows uniformly in the 2D plane of the quantum well. A period of approximately 0.41 mT is obtained. Given the dimensions of the junction, it corresponds to an effective length of $L_{\mathrm{eff}} = L + 2\lambda = 1.3\,\mu$m and yields a penetration length of $\lambda = 430$ nm. This result is agrees with that of Hart *et al.* [22]. The plot in Fig. 5.9 shows a small asymmetry between the positive and negative field directions. This is very likely related to the experimental setup. The white line shows a fit based on the standard Fraunhofer diffraction pattern using Eq. 5.4. The central lobe and the first side lobes are fitted quite well by the standard Fraunhofer formula. For higher fields, the measured data deviates from the expected theory as the experimental periodicity gets larger and the diffraction pattern decays in general faster. Both effects have been predicted by Meier *et al.* [39] for long ballistic SNS junctions taking disordered

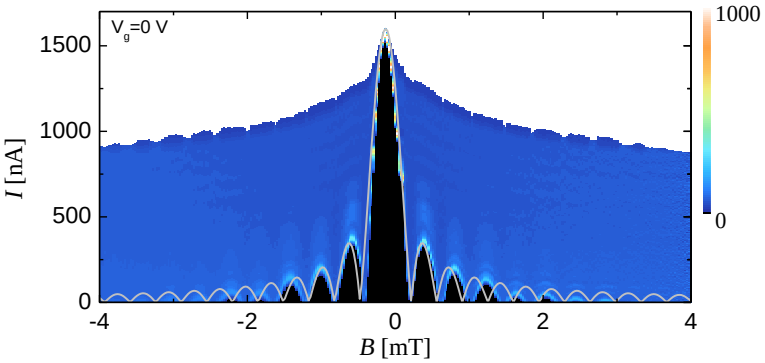

Figure 5.9: Differential resistance dV/dI as a function of dc current and magnetic field for $V_g = 0$ V at 30 mK. Black areas indicate the superconducting regime. The white curve shows a standard Fraunhofer fit with an effective area of $4 \times 1.3 = 5.2\,\mu m^2$.

edges into account which is close to the regime of our junctions. The authors predict at fields larger than $B \simeq \Phi_0/l^2$, the supercurrent decays faster and the periodicity becomes longer. The transition frequency was estimated to be approximately $B \simeq 1$ mT. This agrees well with the magnetic field scales. Another possibility which can explain the deviations in the measured diffraction pattern from the standard Fraunhofer pattern can be flux focusing. This effect is extensively discussed by Suominen *et al.* [12]. The authors account for magnetic field focusing at the edges of the sample caused by the screening of magnetic fields of the superconducting leads. For a certain geometry, this leads to a local enhancement of the magnetic field which can also increase the periodicity. However, because of a significant difference in the design of the Josephson junction in their work, a direct comparison of the results can not be done. In fact our geometry should be less affected by flux focusing effects as our leads extend a certain distance over the mesa. In order to be able to completely analyse the deviation from the standard Fraunhofer pattern a more systematic investigation of dimensions and length scales needs to be done in future work.

Fig. 5.10 shows the differential resistance as a function of magnetic field for various applied gate voltages. As the gate voltage is decreased, the critical current decreases and the diffraction pattern is similar to that of a dc SQUID for $V_g = -1.3$ and -1.6 V. The first signature for a SQUID like behaviour is the presence of a maximum rather than a minimum at multiples of $\Phi = n\Phi_0$, $n \in \mathbb{Z}$. This behaviour demonstrates that a sizeable part of the supercurrent flows along the edges of the sample [22] which is expected in the presence of QSH edge channels. Additionally, a narrowing of the central lobe is observed in both cases and the relative height of the central to the higher order lobes becomes smaller. In contrast to Hart *et al.* [40] a very strong odd/even modulations is observed: the first and third lobes are substantially smaller than the second and fourth. In particular, at $V_g = -1.35$ V, the first and third lobes are completely suppressed and yields an apparent doubling of the period (from Φ_0 to to $2\Phi_0$) at low fields, before a conventional period is recovered for larger fields. Finally, for more negative gate voltages $V_g = -2$ V, the pattern progressively returns to a Fraunhofer one, with some strong distortions, especially at high

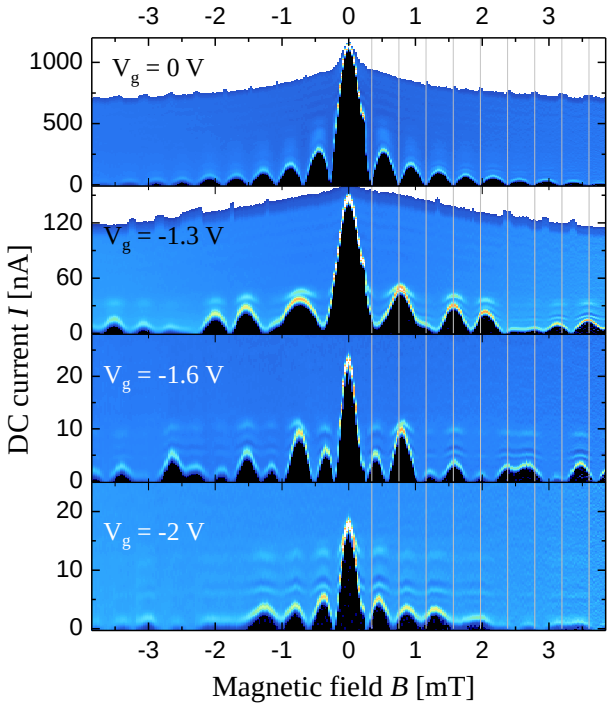

Figure 5.10: Maps of differential resistance dV/dI as a function of magnetic field B and dc current bias I for four different gate voltages. The black areas illustrate the superconducting regime while blue resembles the resistive regime. Vertical grey lines indicate minima of the Fraunhofer pattern, where Φ is a multiple of Φ_0, that correspond to maxima of the SQUID pattern.

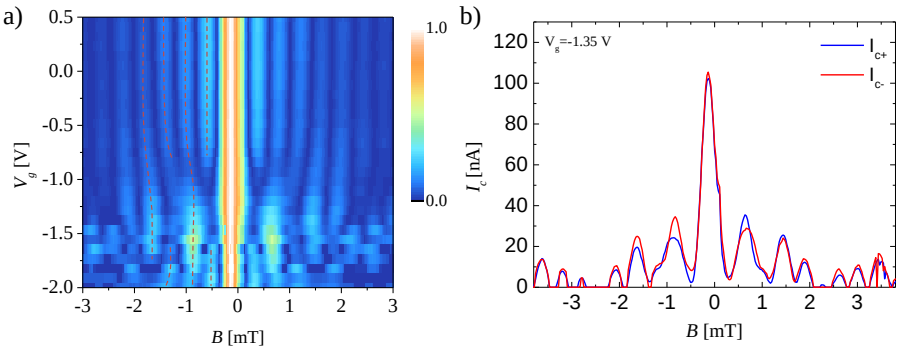

Figure 5.11: a) Normalized critical current as a function of magnetic field B and gate voltage V_g. b) Critical current I_c as a function of B for two sweep directions (positive as a blue line, negative as a red line), following the symmetry relation .

fields. This is likely to be due to the low mobility and small supercurrent in the p-regime. This suggests that the current flow returns to a 2D configuration, with inhomogeneities.

To investigate the development of the Φ_0 to $2\Phi_0$ transition, Fig. 5.11a) shows the normalized critical current as a map of gate voltage V_g and magnetic field B. For 0 to -0.8 V the pattern remains close to a Fraunhofer pattern, but the first and third lobes progressively disappear and are missing between -1 V and -1.5 V; This is emphasized by the dotted red lines. For -1.6 V, the first and third lobes reappear. When driving the gate from -1.6 V to -2 V, a standard Fraunhofer pattern is progressively recovered. This graph also shows the evolution from a maximum to a minimum when the gate voltage is lowered and central lobe is narrowed.

It is tempting, to associate our observations of the anomalous doubled of the lobes period to a SQUID-like pattern with periodicity $2\Phi_0$ that originates from the 4π periodicity. Dc measurements are sensitive to relaxation processes that, in principle, restore a conventional Φ_0 periodicity [25, 41, 42]. It is unlikely that our devices are free of quasiparticle poisoning during the time scale of the experiment and thus do not expect a 2ϕ periodic Fraunhofer pattern.

There exist several theoretical models [43, 44] which explain odd–even patterns and small deviations from a SQUID pattern [38] via skewed current-phase relations or additional coupling between edges. Both effects are predicted to be dependent on temperature, while the even odd pattern in our case does not vanish with increasing temperature as visible in Fig. 5.12. There, the differential resistance is shown as a function of perpendicular magnetic field at $V_g = -1.35$ V, where the even odd pattern is most pronounced. As the temperature is increased a gradual decrease in the amplitude of the critical current is observed but the strong asymmetry between the even and odd lobes persists. An alternative mechanism to explain the interference pattern is the interplay of the Zeeman effect and spin–orbit coupling, which should occur in our material system [45, 46]. The interference pattern in the even odd regime shows a peculiar symmetry relation of the critical current, $I_{c+}(B) = I_{c-}(-B)$, where $\pm$ indicate the sweep direction of the bias current and $+B$ and $-B$ the magnetic field direction [Fig. 5.11b)]. In contrast, it is asymmetric both

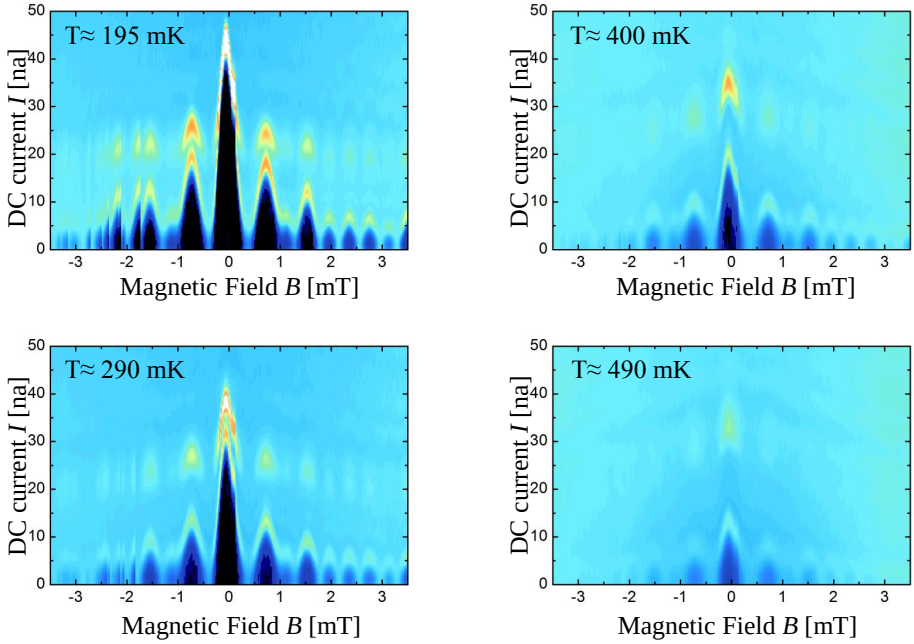

Figure 5.12: Differential resistance as a function of dc current and magnetic field at $V_g = 1.35\,\mathrm{V}$ for various temperatures. By increasing the temperature the critical current is reduced and therefore also the visibility of the diffraction pattern, but the even-odd pattern persists for all temperatures.

in the magnetic field and the sweep direction. Further investigation in a more suitable geometry or the direct measurement of the current phase relationship would be required to clarify the role of these mechanisms.

So far, sections 5.2.3 and 5.3 summarized and analysed the dc behaviour of the JJ. In section 5.4 the response to an external ac bias is discussed.

5.4. RESPONSE OF A TOPOLOGICAL JOSEPHSON JUNCTION TO RF IRRADIATION

The presence of gapless Andreev bound states can, in principle, be detected via the 4π-periodic contribution to the supercurrent. In practice, such detection in dc transport can be complicated by additional contributions from conventional 2π-periodic modes[47, 48] that carry a current $I_{2\pi}\sin\phi$ and by relaxation processes that can restore a 2π-periodic supercurrent [17, 26, 49]. To reveal the possible 4π-periodic characteristics, the dynamics of the junction is most conveniently probed by studying the ac Josephson effect. The I–V characteristic of the sample is measured using a dc current bias with the addition of an rf driving current, coupled to the device via a nearby antenna which leads to the formation of Shapiro steps as visible in Fig. 5.13. For high rf frequencies (6.6 GHz, blue), all steps are visible and a conventional sequence of Shapiro steps at $V = nhf/2e$, $n \in \mathbb{Z}$ is observed. As the frequency is lowered to $f = 1.0$ GHz, we observe the progressive vanishing of all the odd steps up to $n = 9$. This behaviour is highlighted by plotting the histogram as visible in Fig. 5.13b). There, peaks signal the presence of Shapiro steps. By lowering the rf frequency, it is possible to observe a gradual disappearance of the odds steps. Although a

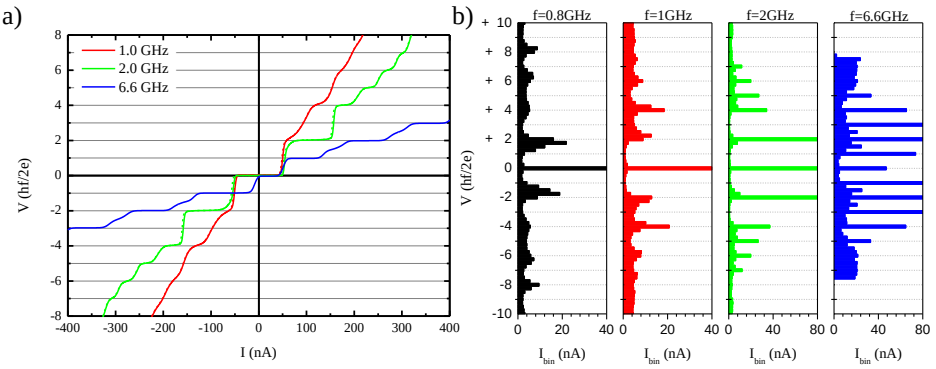

Figure 5.13: a) $I-V$ traces at $V_g = -1.1$ V for various rf frequencies. The power is always chosen such that it is below the first crossing b) Histograms obtained by binning the $I-V$ traces with a step size of $0.25hf/2e$. Peaks in the histogram signal the presence of Shapiro steps. By lower the frequency the odd steps start to disappear gradually.

pure 4π-periodic supercurrent should lead directly to an even sequence of Shapiro steps (as a direct consequence of the substitution $\phi \to \phi/2$ in the Josephson equations). In our experiment this is only visible at a low frequency. Our junction is expected to contain both gapless bound states and a number of residual conventional modes. Hence, the supercurrent I_s can be written as $I_c = I_{2\pi}\sin\phi + I_{4\pi}\sin\phi/2$. We have seen in the previous

chapter 4 that even in the presence of a strong 2π-periodic contribution, a 4π-periodic response can be observed when the time dependence of the voltage V to the current bias I is most anharmonic, namely at a low frequency, low dc bias or low power. Odd steps are then missing if the excitation rf frequency f is lower than $f_{4\pi} = 2eR_N I_{4\pi}/h$. This allows the amplitude of the 4π-periodic supercurrent $I_{4\pi}$ to be estimated. As a crossover frequency the fully suppressed $n = 3$ step is chosen which occurs for $V_g = -1.1\,\mathrm{V}$ at around $f_{4\pi} = 2\,\mathrm{GHz}$. With the normal state resistance of approximately $300\,\Omega$ the critical current yields $I_{4\pi} \simeq 10\,\mathrm{nA}$. This current is expected to be carried by two gapless Andreev bound states, one on each edge. This value is comparable with the maximum current a single channel is able to carry i.e. $I_{\mathrm{single}} = \frac{e}{\hbar}\Delta_{\mathrm{Ind}} \simeq 4\,\mathrm{nA}$. These numbers need to be taken with care as the normal state resistance R_n is largely dominated by bulk transport in the plane, and not by edge states. Nevertheless, this estimate makes two edges modes a plausible explanation for the 4π-periodic contribution. Apart from gapless Andreev states, gapped Andreev bound states with a high transparency could also result in a 4π-periodic contribution in the supercurrent in the presence of Landau–Zener transitions at the avoided crossing $\phi = \pi$, and 3π as extensively discussed in chapter 4. However, Landau–Zener transitions have increasing probabilities with increasing dc voltage or frequency. Given our observations of missing steps just at low frequencies, this possibility appears unlikely.

Recently, a 8π-periodic Josephson effect rather than a 4π-periodic contribution was proposed taking Coulomb interaction or magnetic impurities and coupling of Andreev bound states to the continuum in a QSH system into account [50, 51]. In this experimental work, we observe no sign of such an effect in the response of our devices.

POWER AND FREQUENCY DEPENDENCE UNDER RF RADIATION

For completeness we now address the dependence of the Shapiro steps on the rf power. This was already discussed in detail in chapter 3 for the case of a 3D TI junction and is only mentioned briefly here as the behaviour is similar. The left column of Fig. 5.14 shows the differential voltage dV/dI as a function of applied current and rf power P_{rf} for three different frequencies at $V_g = -1.1\,\mathrm{V}$. The right column shows the corresponding voltage histograms normalized to the expected step size $hf/2e$. For low power levels but a high frequency (6 GHz), Shapiro steps appear consecutively from low to high indices n and all steps are visible. Even fractional steps $n = 1/2$ and $n = 3/2$ which might stem from non sinusoidal current-phase relationship or capacitive effects are visible. For lower frequencies, odd steps progressively disappear (starting from low step indices). Although maxima are seen in Fig. 5.14a) at 1 GHz for $n = 0, 2, 4$, the first and third Shapiro steps are fully suppressed. As visible here, hysteresis is occasionally found to induce a weak asymmetry at low power values, which affects the $n = \pm 1$ step at low frequency and low power. For high power values, an oscillatory pattern (reminiscent of Bessel functions) in the voltage bias case [18] is observed. However, the pattern is modified (when compared with that seen for a higher-frequency excitation) [52], which develop from the suppression of the first and third maxima of the oscillations. We interpret these features as signalling the progressive transformation from a 2π- to a 4π-periodic pattern with halved-period oscillations that correspond to a halved number of steps.

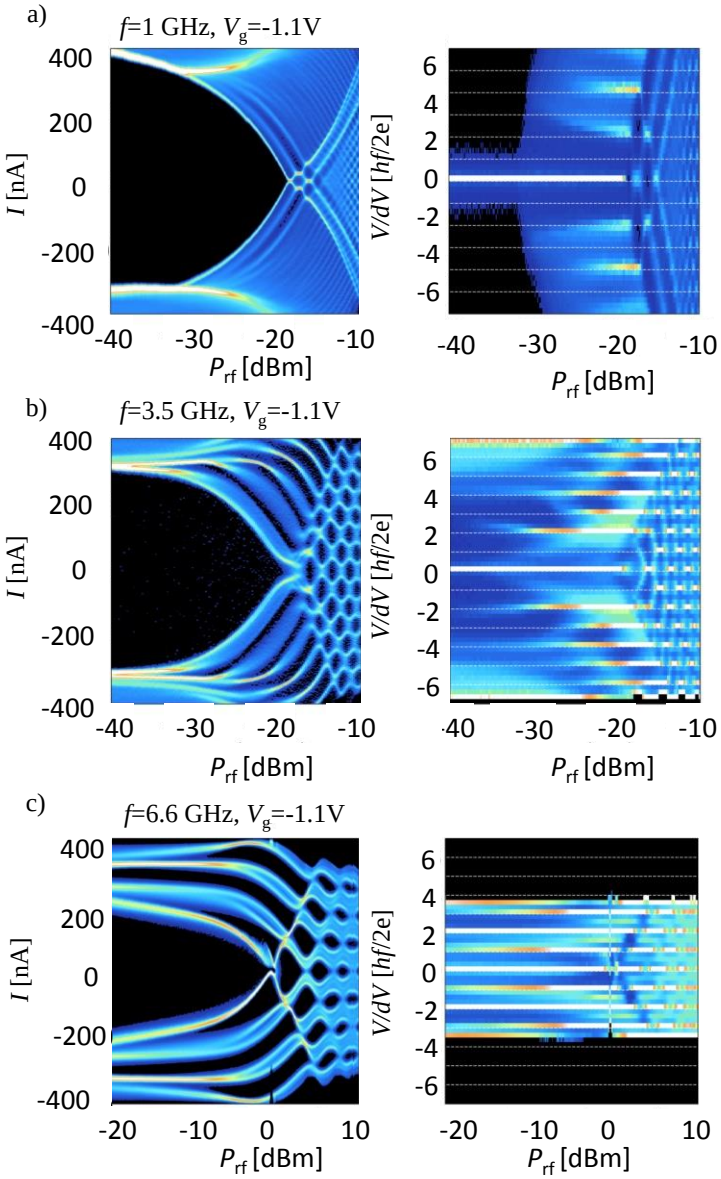

Figure 5.14: Left column: 2D map of the differential resistance dV/dI as a function of applied rf power P_{rf} for three different frequencies and at gate voltage $V_g = -1.1$ V. Right column: normalized histogram as a function of voltage drop V across the junction and applied P_{rf} for the same gate voltage and frequencies as in the left column.

GATE DEPENDENCE OF THE SHAPIRO RESPONSE UNDER RF IRRADIATION

Next, we investigate the dependence of the Shapiro response on gate voltage V_g. A general observation is that odd steps vanish at low frequencies for a very wide range of gate voltages, from $V_g \geq -1.3$ up to +0.5 V. The visibility of an even sequence is in agreement with the previously introduced criterion $f < f_{4\pi}$, and demonstrates that a 4π-periodic contribution is present in addition to a conventional 2π-periodic component. The latter originates most probably from bulk modes, signalling the expected coexistence of topological edge states with modes from the conduction band [53]. This would mean that the edge states do not hybridise strongly with the bulk bands similar to the Dirac screening of the surface states in 3D TI insulators developed in Ref. [54]. The reason To show that the 4π-periodic modes are unveiled progressively as the number of bulk modes is decreased for negative voltages, we calculate the ratios $Q_{i,i+1}$ of the maximum amplitude of two consecutive steps as a function of gate voltage for a certain frequency. The obtained graphs for two frequencies are displayed in Fig. 5.15. Simulations using the resistively shunted junction (RSJ) model predict ratios $Q_{i,i+1}$, which are close to unity for a conventional junction; the results are indicated by the shaded grey area. Ratios that approach zero indicate the suppression and disappearance of the lower Shapiro steps. For low frequencies i.e. 1 GHz, the odd steps ratios Q_{12}, Q_{34} and Q_{56} start to be suppressed around $V_g = -1.3$ V while the ratio of two even steps Q_{24} is only suppressed around that value but close to the expected grey area for values below and above. This fact is connected to the visibility of some steps at very low frequencies. It is important to note, that for such low frequencies, all odd steps are suppressed up to high gate voltages where we are expecting a large contribution of bulk modes or even a hybridisation of bulk and edge modes. For values $V_g < -1.3$ V, the ratios are close to the expected conventional behaviour and do not show a suppression of odd steps. In order to show that the missing of odd steps occurs stronger around the expected gap area the rf-frequency was increased such that the criterion $f < f_{4\pi}$ is not easily met for even small contributions of the 4π supercurrent. The ratios for 3.5 GHz are shown in Fig. 5.15b). Both ratios Q_{12} and Q_{34} indicate that the visibility of the even sequence of steps is improved between $V_g = -1.3$ and -0.9 V but even for higher frequencies, a suppressed first step remains up to positive gate voltages. Thus, the ac response of our junctions strongly signals the presence of a strong 4π-periodic contribution from the supercurrent that appears more clearly in this range close to the QSH transition. This behaviour is in line with the previous measurements on a 3D TI JJ described in chapter 2, where we were are able to observe the missing of only the first Shapiro step. In the case of the 2DTI JJ, the results are more clear as we observe even higher order missing of odd steps. The number of conventional bulk modes is lower as in the 3D TI and, therefore, the transition frequency $f_{4\pi}$. This makes it harder to resolve more than one missing odd step as the step size and also the visibility are reduced by lowering the frequency.

5.5. SHAPIRO STEPS OF A NON-TOPOLOGICAL WEAK LINK

To assess the topological origin of the 4π-periodic supercurrent, we now examine a narrower HgTe quantum well. The thickness is below d_c and does not exhibit an inverted band structure and therefore also no QSH effect [14]. For this purpose a Josephson junction was fabricated using the substrate QC0260, with a 5.5 nm thick quantum well

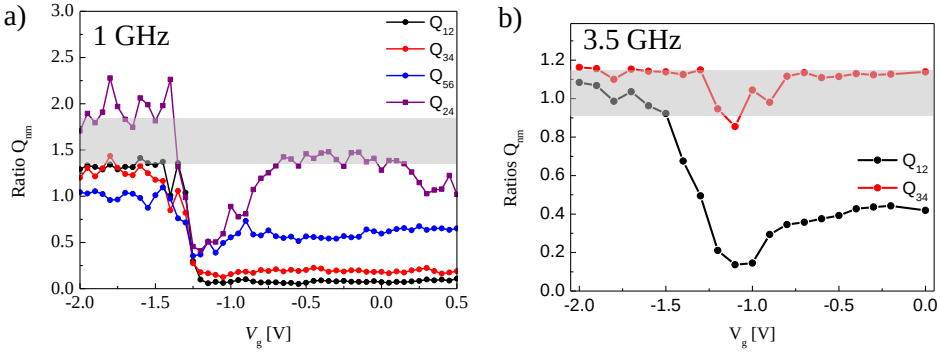

Figure 5.15: Ratios Q_{ij} as a function of gate voltage for 1 GHz with i, j being integer in a) and 3.5 GHz in b). The grey shaded area is the expected ratio in the absence of a 4π-contribution calculated with RSJ simulations.

and a 51 nm thick capping layer. Usually thinner quantum wells suffer from a lower mobility than thicker ones as the former are more strongly affected by local thickness variations or roughness. This was compensated in the present material by growing a thicker capping layer which increases the mobility. The sample was fabricated the very same way as the inverted device with only the etching time of the superconducting contacts being adjusted. The material properties, i.e. mobility of $\mu = 150 \times 10^3 \text{cm}^2/\text{Vs}$ at a density of $n = 5 \times 10^{11} \text{cm}^2$ (for $V_g = 0\,\text{V}$) were obtained from a reference Hall-bar and yield a mean free path, which is comparable to that of the inverted device. As all material characteristics apart from the inversion of the bands by changing the quantum well thickness are similar compared to the inverted device it allows the connection between the topological properties and the presence of a 4π-periodic supercurrent to be tested.

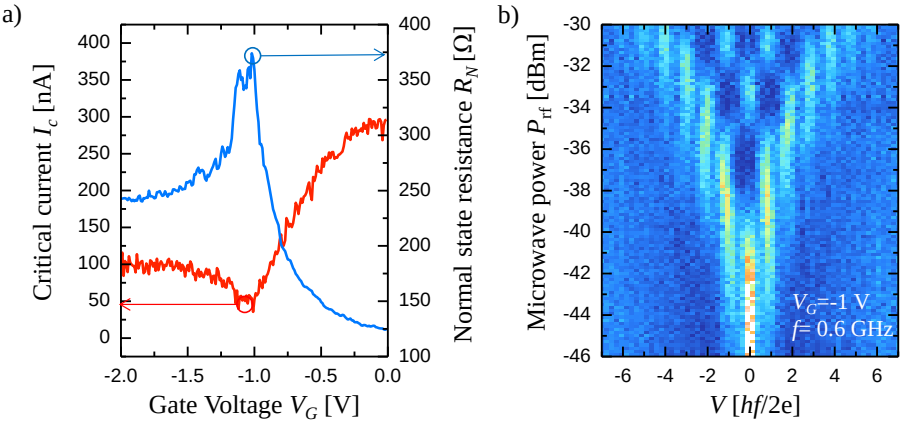

Figure 5.16: a) Critical current I_c and normal state resistance R_n of a non-topological Josephson junction as a function of gate voltage V_g. b) 2D map of the voltage distribution as a function of the dc voltage (in normalized units) and the rf excitation power P_{rf}, taken at $V_g \approx -1V$ and frequency $f = 0.6\,\text{GHz}$.

The measurement of the critical current I_c enables the identification of the n- and

p-conduction regimes, although the gap, around $V_g \approx -1\,\mathrm{V}$, is not very pronounced (Fig. 5.16a). When measuring the Shapiro response to an rf excitation, we do not observe any missing odd step for any of the gate voltages, neither in the n- nor p-regimes, nor close to the gap. As an example, we show in Fig. 5.16b) a measurement taken close to the gap at $V_g = -1\,\mathrm{V}$ and at a very low frequency $f = 0.6\,\mathrm{GHz}$. This is the regime where the 4π-behaviour is expected to be strongest. For such a frequency close to our detection limit, all the steps are still visible.

To conclude, an inverted band structure and therefore the presence of topological edge states is a necessary ingredient for the observation of the 4π-periodic supercurrent.

5.6. BREAKING TIME REVERSAL SYMMETRY WITHOUT A MAGNETIC FIELD

At this point it is worth to recall the Andreev bound state spectrum of a helical edge channel in absence of a magnetic field as depicted in Fig. 5.17 in blue. As long as time reversal symmetry is preserved, Kramers degeneracy enforces a degeneracy at the time reversal invariant momenta $\phi = 2n\pi$, $n \in \mathbb{Z}$. This degeneracy implies that at e.g. $\phi = 0$ the ABS touches the continuum states and any infinitesimal disturbance in the system (noise fluctuations) can relax the electron in the continuum states, which restores a conventional 2π-periodicity as the state can relax every 2π. This problem was already realized by Fu and Kane [3]. Therefore, they introduced a finite Zeeman field to lift this degeneracy as indicated by the red curve in Fig. 5.17. In our experiment, we do not explicitly break TRS by applying a magnetic field and do not expect a decoupling from the continuum states. Therefore, we have to answer the question why we are observing the 4π-periodic component at all. Here, we discuss three potential decoupling mechanisms from the continuum states without a magnetic field, namely (i) backscattering of the edge channels due to impurities, (ii) dc bias and (iii) non-equilibrium reservoirs.

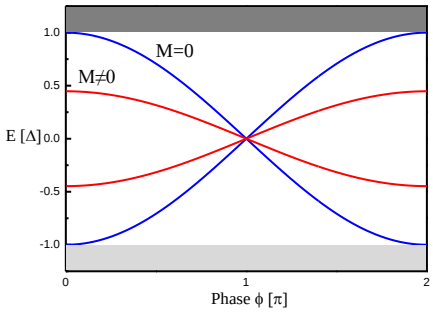

Figure 5.17: Schematic of topological Andreev bound state for zero mass M (blue) and in presence of a finite mass (red).

5.6.1. BACKSCATTERING OF HELICAL EDGE CHANNELS

The first assumption in the Fu and Kane model is the perfect transmission of the edge channels due to TRS. Thus, breaking TRS also lifts the protection of the edge channels. Experimentally, it is known that the edge channels seem to have non perfect transmission if the edge length is too long. So far, the exact process is not yet known. It was shown for example by Peng *et al.* [51] that a localized magnetic impurity allows scattering of the QSH edge channels and this leads to a 8π-periodicity of the topological ABS. As far as we know we do not have magnetic impurities in our system but several other proposals explain mechanism which lead to backscattering of edge states such as the Rashba spin-orbit coupling [55, 56] or scattering in neighbouring electron reservoirs [57, 58]. Another very recent proposal takes the roughness of the edges into account which may spontaneously break time reversal symmetry [59]. If one of the theories applies in our case, it would justify a local breaking of TRS even without an applied magnetic field.

Additionally, the conductance in the present device inside the gap is much higher than the expected quantized value of $2e^2/h$, therefore interaction with bulk channels is likely to be present as well. The backscattering of edge channels and the interaction with the bulk modes is experimentally not properly investigated yet and also the interplay of disorder interaction effects and superconductivity has not been treated theoretically yet. In summary, it is very likely that a backscattering mechanism might destroy the perfect conduction of the edge channels which might act as a source of time-reversal symmetry breaking.

5.6.2. BREAKING OF TRS BY CURRENT BIAS

Romito *et al.* [60] used the fact that a supercurrent creates a phase gradient through the device which can be effectively treated as a Zeeman field in the case of QSH edge channels. Furthermore, the Edelstein effect, i.e. an equilibrium spin polarization by driving a current, can lift the degeneracy. Tkachov found huge g-factors of the order of 1000 for the superconducting helical edge channels [61]. This effect, similar to Romito *et al.*, can be interpreted as an effective Zeeman field which decouples the gapless Andreev bound states from the continuum. The strenght of the Edelstein-field can be estimated by

$$H_E = \frac{v_F \hbar k}{2}, \tag{5.5}$$

where v_F is the Fermi velocity and k the momentum. The momentum is directly connected to the phase gradient $k = \nabla\phi$. The phase gradient is then directly proportional to the applied bias. The drift velocity v_D of the edge channels can be roughly estimated by calculating the current density in the quantum well $I = Wj$; with the current density $j = nev_D$, where n is the electron density of the system and e the elementary charge. This can be related to the momentum by $\hbar k = mv_D$. By using the following values for the mass of the electron bands $m^* = 0.02m_e$, a width of $W = 4\,\mu\text{m}$, a current of $I = 100\,\text{nA}$ and a density of $n \approx 5 \times 10^{11}\,\text{cm}^{-2}$, the momentum yields $k \approx 3 \cdot 10^3\,\text{m}^{-1}$. Then, using the Fermi velocity of the electron bands $v_F \approx 5 \cdot 10^5\,\text{m/s}$ [62], we obtain an Edelstein energy $H_E \approx 3\,\mu\text{eV}$. This is a reasonable number and it should not affect the induced energy gap ($\Delta_i \approx 100\,\mu\text{eV}$) much.The energy scale for rf radiation around 1 GHz is $\approx 4\,\mu\text{eV}$ and thus may be enough to decouple the states of the continuum.

5.6.3. NON EQUILIBRIUM POUPLATION

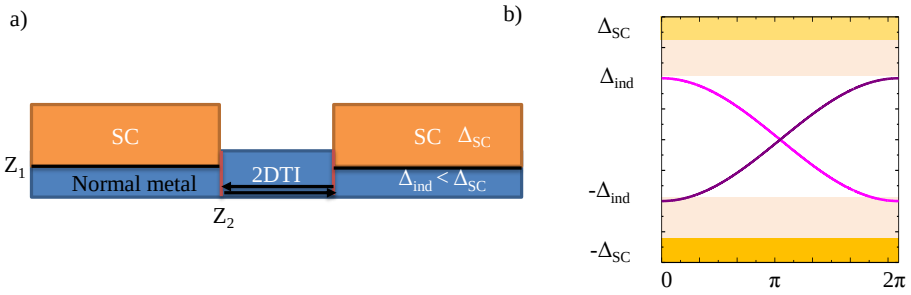

Figure 5.18: a) Sketch of a topological Josephson junction. A superconductor is deposited on top of the quantum spin Hall insulator and induces a finite pairing amplitude Δ_{ind} into the topological insulator. b) Andreev bound state spectrum of a topological Josephson junction between two proximitized metals.

In most theoretical proposals for inducing superconductivity into topological insulators, the question how the superconductivity is induced, is often neglected. In our experiment we induce pair correlations by proximitizing the quantum well with Al, a *bona fide* superconductor as sketched in Fig. 5.18a). Therefore, we first need to etch some of the material and then deposit the Al. Both processes most likely reduce the quality of the underlying material or even destroy its topological properties. The proximity effect turns the material superconducting but the superconducting gap in the quantum well (Δ_{ind}) is likely to be smaller than the superconducting gap of the main superconductor. This kind of effect is extensively discussed in chapter 7. Andreev bound states form subsequently between the two proximitzied normal metals as indicated in Fig. 5.18. As the quantum well is only a few nanometres thick, it is likely that it does not form a proper continuum and thus the electrons are separated from the continuum of the superconductor.

5.7. CONCLUSION

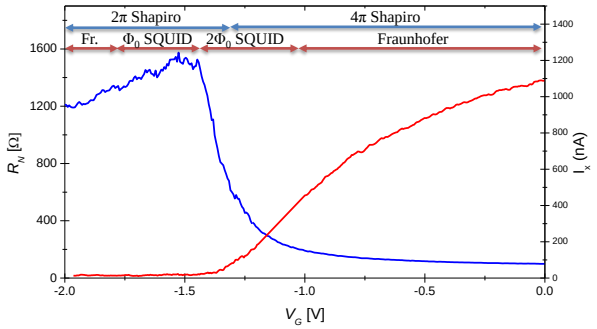

Figure 5.19: Overview over the observed phenomena in the topological Josephson junction as a function of gate voltage: The normal state resistance R_N (blue) and critical current I_c (red) as a function of gate voltage V_g. The red and blue arrows summarize the ranges for observed diffraction patterns and Shapiro responses.

The response to rf irradiation strongly suggests the presence of a 4π-periodic supercurrent in the device with a contribution compatible with two modes. It is most visible when the bulk bands are depleted as indicated by the Fraunhofer interference pattern and the normal state resistance. In this region, the current flow is mostly along the edges of the sample (as indicated by the SQUID features, with possible indications of spin–orbit and Zeeman effects). Although the QSH regime is not clearly identified by its quantized conductance, it appears that the 4π-periodic contribution is also detected in the whole n-conduction band, but is rapidly suppressed when driving the gate voltage towards the p-conduction regime. This suggests that the 4π-periodic edge modes coexist in parallel with bulk modes of the conduction band; this is consistent with previous predictions [53] and observations in our material system [22, 63]. In contrast, a Josephson junction made of a topologically trivial quantum well exhibits a conventional Shapiro response. Together, this set of observations strongly points to the existence of the topological gapless Andreev bound states as predicted by Fu and Kane [3] in Josephson junctions produced on the well-characterized QSH insulator HgTe. Although further developments are required to comprehend fully the richness of the observed phenomena, Josephson junctions in HgTe quantum wells and at zero magnetic field appear promising for the future realization of Majorana end states and possibly scalable Majorana qubits.

BIBLIOGRAPHY

[1] A. Y. Kitaev, *Unpaired majorana fermions in quantum wires,* Physics-Uspekhi **44**, 131 (2001).

[2] C. Nayak, S. H. Simon, A. Stern, M. Freedman, and S. Das Sarma, *Non-Abelian anyons and topological quantum computation,* Reviews of Modern Physics **80**, 1083 (2008).

[3] L. Fu and C. Kane, *Josephson current and noise at a superconductor/quantum-spin-Hall-insulator/superconductor junction,* Physical Review B **79**, 161408 (2009).

[4] J. Alicea, *New directions in the pursuit of Majorana fermions in solid state systems,* Reports on Progress in Physics **75**, 076501 (2012).

[5] C. W. J. Beenakker, *Search for Majorana fermions in superconductors,* Annual Review of Condensed Matter Physics **4**, 15 (2013).

[6] Y. Oreg, G. Refael, and F. von Oppen, *Helical Liquids and Majorana Bound States in Quantum Wires,* Physical Review Letters. **105**, 177002 (2010).

[7] R. M. Lutchyn, J. D. Sau, and S. Das Sarma, *Majorana Fermions and a Topological Phase Transition in Semiconductor-Superconductor Heterostructures,* Physical Review Letters. **105**, 077001 (2010).

[8] V. Mourik, K. Zuo, S. M. Frolov, S. R. Plissard, E. P. a. M. Bakkers, and L. P. Kouwenhoven, *Signatures of Majorana Fermions in Hybrid Superconductor-Semiconductor Nanowire Devices,* Science **336**, 1003 (2012).

[9] L. P. Rokhinson, X. Liu, and J. K. Furdyna, *The fractional a.c. Josephson effect in a semiconductor–superconductor nanowire as a signature of Majorana particles,* Nature Physics **8**, 795 (2012).

[10] S. Heedt, N. Traverso Ziani, F. Crepin, W. Prost, S. Trellenkamp, J. Schubert, D. Grützmacher, B. Trauzettel, and T. Schäpers, *Signatures of interaction-induced helical gaps in nanowire quantum point contacts,* Nature Physics **13**, 563 (2017).

[11] C.-X. Liu, J. D. Sau, T. D. Stanescu, and S. D. Sarma, *Andreev bound states versus Majorana bound states in quantum dot-nanowire-superconductor hybrid structures: Trivial versus topological zero-bias conductance peaks,* arXiv preprint arXiv:1705.02035 (2017).

[12] H. J. Suominen, J. Danon, M. Kjaergaard, K. Flensberg, J. Shabani, C. J. Palmström, F. Nichele, and C. M. Marcus, *Anomalous fraunhofer interference in epitaxial superconductor-semiconductor josephson junctions,* Physical Review B **95**, 035307 (2017).

[13] B. A. Bernevig, T. L. Hughes, and S.-C. Zhang, *Quantum Spin Hall Effect and Topological Phase Transition in HgTe Quantum Wells,* Science **314**, 1757 (2006).

[14] M. König, S. Wiedmann, C. Brüne, A. Roth, H. Buhmann, L. W. Molenkamp, X.-L. Qi, and S.-C. Zhang, *Quantum Spin Hall Insulator State in HgTe Quantum Wells,* Science **318**, 766 (2007).

[15] N. Samkharadze, A. Bruno, P. Scarlino, G. Zheng, D. P. Divincenzo, L. Dicarlo, and L. M. K. Vandersypen, *High-Kinetic-Inductance Superconducting Nanowire Resonators for Circuit QED in a Magnetic Field,* Physical Review Applied **5**, 1 (2016).

[16] C. W. J. Beenakker, D. I. Pikulin, T. Hyart, H. Schomerus, and J. P. Dahlhaus, *Fermion-parity anomaly of the critical supercurrent in the quantum spin-Hall effect,* Physical Review Letters **110**, 1 (2013).

[17] H.-J. Kwon, K. Sengupta, and V. M. Yakovenko, *Fractional ac Josephson effect in unconventional superconductors,* Low Temperature Physics **30**, 613 (2004).

[18] P. Russer, *Influence of Microwave Radiation on Current-Superconducting proximity effect and majorana fermions at the surface of a topological insulatorVoltage Characteristic of Superconducting Weak Links,* Journal of Applied Physics **43**, 2008 (1972).

[19] J. Wiedenmann, E. Bocquillon, R. S. Deacon, S. Hartinger, O. Herrmann, T. M. Klapwijk, L. Maier, C. Ames, C. Brüne, C. Gould, A. Oiwa, K. Ishibashi, S. Tarucha, H. Buhmann, and L. W. Molenkamp, *4π-periodic Josephson supercurrent in HgTe-based topological Josephson junctions,* Nature Communications **7**, 10303 (2016).

[20] F. Domínguez, F. Hassler, and G. Platero, *Dynamical detection of Majorana fermions in current-biased nanowires,* Physical Review B **86**, 140503 (2012).

[21] A. Barone and G. Paterno, *Physics and applications of the Josephson effect*, Vol. 1 (Wiley Online Library, 1982).

[22] S. Hart, H. Ren, T. Wagner, P. Leubner, M. Mühlbauer, C. Brüne, H. Buhmann, L. W. Molenkamp, and A. Yacoby, *Induced superconductivity in the quantum spin Hall edge,* Nature Physics **10**, 638 (2014).

[23] S. Shapiro, *Josephson Currents in Superconducting Tunneling: The Effect of Microwaves and Other Observations,* Physical Review Letters **11**, 80 (1963).

[24] P. San-Jose, E. Prada, and R. Aguado, *AC Josephson effect in finite-length nanowire junctions with Majorana modes,* Physical Review Letters **108** (2012).

[25] M. Houzet, J. S. Meyer, D. M. Badiane, and L. I. Glazman, *Dynamics of Majorana States in a Topological Josephson Junction,* Physical Review Letters **111**, 046401 (2013).

[26] D. M. Badiane, M. Houzet, and J. S. Meyer, *Nonequilibrium Josephson Effect through Helical Edge States,* Physical Review Letters **107**, 177002 (2011).

[27] L. Fu and C. L. Kane, *Superconducting Proximity Effect and Majorana Fermions at the Surface of a Topological Insulator,* Physical Review Letters **100**, 096407 (2008).

[28] A. Pfeuffer-Jeschke, *Bandstruktur und Landau-Niveaus quecksilberhaltiger II-VI-Heterostrukturen*, Ph.D. thesis, Universität Würzburg (2000).

[29] B. Zhou, H.-Z. Lu, R.-L. Chu, S.-Q. Shen, and Q. Niu, *Finite size effects on helical edge states in a quantum spin-Hall system.* Physical Review Letters **101**, 246807 (2008).

[30] C. Brüne, A. Roth, E. G. Novik, M. König, H. Buhmann, E. M. Hankiewicz, W. Hanke, J. Sinova, and L. W. Molenkamp, *Evidence for the ballistic intrinsic spin Hall effect in HgTe nanostructures,* Nature Physics **6**, 448 (2010).

[31] J. Strunz, *Optimierung von BaF2 Masken zur Defintion von Mikrokanalstrukturen für die Untersuchung hydrodynamischer Effekte in HgTe\ HgCdTe Heterostrukturen*, Master's thesis, Julius-Maximilians-Universität Würzburg (2016).

[32] G. E. Blonder, M. Tinkham, and T. M. Klapwijk, *Transition from metallic to tunneling regimes in superconducting microconstrictions: Excess current, charge imbalance, and supercurrent conversion,* Physical Review B **25**, 4515 (1982).

[33] K. Flensberg, J. B. Hansen, and M. Octavio, *Subharmonic energy-gap structure in superconducting weak links,* Physical Review B **38**, 8707 (1988).

[34] P. Capper, *Properties of Narrow-Gap Cadmium-Based Compounds* (IET, 1994).

[35] H. B. Heersche, P. Jarillo-Herrero, J. B. Oostinga, L. M. Vandersypen, and A. F. Morpurgo, *Bipolar supercurrent in graphene,* Nature **446**, 56 (2007).

[36] M. Veldhorst, M. Snelder, M. Hoek, T. Gang, V. K. Guduru, X. L. Wang, U. Zeitler, W. G. van der Wiel, a. a. Golubov, H. Hilgenkamp, and a. Brinkman, *Josephson supercurrent through a topological insulator surface state.* Nature materials **11**, 417 (2012).

[37] M. Tinkham, *Introduction to superconductivity* (Courier Corporation, 1996).

[38] V. S. Pribiag, B. J. A., F. Qu, M. C. Cassidy, C. Charpentier, W. Wegscheider, and L. P. Kouwenhoven, *Edge-mode superconductivity in a two-dimensional topological insulator,* Nature Nanotechnology **10**, 593 (2015).

[39] H. Meier, V. I. Fal'ko, and L. I. Glazman, *Edge effects in the magnetic interference pattern of a ballistic SNS junction,* Physical Review B **93**, 184506 (2016).

[40] S. Hart, H. Ren, T. Wagner, P. Leubner, M. Mühlbauer, C. Brüne, H. Buhmann, L. W. Molenkamp, and A. Yacoby, *Induced Superconductivity in the Quantum Spin Hall Edge,* arXiv:1312.2559 [cond-mat] (2013).

[41] L. Fu and C. Kane, *Superconducting Proximity Effect and Majorana Fermions at the Surface of a Topological Insulator,* Physical Review Letters **100**, 096407 (2008).

[42] J. H. Lee, G. H. Lee, J. Park, J. Lee, S. G. Nam, Y. S. Shin, J. S. Kim, and H. J. Lee, *Local and nonlocal fraunhofer-like pattern from an edge-stepped topological surface josephson current distribution,* Nano Letters **14**, 5029 (2014).

[43] B. Baxevanis, V. P. Ostroukh, and C. W. J. Beenakker, *Even-odd flux quanta effect in the Fraunhofer oscillations of an edge-channel Josephson junction,* Physical Review B **91** (2015).

[44] G. Tkachov, P. Burset, B. Trauzettel, and E. M. Hankiewicz, *Quantum interference of edge supercurrents in a two-dimensional topological insulator,* Physical Review B **92**, 045408 (2015).

[45] F. Dolcini, M. Houzet, and J. S. Meyer, *Topological Josephson ϕ_0 junctions,* Physical Review B **92**, 1 (2015).

[46] A. Rasmussen, J. Danon, H. Suominen, F. Nichele, M. Kjaergaard, and K. Flensberg, *Effects of spin-orbit coupling and spatial symmetries on the Josephson current in SNS junctions,* Physical Review B **93** (2016).

[47] A. D. K. Finck, C. Kurter, Y. S. Hor, and D. J. Van Harlingen, *Phase coherence and andreev reflection in topological insulator devices,* Physical Review X **4**, 1 (2014).

[48] L. Galletti, S. Charpentier, M. Iavarone, P. Lucignano, D. Massarotti, R. Arpaia, Y. Suzuki, K. Kadowaki, T. Bauch, a. Tagliacozzo, F. Tafuri, and F. Lombardi, *Influence of topological edge states on the properties of Al/Bi_2Se_3/Al hybrid Josephson devices,* Physical Review B **89**, 134512 (2014).

[49] D. I. Pikulin and Y. V. Nazarov, *Phenomenology and dynamics of a Majorana Josephson junction,* Physical Review B **86**, 140504 (2012).

[50] F. Zhang and C. L. Kane, *Time-reversal-invariant Z_4 fractional josephson effect,* Physical Review Letters. **113**, 036401 (2014).

[51] Y. Peng, Y. Vinkler-Aviv, P. W. Brouwer, L. I. Glazman, and F. von Oppen, *Parity anomaly and spin transmutation in quantum spin hall josephson junctions,* Physical Review Letters. **117**, 267001 (2016).

[52] J. Wiedenmann, E. Bocquillon, R. S. Deacon, S. Hartinger, O. Herrmann, T. M. Klapwijk, L. Maier, C. Ames, C. Brüne, C. Gould, A. Oiwa, K. Ishibashi, S. Tarucha, H. Buhmann, and L. W. Molenkamp, *4π-periodic Josephson supercurrent in HgTe-based topological Josephson junctions,* Nature Communications **7**, 10303 (2016).

[53] X. Dai, T. L. Hughes, X.-L. Qi, Z. Fang, and S.-C. Zhang, *Helical edge and surface states in HgTe quantum wells and bulk insulators,* Physical Review B **77**, 125319 (2008).

[54] C. Brüne, C. Thienel, M. Stuiber, J. Böttcher, H. Buhmann, E. G. Novik, C.-X. Liu, E. M. Hankiewicz, and L. W. Molenkamp, *Dirac-Screening Stabilized Surface-State Transport in a Topological Insulator,* Physical Review X **4**, 41045 (2014).

[55] F. Geissler, F. m. c. Crépin, and B. Trauzettel, *Random Rashba spin-orbit coupling at the quantum spin Hall edge,* Physical Review B **89**, 235136 (2014).

[56] T. L. Schmidt, S. Rachel, F. von Oppen, and L. I. Glazman, *Inelastic Electron Backscattering in a Generic Helical Edge Channel,* Physical Review Letters. **108**, 156402 (2012).

[57] J. I. Väyrynen, M. Goldstein, and L. I. Glazman, *Helical Edge Resistance Introduced by Charge Puddles,* Physical Review Letters. **110**, 216402 (2013).

[58] S. Essert, V. Krueckl, and K. Richter, *Two-dimensional topological insulator edge state backscattering by dephasing,* Physical Review B **92**, 205306 (2015).

[59] J. Wang, Y. Meir, and Y. Gefen, *Spontaneous Breakdown of Topological Protection in Two Dimensions,* Physical Review Letters. **118**, 046801 (2017).

[60] A. Romito, J. Alicea, G. Refael, and F. von Oppen, *Manipulating Majorana fermions using supercurrents,* Physical Review B **85**, 020502 (2012).

[61] G. Tkachov, *Giant spin splitting and 0- π Josephson transitions from the Edelstein effect in quantum spin Hall insulators,* Physical Review B **95**, 245407 (2017).

[62] A. M. Shuvaev, G. V. Astakhov, G. Tkachov, C. Brüne, H. Buhmann, L. W. Molenkamp, and A. Pimenov, *Terahertz quantum Hall effect of Dirac fermions in a topological insulator,* Physical Review B **87**, 121104 (2013).

[63] K. C. Nowack, E. M. Spanton, M. Baenninger, M. König, J. R. Kirtley, B. Kalisky, C. Ames, P. Leubner, C. Brüne, H. Buhmann, L. W. Molenkamp, D. Goldhaber-Gordon, and K. A. Moler, *Imaging currents in HgTe quantum wells in the quantum spin Hall regime,* Nature Materials **12**, 787 (2013).

6

JOSEPHSON EMISSION FROM HGTE-BASED TOPOLOGICAL JUNCTIONS

This chapter is based on the publication: JOSEPHSON RADIATION FROM GAPLESS ANDREEV BOUND STATES IN HGTE-BASED TOPOLOGICAL JUNCTIONS.
R.S. Deacon, J. Wiedenmann, E. Bocquillon, F. Dommínguez, T. M. Klapwijk, P. Leubner, C. Brüne, E.M. Hankiewicz, S. Tarucha, K. Ishibashi, H. Buhmann, and L.W. Molenkamp, *Physical Review Letters X 7, 021011* (2017).

In this chapter the Josephson radiation emitted from a weak link based on an inverted HgTe quantum well, a material which hosts helical edge channels is probed. This technique is especially powerful, as it allows the frequency of the Josephson junction to be probed directly. Therefore, a new measurement setup needed to be developed which enables the measurement of the high frequency emission. With this setup, it has been possible to measure the emitted spectrum and find emission at half the conventional Josephson frequency $f_J/2$, a clear signature of a 4π-periodic supercurrent. This 4π-periodic supercurrent is predicted in a topological Josephson junction. The results are in agreement with the previous chapters 3 to 5, i.e. a coexistence of a 2π- and a 4π-periodic supercurrent. The 2π-periodicity is dominating at high frequencies while the 4π-periodicity is controlling the response of the weak link at low frequencies. A reference device based on a non-inverted HgTe quantum well shows only trivial emission at f_J over the whole accessible parameter range. The coherence time of the Andreev bound states has been estimated from the line width of the emission spectra. For the unconventional emission at $f_J/2$ a coherence time of $0.3-4$ ns is found, generally shorter than the f_J emission ($3-4$ ns).

6.1. INTRODUCTION TO EMISSION SPECTRUM OF A TOPOLOGICAL JOSEPHSON JUNCTION

A fixed voltage bias V_{dc} applied to a conventional Josephson junction with a $\sin\phi$ periodic current phase relation is converted to an ac current with frequency $f_J = 2eV_{dc}/h$. This process can be understood as the energy change of a Cooper pair tunnelling across the junction as depicted in Fig. 6.1 a) and is called the ac Josephson effect. This effect has been experimentally confirmed [1–3] for tunnel junctions with a pure sinusoidal current phase relation. If the barrier between the two superconducting leads is for example a clean metal, the normal state transmission t can take values between 0 and 1, where 0 refers to 0 transmission and 1 to 100% transmission respectively. For high transmitting modes, as shown in Fig. 6.1b) (red), the Josephson current also contains higher harmonics, which may also lead to emission at higher frequencies (nf_J with $n \in \mathbb{N}$). A topological Josephson junction in contrast is predicted to host a pair of gapless ABS [blue curves in Fig. 6.1b)]. The doubled periodicity of this ABS leads to emission of half the Josephson frequency $f_J/2$. This effect is of the same origin, i.e. Majorana bound states, as the missing odd Shapiro steps discussed in the previous chapters but has the advantage that no ac bias needs to be applied to the junction which leads to complex dynamics of the Josephson junction. The analysis of the rf emission of a voltage biased topological Josephson junction is therefore a powerful, passive and direct way of probing the properties of such a junction. The problem is that the radiated power of a single junction is rather low and difficult to measure[4]. Therefore a new measurement setup was developed.

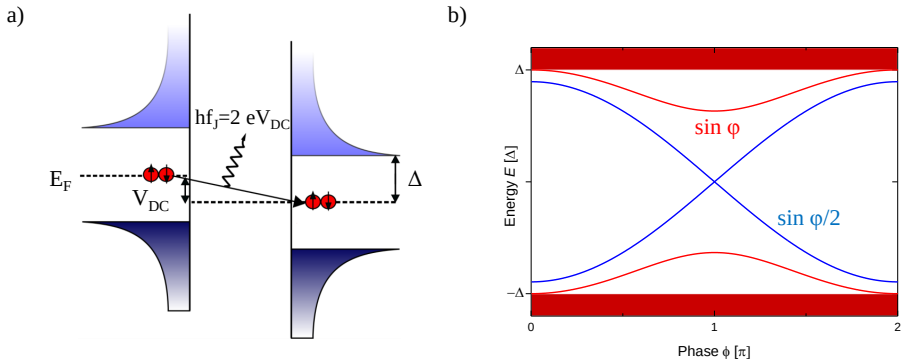

Figure 6.1: a) Schematic of the Josephson radiation process. A Cooper-pair (red dots) from the left lead tunnels through a barrier. The energy difference of the applied bias V is absorbed by the environment by emitting a photon with frequency f_J. b) Spectrum of a topologically protected (blue) and conventional (red) Andreev bound state.

In this chapter the study of the Josephson emission from a weak link based on a HgTe quantum well with an inverted as well as a non inverted quantum well is reported in a range from 2 – 10 GHz using cryogenic microwave measurements. On the one hand, the JJ based on the inverted quantum well (quantum well thickness $d \simeq 8\,\text{nm} > d_c =$ 6.3nm), which hosts helical edge channels, shows clear emission, both at the conventional frequency f_J, as well as at $f_J/2$. On the other hand the conventional JJ, based on a HgTe

quantum well with $d = 5\,\text{nm} < d_c$ shows only conventional emission at f_J and $2f_J$. The emission measurements therefore provide a direct signature of the presence of a 4π-periodic supercurrent as expected from gapless Andreev bound states as predicted by Fu and Kane [5–8].

6.2. MEASUREMENT SETUP

In order to measure directly the emission spectrum of the Josephson junction, described in chapter 5, several changes to the experimental setup were made. The detailed measurement setup is presented in Fig. 6.2. The dc part (twisted pairs) are shown in red and blue (blue is the gate line) while the rf components are shown in black. The substrate is mounted on a printed circuit board (PCB) with a coplanar transmission line which collects the radiation emitted from the Josephson junction. The PCB is coupled to the rf measurement via an SMA launcher. A bias-T decouples the dc and rf measurement parts. The signal lines are thermally anchored at each state. A cryogenic high electron mobility transistor (HEMT) (low noise factory LNC4_8C) and two room temperature amplifiers are used to amplify the small emission signal from the single Josephson junction. Finally the signal is measured with a spectrum analyser. The commercial rf components limit the experimentally accessible bandwidth to $2-10\,\text{GHz}$. A directional coupler allows an external rf drive to be applied to perform Shapiro measurements. The dc lines are equipped with self made copper-powder and low pass rc-filters.

An essential element in this experiment is the ability to apply a stable and low bias to the Josephson junction. In this regard, a thin film resistor R_S with a low resistance ($\approx 25\,\Omega$) is used parallel to the junction. Residual switching below a few microvolts still sometimes occurred. Another thin film resistor in series to the junction $R_I \approx 25\,\Omega$ allows the measurement of the current I which flows through the junction[1]. Both resistors are placed in close proximity to avoid stray inductance. An equivalent curcuit of this on-chip circuit is shown on the right side of Fig. 6.2. A typical measurement is done as follows: At a fixed detection frequency f_d, a triangular waveform generator is used to sweep the $I-V$ characteristics. The junction bias and current are amplified at room temperature and measured with a digitizer which is synchronized with the spectrum analyser to the sweeps of the junction current. Both the spectral data and the $I-V$ are averaged over several hundred repetitions to reduce the noise level. A background at zero bias applied to the junction is subtracted from the measurements as it is attributed to stray noise from the environment. It is estimated that the lowest features able to resolve are around 0.1 fW in an 8 MHz bandwidth.

6.3. MEASUREMENT OF THE EMISSION SPECTRUM OF THE TOPOLOGICAL WEAK LINK

A measurement as described in the previous section is shown in Fig. 6.3a). At a fixed biased a finite voltage V develops and a contribution in the spectra of the junction appears. The detection frequency is now fixed at $f_d \simeq 3\,\text{GHz}$ and an applied gate voltage

[1] Parameters for the trivial weak link are $R_S = R_I = 36\,\Omega$. The difference compared to the topological device is due to resistance variations of the thin film resistors at low temperatures.

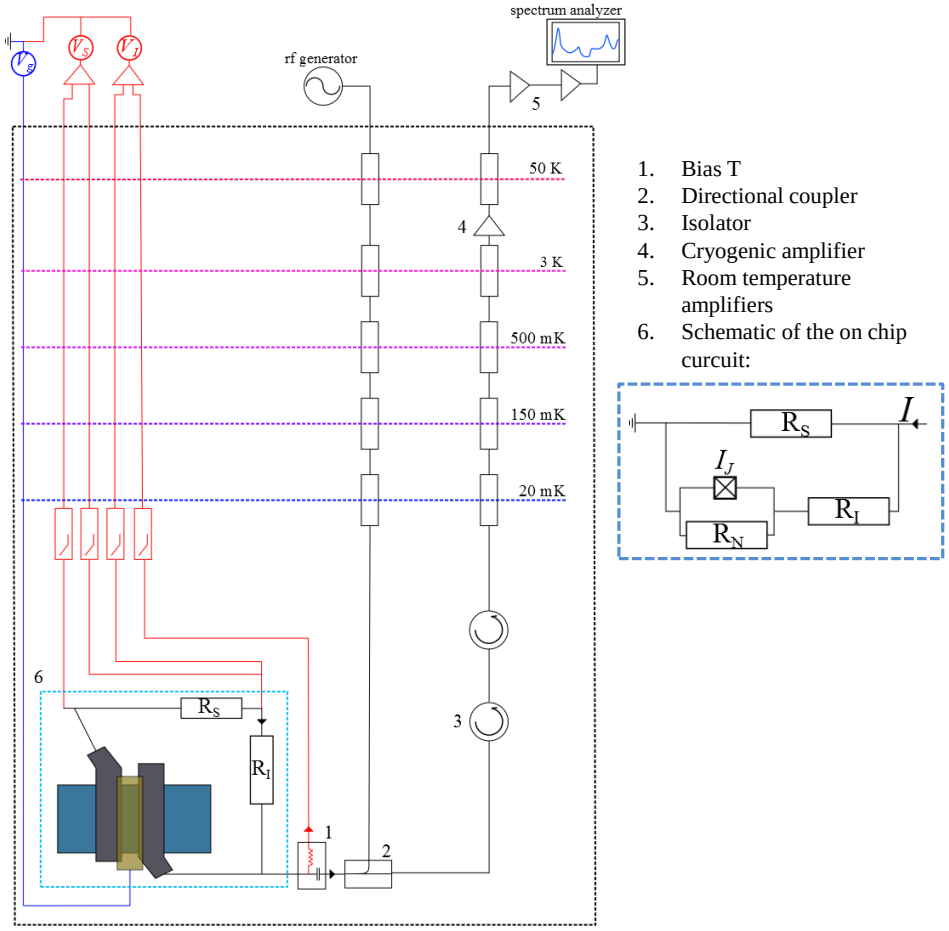

Figure 6.2: Measurement setup: The sample and the thin film resistors R_S and R_I are fitted on a PCB with a coplanar transmission line (blue box) and mounted near the mixing chamber with a base temperature of 20 mK. The dc lines (red and blue) and the rf lines (black) are separated at the bias-T 1. 2 indicates the directional coupler. The rf signal is amplified by a cryogenic HEMT at 3 K and two room temperature amplifiers. It is measured using a spectrum analyser. An equivalent circuit of the shunted Josephson junction is shown on the right side. The dc lines are equipped with copper power and low-pass rc filters. The voltage V_I and also the overall voltage drop is measured.

$V_g = -0.55$ V. At a certain dc voltage, a peak in the emission spectrum (blue) is observed. The corresponding $I-V$-curve is shown in Fig. 6.3a) and b) in red. As visible, a stable bias is obtained down to a few microvolts. The dc voltage can then be identified with the expected values of f_J [grey vertical lines in the Fig. 6.3 a) and b)]. As visible, a strong emission peak at a voltage which corresponds to half the expected Josephson frequency $f_d = f_J/2 = 2eV/h$. This observation is shown for two different gate voltages, i.e. electron densities and is a signature of a 4π-periodic supercurrent. The gate value for Fig. 6.3a) is chosen to be close to the gap (QSHE-regime) and only shows $f_J/2$ emission, while the measurement closer to the valence band, Fig. 6.3b), shows both lines at f_J and $f_J/2$. When

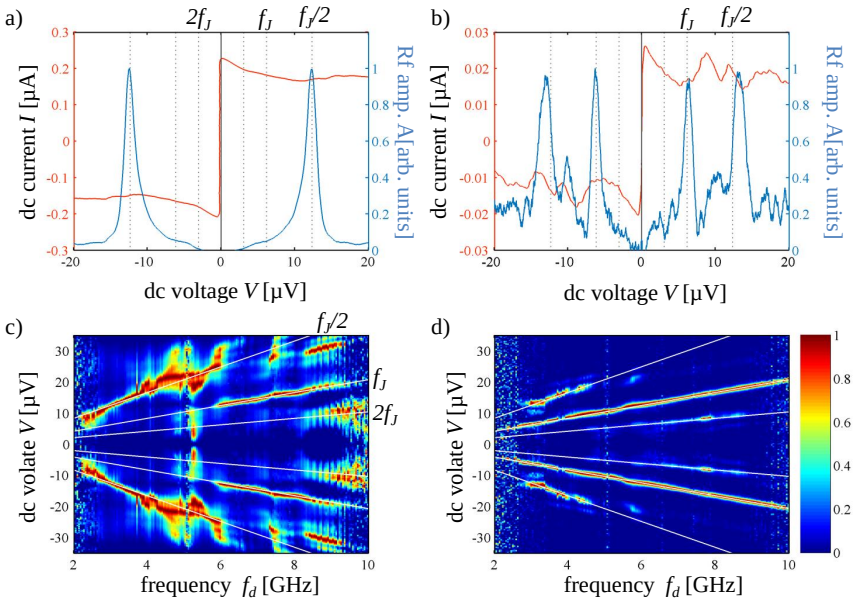

Figure 6.3: Emission spectrum of a quantum spin Hall weak link. a) and b) show $I-V$ curves (red) and the emission spectrum (blue) detected at a fixed detection frequency ($f_d \simeq 3$ GHz) when sweeping the dc bias for $V_g = -0.55$ V and $V_g = -1.4$ V respectively. c) and d) Two dimensional plots of the power collected as a function of voltage and detection frequency for the same gate voltages as in a) and b) respectively.

the detection frequency is swept, one can verify that the emission lines follow the linear relation $f_J = (2eV/h)$. Therefore, the measurements are done for different detection frequencies f_d of the spectrum analyser as shown in Fig. 6.3c) and d). For each value of f_d, the reference at $I = 0$ is subtracted, and the data are normalized to its maximum emission value to correct for frequency-dependent coupling and amplification. In the topological device and for $V_g = -0.55$ V Fig. 6.3c), the color map shows that the emission is entirely dominated by the 4π-periodic supercurrent below $f_d \simeq 5.5$ GHz, before the conventional line is recovered. At higher frequencies, the emission spectrum is influenced by resonant modes within the electromagnetic environment. Such resonances are extremely common in broadband rf measurements, and can be easily identified by a characterization of the electromagnetic environment of the junction. In principle, the resonant modes can lead to two-photon processes (at frequency such that $2hf = eV_{\mathrm{dc}}$, i.e., $f = f_J/2$) that

could mimic the fractional Josephson effect [23,24]. However, one can safely exclude this mechanism. Indeed, two-photon effects are of second order in R_n/R_K, with $R_K = (h/e^2)$, and should always be much less visible than the standard emission at f_J. As such, they cannot solely explain the observation of the radiation at $f_J/2$, and are expected to be weak since the normal state resistance is much lower in our devices ($R_n/R_K \ll 1$). It is still possible that resonances in the electromagnetic environment can enhance the associated emission features. When $V_g \simeq -1.4\,\mathrm{V}$ [Fig. 6.3d)], the colour map reveals that the 4π-periodic component at $f_J/2$ is visible only up to $f_d \simeq 4.5\,\mathrm{GHz}$, while the conventional emission line at f_J is seen in the whole range of frequencies. We now analyse the data

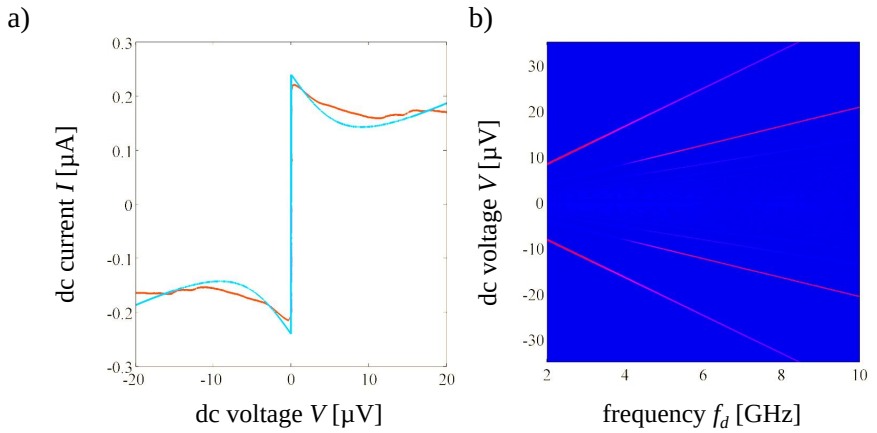

Figure 6.4: Resistively shunted junction simulations. a) Simulated $I-V$ curve (blue) compared with measured data at $V_g = -0.55\,\mathrm{V}$. The simulations are performed for $R_I = R_S = 24\,\Omega$, $R_n = 130\,\Omega$, $I_{4\pi} = 100\,\mathrm{nA}$, and $I_c = 240\,\mathrm{nA}$. b) Simulated Fourier transform of the voltage V in the junction, as a function of detection frequency f_d and voltage V, for the same simulation parameters as in a). A good qualitative agreement is found with Fig. 6.3c). In particular, the predominance of the emission at $f_J/2$ for low voltages (below $12\,\mu\mathrm{V}$) is well reproduced.

plotted in Fig. 6.3d). The strong dominance of 4π-periodic radiation observed in Fig. 6.3d) at low frequencies or voltages may at first sight be surprising, as conventional 2π-periodic modes are also expected to contribute. In fact the observation is in full agreement with the observation of missing odd Shapiro steps at low frequencies and voltages reported in the previous chapters 3 and 5. It can also be explained using the same arguments as presented in chapter 2.11 on the modelling of the two supercurrent RSJ model. To model the experimental data, we perform numerical simulations, in the framework of a resistively shunted junction model, modified to account for the shunt circuit and the 4π-periodic component of the supercurrent. It is then possible to show (c.f. supplementary information of Ref. [9]) that the equation describing the current through the JJ is identical to the standard RSJ equation, but a renormalization of the normal state resistance R_N and critical current I_c has to be taken into account. Thus all arguments considering the interplay of 2π and 4π-periodic supercurrents discussed in chapter 4 are also applicable in the shunted device. To compute the emission spectrum, we successively compute the time-dependent voltage $V(t)$ and its Fourier transform to obtain the amplitudes of each frequency component. The nonlinear response to the two time scales associated with

the combination of 2π and 4π-periodic contributions allows the 4π-periodic terms to be more visible for low voltages and the 2π-periodic dominating the high voltage regime [10]. Computations for increasing voltages V and detection frequency f_d yield a good qualitative agreement with the $I-V$ characteristic as shown in Fig. 6.4a). The $I-V$ curve fitting of the experimental data is determine by the values of I_c and the resistance R_n. The additional resistors R_I and R_S are set to 25 Ω. Best agreement is achieved using $I_c \simeq (240 \pm 10)$ nA and $R_n \simeq (130 \pm 15)\,\Omega$. So far the distribution of the total critical current in 2π- and 4π-periodic contributions has not played any role in the modelling. In a next step, the supercurrent is assumed to consist of two components $I_c = I_{4\pi} + I_{2\pi}$. The emission features are then used to determine a crossover frequency from a 4π-periodic to a 2π-periodic dominating behaviour in order to estimate the amount of 4π-periodic supercurrent. Therefore, a voltage $V_{4\pi} \simeq 12\,\mu$V is taken from Fig. 6.3c) which corresponds to $I_{4\pi} \simeq 0.4 I_c$ approximately 40% of the total critical current. The simulation is shown in Fig. 6.4b). The value for the $I_{4\pi}$ contribution is larger than expected and bigger than the values estimated from the Shapiro measurements in chapter 5. It is worth noting that the absolute value of the $I_{4\pi}$ has to be taken cautiously and strongly depends on the choice of model and parameters.

MEASUREMENT OF THE EMISSION SPECTRUM OF THE TRIVIAL WEAK LINK

The emission spectrum of a weak link based on a non-inverted HgTe quantum well is measured, as a reference to exclude artefacts stemming from the setup or other trivial physical origins for a 4π-emission. The measurements are shown in Fig. 6.5a) and b). As visible over the whole detection frequency range only conventional emission is observed. The emission follows very nicely the expected linear behaviour $f_J = 2eV/h$ over the whole frequency range from 2 – 10 GHz. It is interesting, yet not really understood, that the device shows much less additional features from the environment. This is actually also true for the topological weak link, where the emission line at f_J is much less disturbed and narrower.

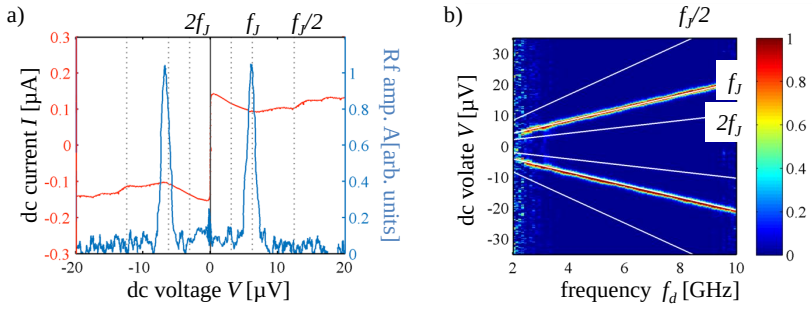

Figure 6.5: Emission spectrum of a non inverted HgTe quantum well weak link. a) shows the $I-V$ curves (red) and the emission spectrum (blue) detected at a fixed detection frequency ($f_d \simeq 3$ GHz) when sweeping the dc bias for $V_g = -0.55$ V and $V_g = -1.4$ V respectively. b) Two dimensional plot of the power collected as a function of voltage and detection frequency.

6.4. GATE DEPENDENCE

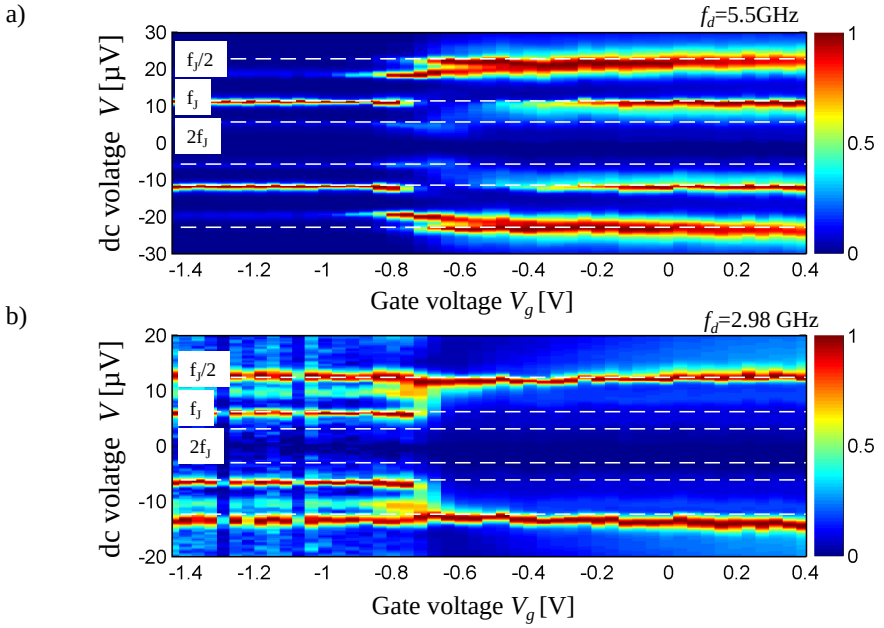

Figure 6.6: Gate dependence of the normalized emitted amplitude A as a function of bias voltage V_{dc} and gate voltage V_g for two detection frequencies. The dashed lines correspond to the indicated frequencies $f_J/2$, f_J and $2f_J$.

We now present data of the dependence of the emitted power as a function of the gate voltage. We observe that the amplitude of the collected signal reflects the amplitude of the critical current, and verify that the amplitude $A \propto I_c$ with good agreement [9, 11]. This confirms the conventional behaviour of the device in the conduction and valence bands of the quantum well, as well as close to the gap. In Figs. 6.6a) and b), we present two sets of measurements of the collected rf amplitude A on the topological weak link, taken at a low ($f_d = 2.98$ GHZ) and high ($f_d = 5.5$ GHz) frequencies. We observe three clear regimes in the emitted power that correlate with the expected band structure. When the gate voltage is above $V_g > -0.4$ V, we observe that emission occurs at f_J and $f_J/2$ for the high frequencies and only $f_J/2$ emission for the low frequency. In this regime we expect the Fermi energy of the device to be in the conduction band, where both edge and bulk modes are present. This observation is again in agreement with the missing odd Shapiro steps in the n-conduction regimes as predicted in Refs. [12, 13]. When the gate voltage is reduced ($V_g < -0.4$ V), we start to deplete the bulk contribution and we observe also in the high frequency regime only $f_J/2$ emission indicating an increase in the 4π-contribution. This voltage range corresponds to the quantum spin Hall regime where edge states are the dominant transport channel. This observation is thus in line with the topological origin of this anomalous spectral line. For $V_g < -0.8$ V, we observe in the low frequency regime both radiation forms f_J and $f_J/2$, which suggests the coexistence of weak gapless

Andreev modes with bulk p-type conventional modes of the valence band. The overall gate voltage dependence is consistent with the expected band structure of a quantum spin Hall insulator. For the high frequency data, we actually observe only conventional emission f_J in this regime.

Beyond the direct detection of a $f_J/2$ emission, the measurements give a new insight into the ABS spectrum of a topological Josephson junction. First, we discuss the unlikelihood of non-adiabatic Landau-Zener transition to be the origin of the observed 4π-periodicity. These transitions turn high transparency conventional modes at sufficient high driving voltage V_{dc} effectively 4π-periodic [7,25,29]. Such effects have been observed for instance in single Cooper pair transistors [14]. The presence of Landau-Zener transitions can, in principle, be evidenced by a strong voltage dependence of the emission features. Assuming Landau-Zener transitions are responsible one expects a crossover from a 2π to a 4π-periodic emission for increasing bias voltage [8, 15]. We detect emission at $f_J/2$ down to 1.5 GHz. If Laundau-Zener transitions are responsible for the 4π-periodic supercurrent it would correspond to a transmission $t \gg 0.995$, which is unlikely as such high transmissions have to our knowledge never been observed in semiconductor superconductor hybrids. In summary, the fact that we observe a transition from 2π- to a 4π-periodic emission with decreasing bias and the high transmission thus tend to exclude Landau-Zener transitions as the origin for the 4π-periodic emission. Furthermore, as the Landau-Zener transition is a stochastic process the transition from a 2π- to a 4π-periodic emission is expected to be gradual as in Ref. [14]. However, we observe only emission at the expected f_J and/or $f_J/2$ but no continuous transition.

Furthermore, the linewidth of the emission lines can give an estimate of the lifetime of the states. In both the trivial and topological weak link, the f_J emission line exhibits a typical width of $\delta V_{2\pi} \simeq 0.5 - 0.8\,\mu\mathrm{V}$ which corresponds to a coherence time of $\tau_{2\pi} = h/(2e\delta V_{2\pi}) \simeq 3 - 4\,\mathrm{ns}$. This timescale is consistent with the visibility of Shapiro steps down to 0.5 GHz [12]. In a conventional JJ the linewidth of the radiation is usually related to fluctuations in the pair or quasiparticle currents [16, 17] or can be dominated by the environment noise [11].

The linewidth of the $f_J/2$ radiation on the other hand can additionally reflect parity poising or ionization into the continuum. The experimental data actually suggest such an additional relaxation mechanism as the coherence time $\tau_{4\pi} \simeq 0.3 - 4\,\mathrm{ns}$ is shorter than $\tau_{2\pi}$. As visible in the graphs of Fig. 6.6 and Fig. 6.3, the linewidth of the $f_J/2$ line varies with gate voltage and emission frequency. On the one hand the linewidth increases when driving the device deeper into the conduction band. This can indicate stronger coupling with additional bulk modes. On the other hand the linewidth tends to increase with increasing frequency. This may be due to similar reasons of coupling the modes stronger or also additional ionization processes might influence the behaviour. So far it is not possible to influence the separate effects and disentangle their influence on the linewidth.

6.5. CONCLUSION

To conclude, we are able to measure the emitted radiation from a topological weak link based on HgTe quantum wells. We find strong emission at half the Josephson frequency $f_J/2$. These results are in full agreement with the previous chapters 3 to 5, where we measured missing odd Shapiro steps in the same parameter regime. Our results tend

to confirm the presence of gapless Andreev bound states in our topological devices and indicate that effects like Landau-Zener transitions can be excluded.

BIBLIOGRAPHY

[1] I. Yanson, V. Svistunov, and I. Dmitrenko, *Experimental Observation of the Tunnel Effect for Cooper Pairs with the Emission of Photons,* Soviet Physics JETP **21**, 650 (1965).

[2] N. F. Pedersen, O. H. Soerensen, J. Mygind, P. E. Lindelof, M. T. Levinsen, and T. D. Clark, *Direct detection of the Josephson radiation emitted from superconducting thin-film microbridges,* Applied Physics Letters **28**, 562 (1976).

[3] R. J. Schoelkopf, J. Zmuidzinas, T. G. Phillips, H. G. LeDuc, and J. A. Stern, *Measurements of noise in josephson-effect mixers,* IEEE Transactions on Microwave Theory and Techniques **43**, 977 (1995).

[4] K. K. Likharev, *Superconducting weak links,* Reviews of Modern Physics **51**, 101 (1979).

[5] L. Fu and C. L. Kane, *Josephson current and noise at a superconductor/quantum-spin-Hall-insulator/superconductor junction,* Physical Review B **79**, 161408 (2009).

[6] H.-J. Kwon, K. Sengupta, and V. M. Yakovenko, *Fractional ac Josephson effect in unconventional superconductors,* Low Temperature Physics **30**, 613 (2004).

[7] D. M. Badiane, M. Houzet, and J. S. Meyer, *Nonequilibrium Josephson Effect through Helical Edge States,* Physical Review Letters **107**, 177002 (2011).

[8] D. I. Pikulin and Y. V. Nazarov, *Phenomenology and dynamics of a Majorana Josephson junction,* Physical Review B **86**, 140504 (2012).

[9] R. S. Deacon, J. Wiedenmann, E. Bocquillon, F. Domínguez, T. M. Klapwijk, P. Leubner, C. Brüne, E. M. Hankiewicz, S. Tarucha, K. Ishibashi, *et al.*, *Josephson radiation from gapless andreev bound states in hgte-based topological junctions,* Physical Review X **7**, 021011 (2017).

[10] F. Domínguez, O. Kashuba, E. Bocquillon, J. Wiedenmann, R. Deacon, T. Klapwijk, G. Platero, L. Molenkamp, B. Trauzettel, and E. Hankiewicz, *Josephson junction dynamics in the presence of 2π-and 4π-periodic supercurrents,* Physical Review B **95**, 195430 (2017).

[11] K. K. Likharev, *Dynamics of Josephson junctions and circuits* (Gordon and Breach science publishers, 1986).

[12] E. Bocquillon, R. S. Deacon, J. Wiedenmann, P. Leubner, T. M. Klapwijk, C. Brüne, K. Ishibashi, H. Buhmann, and L. W. Molenkamp, *Gapless Andreev bound states in the quantum spin Hall insulator HgTe,* Nature Nanotechnology **12**, 137 (2017).

[13] X. Dai, T. L. Hughes, X.-L. Qi, Z. Fang, and S.-C. Zhang, *Helical edge and surface states in HgTe quantum wells and bulk insulators,* Physical Review B **77**, 125319 (2008).

[14] P. M. Billangeon, F. Pierre, H. Bouchiat, and R. Deblock, *Ac Josephson effect and resonant cooper pair tunneling emission of a single cooper pair transistor,* Physical Review Letters **98**, 1 (2007).

[15] J. D. Sau, E. Berg, and B. I. Halperin, *On the possibility of the fractional ac Josephson effect in non-topological conventional superconductor-normal-superconductor junctions,* arXiv preprint arXiv:1206.4596 (2012).

[16] M. J. Stephen, *Theory of a Josephson Oscillator,* Physical Review Letters **21**, 1629 (1968).

[17] A. J. Dahm, A. Denenstein, D. N. Langenberg, W. H. Parker, D. Rogovin, and D. J. Scalapino, *Linewidth of the radiation emitted by a Josephson junction,* Physical Review Letters **22**, 1416 (1969).

7

POINT-CONTACT ANDREEV REFLECTION SPECTROSCOPY ON A THREE DIMENSIONAL TOPOLOGICAL INSULATOR

This chapter is based on the publication: TRANSPORT SPECTROSCOPY OF INDUCED SUPERCONDUCTIVITY IN THE THREE-DIMENSIONAL TOPOLOGICAL INSULATOR HGTE.
J. Wiedenmann, E. Liebhaber, J. Kübert, E. Bocquillon, P. Burset C. Ames, H. Buhmann, T.M. Klapwijk, and L.W. Molenkamp,
Physical Review Letters B ***96****, 165302* (2017).

This part of the thesis presents the results of the study on the proximity induced superconductivity in a three dimensional topological insulator using point-contact Andreev reflection spectroscopy. In this regard, the concept of point-contact spectroscopy using one superconducting and one normal conducting electrode is introduced. Then, the design and fabrication of the HgTe based point-contact is presented. By analysing the conductance as a function of voltage for various temperatures, magnetic field values and gate voltages, we find two energy scales. We model the conductance using the theory as introduced by Blonder, Tinkham and Klapwijk. One energy scale is identified as the induced order parameter of the surface states of 70 μ*eV. It is possible to fit the induced state using a standard quadratic dispersion. We also use a more appropriate model which takes the helical surface states of the topological insulator into account. The second order parameter of* 1.1 *meV is attributed to the superconducting gap of niobium. We explain the transport by a non-equilibrium transformation of the relevant scattering regions when the applied bias is varied.*

7.1. BASICS OF ANDREEV POINT-CONTACT SPECTROSCOPY

In the chapters 2-6 of this thesis, Josephson junction based devices were the focus of investigation. Since the Josephson effect arises from the proximity-induced superconducting state, we are interested in the determination of the energy dependent properties of this induced superconducting state, which in principle serves as a coherent reservoir for the Josephson effect. It is crucial to be able to measure these electronic states directly, in particular because the Josephson-effect itself contains only information about the phase difference and the nature of the current-phase relation, but not about its energy dependence. For this reason we designed an experiment which is based on an NcS_p point-contact to emulate Andreev-spectroscopy of the induced superconducting state as depicted in Fig. 7.4. N is a normal reservoir, which in our case is a topological insulator, c is the constriction, and S_p is the proximity-induced superconductor.

The chapter is structured as follows: First, a general introduction to the concept of point-contact spectroscopy is given. This is extended to point-contacts where one reservoir is superconducting. This technique is called point-contact Andreev spectroscopy (PCAR). A short overview about the theoretical and experimental status of this field is presented. Then, the design and lithographic fabrication of the device is discussed. We start by discussing the conductance without an applied magnetic field and gate voltage and model it based on the theory of Blonder, Tinkham and Klapwijk (BTK) [1]. We explain the transport through the point-contact by a non-equilibrium driven transformation of the relevant scattering regions. At low bias the voltage drop occurs mostly at the interface between the normal reservoir and the induced superconducting state, while at a higher bias the relevant interface is between the normal reservoir and niobium. Finally, we discuss the dependence of the conductance of gate voltage V_G and magnetic field B.

7.1.1. TRANSPORT THROUGH A POINT-CONTACT

Sharvin realized that the resistance through an ideal metallic contact with diameter d smaller than the elastic mean free path l_{mfp} is only determined by the number of channels through that contact and is thus independent of the material quality [2]. These contacts, so called Sharvin contacts or point-contacts, can be used to study scattering mechanisms in materials and understand its Fermi surface [3]. In order to conduct energy resolved spectroscopy the point-contact needs to be in a certain transport regime. The regimes can be classified into the quantum, ballistic, diffusive and thermal regime depending on the size of the diameter of the contact and the electron mean free path. The corresponding situations for the latter three cases are shown in Fig. 7.1. If the diameter a of the point-contact is smaller than a few de-Broglie wave lengths, the electron transport is in the *quantum regime*. The conductance of such a nanostructure is given by the sum of the single channels each contributing $G = e^2/h$ to the total conductance [5] (with lifted spin degeneracy of the channels). The point-contact is in the *ballistic regime* [Fig. 7.1a)], when its diameter is larger than the de-Broglie wavelength but smaller than the mean free path of the electron. The kinetic energy of the electron is determined by the applied bias eV across the contact and statistically does not scatter within the contact region. Sharvin derived an expression for the contact resistance R_S of a point-contact given by $R_S = 2h/(e^2(ak_F)^2)$, where h is the Planck constant and k_F the Fermi momentum. Electrons in this ballistic regime gain kinetic energy in a controlled manner to excite

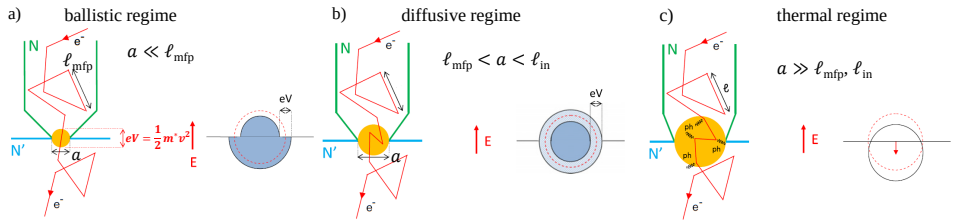

Figure 7.1: Diagram of different transport regimes of a electron e biased with a voltage V through a point-contact with orifice size a. a) The mean free path l_{mfp} of the electrons is longer than a. b) In the thermal regime elastic and inelastic scattering occurs in the point-contact. c) In the diffusive regime elastic scattering but no inelastic scattering is in the point-contact. The figure is adapted from Ref. [4].

elementary excitations and are therefore the basis of energy resolved spectroscopy.

If the elastic mean free path is smaller than the diameter of the orifice, two more possible regimes exist and the inelastic scattering length l_{in} has to be considered. For $l_{\mathrm{in}} > a > l_{\mathrm{mfp}}$ the point-contact is in the *diffusive regime* [Fig. 7.1c)]. In this regime momentum information is lost due to the elastic scattering while the energy information is still available. Hence energy resolved spectroscopy is still possible in the diffusive regime. In the thermal regime the diameter is larger than the elastic and inelastic scattering length [$(a > l_{\mathrm{mfp}}, l_{\mathrm{in}})$ as depicted in Fig. 7.1b)]. Then, the contact is in the thermal regime. This means that within the point-contact the electron is scattered elastically and inelastically loosing both momentum and energy information and is, therefore, not suited for spectroscopy [6]. The resistance of the point-contact then depends on the resistivity of the material, i.e. $R = \rho/(2a)$. The temperature at the point-contact can be estimated by $T^2_{\mathrm{max}} = T^2_{\mathrm{bath}} + V^2/4L$, where L is the so called Lorentz number [3]. Thus, in the thermal regime of a point-contact the temperature dependent resistivity of the point-contact is probed.

7.1.2. POINT-CONTACT ANDREEV REFLECTION SPECTROSCOPY

When one normal metal N of the point-contact is replaced by a supercondcutor S, a dissipative current is converted into a dissipationless current. As there are no free quasiparticle states available inside the superconducting gap an incoming electron with energy $E_F + eV < \Delta$ can only enter the superconductor when a hole with opposite momentum is reflected at the same time. This process transforms two charges into one Cooper pair and thus allows transport through the interface. This process is called Andreev reflection and is illustrated in Fig. 7.2a) and b) [7]. Blonder Tinkham and Klapwijk developed a framework to discuss the transport through a ballistic NS interface. The authors consider a finite interface transparency and analysed the energy dependence of the different scattering processes which are illustrated in Fig. 7.2 b) and c) [1]. The model is very successful in describing the transport through superconducting break junctions and is thus a good basis for our study. We consider a one dimensional situation as shown in Fig. 7.2b) a normal metal is in contact with a superconductor. A dimensionless barrier Z at $x = 0$ is separating the two materials. The barrier is modelled as a repulsive scattering potential $U(x) = Z\hbar v_F \delta(x)$, where v_F is the Fermi velocity and $\hbar$ the reduced Planck constant. The

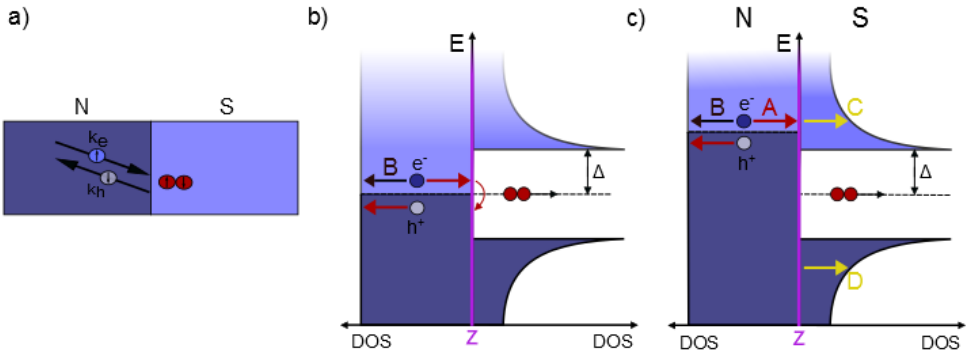

Figure 7.2: a) Real space schematic of the Andreev reflection process. b) and c) Energy dependent scattering processes at the interface of normal metal and a superconductor.

parameter Z is connected with the transmission τ in the normal state of the superconductor by $\tau = (1+Z^2)^{-1}$. An incoming electron can now, depending on its energy E, either be reflected as a hole, reflected as an electron, transmitted as an electron or transmitted as a hole with probabilities A, B, C, D respectively as indicated in Fig. 7.2b) and c). We start in the Bogoliubov-de Gennes basis in one dimension x:

$$\begin{bmatrix} H(x) & \Delta(k,x) \\ \Delta^*(k,x) & -H^*(x) \end{bmatrix} \begin{bmatrix} u_n(x) \\ v_n(x) \end{bmatrix} = E_n \begin{bmatrix} u_n(x) \\ v_n(x) \end{bmatrix}, \tag{7.1}$$

where $H(x)$ describes the normal state Hamiltonian and $\Delta(k,x)$ the spaital and momentum dependence of the superconducting gap. Usually this implies, that the self-consistency equation of the Bogoliubov-de Gennes equation

$$\Delta(x) = V_N \sum_{E>0} v^*(x)u(x)(1-2f(E,T)) \tag{7.2}$$

needs to be fulfilled. Here, $f(E)$ is the Fermi-Dirac distribution at energy E and temperature T, V_N is the interaction constant which at a large distant from the interface ($x \gg \xi$) obtains the bulk value Δ_0. We assume that V_N drops fast ($\Delta = 0$ for $x < 0$) at the interface $x = 0$ which can be described by

$$\Delta(x) = \Delta_0 e^{i\phi}\Theta(x) \tag{7.3}$$

with Θ the Heaviside function. This assumption is called rigid boundary condition and is usually valid in semiconductors as the resistance of the junction is much bigger than that of the bulk superconductor [8].

We now consider an incoming electron

$$\Psi_{\text{inc}} = \begin{bmatrix} 1 \\ 0 \end{bmatrix} e^{ik_e x} \tag{7.4}$$

which can undergo the processes as depicted in Fig. 7.2b) and c) depending on their energy

$$\Psi_{\text{reflected}} = a \begin{bmatrix} 0 \\ 1 \end{bmatrix} e^{ik_h x} + b \begin{bmatrix} 1 \\ 0 \end{bmatrix} e^{-ik_e x} \tag{7.5}$$

$$\Psi_{\text{transmitted}} = c \begin{bmatrix} u \\ v \end{bmatrix} e^{ik'_e x} + d \begin{bmatrix} u \\ v \end{bmatrix} e^{-ik'_h x}. \tag{7.6}$$

The coefficients a, b, c and d are related to the probability amplitudes as $A = aa^*$. The wave vectors can be calculated by inserting this ansatz into the Bogoliubov-de Gennes (BdG) equation which yields $\hbar k_{e,h} = \sqrt{2m(\mu \pm E)}$ and $\hbar k' = \sqrt{2m(\mu \pm \sqrt{E^- \Delta^2})}$ where the electrons (holes) correspond to the positive (negative) solutions and k (k') is the wave vector for the normal (superconducting) area. The boundary conditions for this problem are (i) the continuity of the wave function at the interface namely $\Psi_N(x=0) = \Psi_S(x=0)$ and (ii) the derivative boundary conditions for a $\delta(x)$ potential namely $\hbar/2m[\Psi'_S(x=0) - \Psi'_N(x=0)] = H\Psi(x=0)$. Using these conditions, it is possible to calculate the probabilities $A(E,Z)$. An overview of all the processes with their probabilities depending on barrier height and energy is presented in Tab. 7.1 and the amplitudes for Andreev and normal reflection for various barrier heights as a function of energy are shown in Fig. 7.3. For zero barrier height ($Z=0$), every incoming electron is Andreev reflected (black curve) and the normal reflection is zero (red curve) for $E < \Delta$. For increasing barrier values Z the Andreev probability gets smaller. At the value of the superconducting band gap $E = \Delta$, the high density of the states enhances again the Andreev probability. The normalized conductance through such an NS-interface as a function of applied bias V is given by [1]

$$R_{\text{N}} \frac{\mathrm{d}I_{\text{SN}}}{\mathrm{d}V} = \frac{\mathrm{d}}{\mathrm{dV}} \int_{-\infty}^{+\infty} [f_0(E - eV, T_1) - f_0(E, T_2)][1 + A(eV, Z) - B(eV, Z)]\mathrm{dE}, \tag{7.7}$$

where the normal state resistance R_N is assumed to be the resistance arising from the number of modes contributing to the transport. It is worth emphasizing that the transport not only depends on the reflection coefficients A and B but also on the population of states in the two reservoirs. This equation simplifies in the limit of zero temperature $T \longmapsto 0$ to

$$R_{\text{N}} \frac{\mathrm{d}I_{\text{SN}}}{\mathrm{d}V} = 1 + A(eV, Z) - B(eV, Z) \tag{7.8}$$

and is a direct measure of the energy dependent reflection amplitudes. The corresponding conductance for various values of Z is shown in Fig. 7.3 (green curves). For $Z = 0$, a doubling of the conductance inside the superconducting gap (i.e. $eV < \Delta$) is obtained due to the fact that each incoming electron now transfers a charge $2e$. The normalized conductance drops to one in the normal state as expected; this can be achieved for a high bias $eV \gg \Delta$, or by setting the superconducting gap to zero [$\Delta(T_c, B_c) = 0$]. In the high Z regime, the Andreev amplitude A is close to zero for most voltages. At the superconducting gap edge, the probability has a singularity due to an increased density of states of the superconductor at the gap edge. Therefore, in the large Z limit the differential conductance is a direct measure of the density of states of the superconductor namely

$$R_{\text{N}} \frac{\mathrm{d}I_{\text{SN}}}{\mathrm{d}V} = \frac{E}{\sqrt{E^2 - \Delta^2}}. \tag{7.9}$$

The most crucial limitations of the model for our case are (i) that it is a 1D model and the injection is only perpendicular to the interface (ii) the thickness of the barrier

	Normal state	No barrier ($Z=0$)	No barrier	General Form	General Form
		$E<\Delta$	$E>\Delta$	$E<\Delta$	$E>\Delta$
A	0	1	$\frac{v^2}{u^2}$	$\frac{\Delta^2}{E^2+(\Delta^2-E^2)(1+2Z^2)^2}$	$\frac{u^2v^2}{\gamma^2}$
B	$\frac{Z^2}{1+Z^2}$	0	0	1-A	$\frac{(u^2-v^2)Z^2(1+Z^2)}{\gamma}$
C	$\frac{1}{1+Z^2}$	0	1-A	0	$\frac{u^2(u^2-v^2)(1+Z^2)}{\gamma}$

Table 7.1: Probability amplitudes for Andreev reflection A, normal reflection B and transmission C for an incoming electron onto an SN interface depending on the energy E and the size of the barrier Z. The factors $u^2 = 1-v^2 = \frac{1}{2}(1+\frac{\sqrt{E^2-\Delta^2}}{E})$ are solutions of the BdG-equation and $\gamma = u^2+(u^2-v^2)Z^2$. The transmission of an electron as a hole is given by the conservation of particles as $D = 1-A-B-C$.

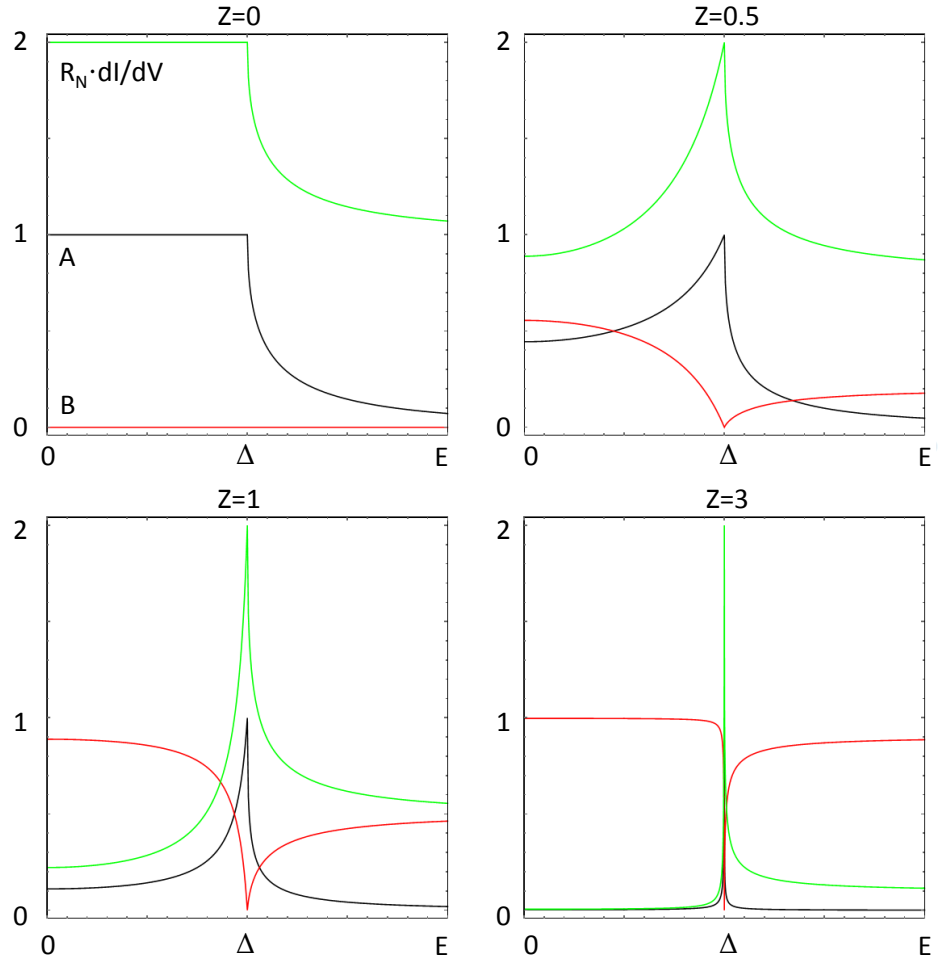

Figure 7.3: Examples for the probability amplitudes for Andreev (normal) reflection coefficients A,(B) in black (red) for different values of the barrier Z as indicated in the figures. The normalized differential conductance $R_N dI/dV$ at $T = 0$ K is shown in green.

is assumed to be zero and (iii) the Fermi surfaces of both materials are assumed to be spherical and the energy dispersion quadratic and spin degenerate. Because of the one dimensional assumption, the superconducting gap is also homogeneous and no directional information can be accessed. All these assumptions can be taken into account if necessary. Nevertheless, the BTK-formalism is the standard framework for the analysis of superconducting point-contact spectroscopy.

7.1.3. POINT-CONTACT ANDREEV REFLECTION SPECTROSCOPY OF PROXIMITY INDUCED SUPERCONDUCTIVITY IN TOPOLOGICAL INSULATORS

Our aim here is to apply Andreev spectroscopy to the proximity-induced superconducting state in a 3D topological insulator (3D TI). The application of Andreev-spectroscopy to low dimensional heterostructures is a much less mature experimental technique than for bulk systems [6, 9–11]. The point-contact has to be lithographically defined and is therefore usually larger than for the bulk systems, where accidentally formed pinholes of smaller dimensions dominate the transport. In addition, the reservoirs constitute a much smaller number of electrons and are usually 2-dimensional. These experimental concerns are exacerbated in the case of spectroscopy on proximity-induced superconductivity because of the need to use two dissimilar materials and, unavoidably, a complex lithographically structured geometry. One constraint is the transmissivity between the main superconductor (S_m) and the material in which the superconducting state is induced. In addition, the geometry to which the induced superconductivity is confined needs to be known and controlled. In fact, very few successful spectroscopic experiments on proximitized systems have been carried out. One example, applied on diffusive systems is by Scheer *et al.* [12], who used mechanical break junctions, an approach that merges bulk point-contact behaviour with thin films. Recently, Kjaergaard *et al.* [13] have presented results of point-contact spectroscopy on the ballistic Al/InAs system, which partially fulfils the experimental requirements. It shows the expected doubling of the quantized conductance steps for point-contacts in the highly transmissive regime, but exhibits also, from a spectroscopic perspective, many puzzling results and, additionally, unexpected behaviour as a function of the tunable point-contact transmissivity. A different geometry was used by Zhang *et al.* [14], with a tunable point-contact as well, but predominantly in the regime of low transmission.

We are interested in the determination of the energy dependent properties of this induced superconducting state, which in principle serves as a coherent reservoir for the Josephson effect as described in chapters 3-6. For this reason, we designed an experiment which is based on a NcS_p point-contact to emulate Andreev-spectroscopy of the induced superconducting state, as schematically shown in Fig. 7.4. The strained HgTe (blue) is defined lithographically to a finite sized bar and covered over a small distance by a conventional superconductor S_m. We assume that an induced superconducting state exists underneath the superconducting material, which we label S_p. We expect that in the state of equilibrium, i.e. no applied voltage across the contact ($V = 0$), the superconductor and the proximitized topological insulator form one coherent quantum state. The current through the sample, assumed to enter from the N-part, is carried away as a supercurrent. Therefore, we do not expect a voltage drop beyond the constriction characterized by

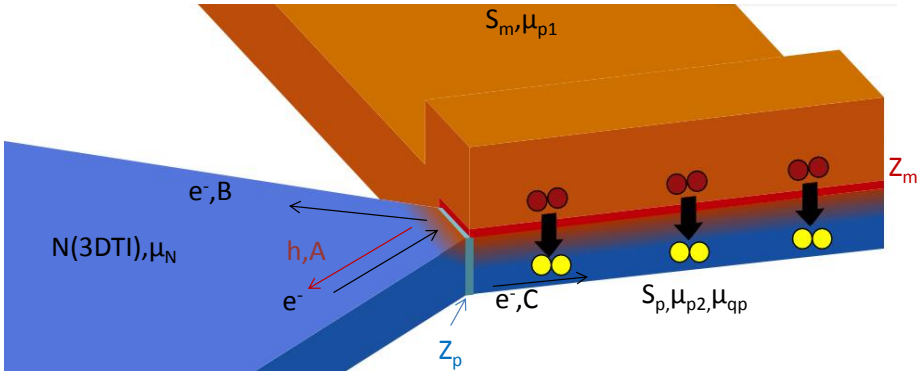

Figure 7.4: Schematic of the experiment: An s-wave superconductor (orange) induces superconducting pairing in an underlying topological insulator (yellow Cooper pairs). This state is connected through a constriction (indicated by the barrier $Z_{\rm p}$) to a normal reservoir. An electron e impinging from the 3D TI reservoir on Z_p can either be Andreev reflected, normal reflected or transmitted with probability amplitudes A,B and C respectively.

a barrier $Z_{\rm p}$. The superconducting side is initially, for $V_{\rm SN} = 0$, characterized by an equilibrium Fermi-function $\mu_{\rm p1} = \mu_{\rm p2}$ at the bath temperature T_b.

Thus, Eq. 7.7 is a good starting point to analyse the data. We do not know the coefficients $A(E)$ and $B(E)$ *a priori*. They contain the spectral information we are interested in. We assume that in Eq. 7.7, $A(E)$ and $B(E)$ are the result of the interaction of the superconductor with the confined bar of the 3D TI with its limited geometry, finite elastic mean free path and finite interfacial transparency $Z_{\rm m}$ [12, 15]. In addition, the normal part is made of a 3D TI where Dirac like surface states dominate the transport [16–18]. It is noted that in the device geometry of Fig. 7.4 no Majorana zero modes are expected to emerge due to the lack of confinement [19] but unconventional superconducting correlations might be observable. In fact, following Burset *et al.* [16], it is possible to extend the standard BTK-model taking the surface states of a topological insulator in the normal and superconducting part into account. Then, the barrier $Z_{\rm p}$ is modelled as an intermediate region to account for any interface scattering between the normal and the superconducting regions. The low-energy electron and hole excitations at the surface of the 3D TI are described by the Bogoliubov-de Gennes equations $H\Psi = E\Psi$, with E the excitation energy. In Nambu (particle-hole) and spin space, with basis $\Psi = [c_\uparrow(k), c_\downarrow(k), c_\uparrow^\dagger(-k), c_\downarrow^\dagger(-k)]^T$, with $c_\sigma(k)$ the annihilation operator for an electron of spin $\sigma = \uparrow, \downarrow$, and momentum k, the Hamiltonian reads as follows

$$H = \begin{pmatrix} h(k) - \mu(x)\sigma_0 & i\sigma_y\Delta(x) \\ -i\sigma_y\Delta(x) & \mu(x)\sigma_0 - h^*(-k) \end{pmatrix}, \tag{7.10}$$

where $\mu(x)$ is the chemical potential and the Pauli matrices $\hat{\sigma}_{0,1,2,3}$ acting on spin space. Here, electron-like quasiparticles are described by the Dirac-Hamiltonian

$$h(k) = v_F\left(k_x\sigma_x + k_y\sigma_y\right), \tag{7.11}$$

with v_F the Fermi velocity and e the electron charge. The pair potential of the superconducting gap is a generic s-wave potential and restricted to the proximitized area. The

intermediate region is modelled as a square potential with thickness d and height V_0. In the thin barrier limit $d \to 0$, the transmission through the intermediate region becomes an oscillatory function of the effective barrier strength $Z_p = V_0 d/\hbar v_F$. This is a typical behaviour of the linear band structure and is related to Klein-tunnelling [20, 21]. The scattering amplitudes A, B, C and D can in principle be obtained in a similar manner as in the standard BTK-model but no analytic expressions exists for them.

Once the scattering amplitudes are known, the zero-temperature conductance of the NS junction is defined as [1]

$$G_{NS}(E) = \int_{-\pi/2}^{\pi/2} \mathrm{d}\theta \cos\theta \left[1 - |b(E,\theta)|^2 + |a(E,\theta)|^2\right]. \tag{7.12}$$

We note that both the conductance and the LDOS are averaged over all incident angles, labeled by $\theta \in [-\pi/2, \pi/2]$. For a finite temperature, the differential conductance can be calculated using Eq. 7.7.

7.2. DESIGN AND FABRICATION OF THE POINT-CONTACT

The NcS_p junctions in this work are based on epitaxially grown layers of strained HgTe. Using magnetotransport measurements, we first characterize the material and discuss the design of the point-contact. Then, we present the fabrication of the point-contact.

7.2.1. CHARACTERIZATION OF THE MATERIAL

The goal of this experiment is to probe the superconductivity induced into the surface states of a three dimensional topological insulator via a point-contact. Therefore, two key requirements on the transport behaviour of the material are important. First, the transport needs to be at least predominately mediated by the topological surface states. Second, for an energy resolved measurements (ballistic regime), the mean free path l_{mfp} must be larger than the size of the orifice a.

Strained HgTe was first proposed to be a topological insulator by Fu and Kane [22] and experimentally verified by Brüne *et al.* [23]. When HgTe is grown on a CdTe substrate the lattice mismatch of the two compounds leads to a tensile strained growth of the HgTe. This opens a band gap in the bulk of the material while gapless surface states with a helical band structure which are protected by topology emerge. In contrast to the uncapped layers in chapter 3, we here use HgTe layers sandwiched between $Hg_{0.3}Cd_{0.7}Te$ capping layers as depicted in Fig. 7.5a). The $Hg_{0.3}Cd_{0.7}Te$ layers have a conventional band structure and protect against surface oxidation, which would otherwise reduce the carrier mobility. The capping layer also protect the strained HgTe during subsequent lithographic processing and thus increase the carrier mobility by about a factor of 10.

In order to ascertain the quality of the layers which are used for the point-contacts, a Hall bar with dimensions length × width ($l \times b = 600\,\mu\mathrm{m} \times 200\,\mu\mathrm{m}$) are fabricated from the same wafers (no. Q2567 and Q2830). As an example, the longitudinal R_{xx} and transversal resistance R_{xy} of substrate Q2830 at zero gate voltage and 4.2 K are shown in Fig. 7.5b). The charge type and density n can be determined from the linear slope of the Hall resistance using $R_{\mathrm{xy}} = B/en$ and this yields $n \approx 4.8 \times 10^{11}\,\mathrm{cm}^{-2}$. The positive slope shows an electron

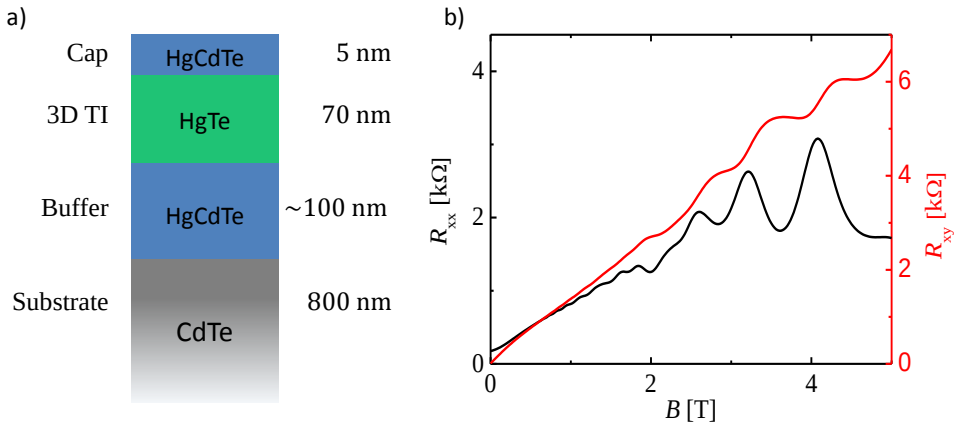

Figure 7.5: a) Layer stack of the capped sample Q2830 as grown by MBE. The thickness of each layer is labelled on the right side. b) Magnetotransport measurements of a Hall bar made from the wafer Q2830. The longitudinal (black) and the Hall (red) resistances are shown for zero gate voltage at 4.2 K.

like behaviour [5]. The mobility μ is given by

$$\mu = \frac{l/b}{R_{xy} n e} \approx 220\,000\,\mathrm{cm}^2/(Vs). \tag{7.13}$$

Using this, one obtains for the mean free path

$$l_{mfp} = \frac{\hbar\mu}{e}\sqrt{\frac{4\pi n}{g_s}} \approx 2.5\,\mu\mathrm{m} \tag{7.14}$$

where we set $g_s = 2$ to take spin degeneracy due to the top and bottom surface states into account. It is noted that this estimate of l_{mfp} is clearly a simplification as it assumes one averaged system. In general the bulk, upper and lower surface or side surfaces can all contribute differently to the total conductance. For the sake of simplicity we ignore this in the estimation for l_{mfp}. Furthermore, clear plateaus are visible in the transversal resistance coinciding with minima of the Shubnikov-de Haas oscillations in the longitudinal resistance, as expected in 2D electron gases. The plateaus occur at integer fractions of $R_K = 25.813\,\Omega$ and can thus be identified as quantum Hall plateaus. This is a clear proof, that the transport of bulk HgTe in high magnetic fields is dominated by 2D states. It is shown in Refs. [24–26], that these states are indeed the topological surface states.

The longitudinal normal state resistance and mobility as a function of gate voltage are shown in Fig. 7.6. The resistance rises with decreasing gate voltages and reaches a local maximum at around −1 V; this is roughly where the charge neutrality point is located i.e. where the slope of the Hall resistance turns from positive to negative p-dominated transport. The mobility is heavily reduced in the p-conducting regime and saturates at approximately $15\,000\,\mathrm{cm}^2/(Vs)$.

To conclude, the mean free path of the HgTe layers in the n-doped regime was estimated around $l_{\mathrm{mfp}} \approx 2.5\,\mu\mathrm{m}$. The magnetotransport shows clear QH plateaus which are an indication of the presence of two dimensional states which was shown to originate from the topological surface states and dominate the transport behaviour [24, 26]. We are able to change the density from a n-doped regime into the p-doped regime by applying a top gate voltage. All these informations are important for of the design and the analysis of the conductance of the point-contact.

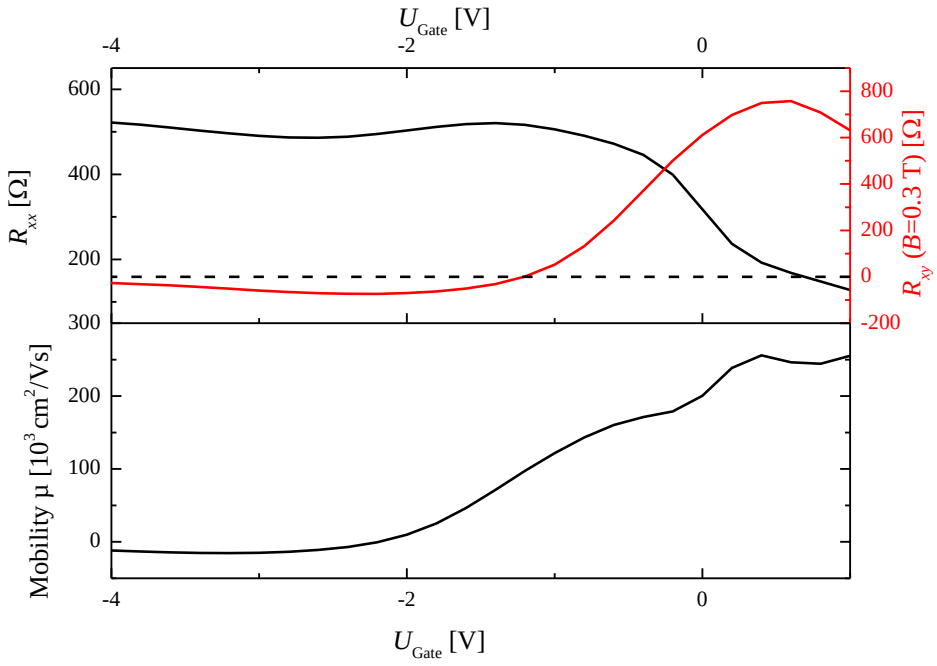

Figure 7.6: Upper panel: Longitudinal resistance R_{xx} (black) and Hall resistance R_{xy} (red) as a function of gate voltage for Q2830 at 4.2 K. The vertical black dashed lines shows the gate voltage where the Hall slope changes sign. Lower panel: Mobility vs gate voltage. The mobility was calculated by measuring $\mathrm{R_{xx}}(B = 0\,\mathrm{T})$ and $\mathrm{R_{xy}}(B = 0.3\,\mathrm{T})$ and assuming a linear slope for the transversal resistance.

7.2.2. DEVICE DESIGN AND FABRICATION

The design of one point-contact is shown in Fig. 7.7. In order to be in the ballistic transport regime the orifice a of the point-contact is chosen to be 1 µm. This is smaller than the mean free path of $l_{\mathrm{mfp}} \approx 2.5\,\mu\mathrm{m}$. The mesa is designed to open at an angle of 45° in order to ensure that the voltage drop occurs predominantly at the constriction. This angle value also ensures that electrons reflected from the walls are not scattered back into the point-contact. The total width of the mesa extends to 13 µm. This dimension is large enough that electrons are fully elastic scattered and the normal part forms a proper Landauer-Büttiker equilibrium reservoir. The elastic scattering length is estimated to be in the similar range as the l_{mfp}. Electric contacts made from AuGe alloy and Au

are applied on the green areas. The ohmic contacts have an almost negligible contact resistance $R_{\text{contact}} < 20\,\Omega$ compared to the constriction.

The mesa extends as a small stripe of 6 µm length from the constriction downwards it is covered by the superconductor. This length is long enough so that non-local effects such as crossed Andreev reflections at both sides of the superconductor are avoided. This is important in view of the fact that the length scale for such effects is determined by the coherence length of niobium ($\xi_{\text{Nb}} \approx 20\,\text{nm}$) used as the superconducting material. The superconductor is designed to form a large reservoir for the electrons and to allow fast spreading of the current densities to avoid heating effects at the point-contact. As a superconductor Nb was chosen due to its large critical temperature, magnetic field and its good interface qualities with HgTe. To be able to perform quasi four-point measurements both the normal and superconducting contacts have two leads. Furthermore, a gate is applied on most of the devices which extends over the whole uncovered mesa which allows control over the charge carriers of the reservoir with respect to the covered part.

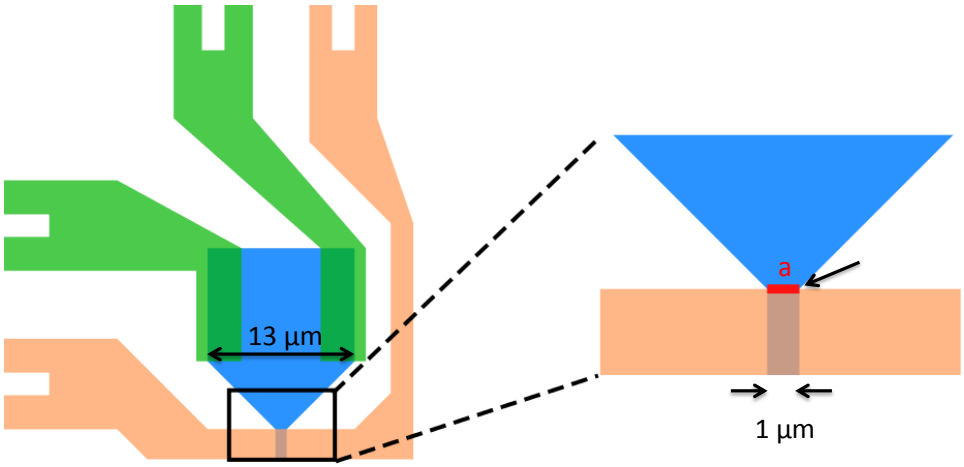

Figure 7.7: Design of a single point superconducting point-contact. The mesa is shown in blue, normal metal in green and the superconductor in orange. The size of the orifice is marked in red.

SAMPLE FABRICATION

The point-contacts are fabricated using conventional electron beam lithography with varying acceleration voltages and poly (methyl methacrylate) (PMMA) resists depending on the demands for the separate etching and evaporation steps. As HgTe is sensitive to temperatures above 90°C, all bake-out and lift-off procedures are carried out well below this temperature. The detailed recipe can be found in the appendix. Before the start of the lithography a piece from the MBE grown substrate of about $3 \times 3\,\text{mm}^2$ is cleaved. As the first step, the HgTe mesa is defined using low energy argon sputtering. During this process, a thin titanium etch shield, separated by a SiO_2 sacrificial layer from the HgTe, protects the mesa. The shield is then removed by a buffered oxide etch dip. In the next step, the superconductor is deposited. Since the interface is buried, the cap layer needs

to be removed, which is done by argon etching, followed by in-situ magnetron sputtering of about 110 nm of niobium. After this, the leads for the ohmic contacts are defined and 50 nm AuGe/50 nm Au is deposited. The contact resistances are usually $\ll 50\,\Omega$. To allow control of the charge carrier density in the 3D TI, a top gate electrode is evaporated on top of the uncovered HgTe as follows. First, a thin HfO_2 insulator is grown at a temperature of 35°C via atomic layer deposition, followed by the deposition of 5 nm of Ti and 150 nm Au. Using the same insulator on reference Hall bar structures, it is possible to tune the density from $1 \times 10^{12}\,\mathrm{cm}^{-2}$ n-type regime to $-1 \times 10^{12}\,\mathrm{cm}^{-2}$ p-type dominated conductance. An SEM picture of the final device without an applied gate is shown in Fig. 7.8b).

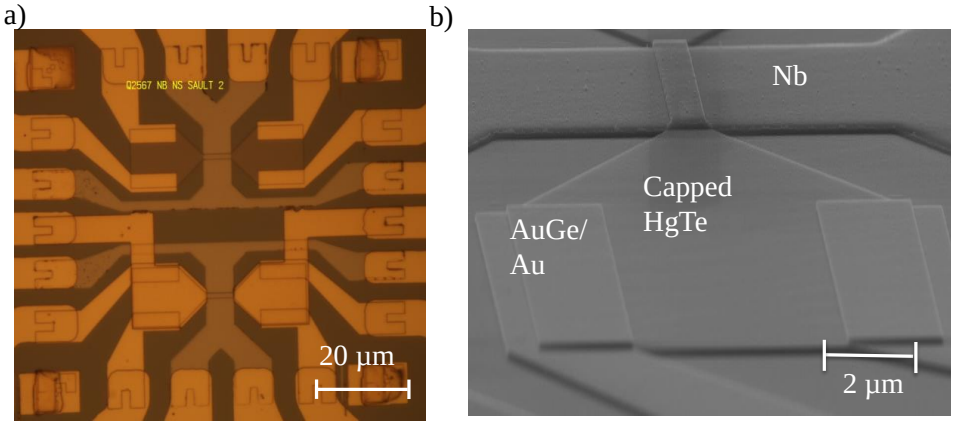

Figure 7.8: a) Optical microscope picture of a finished device with four point-contacts. The upper two devices are without an applied gate while the lower two point-contacts have a gate electrode. b) Scanning electron microscope of one point-contact before the gate was applied.

An optical microscope picture of a finished structure is shown in Fig. 7.8a) and an SEM picture of a point-contact in Fig. 7.8b). The sample is glued into a chip carrier using low temperature varnish and bonded with Au wires.

The sample is inserted into a dilution refrigerator at a base temperature of 30 mK for Device 1 and at 140 mK for Device 2-3. The full measurement circuit including the used electrical filtering is show in Fig. 7.9. The measurements are done using ac- and dc-excitation which are coupled inductively. All electrical lines are equipped with π-filters at room temperature and copper powder filters attached to the mixing chamber plate.

7.3. DISCUSSION OF THE FUNDAMENTAL CONDUCTANCE

The differential conductance across the point-contact for four different devices at zero applied gate voltage and zero magnetic field is shown in Fig. 7.10. At voltages $|V_{SN}| > 1.5\,\mathrm{mV}$, larger than the superconducting gap of niobium Δ_{Nb}, the differential conductance is almost constant and a normal state resistance of $R_N = 160 - 240\,\Omega$ depending on the measured device can be evaluated. For voltages around $V_{SN} \simeq 1.1\,\mathrm{mV}$, the conductance is slightly enhanced and then starts to decrease for voltages $|V| \mapsto 0$. Close to zero bias, the conductance enhances again resulting in a double peak structure around $V_{SN} = 0$,

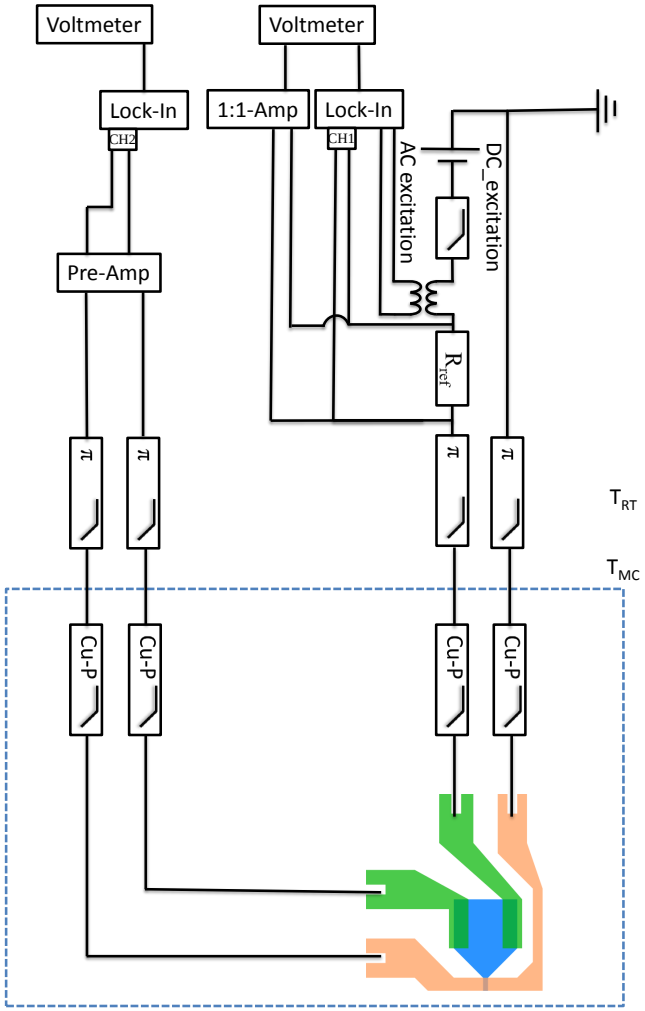

Figure 7.9: Measurement circuit for the SN-devices. The SN-device is contacted via electrical wires thermalised at the mixing chamber of a dilution refrigerator in a four point geometry. The wires are filtered with copper powder filters Cu-P at the mixing chamber and π-filters in the breakout box of the cryostat. The ac- and dc-signals are inductively coupled and measured by lock-in amplifiers and voltmeters. The voltage signal at the point-contact is amplified. A reference resistor R_{ref} was used to determine the current flowing in the circuit.

with a peak separation of about 100 μV for Device 1, and slightly different for the other devices. We observe sample dependent sub-gap features as indicated by the red arrows in Fig. 7.10. The four devices differ with respect to the shape and length of the HgTe bar underneath the superconductor as indicated in the insets of Fig. 7.10. Device 1 is symmetric with a width of $a = 1\,\mu$m and two open ends. Device 2 has a step like shape with partially width a and partially width of 0.6 μm. Similarly, Device 3 but with the wide 'normal' electrode connected to the wide part rather than the more narrow part. Finally, Device 4 is terminated half-way and implies a largely closed HgTe bar. At present it is not clear whether the sub-gap feature should be interpreted as a feature in the relevant non-equilibrium distribution entering Eq. 7.7 or as reflecting the geometrical influence according to the analysis of Kopnin and Melnikov [27]. Systematic shape-dependent experiments are needed to map and evaluate this dependence accurately and to test the origin.

The change in conductance at around 1.1 mV can be attributed to the size the superconducting gap of the niobium film. The conductance increases slightly as expected at the superconducting gap edge. For lower voltages the conductance reduces, an indication of dominant normal $B(E)$ reflections over Andreev reflections $A(E)$ [$B(E)/A(E) > 1$].

Following Ref. [27], it can be assumed that some superconducting correlations are induced from the bulk superconductor into the underlying material with a certain efficiency depending on the interface quality. This process can be understood in the framework of Andreev reflections at the interface transforming Cooper pairs into electrons. The efficiency of this process is given by the height of the barrier which we label Z_{m} as shown in Fig. 7.4 and is located between the niobium film and the HgTe. The soft gap edge may be due to pair-breaking mechanisms, disorder or spatial gradients and angle averaging due to the two dimensionality, which can easily smear out a sharp gap or make it even vanish [4].

Close to zero bias the conductance is enhanced. There exist several parasitic mechanisms which can be responsible for an enhanced conductance, such as reflectionless tunnelling [28], reentrance effect [29] or weak anti-localization. Thus, we need to first discard these kinds of effects. The reentrance effect [30, 31] occurs in diffusive contacts where an incoming electron reaches the SN interface through a lot of scatterers but the Andreev reflected hole returns the time reversed path. If this process is fully phase coherent at low temperatures, the two path interferences cancel and $G_{\mathrm{NS}} = G_{\mathrm{NN}}$. This has the consequence that at zero bias the normal state resistance is recovered which is not observed in the present measurements. Furthermore, only a single peak is expected to occur in the case of the reentrance effect. Reflectionless tunnelling is an effect which again occurs in very disordered materials where the SN interface has a very low transmission, i.e., a high barrier Z [32]. An incoming electron is then trapped in the point-contact region and is reflected several times at this barrier which increases the transmission again. This effect would yield a single peak at zero bias. Both effects, reflectionless tunnelling and reentrance effect occur in rather disordered metals, while our point-contact is expected to be in the ballistic regime and has a low resistance. We have been able to exclude weak anti-localization by measuring the conductance between the two normal leads without observing a sign of a zero bias peak. Thus, we can identify the central peak as enhanced conduction originating from AR at the point-contact from the induced superconductivity.

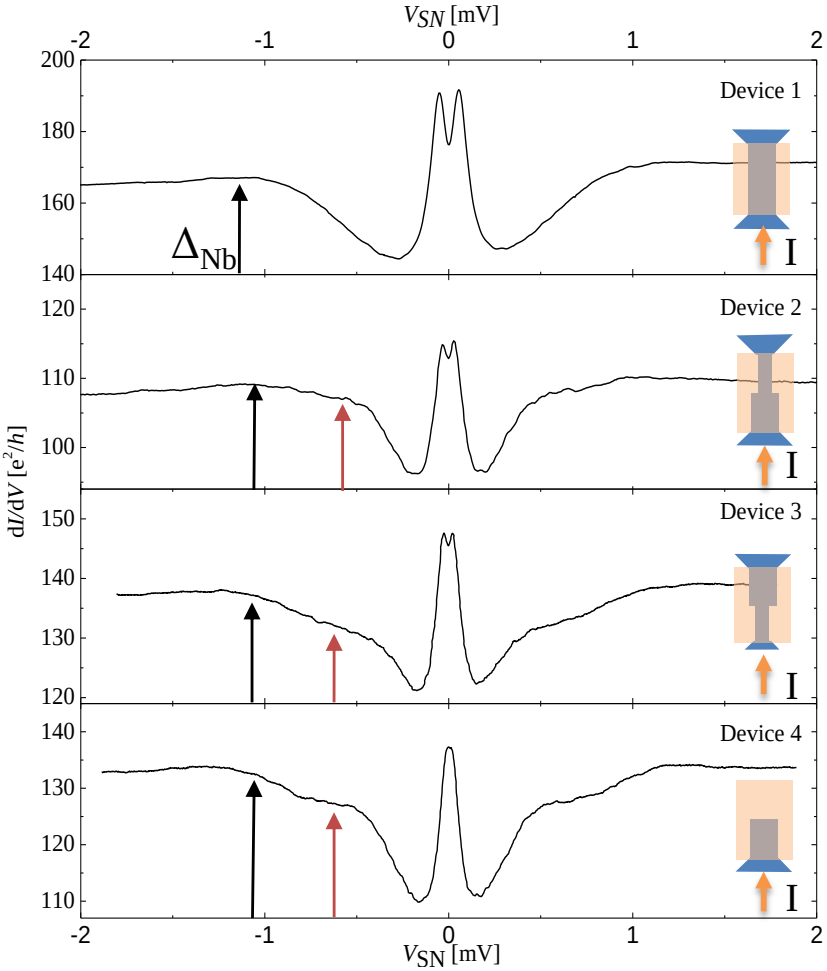

Figure 7.10: dI/dV measurements for four devices. The devices differ by the 'connectivity' of the HgTe bar, covered by niobium, as indicated in the inset. The orange arrows indicate the current current direction. The red arrow indicates a sample dependent sub gap feature and the black arrow signals the position of the niobium gap Δ_{Nb}.

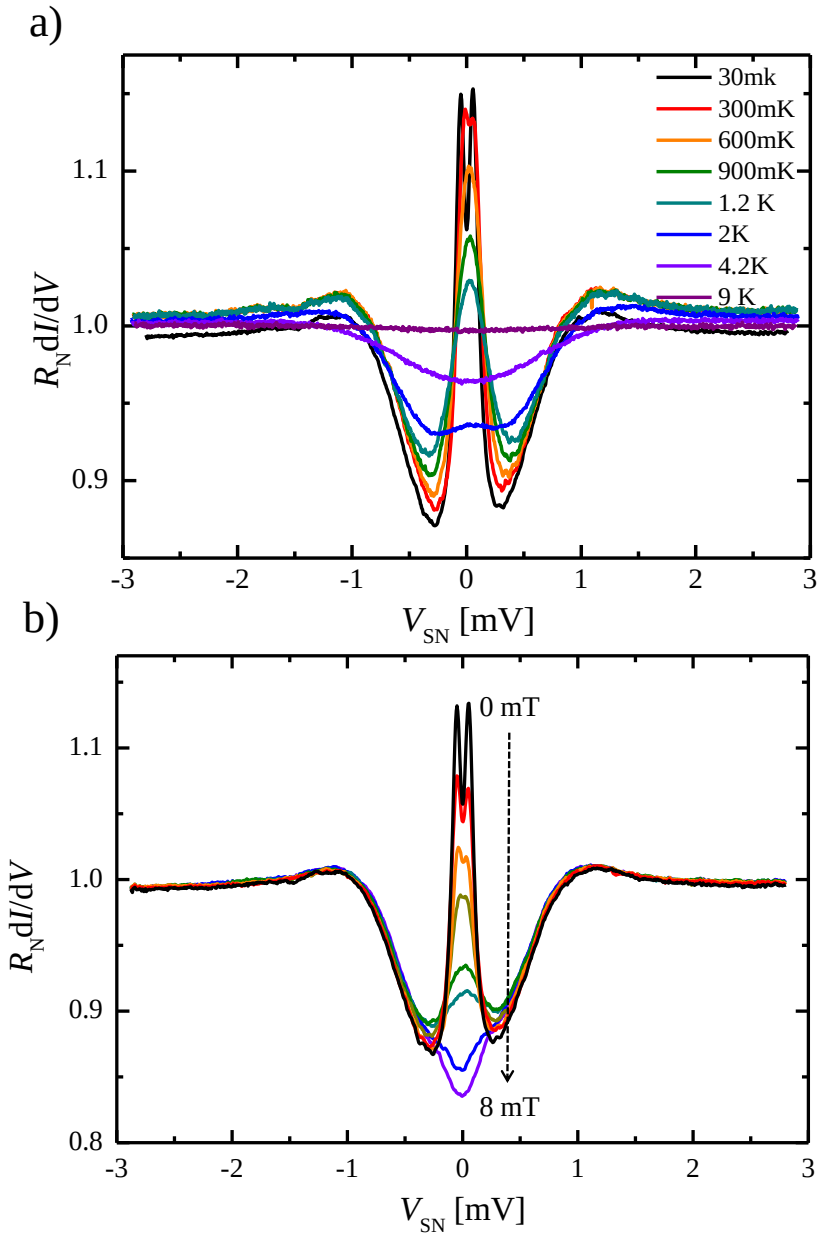

Figure 7.11: a) Conductance of Device 1 normalized to the resistance R_N at $T = 9$ K (purple). Panel b) shows the conductance measured at 30 mK for increasing (small) magnetic field values. For clarity, a small vertical shift has been removed in the presentation of the data to highlight that the high voltage part of the conductance overlap for these magnetic field strengths.

We further investigate the behaviour of the conductance, as a function of temperature. In this regard temperature dependent measurements of Device 1 were conducted; measurements are shown in Fig. 7.11a). An asymmetric background for negative and positive bias is observed for all devices. The data can be normalized by multiplying with the normal state resistance R_N measured at 9 K ($T > T_c$); The result is shown in Fig. 7.11.

With increasing temperature, the double peak feature is smeared out leaving a single zero bias maximum which vanishes at a temperature of about 2 K and merges at higher temperatures to a bell-shaped curve. At these temperatures, the niobium gap $V \simeq \Delta_{\mathrm{Nb}}$ is not affected, indicating two separate energy scales. The height of the zero bias anomaly is at base temperature of the dilution refrigerator several tens of conductance quanta.

Panel b) of Fig. 7.11 shows the conductance measured at 30 mK for increasing values of magnetic field applied perpendicular to the sample. We verified that the response is independent of the direction of the applied magnetic field (perpendicular to the sample plane, parallel to the SN interface, and perpendicular to the SN interface). For clarity, a small vertical shift has been removed in the presentation of the data in Fig. 7.11b) to highlight the fact that the high voltage part of the conductance is unaffected to these magnetic field strengths. This is expected for the Nb gap as the critical magnetic field is much larger ($B_c \approx 2-3$ T). Evidently, the central peak can be suppressed completely by applying a much smaller magnetic field (within $\pm 5-10$ mT). We attribute this central bell-shaped peak, which evolves into a two peak structure, as a manifestation of the proximity-induced superconducting order parameter as given by Eq. 7.2.

7.4. MODELLING USING THE BLONDER TINKHAM KLAPWIJK THEORY

In order to get a more quantitative information on the two energy scales and barrier heights, the induced and niobium superconducting gap is modelled using the BTK-theory as introduced in Eq. 7.7. The singularities of the superconducting gap edge, especially at the niobium gap, are smeared out. This can be treated by a phenomenological broadening parameter which was introduced by Dynes *et al.* [33] and is then straightforward to incorporate this into the BTK formalism [34–36]. In this connection, an imaginary damping term $i\Gamma$ is introduced into the superconducting density of states expression and one obtains:

$$N_S(E,\Gamma) = \mathrm{Re}\left[\frac{E - i\Gamma}{\sqrt{(E-i\Gamma)^2 - \Delta^2}}\right]. \tag{7.15}$$

The effect for various values of Γ/Δ is shown in Fig. 7.12. The superconducting singularity gets softer and broader with increasing value of Γ.

PROXIMITY INDUCED GAP

In Fig. 7.13a), data for different temperatures are compared with standard BTK-modelling using Eq. 7.7 (cyan) and the model from Burset *et al.* [16] (magenta) both leading to very reasonable agreements with the experimental data. In this figure we have renormalized the data differently. We have chosen the conductance value at the edge of the grey zone in Fig. 7.13b), as a reasonable approximation to the real value of R_N entering Eq. 7.7. From the comparison shown in Fig. 7.13a), we conclude that we find a proximity-induced order

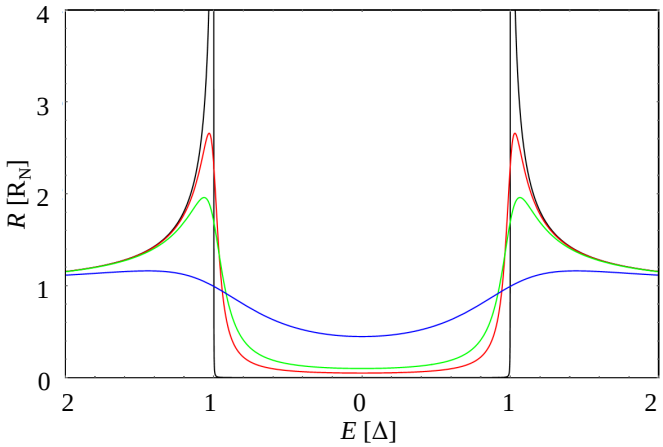

Figure 7.12: The normalized differential conductance R/R_N is plotted for various broadening parameters in the high $Z \gg 1$ limit. The quasiparticle broadening values are $\Gamma = 0/\Delta$ (black), $\Gamma = 0.05/\Delta$ (red), $\Gamma = 0.1/\Delta$ (green), and $\Gamma = 0.5/\Delta$ (blue).

parameter $\Delta_p = 70\,\mu eV$ in agreement with both models. Fits using Eq. 7.7 were obtained with a small barrier height $Z_p = 0.4$. In applying this model, we have assumed that the proximity-induced order parameter Δ_p leads to a standard BCS like behaviour of the amplitudes $A(E)$ and $B(E)$ as a function of energy and that the normal state is described by a parabolic band dispersion. The model might therefore not capture the microscopic details but makes it suitable to be compared to other systems. We assume that this barrier (labelled Z_p) is located at the orifice. In principle this interface is crystalline and thus no or just a small barrier is expected. The quality of the TI below the Nb is very likely reduced compared to the covered HgTe due to IBE and the depositing Nb. This leads to a local doping and thus a Fermi velocity mismatch or different strain of the two TI regions [37]. Therefore, a finite but rather small barrier is justified at the point-contact in agreement with the BTK fitted value.

Burset *et al.* [16] studies the conductance of a NS junction on the surface of a topological insulator and is thus appropriate in our case. The contact between the normal region and the induced superconducting reservoir is modelled as a square potential barrier, where the dimensionless barrier strength Z_p is defined as the product of the barrier height and width. The sub-gap tunnel conductance of the NS junction is then an oscillatory function of the barrier strength Z_p and minimum for values $Z_p = (n+1/2)\pi$, with n an integer [20, 21]. By applying this model to our experimental data, a rather large barrier can be used. The enhanced conductance can then be seen as a signature of the helical surface states where highly transparent modes are always expected due to Klein tunnelling. We interpret the low voltage data as a probe of the induced superconducting state in the 3D TI of strained HgTe. There is no reason to expect *a priori* an s-wave order parameter. In fact, we expect deviations, such as for example calculated by Burset *et al.* [16]. Since the actual spectra depend on several parameters, a larger data-set is needed to provide a reliable analysis to show the influence of the helical Dirac nature of the surface states.

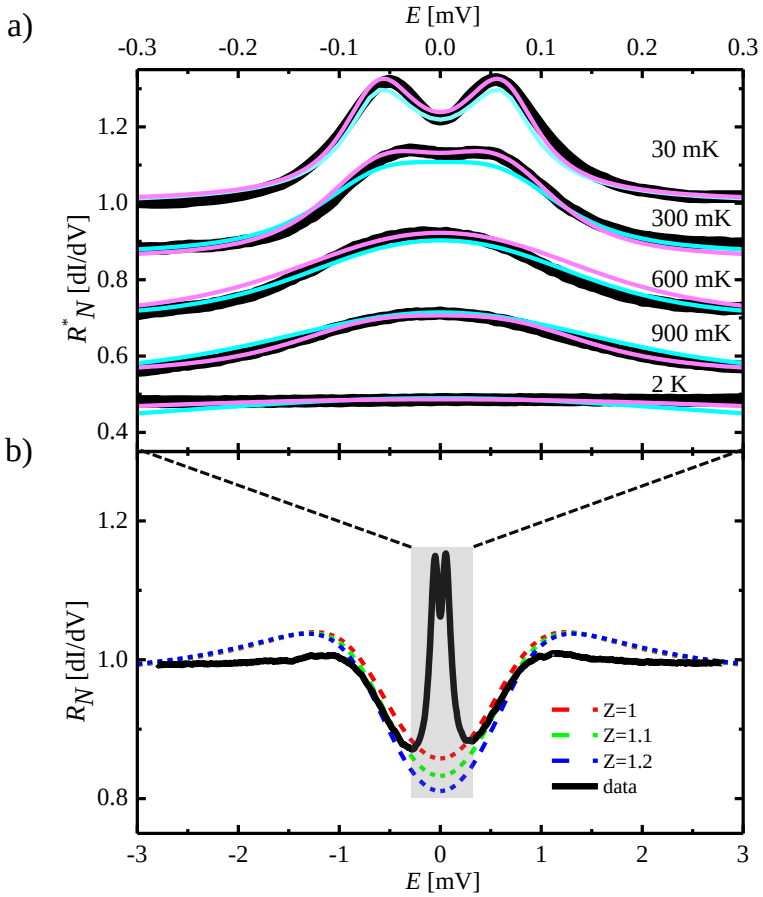

Figure 7.13: In a) the central split peak (gray zone of b)) is compared to an analysis using Eq. 7.7 (cyan) with a fixed value of $Z_p = 0.4$ and a broadening parameter $\Gamma \approx 0.025\Delta_p$. The magenta lines show a comparison with the model developed in Ref. [16] with a broadening parameter $\Gamma < 0.015\Delta_p$. The value of Δ_p in both models is 70 µeV. (In panel a) we have abandoned the normalization of the data on R_N at high voltages and in the normal state. Instead we have chosen to take the conductance value at the edge of the grey zone. The precise value is a bit arbitrary, but should be close to this value. The curves are offset for better visibility.) b) Conductance of Device 1 normalized with the normal state resistance R_N above the critical temperature $T > T_c$ at 30 mK. The grey area indicates the voltage-range where we assume an equilibrium proximity-induced superconducting state. The dashed lines show fits using Eq. 7.7 for three different Z_m parameters and a broadening of $0.7\Delta_{Nb}$.

Especially the values of the barriers and broadening parameters can deviate from the real values, which have to be combined with the expected A and B amplitudes. The question is still open with respect to which model describes the experiment properly. Nevertheless, this does not affect the conclusion that we can draw with respect to the identification of the regime, where spectroscopy of the induced superconducting state can reliably be performed.

NIOBIUM GAP

It is possible to achieve good qualitative agreement with the outer (niobium) gap using a barrier of $Z_{\mathrm{m}} \approx 1.1$ and $\Delta_{\mathrm{Nb}} = 0.8\,\mathrm{meV}$ as depicted in Fig. 7.13b). A large broadening parameter of $\Gamma_{\mathrm{m}} \approx 0.7\Delta_{\mathrm{Nb}}$ is needed. This barrier indicates a rather low transparency and bad proximity effect of the Nb/HgTe interface. The reduced value of the Nb gap in contrast to the gap estimated from the critical temperature of the niobium film $\approx 1.1\,\mathrm{meV}$ ($T_c \approx 9\,\mathrm{K}$) can be due to the fact that the first sputtered layers react with the HgTe and have therefore a reduced purity and thus a reduced energy gap. The coherence length of niobium is rather short $\approx 20\,\mathrm{nm}$. This length scale is directly correlated to the strength of the proximity effect [38]. Thus, mostly the Nb with a reduced quality close to the HgTe is responsible for the transport and justifies a reduced Δ_{Nb} in the modelling. Additionally, spatial gradients on the large surface area of the HgTe bar can broaden the singularity.

7.5. DISCUSSION OF THE TRANSPORT THROUGH THE POINT-CONTACT

Given the identification of the induced superconducting gap in the topological surface states Δ_{p} and the niobium gap Δ_{Nb}, we propose an interpretation and explain the transport in our system.

The uncovered 3D TI part can be treated as a source of (ballistic) electrons. The electrons inside this area are in thermal equilibrium and can be defined by a constant chemical potential μ_N. The incoming electrons can enter independently on their energy and phase. The phase itself is randomized inside the reservoir. These statements do not hold for the proximitized topological insulator as the region might be smaller than one inelastic scattering length and electrons are trapped by the presence of two barriers. Furthermore, the proximitized part is confined to a bar with a size depending on the measured device as indicated in the inset of Fig. 7.10 with measurable consequences in the sub gap spectrum of Δ_{Nb} which could arise for example due to geometrical resonances. Therefore, the scattering problem can not be reduced to a single delta like barrier located at the orifice of the point-contact but the whole region from the point-contact to the bulk s-wave superconductor needs to be taken into account.

In the equilibrium case ($V_{\mathrm{SN}} = 0$) at zero temperature as depicted in Fig. 7.14a), the superconductor exhibits a gap of $2\Delta_{\mathrm{Nb}}$ which, via the proximity effect, induces a mini-gap $2\Delta_{\mathrm{p}}$ into the TI below. We assume that the resulting local density of states is gapped at zero energy and features gap edges at Δ_{p} and Δ_{Nb} as depicted in Fig. 7.14a)[27, 39–41]. For a finite voltage bias, the current in $\mathrm{S_p}$ is carried away as a supercurrent. Cooper pairs can travel freely between $\mathrm{S_m}$ and $\mathrm{S_p}$ ($\mu_{\mathrm{p1}} = \mu_{\mathrm{p2}}$ and $\mu_{\mathrm{qp}} = 0$). The voltage-drop occurring at the interface indicated by Z_{p} in Fig. 7.14a), is due to the difference in electrochemical

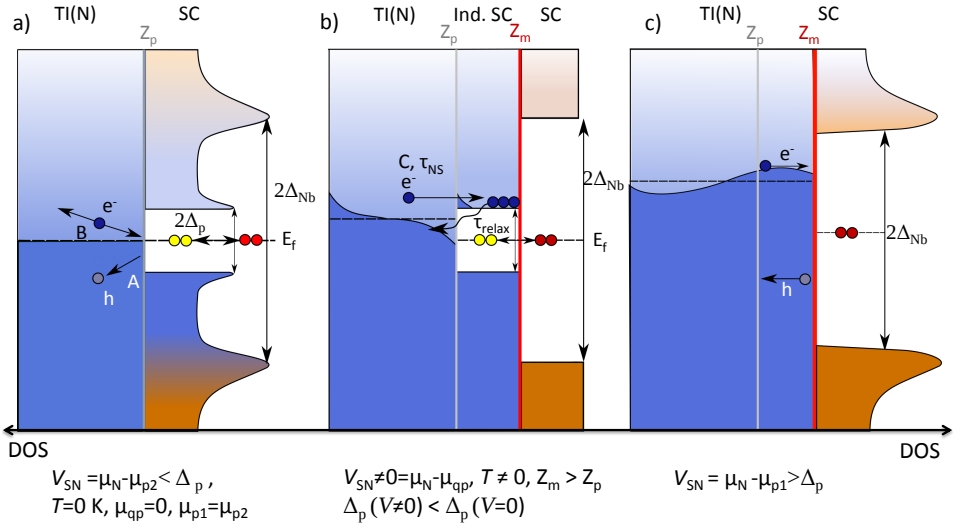

Figure 7.14: Semiconductor band representation of the normal constriction superconductor system for different bias regimes. The normal part N is the topological insulator TI. The constriction is initially characterized by a barrier Z_p and the superconductor by a pair potential Δ_p. In a) the system is at zero bias and zero temperature. The voltage difference will emerge at the narrow point-contact and Andreev reflections (normal reflections) occur there with probability A (B). In b) at finite temperature and finite bias electrons from higher energies are allowed to enter the proximity-induced superconductor. For even higher bias, the proximity-induced superconducting state S_p is quenched ($\Delta_p \to 0$) and the situation as depicted in c) is present. Then, at higher voltages transport is measured between a normal reservoir being the 3D TI HgTe and the superconductor niobium with an interface resistance characterized by Z_m.

potentials between N on the left of Z_p and S_p on the right of Z_p ($V_{SN} = \mu_N - \mu_{p1}$). The scale of the relevant Sharvin resistance is controlled by the number of modes at the Z_p location and by the value of Z_p. Due to the small barrier a high Andreev reflection probability leads to an increased conductance.

For voltages larger than 0.5 meV, the conductance curves in Fig. 7.11b) all superimpose, if we exclude the central part interpreted as the proximity-induced order parameter. The data outside the central part can no longer be interpreted as the conductance of an NcS point-contact at Z_p. The electronic states in the HgTe bar underneath the niobium are no longer correlated as expressed in Eq. 7.2. For increasing voltage at the location Z_p, higher energy quasiparticles are injected into the HgTe bar with a probability C as depicted in Fig. 7.14b). They cannot escape into an equilibrium reservoir because of the large gap of the superconductor niobium and $Z_p < Z_m$. As Andreev reflections allow charge flow but no energy transfer the only other relaxation mechanism for the hot electrons is electron-phonon coupling which is likely to be small at the investigated temperatures. A charge imbalance is build up [41]. Therefore, $f_0(E)$ in Eq. 7.2 becomes a non-equilibrium distribution with relatively hot electrons, which leads in general to a destruction of the proximity-induced order parameter Δ_p, in the same way as a small magnetic field quenches this induced superconducting state. Hence, beyond a voltage of about 0.5 meV the system has changed and we are left with a non-superconducting HgTe bar in contact with niobium as shown in Fig 7.14c) with an interface with an unknown transmissivity parametrized by Z_m.

One has to keep in mind that if the process is present, values for the induced superconductivity and the transmission through the point-contact might be underestimated. This argument is enforced by the fact that the critical temperature related to the induced gap is $T_{Cind} \approx 300$ mK but a finite central peak is still visible at 1.2 K.

7.6. GATE AND MAGNETIC FIELD DEPENDENCE OF THE CONDUCTANCE

We also studied the influence of the AR probability at the point-contact as a function of the Fermi energy in the normal reservoir by applying different gate voltages. The normal state resistance of Device 2 versus the gate voltage is shown in Fig. 7.15b). The curves are normalized to the resistance $R_N(T > T_c)$ for each gate voltage individually. The behaviour is comparable to a reference Hall-bar. There, by studying the slope of the Hall resistance, we were able to tune the density from initially n-doped, over the charge neutrality point into the hole dominated regime. Due to the high mobility in the n-conducting regime, the point-contact is expected to be ballistic in this regime. By tuning into the p-regime the mobility reduces by about a factor of ten and the mean free path is now smaller than the size of the point-contact and, thus expected to be in the diffusive regime. From the conductance curves (Fig. 7.15a) it is clear that we no longer observe a signature of the niobium pairing potential in the p-regime. Upon changing the gate voltage, features at the scale of the niobium gap disappear upon approaching the charge neutrality point (at $-2.2\ V$). The only significant voltage-dependent feature is around $\pm$ 100 μeV. We assume that this observation is a signature that the NcS point-contact is probing the induced superconducting state of the HgTe bar in a diffusive proximity-system, leading to

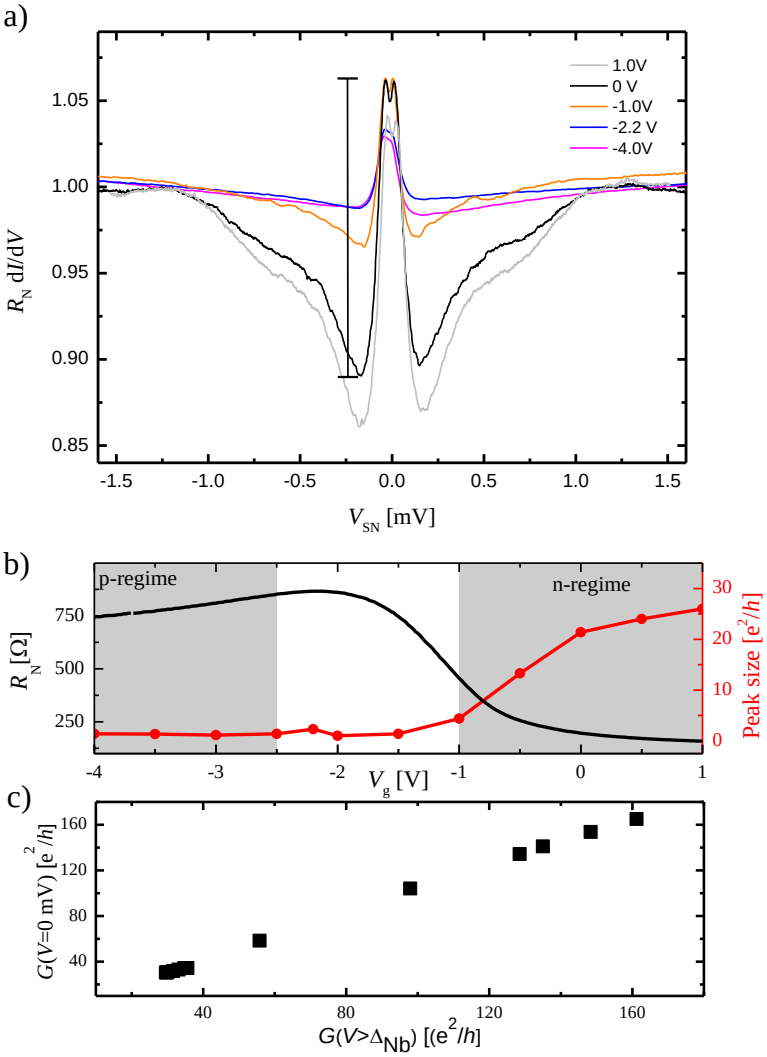

Figure 7.15: a) Gate dependence of normalized conductance of Device 2 at $B = 0$ T from 1 V to −4 V. The black bar indicates how the height of the central peak is evaluated in panel b). b) Normal state Resistance R_N versus gate voltage (black) and size of the peak (red) defined as indicated in a) by the black bar for $V_g = 0$. c) Normal state conductance versus zero bias conductance is shown.

a mini-gap.

The height of the zero bias anomaly as a function of gate voltage is quantified as indicated in Fig. 7.15a) by the black bar for $V_g = 0$ ($dI/dV(T = 30\,\mathrm{mK}) - dI/dV(T > T_c)$) and plotted in Fig. 7.15b) as red dots. The amplitude is several tens of e^2/h in the n-conducting regime and decreases constantly up to the charge neutrality point (CP) region where it saturates at a value of 1-2 e^2/h depending on the sample. Another way of looking at the height of the zero bias anomaly is shown in Fig. 7.15c) where the conductance below the niobium gap is compared with the normal state conductance above Δ_{Nb}. Here, an almost linear behaviour is found with a slope close to one indicating that the height of the peak scales with the normal state resistance. A momentum mismatch is created by changing the density on the normal part while the superconducting region is unaffected, the peak survives indicating constant AR probability independent of the barrier. In fact, by using an effective barrier which takes the Fermi velocity mismatch into account $Z_{\mathrm{eff}} = \sqrt{Z^2 + (1-r)^2/4r}$ where $r = v_{\mathrm{FN}}/v_{\mathrm{FS}} \approx \sqrt{n_{\mathrm{N}}/n_{\mathrm{S}}}$ is the ratio of the Fermi velocities of the superconducting v_{FS} compared to the normal part v_{FN}, one can give a rough estimate of the effect of the density change of a system with a purely parabolic band structure [42]. Also the density of the proximitised part is unknown, a lower bound for the estimated change of density in the N part by comparing with Hall-bar measurements is $n_{\mathrm{N}}(1\,\mathrm{V}) \approx 10 \times 10^{11}\,\mathrm{cm}^{-2}$ to $n_{\mathrm{P}}(\text{-}4\,\mathrm{V}) \approx -10 \times 10^{11}\,\mathrm{cm}^{-2}$. Using these assumptions, variations in Z_{p} in at least the range shown in Fig. 7.3 are expected and should clearly influence the size of the zero bias anomaly which is not observed in the measurements. A reduced influence of a barrier is expected for systems with a linear dispersion [21, 43] and could be related to a phenomenon called superconducting Klein-tunnelling or perfect Andreev reflection predicted by Tkachov *et al.* [44].

7.7. GENERAL REMARK ABOUT OUR ANALYSIS

The analysis of our data has lead us to discuss the conductance data resulting from the transport through three different electron systems (N, $\mathrm{S_p}$ and $\mathrm{S_m}$), separated by two interfaces of transparency Z_{p} and Z_{m}. Following Beenakker [45] it is assumed that any contact between a normal reservoir and a superconducting reservoir is given by

$$G_S = 2G_0 \frac{G_N^2}{(2G_0 - G_N)^2} \tag{7.16}$$

with $G_0 = 2e^2/h$ the quantum unit of conductance, G_N the conductance in the normal state, and G_S the conductance with one of the electrodes superconducting. This expression is the zero-voltage limit of the classical BTK-formula for different values of transmissivity Z. In order to calculate G_S, often the conductance at $V > \Delta_s$ is used as G_N [see also Fig. 7.15c)] and implying that this experimental value is independent of the applied bias. The most important implication in our case is that one measures at high voltages not a proximity-induced superconducting gap, but rather the parent superconductor. We suggest that the low voltage data should be understood by acknowledging that the scattering region and the equilibrium reservoirs at $V_{\mathrm{SN}} = 0$ should be defined differently from the one at higher voltages, such as in our case $V > 0.8\,\mathrm{meV}$.

7.8. CONCLUSION

In conclusion, a ballistic Andreev point-contact based on the topological insulator HgTe was successfully fabricated and transport spectroscopy of the proximity-induced pair-potential was carried out. It was possible to identify an induced superconducting order parameter in the HgTe of about $\Delta_p = 70\mu eV$. In addition, to explain the transport through the device, we take into account how to identify the relevant Fermi-distribution function over the energies, implying the relevance of a non-equilibrium distribution function in analysing the data. The induced superconducting state is quenched by increasing the bias across the device or by applying a small magnetic field. These results are an important step towards a better understanding and engineering of topological superconductivity as it allows control and measurement of the size of the induced superconducting gap. It may also serve as a building block for further analysis of the 4π-Josephson effect as reported in chapters 3-6 [46–48].

BIBLIOGRAPHY

[1] G. E. Blonder, M. Tinkham, and T. M. Klapwijk, *Transition from metallic to tunneling regimes in superconducting microconstrictions: Excess current, charge imbalance, and supercurrent conversion,* Physical Review B **25**, 4515 (1982).

[2] Y. V. Sharvin, *A Possible Method for Studying Fermi Surfaces,* Soviet Journal of Experimental and Theoretical Physics **21**, 655 (1965).

[3] Y. G. Naidyuk and I. K. Yanson, *Point-contact spectroscopy*, Vol. 145 (Springer Science & Business Media, 2005).

[4] D. Daghero and R. S. Gonnelli, *Probing multiband superconductivity by point-contact spectroscopy,* Superconductor Science and Technology **23**, 43001 (2010).

[5] C. W. J. Beenakker and H. van Houten, *Quantum Transport in Semiconductor Nanostructures,* in *Semiconductor Heterostructures and Nanostructures*, Solid State Physics, Vol. 44, edited by H. Ehrenreich and D. Turnbull (Academic Press, 1991).

[6] D. Daghero, M. Tortello, G. A. Ummarino, and R. S. Gonnelli, *Directional point-contact Andreev-reflection spectroscopy of Fe-based superconductors: Fermi surface topology, gap symmetry, and electron–boson interaction,* Reports on Progress in Physics **74**, 124509 (2011).

[7] A. Andreev, *Thermal conductivity of the intermediate state of superconductors, II,* Journal of Experimental and Theoretical Physics (JETP) **20**, 1490 (1965).

[8] K. K. Likharev, *Superconducting weak links,* Reviews of Modern Physics **51**, 101 (1979).

[9] G. Deutscher, *Andreev Saint-James reflections: A probe of cuprate superconductors,* Reviews of Modern Physics **77**, 109 (2005).

[10] M. Eschrig, *Spin-polarized supercurrents for spintronics: a review of current progress,* Reports on Progress in Physics **78**, 104501 (2015).

[11] R. J. Soulen, J. M. Byers, M. S. Osofsky, B. Nadgorny, T. Ambrose, S. F. Cheng, P. R. Broussard, C. T. Tanaka, J. Nowak, J. S. Moodera, A. Barry, and J. M. D. Coey, *Measuring the spin polarization of a metal with a superconducting point contact,* Science **282**, 85 (1998).

[12] E. Scheer, W. Belzig, Y. Naveh, M. H. Devoret, D. Esteve, and C. Urbina, *Proximity Effect and Multiple Andreev Reflections in Gold Atomic Contacts,* Physical Review Letters. **86**, 284 (2001).

[13] M. Kjærgaard, F. Nichele, H. J. Suominen, M. Nowak, M. Wimmer, A. Akhmerov, J. Folk, K. Flensberg, J. Shabani, C. Palmstrøm, *et al.*, *Quantized conductance doubling and hard gap in a two-dimensional semiconductor–superconductor heterostructure,* Nature communications **7**, 12841 (2016).

[14] H. Zhang, Ö. Gül, S. Conesa-Boj, K. Zuo, V. Mourik, F. K. de Vries, J. van Veen, D. J. van Woerkom, M. P. Nowak, M. Wimmer, D. Car, S. Plissard, E. P. A. M. Bakkers, M. Quintero-Pérez, S. Goswami, K. Watanabe, T. Taniguchi, and L. P. Kouwenhoven, *Ballistic Majorana nanowire devices,* ArXiv e-prints (2016), arXiv:1603.04069 [cond-mat.mes-hall] .

[15] D. Averin and A. Bardas, *ac Josephson Effect in a Single Quantum Channel,* Physical Review Letters. **75**, 1831 (1995).

[16] P. Burset, B. Lu, G. Tkachov, Y. Tanaka, E. M. Hankiewicz, and B. Trauzettel, *Superconducting proximity effect in three-dimensional topological insulators in the presence of a magnetic field,* Physical Review B **92**, 205424 (2015).

[17] A. M. Black-Schaffer and A. V. Balatsky, *Odd-frequency superconducting pairing in topological insulators,* Physical Review B **86**, 144506 (2012).

[18] M. Snelder, A. A. Golubov, Y. Asano, and A. Brinkman, *Observability of surface Andreev bound states in a topological insulator in proximity to an s -wave superconductor,* Journal of Physics: Condensed Matter **27**, 315701 (2015).

[19] M. Snelder, A. A. Golubov, Y. Asano, and A. Brinkman, *Observability of surface Andreev bound states in a topological insulator in proximity to an s-wave superconductor,* Arxiv preprint **315701**, 1 (2015), arXiv:arXiv:1503.06026v1 .

[20] S. Bhattacharjee and K. Sengupta, *Tunneling Conductance of Graphene NIS Junctions,* Physical Review Letters. **97**, 217001 (2006).

[21] J. Linder and A. Sudbø, *Tunneling conductance in s- and d-wave superconductor-graphene junctions: Extended Blonder-Tinkham-Klapwijk formalism,* Physical Review B **77**, 1 (2008), 0712.0831 .

[22] L. Fu and C. L. Kane, *Topological insulators with inversion symmetry,* Physical Review B **76**, 045302 (2007).

[23] C. Brüne, C. X. Liu, E. G. Novik, E. M. Hankiewicz, H. Buhmann, Y. L. Chen, X. L. Qi, Z. X. Shen, S. C. Zhang, and L. W. Molenkamp, *Quantum Hall Effect from the Topological Surface States of Strained Bulk HgTe,* Physical Review Letters **106**, 126803 (2011).

[24] C. Brüne, C. Thienel, M. Stuiber, J. Böttcher, H. Buhmann, E. G. Novik, C.-X. Liu, E. M. Hankiewicz, and L. W. Molenkamp, *Dirac-Screening Stabilized Surface-State Transport in a Topological Insulator,* Physical Review X **4**, 41045 (2014).

[25] C. Brüne, C. X. Liu, E. G. Novik, E. M. Hankiewicz, H. Buhmann, Y. L. Chen, X. L. Qi, Z. X. Shen, S. C. Zhang, and L. W. Molenkamp, *Quantum Hall Effect from the Topological Surface States of Strained Bulk HgTe,* Physical Review Letters **106**, 126803 (2011).

[26] D. A. Kozlov, Z. D. Kvon, E. B. Olshanetsky, N. N. Mikhailov, S. A. Dvoretsky, and D. Weiss, *Transport Properties of a 3D Topological Insulator based on a Strained High-Mobility HgTe Film,* Physical Review Letters **112**, 196801 (2014).

[27] N. B. Kopnin and A. S. Melnikov, *Proximity-induced superconductivity in two-dimensional electronic systems,* Phys. Rev. B **84**, 064524 (2011).

[28] B. J. van Wees, P. de Vries, P. Magnée, and T. M. Klapwijk, *Excess conductance of superconductor-semiconductor interfaces due to phase conjugation between electrons and holes,* Physical Review Letters **69**, 510 (1992).

[29] H. Courtois, P. Charlat, P. Gandit, D. Mailly, and B. Pannetier, *The Spectral Conductance of a Proximity Superconductor and the Reentrance Effect,* Journal of Low Temperature Physics **116**, 187 (1999).

[30] T. M. Klapwijk, *Proximity Effect From an Andreev Perspective,* Journal of Superconductivity **17**, 593 (2004).

[31] C. W. J. Beenakker, *Random-matrix theory of quantum transport,* Review of Modern Physics **69**, 731 (1997).

[32] J. Melsen and C. Beenakker, *Reflectionless tunneling through a double-barrier NS junction,* Physica B: Condensed Matter **203**, 219 (1994).

[33] R. C. Dynes, V. Narayanamurti, and J. P. Garno, *Direct measurement of quasiparticle-lifetime broadening in a strong-coupled superconductor,* Physical Review Letters **41**, 1509 (1978).

[34] Y. De Wilde, T. Klapwijk, A. Jansen, J. Heil, and P. Wyder, *Quasi-particle lifetime broadening in normal—superconductor junctions with UPt_3,* Physica B: Condensed Matter **218**, 165 (1996).

[35] M. Grajcar, A. Plecenik, P. Seidel, and A. Pfuch, *Influence of inelastic effects on differential conductance of a high-Tc superconductor/metal junction,* Physical Review B **51**, 16185 (1995).

[36] A. Pleceník, M. Grajcar, A. Beňačka, P. Seidel, and A. Pfuch, *Finite-quasiparticle-lifetime effects in the differential conductance of $Bi_2Sr_2CaCu_2O_y$/Au junctions,* Physical Review B **49**, 10016 (1994).

[37] Y.-Y. Chang, C.-Y. Mou, and C.-H. Chung, *Andreev reflection in 2d relativistic materials with realistic tunneling transparency in normal-metal-superconductor junctions,* arXiv preprint arXiv:1701.00591 (2017).

[38] M. Snelder, M. Stehno, A. Golubov, C. Molenaar, T. Scholten, D. Wu, Y. Huang, W. van der Wiel, M. Golden, and A. Brinkman, *Conductance spectroscopy of a proximity induced superconducting topological insulator,* arXiv preprint arXiv:1506.05923 (2015).

[39] W. Belzig, C. Bruder, and G. Schoen, *Local Density of States in a Dirty Normal Metal connected to a Superconductor,* Physical Review B **54**, 5 (1996).

[40] A. A. Golubov and M. Y. Kupriyanov, *Quasiparticle current in ballistic NcNS junctions,* Physica C: Superconductivity and its Applications **259**, 27 (1996).

[41] A. F. Volkov, A. V. Zaitsev, and T. M. Klapwijk, *Proximity effect under nonequilibrium conditions in double-barrier superconducting junctions,* Physica C: Superconductivity **210**, 21 (1993).

[42] G. E. Blonder and M. Tinkham, *Metallic to tunneling transition in Cu-Nb point contacts,* Physical Review B **27**, 112 (1983).

[43] S. Bhattacharjee and K. Sengupta, *Tunneling conductance of graphene NIS junctions,* Physical Review Letters **97**, 1 (2006).

[44] G. Tkachov and E. M. Hankiewicz, *Helical Andreev bound states and superconducting Klein tunneling in topological insulator Josephson junctions,* Physical Review B **88** (2013).

[45] C. W. J. Beenakker, *Quantum transport in semiconductor-superconductor microjunctions,* Physical Review B **46**, 12841 (1992).

[46] J. Wiedenmann, E. Bocquillon, R. S. Deacon, S. Hartinger, O. Herrmann, T. M. Klapwijk, L. Maier, C. Ames, C. Brüne, C. Gould, A. Oiwa, K. Ishibashi, S. Tarucha, H. Buhmann, and L. W. Molenkamp, *4π-periodic Josephson supercurrent in HgTe-based topological Josephson junctions,* Nature Communications **7**, 10303 (2016).

[47] E. Bocquillon, R. S. Deacon, J. Wiedenmann, P. Leubner, T. M. Klapwijk, C. Brüne, K. Ishibashi, H. Buhmann, and L. W. Molenkamp, *Gapless Andreev bound states in the quantum spin Hall insulator HgTe,* Nature Nanotechnology **12**, 137 (2017).

[48] R. S. Deacon, J. Wiedenmann, E. Bocquillon, F. Domínguez, T. M. Klapwijk, P. Leubner, C. Brüne, E. M. Hankiewicz, S. Tarucha, K. Ishibashi, *et al.*, *Josephson radiation from gapless andreev bound states in hgte-based topological junctions,* Physical Review X **7**, 021011 (2017).

SUMMARY

This thesis describes the studies of topological superconductivity, which is predicted to emerge when pair correlations are induced into the surface states of 2D and 3D topological insulators (TIs). In this regard, experiments have been designed to investigate the theoretical ideas first pioneered by Fu and Kane that in such system Majorana bound states occur at vortices or edges of the system [Phys. Rev. Lett. 100, 096407 (2008), Phys. Rev. B 79, 161408 (2009)]. These states are of great interest as they constitute a new quasiparticle which is its own antiparticle and can be used as building blocks for fault tolerant topological quantum computing.

After an introduction in chapter 1, chapter 2 of the thesis lays the foundation for the understanding of the field of topology in the context of condensed matter physics with a focus on topological band insulators and topological superconductors. Starting from a Chern insulator, the concepts of topological band theory and the bulk boundary correspondence are explained. It is then shown that the low energy Hamiltonian of mercury telluride (HgTe) quantum wells of an appropriate thickness can be written as two time reversal symmetric copies of a Chern insulator. This leads to the quantum spin Hall effect. In such a system, spin-polarized one dimensional conducting states form at the edges of the material, while the bulk is insulating. This concept is extended to 3D topological insulators with conducting 2D surface states. As a preliminary step to treating topological superconductivity, a short review of the microscopic theory of superconductivity, i.e. the theory of Bardeen, Cooper, and Shrieffer (BCS theory) is presented. The presence of Majorana end modes in a one dimensional superconducting chain is explained using the Kitaev model. Finally, topological band insulators and conventional superconductivity are combined to effectively engineer p-wave superconductivity. One way to investigate these states is by measuring the periodicity of the phase of the Josephson supercurrent in a topological Josephson junction. The signature is a 4π-periodicity compared to the 2π-periodicity in conventional Josephson junctions. The proof of the presence of this effect in HgTe based Josephson junction is the main goal of this thesis and is discussed in chapters 3 to 6.

Chapter 3 describes in detail the transport of a 3D topological insulator based weak link under radio-frequency radiation. The chapter starts with a review of the state of research of (i) strained HgTe as 3D topological insulator and (ii) the progress of inducing superconducting correlations into the topological surface states and the theoretical predictions of 3D TI based Josephson junctions. Josephson junctions based on strained HgTe are successfully fabricated. Before studying the ac driven Josephson junctions, the dc transport of the devices is analysed. The critical current as a function of temperature is measured and it is possible to determine the induced superconducting gap. Under rf illumination Shapiro steps form in the current voltage characteristic. A missing first step at low frequencies and low powers is found in our devices. This is a signature of a 4π-periodic supercurrent. By studying the device in a wide parameter range - as a

function of frequency, power, device geometry and magnetic field - it is shown that the results are in agreement with the presence of a single gapless Andreev doublet and several conventional modes.

Chapter 4 gives results of the numerical modelling of the $I-V$ dynamics in a Josephson junction where both a 2π- and a 4π-periodic supercurrents are present. This is done in the framework of an equivalent circuit representation, namely the resistively shunted Josephson junction model (RSJ-model). The numerical modelling is in agreement with the experimental results in chapter 3. First, the missing of odd Shapiro steps can be understood by a small 4π-periodic supercurrent contribution and a large number of modes which have a conventional 2π-periodicity. Second, the missing of odd Shapiro steps occurs at low frequency and low rf power. Third, it is shown that stochastic processes like Landau Zener tunnelling are most probably not responsible for the 4π contribution.

In a next step the periodicity of Josephson junctions based on quantum spin Hall insulators using are investigated in chapter 5. A fabrication process of Josephson junctions based on inverted HgTe quantum wells was successfully developed. In order to achieve a good proximity effect the barrier material was removed and the superconductor deposited without exposing the structure to air. In a next step a gate electrode was fabricated which allows the chemical potential of the quantum well to be tuned. The measurement of the diffraction pattern of the critical current I_c due to a magnetic field applied perpendicular to the sample plane was conducted. In the vicinity to the expected quantum spin Hall phase, the pattern resembles that of a superconducting quantum interference device (SQUID). This shows that the current flows predominantly on the edges of the mesa. This observation is taken as a proof of the presence of edge currents. By irradiating the sample with rf, missing odd Shapiro steps up to step index $n = 9$ have been observed. This evidences the presence of a 4π-periodic contribution to the supercurrent. The experiment is repeated using a weak link based on a non-inverted HgTe quantum well. This material is expected to be a normal band insulator without helical edge channels. In this device, all the expected Shapiro steps are observed even at low frequencies and over the whole gate voltage range. This shows that the observed phenomena are directly connected to the topological band structure. Both features, namely the missing of odd Shapiro steps and the SQUID like diffraction pattern, appear strongest towards the quantum spin Hall regime, and thus provide evidence for induced topological superconductivity in the helical edge states.

A more direct way to probe the periodicity of the Josephson supercurrent than using Shapiro steps is the measurement of the emitted radiation of a weak link. This experiment is presented in chapter 6. A conventional Josephson junction converts a dc bias V to an ac current with a characteristic Josephson frequency $f_J = eV/h$. In a topological Josephson junction a frequency at half the Josephson frequency $f_J/2$ is expected. A new measurement setup was developed in order to measure the emitted spectrum of a single Josephson junction. With this setup the spectrum of a HgTe quantum well based Josephson junction was measured and the emission at half the Josephson frequency $f_J/2$ was detected. In addition, f_J emission is also detected depending on the gate voltage and detection frequency. The spectrum is again dominated by half the Josephson emission at low voltages while the conventional emission is determines the spectrum at high voltages. A non-inverted quantum well shows only conventional emission over the whole gate

voltage and frequency range. The linewidth of the detected frequencies gives a measure on the lifetime of the bound states: From there, a coherence time of 0.3–4 ns for the $f_J/2$ line has been deduced. This is generally shorter than for the f_J line (3–4 ns).

The last part of the thesis, chapter 7, reports on the induced superconducting state in a strained HgTe layer investigated by point-contact Andreev reflection spectroscopy. For the experiment, a HgTe mesa was fabricated with a small constriction. The diameter of the orifice was chosen to be smaller than the mean free path estimated from magnetotransport measurements. Thus one gets a ballistic point-contact which allows energy resolved spectroscopy. One part of the mesa is covered with a superconductor which induces superconducting correlations into the surface states of the topological insulator. This experiment therefore probes a single superconductor normal interface. In contrast to the Josephson junctions studied previously, the geometry allows the acquisition of energy resolved information of the induced superconducting state through the measurement of the differential conductance dI/dV as a function of applied dc bias for various gate voltages, temperatures and magnetic fields. An induced superconducting order parameter of about 70 μeV was extracted but also signatures of the niobium gap at the expected value around $\Delta_{\mathrm{Nb}} \approx 1.1$ meV have been found. Simulations using the theory developed by Blonder, Tinkham and Klapwijk and an extended model taking the topological surface states into account were used to fit the data. The simulations are in agreement with a small barrier at the topological insulator-induced topological superconductor interface and a high barrier at the Nb to topological insulator interface. To understand the full conductance curve as a function of applied voltage, a non-equilibrium driven transformation is suggested. The induced superconductivity is suppressed at a certain bias value due to local electron population. In accordance with this suppression, the relevant scattering regions change spatially as a function of applied bias.

To conclude, it is emphasized that the experiments conducted in this thesis found clear signatures of induced topological superconductivity in HgTe based quantum well and bulk devices and opens up the avenue to many experiments. It would be interesting to apply the developed concepts to other topological matter-superconductor hybrid systems. The direct spectroscopy and manipulation of the Andreev bound states using circuit quantum electrodynamic techniques should be the next steps for HgTe based samples. This was already achieved in superconducting atomic break junctions by the group in Saclay [Science 2015, 349, 1199-1202 (2015)]. Another possible development would be the on-chip detection of the emitted spectrum as a function of the phase ϕ through the junction. In this connection, the topological junction needs to be shunted by a parallel ancillary junction. Such a setup would allow the current phase relation $I(\phi)$ directly and the lifetime of the bound states to be measured directly. By coupling this system to a spectrometer, which can be another Josephson junction, the energy dependence of the Andreev bound states $E(\phi)$ could be obtained. The experiments on the Andreev reflection spectroscopy described in this thesis could easily be extended to two dimensional topological insulators and to more complex geometries, like a phase bias loop or a tunable barrier at the point-contact. This work might also be useful for answering the question how and why Majorana bound states can be localized in quantum spin Hall systems.

ZUSAMMENFASSUNG

Die vorliegende Dissertation befasst sich mit der experimentellen Untersuchung von topologischer Supraleitung, die durch die Kombination von konventionellen Supraleitern mit 2D- und 3D- topologischen Isolatoren (TI) entsteht. Diesbezüglich wurden Experimente durchgeführt, die auf zwei bahnbrechenden Arbeiten von Fu und Kane [Phys. Rev. Lett. 100, 096407 (2008), Phys. Rev. B 79, 161408 (2009)] aufbauen. Diesen zufolge wird in supraleitenden topologischen Isolatoren ein neuartiges Quasiteilchen, ein sogenanntes Majorana-Fermion, vorhergesagt. Das große Interesse an diesem Teilchen beruht auf dessen besonderen Eigenschaften. Es sind Fermionen mit halbzahligen Spin, jedoch besitzen sie keine Ladung und es ist gleichzeitig sein eigenes Antiteilchen. Darüber hinaus besitzt das Teilchen im Vergleich zu konventionellen Fermionen eine andere Austauschstatistik und zählt daher zu den sogenannten nicht-abelschen Anyonen. Aufgrund dieser Eigenschaften wurde vorhergesagt, dass sie für weniger fehleranfällige Quantenbits als Bauteile für einen Quantencomputer verwendet werden können.

Nach einer Einleitung in Kapitel 1 folgt in Kapitel 2 eine Einführung in das Konzept von Topologie in der Festkörperphysik. Der Schwerpunkt liegt dabei auf zwei Materialklassen, topologischen Isolatoren und topologische Supraleiter. Zunächst wird ein Zweibandmodell, der Chern-Isolator, beschrieben, um das Konzept von topologischen Isolatoren und die Entstehung von Oberflächenzuständen darzulegen. Es ist möglich die Bandstruktur von Quecksilbertellurid- (HgTe-) Quantentrögen als zwei zeitumkehrinvariante Kopien des Chern-Isolators zu interpretieren, was zu einem 2D topologischen Isolator führt. Das Konzept von 2D-TIs wird auf drei Dimensionen erweitert. Eine Einführung in konventionelle Supraleitung und insbesondere die mikroskopische Theorie von Bardeen, Cooper und Schrieffer dient einem pädagogischen Zugang zur topologischen Supraleitung. Eine eindimensionale supraleitenden Kette, entwickelt von Alexei Kitaev, dient der Erklärung für die Entstehung von Majorana-Fermionen in p-Wellen Supraleitern. Es ist möglich diesen Zustand durch die Kombination von konventionellen Supraleitern und topologischen Isolatoren zu verwirklichen. In dieser Dissertation wird die erwartet topologische Supraleitung in einem sogenannten Josephson-Kontakt untersucht. Dabei wurde vorhergesagt, dass in einem "topologischen Josephson-Kontakt"die Phase des Suprastromes eine 4π-Periodizität besitzt, während ein normaler Josephson-Kontakt 2π-periodisch ist. Ziel dieser Arbeit ist der experimentelle Nachweis der 4π-Periodizität des Suprastroms in Josephson-Kontakten, die auf HgTe-Bauelementen beruhen. Als Methodik eignet sich die Messung der Shapiro-Plateaus und der Emission des Josephson-Kontaktes an, die ausführlich in den Kapiteln 3 bis 6 werden.

In Kapitel 3 wird der Transport in Josephson-Kontakten, die auf dem dreidimensionalen topologischen Isolator HgTe beruhen unter Einfluss von Mikrowellenstrahlung detailliert ausgeführt. Dieser Teil beginnt mit einem Überblick über die Eigenschaften von HgTe als dreidimensionaler topologischer Isolator und zeigt insbesondere den Nachweis der Oberfächenleitung von relativistischen Elektronen auf. Des Weiteren wird der Stand

der Forschung von Josephson-Kontakten auf diesem Materialsystem dargelegt. In solchen Strukturen werden nämlich aufgrund von Majorana-Fermionen gebundene Andreev-Zustände erwartet, welche sich in der Mitte der supraleitenden Bandlücke (bei null Energie) kreuzen. Sie werden als "gapless Andreev Bound States"bezeichnet. Die Existenz dieser Zustände kann durch den Nachweis einer 4π-Periodizität der Phase des Suprastroms bewiesen werden. Da die endliche Lebensdauer dieser Zustände "langsamen"dc-Messungen den Nachweis der Periodizität nicht erlauben, wird Strahlung im Gigahertz Frequenzbereich verwendet. Josephson-Kontakte aus 3D-HgTe-Heterostrukturen werden erfolgreich lithografiert. Zunächst werden die Strukturen mit dc-Messungen charakterisiert und es wird gezeigt, dass der Suprastrom einen Josephson-Effekt aufweist. Die Temperaturabhängigkeit des kritischen Stroms wird simuliert, wodurch die Bestimmung der Größe der induzierten supraleitenden Bandlücke ermöglicht wird. Durch Mikrowellenstrahlung entstehen Shapiro-Plateaus in der Strom-Spannungskennlinie $I-V$-Kurve. Der Spannungsabstand von zwei aufeinander folgenden Plateaus spiegelt die Periodizität des Josephsonstroms wider. Zu erwarten wäre, dass der Abstand in einem topologischen Josephson-Kontakt im Vergleich zu einem konventionellen Josephson-Kontakt doppelt so groß ist (oder anders formuliert: die ungeradzahligen Plateau-Indizes fehlen). In den Strom-Spannungskennlinien wird jedoch beobachtet, dass der erste erwartete Schritt ausbleibt. Alle höheren ungeradzahligen Schritte sind sichtbar. Durch die Untersuchung des Phänomens als Funktion von Mikrowellenfrequenz, Mikrowellenamplitude, Magnetfeldstärke und Probengeometrie wird argumentiert, dass die Ergebnisse der Experimente mit einem topologischen Andreev-Zustand und einer großen Zahl konventioneller Moden vereinbar sind.

Um die experimentellen Ergebnisse aus Kapitel 3 nachzuvollziehen, werden in Kapitel 4 die $I-V$-Kennlinie eines Josephson-Kontaktes mit einer linearen Kombination eines 2π- und eines 4π-periodischen Suprastroms unter Mikrowellenstrahlung numerisch simuliert. Dies erfolgt durch ein Netzwerkmodell, welches aus einem Josephson-Kontakt in Parallelschaltung zu einem ohmschen Widerstand besteht (RSJ-Modell). Die Ergebnisse aus Kapitel 3 können nur durch das Vorhandensein eines 4π-periodischem Suprastroms $I_{4\pi}$ eindeutig numerisch simuliert werden. Darüber hinaus wird herausgestellt, dass eine Kopplung des Systems an die 4π-periodische Komponente möglich ist, obwohl der Beitrag zum Gesamtstrom I_c sehr klein ist ($I_{4\pi} \ll I_c$).

Die Grundlage für die Experimente in Kapitel 5 bildet ein Josephson-Kontakt, der auf einem invertierten HgTe-Quantentrog basiert. Dieser besitzt helikale Randkanäle, welche mit Supraleitern topologisch geschützte Andreev-Zustände formen. Hierfür ist zuerst ein neuer Lithographieprozess zur Herstellung der Proben entwickelt worden. Da sich der HgTe-Quantentrog unter einer $Hg_{0.3}Cd_{0.7}Te$-Barriere befindet, muss diese für eine gute induzierte Supraleitung lokal entfernt und der Supraleiter aufgetragen werden, ohne das Vakuum zu brechen. Zur Variation der Ladungsträgerdichte im Josephson-Kontakt wird eine Feldeffektelektrode auf der Struktur platziert. Die Messung des Beugungsmusters des kritischen Stroms als Funktion des Magnetfeldes erlaubt es, die Stromverteilung in der Probe zu untersuchen. Das Beugungsmuster ähnelt dem eines supraleitenden Quanteninterferenzbauelement [engl. Superconducting Quantum Interference Device: (SQUID)] und zeigt, dass der Strom vorwiegend am Rand der Probe fließt. Durch die Bestrahlung mit Mikrowellen werden fehlende ungeradzahlige Shapiro-Plateaus bis zum

Stufenindex $n = 9$ beobachtet. Dies verdeutlicht, dass der Strom eine 4π-periodischen Beitrag aufweist. Das Experiment wird mit einem nicht-invertierten HgTe-Quantentrog wiederholt. Dieser ist nicht in der Quanten-Spin-Hall-Phase und zeigt über den gesamten Parameterbereich alle erwarteten Shapiro-Plateaus, was beweist, dass die Topologie der Probe eine wichtige Eigenschaft ist, um die 4π-Periodizität zu beobachten. Beide Effekte, das SQUID-Beugungsmuster und die verschwindenden ungeradzahligen Shapiro-Plateaus, sind in der Nähe der Quanten-Spin-Phase am sichtbarsten und können daher als Beweis für induzierte topologische Supraleitung in spinpolarisierten Randkanälen interpretiert werden.

Eine Messmethode zur direkten Bestimmung der Periodizität des Suprastromes, anders als die Verwendung von Shapiro-Plateaus, ist die Messung der Josephson-Emission, was in Kapitel 6 beschrieben wird. Ein topologischer Josephson-Kontakt emittiert Strahlung bei der halben Josephsonfrequenz $f_J/2$ aufgrund der 4π-Periodizität des Josephsonstromes. Hierfür wird ein neuer experimenteller Aufbau entwickelt, um das kleine Emissionssignal eines einzelnen Josephson-Kontaktes zu verstärken. Dieser neue Aufbau erlaubt es, das Spektrum eines invertierten HgTe-Quantentrog zu messen und eine Emission bei $f_J/2$ zu detektieren. Je nach Ladungsträgerdichte und Detektionfrequenz wird auch gewöhnliche Emission bei f_J im Spektrum beobachtet. Generell dominiert aber bei niedriger Spannung die $f_J/2$-Emission und bei höheren Spannungen die f_J. Da Spannung und ac-Frequenz durch die zweite Josephson-Gleichung proportional zueinander lässt sich das Verhalten mit den Ergebnissen der Shapiro-Plateau-Messungen vereinbaren. Darüber hinaus ist aus der Linienbreite der Emissionssignale eine Lebensdauer für die ABS in der Größenordnung von $0.3 - 4\,\mathrm{ns}$ für die $f_J/2$-Emission und $3 - 4\,\mathrm{ns}$ für die f_J-Emission abgeschätzt worden. Ein nicht-invertierter Quantentrog zeigt im Vergleich zum invertierten nur gewöhnliche Emission bei f_J über den gesamten zugänglichen Frequenz- und Ladungsträgerbereich.

Im letzten Teil der Arbeit, in Kapitel 7, wird die in den 3D-topologischen Isolator HgTe induzierte Supraleitung mit Hilfe von Andreev-Punktkontaktspektroskopie untersucht. Hierfür wird eine HgTe-Struktur mit einer Verengung fabriziert, deren Durchmesser kleiner als die mittlere freie Weglänge der topologischen Oberflächenzustände ist und somit eine energieabhängige Spektroskopie des Zustandes erlaubt. Auf einer Seite der Verengung werden supraleitende Paarkorrelationen durch einen gewöhnlichen Supraleiter Niob induziert. Diese Struktur ermöglicht daher die Untersuchung der Grenzfläche zwischen einem Supraleiter und einem Normalleiter (topologischer Isolator). Durch die Messung der differentiellen Leitfähigkeit dI/dV als Funktion der dc-Spannung ist es möglich die Energieabhängigkeit der Supraleitung zu untersuchen. Eine induzierte supraleitenden Bandlücke von $70\,\mu\mathrm{eV}$ wird gefunden. Die Leitfähigkeit zeigt Signaturen einer weiteren supraleitende Bandlücke des konventionellen Supraleiters Niob von $\Delta_{\mathrm{Nb}} \approx 1.1\,\mathrm{meV}$. Die Leitfähigkeit wird zum einen mit der Theorie von Blonder, Tinkham und Klapwijk modelliert und zum anderen mit einem erweiterten Modell, welches die 2D Oberflächenzustände des topologischen Isolators berücksichtigt simuliert. Für die Grenzfläche topologischer Isolator mit topologischem Supraleiter wird eine hohe Transmissionswahrscheinlichkeit (niedrige Barriere) festgestellt, während an der Grenzfläche zwischen dem konventionellen Supraleiter und dem topologischen Isolator eine hohe Barriere in Übereinstimmung mit dem Modell war. Der Transportmechanismus wird

durch eine Unterdrückung der induzierten Supraleitung durch eine Nichtgleichgewichtsverteilung der Zustände als Funktion der Spannung erklärt.

Die vorliegende Dissertation konnte klare Signaturen von induzierter topologischer Supraleitung in Josephson-Kontakten auf Basis von HgTe-Quantentrögen und Volumenmaterial aufzeigen. Sie kann auch als Ausgangspunkt für eine große Anzahl von weiterführenden Experimenten dienen. Die hier entwickelte Technik und auch Theorie kann auf andere topologische Zustände in Verbindung mit Supraleitern angewandt werden. Ein weiteres Experiment für HgTe-Strukturen ließe sich beispielsweise mit Hilfe von supraleitenden Resonatoren die Spektroskopie und Manipulation der mikroskopischen topologischen Andreev-Zustände durchführen. Diese Technik wurde schon erfolgreich von Janvier *et al*. auf mechanisch kontrollierten supraleitenden Bruchkontakten angewandt [Science 2015, 349, 1199-1202 (2015)]. Eine alternative Technik zur Spektroskopie der Andreev Zustände benötigt konventionelle Josephson-Kontakte in Kombination mit topologischen Kontakten. Die konventionellen Kontakte erlauben die Kontrolle der supraleitenden Phase und dienen als Spektrometer. Die Andreev-Punktkontaktspektroskopie kann auf zweidimensionale topologische Isolatoren erweitert werden. Auch kann eine supraleitende Schleife, welche die Kontrolle über die Phase und eine veränderbare Barriere ermöglicht, neue Einblicke in die Transportmechanismen geben. Solche Untersuchungen bieten Ansatzpunkte für die Lokalisierung von Majorana-Zuständen in Quanten-Spin-Hall-Systemen.

A

FABRICATION OF THE 3DTI JOSEPHSON JUNCTION

Every sample production starts with a MBE grown substrate cleaved into a roughly 3 mm × 3 mm big sample piece. This is cleaned in acetone using an ultrasonic bath (US), isopropanole and deionized water (DI-water). The process presented for the uncapped 3DTI was done without the use of the cluster.

Mesa definition

- Deposit sacrifical layer 10 nm SiO by PECVD at 80 °C.
- Spincoat 950K 3 % PMMA in ethyl lactate at 7000 rpm for 40 s and soft bake for 10 min at 80 °C.
- Ebeam exposure of the mesa structure with 2.5 kV with an aperture of 30 µm and an area dose of 70 µC/cm^2 and a magnification of 805 and 81.92 µm writefield.
- Development in isopropanol for 60 s, rinse in water and dry with nitrogen.
- E-gun evaporation of 20 nm Ti as a etch shield.
- Lift-off in acetone at 50 °C for about 25 min. Remove the metal with acetone spray and clean again in acetone, isopropanol and DI-water. Dry with nitrogen.
- Remove sacrifical SiO-layer in RIE with 15 s SiN etch program and clean PMMA residuals with 10 s mini clean program.
- Use argon sputtering to etch through the cap and and quantum well with (1 kV/1 kV/8 mA settings. Check for position dependend etch rates.).
- Remove titanium etch mask with buffered oxide etch 1:7 for 50 s.
- Clean in acetone, isopropanol and DI-water.

Deposition of the superconductor

- Spincoat 950K 3 % PMMA in ethyl lactate at 7000 rpm for 40 s and soft bake for 10 min at 80 °C.
- Ebeam exposure of the mesa structure with 2.5 kV with an aperture of 30 µm and an area dose of 70 µC/cm^2 and a magnification of 805 and 81.92 µm writefield.
- Development in isopropanol for 60 s, rinse in water and dry with nitrogen.
- Cleaning of the contact area with 5 to 6 s of Ar plasma.
- Take care that the path through the cleanroom from the etching chamber to the sputter chamber is free.
- Run! Transfer to the sputter chamber of the MBE to minimize oxidation time.
- Presputter about 50 nm of Nb
- Deposition of 70 nm Nb, 10 nm Al and 10 nm Ru at an relative angel of 20◦
- Lift-off in acetone at 50 °C for about 25 min. Remove the metal with acetone spray and clean again in aceton
- Clean in acetone, isopropanol and DI-water.

Optical contacts

- Spincoat HMDS at 6000 rpm for 20 s
- Spincoat ARN 4340 at 6000 rpm for 20 s and bake for 2 min at 80 °C.
- Expose for 20 s (8 W).
- Post-bake for 6 min at 80 °C.
- Development in AR 300-47 for 40 s.
- Short argon sputtering cleaning 5−10 *s* (1 kV/1 kV/8 mA settings). This step increases the sticking of the following metal layers and makes the bonding much easier.
- E-gun evaporation of 50 nm AuGe and 50 nm of Au.
- Lift-Off in acetone at 50 °C for 15 minutes.

B

FABRIACTION OF THE QSHI JOSEPHSON JUNCTION

Mesa definition

- Deposit sacrifical layer 10 nm SiO by PECVD at 80 °C.
- Spincoat 950K 3 % PMMA in ethyl lactate at 7000 rpm for 40 s and soft bake for 10 min at 80 °C.
- Ebeam exposure of the mesa structure with 2.5 kV with an aperture of 30 µm and an area dose of 70 µC/cm^2 and a magnification of 805 and 81.92 µm writefield.
- Development in isopropanol for 60 s, rinse in water and dry with nitrogen.
- E-gun evaporation of 20 nm Ti as a etch shield.
- Lift-off in acetone at 50 °C for about 25 min. Remove the metal with acetone spray and clean again in acetone, isopropanol and DI-water. Dry with nitrogen.
- Remove sacrifical SiO-layer in RIE with 15 s SiN etch program and clean PMMA residuals with 10 s mini clean program.
- Use argon sputtering to etch through the cap and and quantum well with (1 kV/1 kV/8 mA settings. Check for position dependend etch rates.).
- Remove titanium etch mask with buffered oxide etch 1:7 for 50 s.
- Clean in acetone, isopropanol and DI-water.

Superconducting contacts

- Spincoat 600K 6 % 6000 rpm for 40 s and bake for 10 min at 80 °C. Spincoat 950K 4 % 6000 rpm for 40 s and bake for 10 min at 80 °C.

- Ebeam exposure of the superconducting structure using proximity correction with 30 kV with an aperture of 20 µm and an area dose of 240 µC/cm^2 and a magnification of 870 and 81.92 µm writefield.
- Development in MIBP:IPA 1:3 for 60 s, development stop in IPA 30 s and DI-water.
- Use argon sputtering (1 kV/1 kV/8 mA settings) to etch through the cap layer of the mesa as the superconductor needs to be placed as close as possible to the HgTe layer for a good proximity effect. In-situ transfer to the evaporation chamber in the cluster tool.
- Evaporation of 5 nm Ti, 150 nm Al, 10 nm Ti and 10 Au.
- Lift-Off in acetone at 50 °C for 15 minutes.
- Clean in acetone, isopropanol and DI-water.

Gate electrode

- Spincoat 600K 6 % 6000 rpm for 40 s and bake for 10 min at 80 °C. Spincoat 950K 4 % 6000 rpm for 40 s and bake for 10 min at 80 °C.
- Ebeam exposure of the superconducting structure using proximity correction with 30 kV with an aperture of 20 µm and an area dose of 200 – 240 µC/cm^2 and a magnification of 870 and 81.92 µm writefield.
- Development in MIBP:IPA 1:3 for 60 s, development stop in IPA 30 s and DI-water.
- To remove PMMA residuals a short 5 s RIE mini clean step is done. This step is crucial that the ALD insulator sticks well on the surface.
- ALD growth of HfO_2. 90 cycles (approx $15-20\,nm$) at 35 °C.
- E-gun evaporation of 5 nm Ti and 150 nm of Au.
- Lift-Off in acetone at 50 °C for 15 minutes (a short ultra sonic bath of about 1 – 2 min was used to avoid side walls of the insulator).
- Clean in acetone, isopropanol and DI-water.

Optical contacts

- Spincoat ARN 4340 at 6000 rpm for 20 s and bake for 2 min at 80 °C.
- Expose for 20 s (8 W).
- Post-bake for 6 min at 80 °C.
- Development in AR 300-47 for 40 s.
- Short argon sputtering cleaning $5-10\,s$ (1 kV/1 kV/8 mA settings). This step increases the sticking of the following metal layers and makes the bonding much easier.
- E-gun evaporation of 50 nm AuGe and 50 nm of Au.
- Lift-Off in acetone at 50 °C for 15 minutes.

C

SAMPLE FABRICATION OF THE ANDREEV POINT-CONTACT

Mesa definition

- Deposit sacrifical layer 10 nm SiO by PECVD at 80 °C.
- Spincoat 950K 3 % PMMA in ethyl lactate at 7000 rpm for 40 s and soft bake for 10 min at 80 °C.
- Ebeam exposure of the mesa structure with 2.5 kV with an aperture of 30 µm and an area dose of 70 µC/cm^2 and a magnification of 805 and 81.92 µm writefield.
- Development in isopropanol for 60 s, rinse in water and dry with nitrogen.
- E-gun evaporation of 20 nm Ti as a etch shield.
- Lift-off in acetone at 50 °C for about 25 min. Remove the metal with acetone spray and clean again in acetone, isopropanol and DI-water. Dry with nitrogen.
- Remove sacrifical SiO-layer in RIE with 15 s SiN etch program and clean PMMA residuals with 10 s mini clean program.
- Use argon sputtering to etch through the cap and bulk layer with (1 kV/1 kV/8 mA settings. Check for position dependend etch rates.).
- Remove titanium etch mask with buffered oxide etch 1:7 for 50 s.
- Clean in acetone, isopropanol and DI-water.

Superconducting contacts

- Spincoat 600K 6 % 6000 rpm for 40 s and bake for 10 min at 80 °C. Spincoat 950K 4 % 6000 rpm for 40 s and bake for 10 min at 80 °C.

- Ebeam exposure of the superconducting structure using proximity correction with 30 kV with an aperture of 20 µm and an area dose of 240 µC/cm^2 and a magnification of 870 and 81.92 µm writefield.
- Development in MIBP:IPA 1:3 for 60 s, development stop in IPA 30 s and DI-water.
- Use argon sputtering (1 kV/1 kV/8 mA settings) to etch through the cap layer of the mesa as the superconductor needs to be placed as close as possible to the HgTe layer for a good proximity effect. In-situ transfer to the sputter chamber in the cluster tool.
- Sputtering of about 100 nm of niobium with 200 W power and the close up position.
- Lift-Off in acetone at 50 °C for 15 minutes.
- Clean in acetone, isopropanol and DI-water.

Normal contacts

- Spincoat 950K 3 % PMMA in ethyl lactate at 7000 rpm for 40 s and soft bake for 10 min at 80 °C.
- Ebeam exposure of the mesa structure with 2.5 kV with an aperture of 30 µm and an area dose of 70 µC/cm^2 and a magnification of 805 and 81.92 µm writefield.
- Development in isopropanol for 60 s, rinse in water and dry with nitrogen.
- Short argon sputtering cleaning step to remove PMMA residuals and the oxide barrier of 5 s (1 kV/1 kV/8 mA settings).
- E-gun evaporation of 50 nm AuGe and 50 nm of Au.
- Lift-Off in acetone at 50 °C for 15 minutes.
- Clean in acetone, isopropanol and DI-water.

Gate insulator

- Spincoat 600K 6 % 6000 rpm for 40 s and bake for 10 min at 80 °C. Spincoat 950K 4 % 6000 rpm for 40 s and bake for 10 min at 80 °C.
- Ebeam exposure of the superconducting structure using proximity correction with 30 kV with an aperture of 20 µm and an area dose of 200 – 240 µC/cm^2 and a magnification of 870 and 81.92 µm writefield.
- Development in MIBP:IPA 1:3 for 60 s, development stop in IPA 30 s and DI-water.
- To remove PMMA residuals a short 5 s RIE mini clean step is done. This step is crucial that the ALD insulator sticks well on the surface.
- ALD growth of HfO_2. 90 cycles (approx 15 – 20 nm) at 35 °C.
- E-gun evaporation of 50 nm AuGe and 50 – 100 nm of Au.

- Lift-Off in acetone at 50 °C for 15 minutes (a short ultra sonic bath of about 1 – 2 min was used to avoid side walls of the insulator).
- Clean in acetone, isopropanol and DI-water.

Optical contacts

- Spincoat ARN 4340 at 6000 rpm for 20 s and bake for 2 min at 80 °C.
- Expose for 20 s (8 W).
- Post-bake for 6 min at 80 °C.
- Development in AR 300-47 for 40 s.
- Short argon sputtering cleaning 5 – 10 *s* (1 kV/1 kV/8 mA settings). This step increases the sticking of the following metal layers and makes the bonding much easier.
- E-gun evaporation of 50 nm AuGe and 50 nm of Au.
- Lift-Off in acetone at 50 °C for 15 minutes.

LIST OF PUBLICATIONS

- OBSERVATION OF 1/B OSCILLATIONS FROM AN INSULATING TOPOLOGICAL STATE OF MATTER.
  D. Mahler, **J. Wiedenmann**, C. Thienel, F. Schmitt, C. Ames, P. Leubner, C. Brüne, H. Buhmann, D. Di Sante, C. Gould, G. Sangiovanni, and L. W. Molenkamp,
  Submitted to Nature Materials (2017).
- TRANSPORT SPECTROSCOPY OF INDUCED SUPERCONDUCTIVITY IN THE THREE-DIMENSIONAL TOPOLOGICAL INSULATOR HGTE.
  J. Wiedenmann, E. Liebhaber, J. Kübert, E. Bocquillon, P. Burset C. Ames, H. Buhmann, T.M. Klapwijk, and L.W. Molenkamp,
  Submitted to Physical Review B (2017).
- JOSEPHSON JUNCTION DYNAMICS IN THE PRESENCE OF 2π- AND 4π-PERIODIC SUPERCURRENTS.
  F. Domínguez, O. Kashuba, E. Bocquillon, **J. Wiedenmann**, R.S. Deacon, T.M. Klapwijk, G. Platero, L.W. Molenkamp, B. Trauzettel, and E.M. Hankiewicz,
  Physical Review Letters B 95, 195430 (2017).
- JOSEPHSON RADIATION FROM GAPLESS ANDREEV BOUND STATES IN HGTE-BASED TOPOLOGICAL JUNCTIONS.
  R.S. Deacon, **J. Wiedenmann**, E. Bocquillon, F. Dommínguez, T. M. Klapwijk, P. Leubner, C. Brüne, E.M. Hankiewicz, S. Tarucha, K. Ishibashi, H. Buhmann, and L.W. Molenkamp,
  Physical Review Letters X 7, 021011 (2017).
- GAPLESS ANDREEV BOUND STATES IN THE QUANTUM SPIN HALL INSULATOR HGTE.
  E. Bocquillon, R.S. Deacon, **J. Wiedenmann** , P. Leubner., T.M. Klapwijk, C. Brüne, K. Ishibashi, H. Buhmann and L.W. Molenkamp,
  Nature Nanotechnology 12, 137–143 (2017).
- SEARCHING FOR MAJORANA MODES IN HGTE TOPOLOGICAL INSULATOR JOSEPHSON JUNCTIONS.
  R.S. Deacon, **J. Wiedenmann**, E. Bocquillon, T.M. Klapwijk, C. Ames, C. Brüne, S. Tarucha, K. Ishibashi, H. Buhmann, L.W. Molenkamp
  AAPPS 26, 3 (2016).
- 4π-PERIODIC JOSEPHSON SUPERCURRENT IN HGTE-BASED TOPOLOGICAL JOSEPHSON JUNCTIONS.
  J. Wiedenmann, E. Bocquillon, R.S. Deacon, S. Hartinger, O. Herrmann, T.M. Klapwijk, L. Maier, C. Ames, C. Brüne, C. Gould, A. Oiwa, K. Ishibashi, S. Tarucha, H. Buhmann, and L.W. Molenkamp,
  Nature Communications, 10303 (2016).

ACKNOWLEDGEMENTS

The success of this PhD would have not been possible without the help of a large number of people. In this part I would like to express my gratitude to all of you.

I was lucky enough to be part of an extremely skilled, ambitious, and smart collaboration with Erwann, Russell and Teun. I am heavily in debt of these three people, all helping me in various aspects of my PhD. The work with you was always joyful and of high quality. Hopefully, the Würzburg-Paris-Delft-Riken-collaboration is far from being over. It was a pleasure working with you Sirs!

Laurens, thank you for the opportunity for accepting me as a PhD in your chair, the trust in me, representing you at various international conferences. Your chair is a really special place which can easily compete (and even exceed) with the possibilities in Harvard, Copenhagen or other high profile centers. I really enjoyed being part of EP3.

Hartmut, I would like to thank you for accepting me as one of your PhD students, the nice atmosphere you are creating in the group and the freedom in research.

Michael, thank you so much for the careful and always critical proof reading of my thesis and the continuous encouragements.

Björn, I want to express my gratitude to you for accepting my (apparently) unconventional request to have a theoretical physicist as a second referee of my thesis and the always useful and high-quality discussions during the Friday meetings in the past years. In this context I would also like to thank Prof. Bode for being the third referee in my defense and Prof. Hinrichsen for chairing this event.

My work was always supported by several bachelor and master students, namely: Eva, Lena Markus, Johannes, Julian, and Felix. You have all been of great help and I wish you all the best for your future.

It is important to mention all the battle scarred old fellows and veterans who welcomed me in the group and introduced me to the EP3 have to be mentioned as well. Worthy mentions include, Cornelius for introducing me into the lab and being my supervisor during my master thesis. I think our time was successful and unfortunately this was never rewarded with the appropriate scientific output. Luis, you were a great teacher in the cleanroom! Thank you very much for the patience. In this context I would like to mention Holger and Budy for making the lab days entertaining and the help in cryogenic and technical questions. Furthermore, Philipp and Christopher for supplying me with great material, on demand, all the time!

Thanks to all the people participating in the daily Kaffeerunde, lab-beer fridays (and all other days) and the general jibber jabber: Madder, David, Mirko, Simon, Olli, Lukas, Raimund and Gracy and of course our newly established band (Willi, Matthias and Angelika have not been mentioned yet). I doubt that there is any other group in the world where the Professor plays the guitar and the secretary sings next to a Ebeam machine (but its okay after six o'clock). It started from a stupid Christmas party idea but evolved to something really cool.

Thanks to all the other members of the EP3 for the mostly nice atmosphere in the group.

It is important to mention the often invisible people in the background. Without Volkmar, Joe and Tanja in the cleanroom, work would be not so smooth. The endless helium supply by Cornelius and Roland is of great value. The mechanical and electrical workshop was always helpful and quick to fix things I broke. Here I would like to thank especially Utz and Rainer.

All the theory attendants of the Friday meeting deserve to be mentioned as well. Thank you for the useful discussions, especially Fernando, Alex and Ewelina. I also want to thank Pablo for his quick and great help in modeling the data to satisfy a referee.

I would like to thank the 'Super' group (Amandeep, Sandeep, Martin and Olli) to cover my back during the process of writing this thesis and I am looking forward for an exciting next year.

The funding of my position by the Elitenetzwerk Bayern has to mentioned as well.

Finally, I would like express my gratitude to my family and especially my girlfriend Kristin for always supporting me and pretending interest when talking in unsolvable incomprehensible riddles to you.